PROBING THE ASTHENOSPHERE BENEATH THE AUSTRALIAN REGION WITH SURFACE GPS/GNSS

by

Bogdan Matviichuk, MSc

School of Geography, Planning, and Spatial Sciences
College of Sciences and Engineering

Submitted in fulfilment of the requirements for the degree of Doctor of Philosophy (Geomatic Engineering)

University of Tasmania
December 2021

To my wife, Anna

Declaration of originality

This thesis contains no material which has been accepted for a degree or diploma by the University or any other institution, except by way of background information and duly acknowledged in the thesis, and to the best of my knowledge and belief no material previously published or written by another person except where due acknowledgement is made in the text of the thesis, nor does the thesis contain any material that infringes copyright.

Bogdan Matviichuk
(30 May 2021)
PhD Candidate
School of Geography, Planning, and Spatial Sciences
University of Tasmania

Statement of authority of access

The publishers of the papers comprising Chapters 2, 3 and 4 hold the copyright for that content, and access should be sought from the respective journals.

Bogdan Matviichuk
(30 May 2021)
PhD Candidate
School of Geography, Planning, and Spatial Sciences
University of Tasmania

Statement regarding published work

Chapter 2 was published by Copernicus Publications as Matviichuk, B., King, M. A., & Watson, C. S. (2020). Estimating ocean tide loading displacements with GPS and GLONASS. *Solid Earth*, *11*(5), 1849–1863. https://doi.org/10.5194/se-11-1849-2020. This is an open access article under the terms of the Creative Commons Attribution 4.0 License, which permits use, distribution and reproduction in any medium, provided the original work is properly cited.

Chapter 3 was published by Wiley as Matviichuk, B., King, M. A., Watson, C. S., & Bos, M. S. (2021b). Limitations in One-Dimensional (an)Elastic Earth Models for Explaining GPS-Observed M2 Ocean Tide Loading Displacements in New Zealand. *Journal of Geophysical Research: Solid Earth*, *126*(6). https://doi.org/10.1029/2021JB021992. This is an article under the terms of the Creative Commons Attribution License, which permits use, distribution and reproduction in any medium, provided the original work is properly cited.

Chapter 4 has been submitted and is under review with Journal of Geodesy, 28 May 2021.

The remaining non published content of the thesis may be made available for loan and limited copying and communication in accordance with the Copyright Act 1968.

Bogdan Matviichuk
(30 May 2021)
PhD Candidate
School of Geography, Planning, and Spatial Sciences
University of Tasmania

Statement of co-authorship

The following people and institutions contributed to the publication of work undertaken as part of this thesis:

Candidate Bogdan Matviichuk, School of Geography, Planning, and Spatial Sciences, University of Tasmania

Author 1 Matt King, University of Tasmania (Primary Supervisor)

Author 2 Christopher Watson, University of Tasmania (Supervisor)

Author 3 Machiel Bos, Instituto Dom Luiz (IDL), University of Beira Interior (Co-author)

Author details and their roles:

Paper 1: Matviichuk, B., King, M. A., & Watson, C. S. (2020). Estimating ocean tide loading displacements with GPS and GLONASS. *Solid Earth*, *11*(5), 1849–1863. https://doi.org/10.5194/se-11-1849-2020.

Located in Chapter 2. Matviichuk (80 %), King (10 %), Watson (10 %)

BM was the primary author who developed the idea, acquired the data, executed the analysis and validation of the results, and was responsible for the manuscript preparation. MK and CW motivated and assisted in the design of the study, contributed to the interpretation and critically revised the manuscript. All authors helped refine the manuscript and gave final approval for publication.

Paper 2: Matviichuk, B., King, M. A., Watson, C. S., & Bos, M. S. (2021b). Limitations in One-Dimensional (an)Elastic Earth Models for Explaining GPS-Observed M2 Ocean Tide Loading Displacements in New Zealand. *Journal of Geophysical Research: Solid Earth*, *126*(6). https://doi.org/10.1029/2021JB021992.

Located in Chapter 3. Matviichuk (80 %), King (10 %), Watson (5 %), Bos (5 %)

BM was the primary author who developed the idea, acquired the data, executed the analysis and validation of the results, and was responsible for the manuscript preparation. MK and CW motivated and assisted in the design of the study, contributed to the interpretation and critically revised the manuscript. MB assisted with the numerical modelling, interpretation of the results and revision of the manuscript. All authors helped refine the manuscript and gave final approval for publication.

Paper 3: Matviichuk, B., King, M. A., Watson, C. S., & Bos, M. S. (2021a). Comparison of state of the art observed and predicted OTL displacements across the Australian continent. *Journal of Geodesy*, (in review)

Located in Chapter 4. Matviichuk (80 %), Bos (10 %), King (7 %), Watson (3 %)

BM was the primary author who developed the idea, acquired the data, executed the analysis and validation of the results, and was responsible for the manuscript preparation. MK and CW motivated and assisted in the design of the study, contributed to the interpretation and critically revised the manuscript. MB assisted with the numerical modelling, interpretation of the results and revision of the manuscript. All authors helped refine the manuscript and gave final approval for publication.

We the undersigned agree with the above stated proportion of work undertaken for each of the above published (or submitted) peer-reviewed manuscripts contributing to this thesis:

Bogdan Matviichuk (30 May 2021)
Candidate
School of Geography, Planning, and Spatial Sciences

Matt King (25 June 2021)
Primary Supervisor
School of Geography, Planning, and Spatial Sciences

Elaine Stratford (27 June 2021)
Associate Executive Dean
College of Sciences and Engineering

Abstract

PROBING THE ASTHENOSPHERE BENEATH THE AUSTRALIAN REGION WITH SURFACE GPS/GNSS

by Bogdan MATVIICHUK

The gravitational potential of celestial bodies, for example the Moon and the Sun, generates oscillating displacements of the Earth's surface, otherwise known as solid Earth Body Tides (SEBT). The magnitude of SEBT displacements reach heights of 40 cm and above. The changing gravitational potential over the surface of the earth at any given time induces the redistribution of the atmospheric and global ocean masses creating atmospheric and ocean tide loading displacements (ATLD and OTLD). The latter, OTLD, generally affects coastal areas with displacements up to 10 cm that decrease with distance inland. The periodical displacements affect geodetic observations (e.g., GNSS, SLR, VLBI, DORIS) used in scientific applications requiring geophysical interpretation (e.g., sea level rise, glacial isostatic adjustment) and corrections need to be applied to obtain unbiased measurements and thus a meaningful interpretation.

The energy associated with the SEBT is distributed pseudo-evenly over the Earth's interior while the loading-associated energy acts mainly on the outer shell – the Lithosphere and Upper Mantle. The Earth's rheological response to both ATLD and OTLD phenomena affects, in most cases, the elastic structure to depths of approximately 100 km. The inversion of observed tidal displacements may be used to infer the rheological properties of the lithosphere and asthenosphere at tidal frequencies – these may then be used to constrain geophysical models of the Upper Mantle. Improvements in these models are required in order to more accurately monitor elastic stresses, predict isostatic adjustment and stress relief events such as earthquakes.

Making use of the Global Positioning System (GPS) measurements to estimate tidal deformation of the Earth is now a well established approach. Expanding this to also include non-GPS Global Navigation Satellite Systems (GNSS) such as Russian GLObal Navigation Satellite System (GLONASS) is a current area of activity in the geodetic community. The use of GNSS more broadly to study tidal deformations of the Earth is the focus of this thesis.

National GNSS networks are essential for a wide variety of applications; these range from the geodetic to construction and agriculture, and due to an increasing need for improved spatial coverage are being actively expanded. GNSS sites observe tidal displacement directly, and a dense network of sites can enable the computation of tidal displacement at high spatial resolution. There are known limitations of GPS-only estimates of tidal deformation to infer the elastic structure of the Earth. A key limitation relates to the GPS orbital and constellation repeat periods. The GLONASS constellation has a different orbital configuration with constellation repeat periods well away from solar-related tidal frequencies.

Thus, GLONASS observations, in theory, should have less systematic error at frequencies problematic with GPS and important to tidal modelling.

This thesis develops our understanding of the GNSS estimation of OTLD and its application to inferences of geophysical properties through the analysis of three GNSS datasets: a subset of coastal stations in the United Kingdom, and sites across the New Zealand and Australia. The datasets span different spatial scales and tectonic conditions, but all have vast coastal areas that experience large tidal displacements. The variations between these datasets enable an assessment of the sensitivity to a wide range of conditions. In all cases, GNSS observations are compared to OTLD models after subtraction of modelled SEBT.

The thesis commences with an assessment of the performance of the GLONASS constellation in observing tidal loading displacements using previously published GPS-only results from western Europe as a baseline for the comparison. Combining GPS and GLONASS constellation observations improved the GPS-only geodetic timeseries, performing comparably for constituents M_2, N_2, O_1, P_1 and Q_1 to GPS-only with ambiguities resolved. The residuals of K_2 and K_1 constituents (GNSS-observed minus model) were improved with GPS+GLONASS but were shown to still be biased. The GLONASS S_2 constituent estimates were shown to have an elevation cutoff angle dependency while GPS estimates possessed a constant bias in the case of floating ambiguities solutions. Ambiguity resolution was demonstrated to substantially reduce the observed GPS bias.

Next, M_2 OTLD were analysed nearby an active tectonic margin using sites from the national geodetic network of New Zealand. Application of an anelastic dissipation correction, and varying water density and compressibility substantially improved the agreement between the various models and observed OTLD. Despite this, some regional spatially-coherent unmodelled residual signals remain in the North Island with significant magnitudes of up to 0.3 mm. These show substantial variation in phase over $\sim$100 km in the region producing the sharp change of the residual tidal signals between the Taupo Volcanic Zone and the East coast in the North Island. The residuals likely highlight the deficiencies of current models of Earth structure that do not model lateral variations in the rheological structure forced largely by ocean tide loading with negligible unmodelled SEBT.

Finally, the continental scale observations of M_2 and O_1 constituents from sites within the Australian national GNSS network were analysed using the advancements made and lessons learned from the previous two analyses. The scale of the studied region enabled the identification of residual tidal fields that could be associated with inconsistencies in the analysed GNSS orbit and clock products and centre-of-mass biases associated with global ocean tide models.

Each regional assessment undertaken in this thesis contributes to a better understanding of tidal phenomena and the way tides interact with the solid Earth, as well as our ability to observe them using space geodetic techniques. The addition of the dissipation, spatial water density and compressibility corrections was demonstrated to significantly reduce the residual OTLD. Further reduction, however, is limited by the inconsistency of the observed displacements when using different satellite products (e.g., $\sim$0.2 mm for M_2) and ignored lateral variations in the Earth's rheology. Multi-GNSS ambiguity resolution will contribute to the unraveling of this inconsistency and enable reliable geophysical interpretation of multiple tidal constituents to further increase the understanding of the Earth's interior processes and enhance both Earth and ocean tide models that have global implications.

Acknowledgements

What a journey it has been... the flood, the wallabies, the wombats. In writing this acknowledgement, I realise that my journey is more than a degree. It has given me another place I can call home, another group of people I can call family. I feel like there is an immeasurable list of people who have supported me throughout this PhD, this dream of mine.

Starting with my supervisors, Prof. Matt King, and Dr. Christopher Watson. They kicked off this journey and have supported me throughout the degree, including candidature and personal matters. I have learnt a lot from observing two opposing styles of guidance and mentorship that whilst appeared disparate on the surface were in fact complementary. You have given me confidence to question any scientific conclusion – look beyond. The weekly meeting supported this and many new things were discovered and discussed. I am prepared and feel confident to face new challenges ahead working hard by your example.

Also, this PhD could not have been completed without the assistance of Dr. Machiel Bos. His consistent support, valuable feedback together with a vast expertise in modelling tidal changes of the Earth cannot be underestimated. For that, I remain thankful.

Next, my university friends. I would like to thank Hadi Rezvani with whom countless topics were discussed: from middle-eastern culture to the pitfalls of the PhD life. I would like to acknowledge Deb McIntyre and Ron Maj for their unbelievable help on drafting several parts of thesis and just sound advice on the writing process in general.

A special thanks goes to my family for supporting my decision to pursue this PhD. Thank you for believing in my ability to persevere and complete this mammoth task and for keeping fingers crossed.

I would like to acknowledge a very special person in my life, who listened, who supported, who believed, who made all this possible – my wife Anna. It was you who backed me all the way, reminding me of the importance of the journey I have embarked on. Thank you so much, my dear, for pushing me, for keeping me on course for my dreams.

Contents

List of Figures

List of Tables

List of Abbreviations

CE	**C**entre of **E**arth frame
CF	**C**entre of **F**igure frame
CM	**C**entre of **M**ass frame
CoM	**C**entre of **M**ass
CME	**C**ommon **M**ode **E**rror
CN	**C**entre of **N**etwork
CORS	**C**ontinuously **O**perating **R**eference **S**tation
DOY	**D**ay **O**f **Y**ear
ECDF	**E**mpirical **C**umulative for **D**istribution **F**unction
ECMWF	**E**uropean **C**entre for **M**edium-range **W**eather **F**orecasts
GIPSY	**G**NSS-**I**nferred **P**ositioning **Sy**stem and Orbit Analysis Simulation Software
GLONASS	**GLO**bal **N**avigation **S**atellite **S**ystem
GNSS	**G**lobal **N**avigation **S**atellite **S**ystem
GPS	**G**lobal **P**ositioning **S**ystem
IERS	**I**nternational **E**arth **R**otation and Reference Systems **S**ervice
JPL	**J**et **P**ropulsion **L**aboratory
NASA	**N**ational **A**eronautics and **S**pace **A**dministration
OTL	**O**cean **T**ide **L**oading
OTLD	**O**cean **T**ide **L**oading **D**isplacement
PPP	**P**recise **P**oint **P**ositioning
PREM	**P**reliminary **R**eference **E**arth **M**odel
PSD	**P**ower **S**pectral **D**ensity
RINEX	**R**eceiver **In**dependent **Ex**change
RMS	**R**oot **M**ean **S**quare
SLR	**S**atellite **L**aser **R**anging
VLBI	**V**ery **L**ong **B**aseline **I**nterferometry

Chapter 1

Introduction

1.1 Overview

The Earth and its interior is a complex system that cannot be probed with a single geophysical method – infinitely many inversion solutions exist. A combination of geophysical methods and techniques provides additional constraints that can potentially lead to the convergence to a single solution – a unified Earth model. The intention of this thesis is to further advance the methodology of estimating tidal displacements of Earth's crust as a means to advance the geophysical interpretation of the spatially coherent residual tidal displacement fields.

Direct measurements and analysis of tidal displacements are of great of importance as they can provide independent measurements of Earth's elastic parameters that can be used to augment seismological and other geophysical observations of the Earth's elastic and anelastic structure and interior processes. National GNSS networks can not only provide direct measurements of tidal displacements but also have spatially dense coverage, including the coastal areas which are most susceptible to ocean tide loading displacements. The global coverage and increasingly high accuracy of GNSS geodetic observations make GNSS a perfect candidate for assessment of Earth's response to tidal loads.

1.1.1 Development of Plate Tectonics Theory

The phenomena of tidal displacement is based on the displacement of the solid lithosphere – a concept that can be traced back to the development of the principle of isostasy, more than 130 years ago. G.B. Everest, while Surveyor-General to India found a discrepancy in triangulation surveys of the northern Indian plains between positions determined by geodetic and astronomical techniques (Everest & East India Company, 1847). Studies of the geodesic anomaly led to the development of theories of isostasy (Airy, 1855; Pratt, 1854). It was well known that due to mass concentration there must be a specific deflection from the vertical observed especially in mountainous regions, but the computed deflection was less than expected from visible masses. This difference in observed and predicted deflection was first deeply studied in Pratt (1854) and Pratt (1855), and the first "modern" hypothesis of isostasy was formulated in Airy (1855) introducing a mechanical approach to the limit of crust rigidity.

Barrell (1914) introduced the original continental drift idea of a strong outer layer that could flow to maintain isostatic compensations over a mechanically weak layer. The evidence for continental drift were first summed up in Wegener (1912) where Wegener introduced the concept of horizontal movement of the continents and its relation with geophysical observations. This publication had a large influence on the overall understanding of the Earth's history and has since had many accompanying arguments constructed on the nature of the deformation of the Earth's crust.

1.1.2 Earth's asthenosphere

The broad theory of plate tectonics explains the behaviour of the uppermost layers of the Earth, which is divided into a number of thin, quasi-rigid plates which are in relative motion with respect to one another. Those parts of the outer shell that participate in these movements are referred to as the lithosphere, a relatively cool and rigid rock. The rocks beneath the lithosphere comprise the asthenosphere, a highly viscous and ductile-deforming region which allow the lithosphere to slide over it with relatively little resistance (Bo Pedersen, 2011). The presence of a weak layer beneath the lithosphere is associated with geophysical discontinuities in the seismic wave velocities, seismic energy attenuation, and electrical conductivity (Condie, 2016).

The application of the new and promising full-waveform seismic inversion methodology has produced a new class of tomography models suggesting a narrow width of the asthenosphere. These seismic studies have imaged a thin horizontal layer of $\sim$100–200 km depth extent beneath the lithosphere, with heterogeneity structures indicative of channelled flow (e.g., Colli et al., 2013; Fichtner et al., 2009; French et al., 2013).

Numerical simulations of global high-resolution mantle convection models confirm a very strong viscosity reduction in a very thin asthenosphere which allow velocities on the order of $\sim$20 cm/a to arise naturally. These simulations agree with seismological studies that find a thin horizontal layer in a depth of 100–200 km and presence of seismic heterogeneities. The results are also in agreement with recent geological observations of rapid uplift, short-wavelength dynamic topography signals, and V-shaped ridges of oceanic crust, indicative of high sublithospheric velocities (Weismüller et al., 2015).

The fundamental constraints on the interior density and elastic structure and dynamics, including mantle convection, come from the analysis of long-wavelength variations of Earth's geoid with seismic tomography (Hager et al., 1989). Geoid undulations are also caused by the periodical variations due to gravitational pull of celestial bodies, such as the Moon and the Sun. The geophysical tomography of tidal displacements has been demonstrated to be sensitive specifically to the viscoelastic asthenosphere and allows inversion of elastic properties at frequencies not studied before (Latychev et al., 2009; Lau et al., 2017). The derived elastic properties and their spatial distribution can impose additional constraints on the numerical simulations, increasing the accuracy of the derived Earth interior, specifically mantle processes. We follow with a detailed overview of tidal phenomena.

1.1.3 Earth tides and ocean tide loading

The gravitational potential of celestial bodies including the dominant contribution from the Moon and Sun, exerted on the Earth generates oscillating displacements of the Earth's surface, otherwise known as solid Earth Body Tides (SEBT). The eccentricities of the solar and lunar orbits and gravitational interactions with other celestial bodies in space produces a complicated gravitational attraction which results in a wide range of tidal periods known as tidal constituents. The magnitude of SEBT displacements may reach heights of 40 cm and above. The gravitational pull also induces the redistribution of the atmospheric and global ocean masses creating load displacements - Atmospheric Tide Loading (ATLD) and Ocean Tide Loading (OTLD). The latter, OTLD, generally affect coastal areas and can reach up to 10 cm. Periodical displacements affect geodetic observations (e.g., GNSS, SLR, VLBI, DORIS), and corrections need to be applied to obtain unbiased measurements for pursuits requiring geophysical interpretation (e.g., sea level rise, glacial isostatic adjustment) (Baker, 1984).

The energy associated with the SEBT is distributed pseudo-evenly over the Earth's interior while the loading-associated energy acts mainly on the outer shell – Lithosphere and Upper Mantle. The Earth's rheological response to both ATLD and OTLD phenomena affects, in most cases, the elastic structure to depths of 100 km. The inversion of tidal displacements may be used to infer the rheological properties of the lithosphere and asthenosphere at tidal frequencies that could be used to constrain geophysical models of the Upper Mantle. Improvements in these models are required in order to more accurately monitor elastic stresses, predict isostatic adjustment and stress relief events such as earthquakes.

The phenomena are coupled together in a single complex tidal oscillation. The inland areas of the continents experience small OTLD and thus enable precise studies of SEBT displacements. This allowed SEBT models to be tested to a level of accuracy in the order of 1% (Yuan & Chao, 2012) with the majority of the residual tidal displacement associated to the OTLD. The ATLD is concentrated in the two solar tidal constituents and while it can be modelled using meteorological models, the studies to date (e.g., Bos et al., 2015; Martens & Simons, 2020) largely concentrate on the lunar tidal constituents where the effect from ATLD is negligible.

In this thesis the focus is on the residual OTLD, the vector difference between modelled and observed OTLD, with possible unmodelled SEBT displacements treated as negligible. Modelling OTLD requires the a priori knowledge of ocean tide distribution at each tidal frequency and the knowledge of the Earth's rheological structure, with greater sensitivity to the structure of the shallowest 200 km or so. Thus, the residual OTLD can be related either to deficiencies in the ocean tide and/or Earth models. Modern ocean tide models generally have an accuracy of better than 1 cm for all tidal constituents. The accuracy drops only in the shelf (5 cm) and coastal areas (6.5 cm) (see Stammer et al., 2014) which usually produce very localized residual displacement patterns.

1.1.4 Studying tidal displacements with space geodetic methods

Historically, gravimeter or, to a lesser extent, VLBI observations have been used to assess the SEBT, OTLD and ATLD. Sparse spatial coverage limited their possible application to study the deficiencies of the relevant models limiting the possible reconstruction of the tidal displacement fields. National dense GNSS networks are essential for a wide variety of applications, from pure geodetic to construction and agriculture, which is why they are being actively expanded. GNSS data from these sites allow the estimation of tidal displacement and their spatial abundance can be used to provide tidal displacements over large areas (Bos et al., 2015; Ito & Simons, 2011; Yuan & Chao, 2012) or even globally with high spatial resolution (Yuan et al., 2013).

Tidal displacements derived from GNSS observations have already been used to infer the elastic structure of the Earth, however, several limitations are present. While the GPS constellation provides reliable measurement of OTLD at lunar constituents (e.g., M_2 and O_1), problems at solar-related constituents are apparent (e.g., S_2, K_2, K_1). The problems at K_1 and K_2 are directly related to the orbital and constellation repeat periods of the GPS constellation being equal to sidereal day and its harmonic. The K_1 and K_2 tidal displacements are therefore aliased with the GPS satellite orbits and related signals and cannot be reliably extracted from GPS-only coordinate solutions (Schenewerk et al., 2001). Allinson (2004) and King (2006) demonstrated GPS-only systematic errors at S_2 and P_1 in addition to previously mentioned K_1 and K_2, effectively demonstrating GPS issues at all major solar-related constituents.

The GLONASS constellation is located closer to the Earth than the GPS, and has orbital and constellation periods well away from solar periods. Thus, GLONASS observations should have less propagation of unmodelled effects at GPS-problematic tidal frequencies (Urschl et al., 2005). While the GLONASS constellation was completed by 1995, it rapidly declined in terms of operational satellites due to lack of funding, and this resulted in the geodetic community focusing on GPS only. The GLONASS constellation was fully restored in 2010, driving multiple national networks migration to GPS+GLONASS/Multi-GNSS receivers. The necessary timeseries length of 1000 days for reliable OTLD extractions as reported by Bos et al. (2015) is met nowadays by many GNSS sites creating a dense network of sites suitable for OTLD analysis.

1.1.5 Tidal response and Earth's (an)elasticity

GPS-based studies have now considered residual tidal displacements and concluded that there are deficiencies in the Preliminary Reference Earth Model (PREM) (Dziewonski & Anderson, 1981) and other purely elastic models. These include Ito and Simons (2011) and Yuan and Chao (2012) over GPS networks in the western USA, while Bos et al. (2015) found deficiencies of PREM over western Europe.

The above mentioned studies also assessed the transversely isotropic seismic reference model STW105 of Kustowski et al. (2008) while Bos et al. (2015) also analysed an upper mantle seismic tomography model S362ANI (Kustowski et al., 2008) which were demonstrated to perform better than PREM. Next, empirical Green's functions were computed which best-fit the derived OTLD residuals demonstrating improved fit with a reduction of the shear modulus in the asthenosphere, between 80 and 250 km across the western United

States (Ito & Simons, 2011) and between 50 and 340 km depth across western Europe (Bos et al., 2015).

The reference Earth models were derived mostly from the seismological observations of surface, long-period, and body waves. The periods of the selected observation are in the first minutes, ranging from >50 s to >200 s, however, need correction for frequency dependence of the elastic properties between the analysed and the reference frequency of 1Hz (Dziewonski & Anderson, 1981).

The frequency dependence of the elastic properties is related to the energy dissipation, mostly to its real part at tidal frequencies - the anelastic dispersion. The shear modulus is decreased as the period of the stress cycle is increased and observations at different frequencies should not be combined without first correcting them for this effect (Lambeck, 1988). The amount of dissipation is represented by the quality factor Q that is inversely related to the average energy E dissipated per cycle (see Bos et al., 2015; Zschau, 1978):

$$Q^{-1} = \frac{1}{2\pi E^*} \oint \frac{dE}{dt} dt \tag{1.1}$$

Here the contour integral over dE/dt is the energy dissipated during a complete cycle of sinusoidal straining, and E^* is the peak energy stored in the system during the cycle. We note that dissipation is mostly related to the dissipation in the shear modulus, ${Q_\mu}^{-1}$, while bulk modulus dissipation, ${Q_k}^{-1}$, can be effectively ignored at tidal periods. This quality factor is sometimes assumed to be independent of frequency or simply the same at seismic and tidal frequency band, although there is substantial evidence that Q is frequency dependent within some absorption band. The perturbations in the shear modulus μ at the specific frequency ω relative to the 1 Hz reference frequency (ω_0 = 1 Hz), at tidal frequency in our case, is estimated according to Lambeck (1988):

$$\delta\mu(\omega) = \frac{\mu}{Q_\mu} \left[\frac{2}{\pi} \ln(\omega) + i \right] \tag{1.2}$$

While the change in shear modulus within the seismic frequency band may be considered negligible, the variation between tidal ($>$ 12 h) and seismic (consider reference frequency of 1 Hz) frequencies was demonstrated to be responsible for the most part of asthenosphere's shear modulus reduction. Not accounting for the effect may lead to the false increase of the asthenosphere thickness in modelling of OTLD – for example, by around 100 km as was demonstrated by Bos et al. (2015). The same requirement also applies to OTLD forward modelling – a correction needs to be applied to account for the change in the elastic and anelastic properties.

1.2 Research motivation and the knowledge gap

While previous studies were based on GPS-only derived measurements of OTLD (e.g., Bos et al., 2015; Ito & Simons, 2011; King, 2006; Martens & Simons, 2020; Martens et al., 2016;

Thomas et al., 2007), the multi-GNSS networks have greatly expanded since and multiple regional multi-GNSS datasets have become available with often a superb spatial density of sites. Assessment of OTLD using non-GPS constellations and different combinations of constellations is a clear gap and area of interest given the potential to overcome some of the stated limitations of GPS.

The previous GPS-only studies were susceptible to errors at solar-related periods due to constellation and orbit periods being close to one sidereal day. GLONASS-only and GPS+GLONASS derived OTLD estimates should not be susceptible to GPS solar-related errors and have decreased absorption of associated errors into the coordinate timeseries as the constellation period is well away from solar periods. A rigorous assessment of GLONASS-only and GPS+GLONASS solution sensitivities and the differences incurred from different analysis centres orbits and clocks products is critical for further advancing the approach and thus improving the geophysical interpretation. The great amount of accumulated data from upgraded or newly deployed multi-GNSS stations over the last 10 years (since the time when GLONASS constellation was fully restored) and the general expansion of the GNSS networks should contribute to a high-spatial resolution geophysical interpretation of the multi-constituent tidal displacement fields.

The assessment of tidal residuals can be used as a quality check of ocean tide models. The deficiencies in a priori modelled OTLD can result in spurious signals that degrade the quality of geodetic timeseries. In addition, spatial water density and compressibility have not been accounted for in most studies. Depending on the ocean tide amplitude, the combined effect can exceed 0.5 mm in the up component at coastal sites. Improvements in the OTLD modelling, acquired through assessment and addressing the sources of the tidal and earth model related deficiencies, are important to the field of geodesy in general, as well as to relevant areas of geophysics.

The regions of Australia and New Zealand experience large ocean tides and tidal deformations but have not yet been studied in terms of their tidal field distribution either with GPS or GLONASS. The derived displacements in the region of New Zealand should contribute to the knowledge of tidal models, earth models, and their relationship with plate tectonics processes. The latter, tidal perturbations above the subduction plate, has been considered by Zürn et al. (1976) with maximum additional M_2 body tide displacement of up to 0.8% over the subducting zone.

Studying residual tidal displacements around subduction zones may lead to improved understanding of subduction processes. Assessment of the sensitivities of the GNSS-derived OTLD in the areas of rapid spatial variations of elastic properties is of great importance for robust geophysical interpretation of OTLD residuals in the regions of complicated geology.

While assessment of OTLD in Australia from GNSS is of interest on its own, the great scale of the Australian network, its tectonic stability, and marginal OTLD in central Australia should provide information on the possible errors within satellite products associated with unmodelled tidal signals that could potentially be absorbed by the OTLD estimates. Also, the majority of the Australian GNSS network has been upgraded to multi-GNSS thus invoking further assessment of GLONASS constellation and available GPS+GLONASS satellite products.

The change of elastic response at seismic and tidal frequencies should also be considered. Bos et al. (2015) demonstrated the need to consider anelastic dissipation of tidal energy in western Europe. The underlying theory of anelasticity suggests that the effect should be evident, perhaps to different degrees, in other regions. The anelastic response of the Earth is thought to be directly related to the asthenosphere and thus observations could be used to invert the asthenosphere's properties through optimizing Green's functions.

The knowledge gaps can be summarised as follows:

1. We do not know the precise anelastic structure of Earth's media that produces the tidal response and its spatial variation.
2. We do not know how accurately GNSS observations can observe deformations at tidal frequencies, especially away from M_2.

1.3 Benefits from addressing the knowledge gap

Better understanding of the Earth's elastic structure and its dynamics is of critical importance to several areas of science and wider industry and society in terms of precise satellite positioning. First, understanding the rheological structure of the asthenosphere is of relevance to accurately monitor elastic stresses, predict isostatic adjustment and stress relief events such as earthquakes. Second, ocean tide models can be validated through assessment of the residual OTLD. OTLD derived from constellations other than GPS and multi-GNSS combinations could be used to assess solar-related constituents of ocean tide models. Third, as demonstrated by Penna et al. (2007), unmodelled tidal displacements could alias into precise positioning timeseries creating spurious long-period signals, impacting all users of satellite positioning ultimately. These signals could potentially obscure the purely geophysical signals in the timeseries.

Improvements in these models are required in order to more accurately monitor elastic stresses, predict isostatic adjustment and stress relief events such as earthquakes.

1.4 Thesis research questions and objectives

To make a contribution to addressing the identified knowledge gap, three research questions (RQs) emerged. The RQs are accompanied with objectives, setting out the broad direction of the research to follow.

RQ1. What are the benefits from the addition of observations from the GLONASS constellation to GPS when estimating OTLD?

Accurate measurements of OTLD using GNSS stations requires understanding of all the possible variables that may impact the resulting solutions. Before interpretation of the results derived from GLONASS-related solutions, a calibration with previously derived results is needed. RQ1 is addressed in chapter 2 where results from GPS+GLONASS are compared with GPS-only results over a previously studied area of western Europe. We adapted a previous process to optimise coordinate and troposphere process noise to incorporate GLONASS and GPS+GLONASS constellation modes and the eight major tidal constituents (four semidiurnal and four diurnal). The described work shows the first estimates of each of the eight constituents from a combined GPS+GLONASS solutions that uses CODE and ESA orbit and clock products. Chapter 4 demonstrates a similar assessment of GLONASS performance over Australia at M_2 and O_1 while providing process noise tuning results for the eight constituents as in chapter 2.

The objectives that correspond to RQ1 are to assess the performance of the GLONASS constellation in standalone and in combination with GPS on estimating OTLD and are expanded below:

1. Expand the process noise test of Penna et al. (2015) to include additional constellation modes (GLONASS and GPS+GLONASS) using the NASA JPL GipsyX software.
2. Validate the GPS-derived tidal displacement using a previously applied approach with JPL native orbit and clock products and ambiguities fixed.
3. Assess the impact of different orbit products products on GPS-only (JPL, ESA and CODE), GLONASS-only (ESA, CODE) and GPS+GLONASS (ESA, CODE) solutions on the derived OTLD.
4. Interpret the derived residual OTLD estimates relative to the models based on the previously studied and most recent ocean tide atlases (e.g., FES2014b) and a set of Green's functions with an anelastic dissipation correction.

RQ2. Are the derived OTLD estimates sensitive enough to detect the properties of the Earth's interior?

The relationship between geophysical processes in the Earth's interior and their effect on the tidal response of the solid Earth is complex. Chapter 3 addresses RQ2 through assessment of data from New Zealand's GNSS network, specifically the dense array of sites in the Northern Island in the proximity of the Hikurangi subduction zone, including the Taupo Volcanic Zone above it. The coordinate and zenith wet delay process noise values were fine-tuned, and the impact on the resulting residual tidal displacement from inconsistencies in the ocean tide models was assessed. A set of different 1D anelastic Green's functions was explored but the analysis residual OTLD demonstrated the deficiencies of the 1D Earth modeling approach that is currently standard practice.

The objectives of RQ2 are focused on the analysis of OTLD near the active tectonic margin of New Zealand to assess the sensitivities to sharp lateral changes in the elastic properties:

1. Assemble and process the available GNSS data from stations over the New Zealand region

2. Compare OTLD models with GNSS estimates using global and local ocean tide models for New Zealand.

3. Assess the possible effect of three-dimensional variations in rheological structure on the residual OTLD.

RQ3. Are there variations of the residual OTLD field over a large blocks of stable continental crust and what are the possible sources of these variations?

Chapter 4 provides an assessment of GPS+GLONASS constellation mode performance for the tidal displacement estimation over a larger scale – the whole continent of Australia. The first analysis of the residual tidal displacement field in Australia addresses RQ3 by exploring the sensitivity of solutions to different orbit and clock products and additionally addresses RQ1 by assessing the GLONASS performance as standalone and augmentation to GPS over Australian GNSS networks. Chapter 4 demonstrates that assessment of tidal displacement can also be used as a quality control tool for orbit and clock products and ocean tide models.

While the main objective of RQ3 is to compute ocean tide loading displacements over the vast and comparably stable block of continental crust – Australia, the formulated objectives also contribute to answering RQ1 as the analysis is expanded with GLONASS constellation:

1. Process the available stations with GPS, GLONASS and GPS+GLONASS constellation modes using tuned process noise values.

2. Compare derived tidal displacements with that of ambiguity resolved GPS-only solutions (JPL products).

3. Assess differences between ESA and CODE GPS+GLONASS solutions related to the differences between orbit and clock products.

4. Assess global ocean tide models in the region and the impact of their inconsistencies on the OTLD.

5. Analyse the source of residual OTLD in Australia.

1.5 Thesis structure

The thesis seeks to address the identified knowledge gaps, with each of chapters 2, 3, and 4 focuses on different aspects of the residual OTLD interpretation. The thesis is designed as a thesis by publication – each chapter addresses the RQs and is published separately. The structure of the thesis and chapters relation to the RQs and objectives is demonstrated in Fig. 1.1.

Chapter 1, the Introduction, provides the background and context to this research. It has reviewed the plate tectonics theory and the asthenosphere – the weaker layer that enables movement of the plates. It is followed by a brief overview of the theory, dissipation of the tidal energy in the asthenosphere and how this displacements and dissipation can be measured with satellite geodesy in order to arrive at the key knowledge gap that is addressed in this thesis. The chapter then presents the key research questions and subsequent objectives that are proposed as the steps to answer the formulated research question and cover the knowledge gap stated.

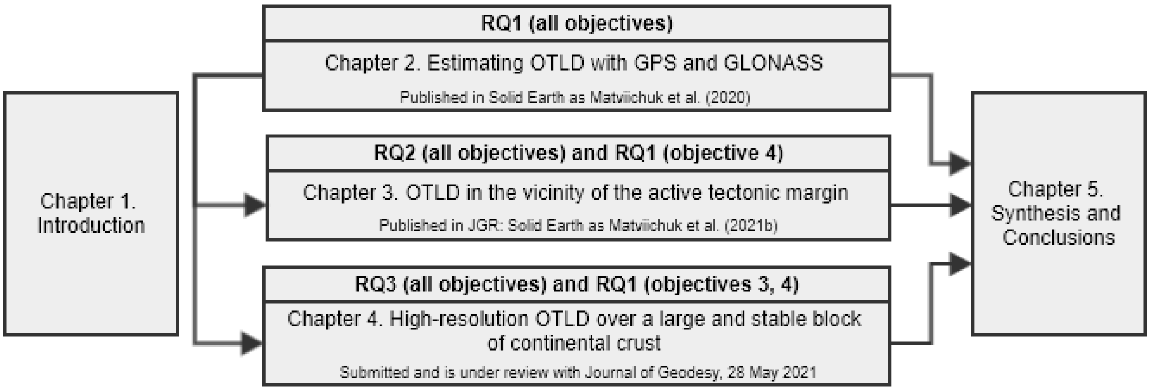

FIGURE 1.1: Thesis structure and link between chapters, research questions and objectives

Chapter 2 seeks to address the first research question, focusing on the validation of derived results relative to the previous studies and then carefully expanding and improving each part of the processing and analysis with an additional GNSS constellation, and additional tidal constituents.

Having investigated the performance of an additional GNSS constellation and the accuracy of the major tidal constituents, chapter 3 progresses to assess the possible interpretation of the residual OTLD, possibly linked to an active tectonic margin, the Hikurangi subduction zone in New Zealand. Chapter 3 corresponds to RQ2 and its objectives as set out above.

Chapter 4 provides a detailed analysis of the OTLD field over large and stable block of continental crust – Australia, using GPS and GLONASS constellations observations, developing further the multi-GNSS OTLD analysis and reviews possible geodetic/geophysical sources of residuals. Chapter 4 seeks to answer RQ3 through related objectives but also contributes to RQ1 with objectives related to multi-GNSS solutions and ocean tide models assessment (Objectives 3 and 4).

Thesis Context sections are provided at the end of each chapter to highlight the role of the chapter in addressing the overarching goals of the thesis and its connection to the following chapter.

Chapter 5 provides overarching conclusions determined from the three analysis chapters and follows with observed limitations. Finally, the thesis contributions to the body of knowledge are summed up and directions for future research are presented.

The appendices contain supporting information for each published chapters and a list of poster presentations undertaken during the PhD candidature.

Chapter 2

Estimating OTLD with GPS and GLONASS

Summary

Ground displacements due to ocean tide loading have previously been successfully observed using Global Positioning System (GPS) data, and such estimates for the principal lunar M_2 constituent have been used to infer the rheology and structure of the asthenosphere. The GPS orbital repeat period is close to that of several other major tidal constituents (K_1, K_2, S_2); thus, GPS estimates of ground displacement at these frequencies are subject to GPS systematic errors. We assess the addition of GLONASS (GLObal NAvigation Satellite System) to increase the accuracy and reliability of eight major ocean tide loading constituents: four semi-diurnal (M_2, S_2, N_2, K_2) and four diurnal constituents (K_1, O_1, P_1, Q_1). We revisit a previous GPS study, focusing on 21 sites in the UK and western Europe, expanding it with an assessment of GLONASS and GPS+GLONASS estimates. In the region, both GPS and GLONASS data have been abundant since 2010.0. We therefore focus on the period 2010.0–2014.0, a span considered long enough to reliably estimate the major constituents. Data were processed with a kinematic precise point positioning (PPP) strategy to produce site coordinate time series for each of three different modes: GPS, GLONASS and GPS+GLONASS. The GPS solution with ambiguities resolved was used as a baseline for performance assessment of the additional modes. GPS+GLONASS shows very close agreement with ambiguity resolved GPS for lunar constituents (M_2, N_2, O_1, Q_1) but with substantial differences for solar-related constituents (S_2, K_2, K_1, P_1), with solutions including GLONASS being generally closer to model estimates. While no single constellation mode performs best for all constituents and components, we propose to use a combination of constellation modes to recover tidal parameters: GPS+GLONASS for most constituents, except for K_2 and K_1 where GLONASS (north and up) and GPS with ambiguities resolved (east) perform best.

This chapter has been published as: Matviichuk, B., King, M. A., & Watson, C. S. (2020). Estimating ocean tide loading displacements with GPS and GLONASS. *Solid Earth*, *11*(5), 1849–1863. https://doi.org/10.5194/se-11-1849-2020. Minor changes have been made to the original published article for consistency in this thesis. This includes general terminology and grammar.

2.1 Introduction

Earth's gravitational interactions with the Sun and the Moon generate solid Earth and ocean tides. These tides produce periodic variations in both the gravity field and Earth's surface displacement. Additionally, the ocean tides produce a secondary deformational effect due to associated periodic water mass redistribution, known as ocean tide loading (OTL) (e.g. Agnew, 2015; Baker, 1984; Jentzsch, 1997). OTL is observable in surface displacements (and their spatial gradients, i.e. tilt and strain) and gravity. Displacement and gravity attenuate approximately as the inverse of the distance from the point load, while gradients have this relation but with distance squared (Baker, 1984). Thus, OTL displacement (OTLD) and gravity changes show greater sensitivity to regional solid Earth structure in comparison to tilt or strain observations (Martens et al., 2016), making this an observation of interest for studying solid Earth rheology.

Global Navigation Satellite Systems (GNSS) are particularly convenient for measuring OTLD due to the widescale deployment of dense instrument arrays. Data from continuous GNSS stations have been shown to provide estimates of OTLD with submillimetre precision using two main approaches as described by Penna et al. (2015): the harmonic parameter estimation approach – OTLD parameters are solved for within a static GNSS solution (e.g. Allinson, 2004; King, 2005; Schenewerk et al., 2001; Thomas et al., 2007; Yuan & Chao, 2012; Yuan et al., 2013); and the kinematic approach – OTLD constituents are predominantly estimated from high-rate kinematic GNSS-derived time series (e.g. Khan & Tscherning, 2001; King, 2006; Martens et al., 2016; Penna et al., 2015; Wang et al., 2020). In this thesis, we follow the kinematic approach.

To date, GNSS-derived OTLD have been estimated using predominantly the US Global Positioning System (GPS). GPS-derived measurements of Earth-surface displacement at tidal periods have been successfully used to observe OTLD and validate ocean tide models (King, 2005; Urschl et al., 2005). The residual displacement between observed and predicted OTLD has been related to deficiencies in ocean tide models, reference-frame inconsistencies, Earth model inaccuracies, the unmodelled constituents' dissipation effect and systematic errors in GPS (e.g. Bos et al., 2015; Ito & Simons, 2011; Thomas et al., 2007; Yuan et al., 2013).

Recent studies have made use of GPS-derived OTLD to study dissipation or anelastic dispersion effects in the shallow asthenosphere at the M_2 frequency (e.g. Bos et al., 2015). This type of investigation has not been easily done previously due to various limiting factors such as the accuracy of ocean tide models and the quality and availability of GPS observations. Recently, however, models have improved dramatically with the use of satellite altimetry (Stammer et al., 2014), and GNSS networks have both expanded and have improved data quality. Together, this has enabled the exploration of limitations in the global seismic Preliminary Reference Earth Model (PREM) (Dziewonski & Anderson, 1981) with GPS observations in the western United States (Ito & Simons, 2011; Yuan & Chao, 2012), western Europe (Bos et al., 2015), South America (Martens et al., 2016), the East China Sea region (Wang et al., 2020) and globally (Yuan et al., 2013). These limitations are associated partially with the incompatibility of the elastic parameters within the seismic (1 s period) and the tidal frequency bands and the anelasticity of the upper layers of the Earth, particularly the asthenosphere. The latter was studied through modelling the GPS-observed residuals of the major lunar tidal constituent, M_2, by Bos et al. (2015) and later Wang et al. (2020), while Lau et al. (2017) used M_2 residual from the global study of Yuan et al. (2013) to constrain Earth's deep-mantle buoyancy.

Previous studies have highlighted an apparently large error in solar-related constituents estimated from GPS, in particular K_2 and K_1. This is in part due to their closeness to the GPS orbital (K_2) and constellation (K_1) repeat periods, which strongly aliases with orbital errors. The closeness to the GPS constellation repeat period may induce interference from other signals such as site multipath which will repeat with this same characteristic period (Schenewerk et al., 2001; Thomas et al., 2007; Urschl et al., 2005). Additionally, the P_1 constituent has a period close to that of 24 h, which is the time span used for the International GNSS Service (IGS)-standard orbit and clock products (Griffiths & Ray, 2009), and hence may be contaminated by day-to-day discontinuities present in the products (Ito & Simons, 2011).

Urschl et al. (2005) proposed that the addition of GLONASS (GLObal NAvigation Satellite System), a GNSS developed and maintained by Russia (USSR before 1991), could improve the extraction of K_2 and K_1 constituents as the orbit period of the GLONASS satellites ($\sim$11 h 15 min 44 s) and constellation repeat period ($\sim$8 d) are well separated from major tidal frequencies. However, for many years, GLONASS suffered from an unstable satellite constellation and very sparse network of continuous observing stations. This has been progressively addressed over the last decade to the point where many national networks now include a high density of GLONASS (and other GNSS) receivers.

We seek to improve estimates of OTLD from continuous GNSS data, especially for constituents that are subject to systematic error in GPS-only solutions (e.g. S_2, K_2, K_1, P_1) as found in previous studies (Allinson, 2004; King, 2006; Yuan & Chao, 2012). We do this by using both GLONASS and GPS data to estimate amplitudes and phases for the eight major OTLD constituents (M_2, S_2, N_2, K_2, K_1, O_1, P_1, Q_1). As in the very recent study of Abbaszadeh et al. (2020), our work focuses particularly on understanding the sensitivity of estimates to different processing choices, although our work focuses on quite dense network in western Europe, while their work focused on a globally distributed set of stations.

2.2 Dataset

The sites used in our study are shown in Fig. 2.1, with a focus on south-west England where a large M_2 OTLD signal is present (see Table A.1). Of the 21 stations, 14 stations are in south-west England: covering both sides of the Bristol Channel (ANLX, SWAS, CARI, CAMO, PADT, APPL, TAUT) and northern coast of the English Channel up to Herstmonceux (PMTH, PRAE, EXMO, PBIL, POOL, CHIO, SANO, HERT) with one site (BRST) in the south. Two sites are in northern England (WEAR, LOFT) and two in Scotland (LERI, BRAE), with one site in central Europe (ZIM2). All sites are equipped with GPS+GLONASS

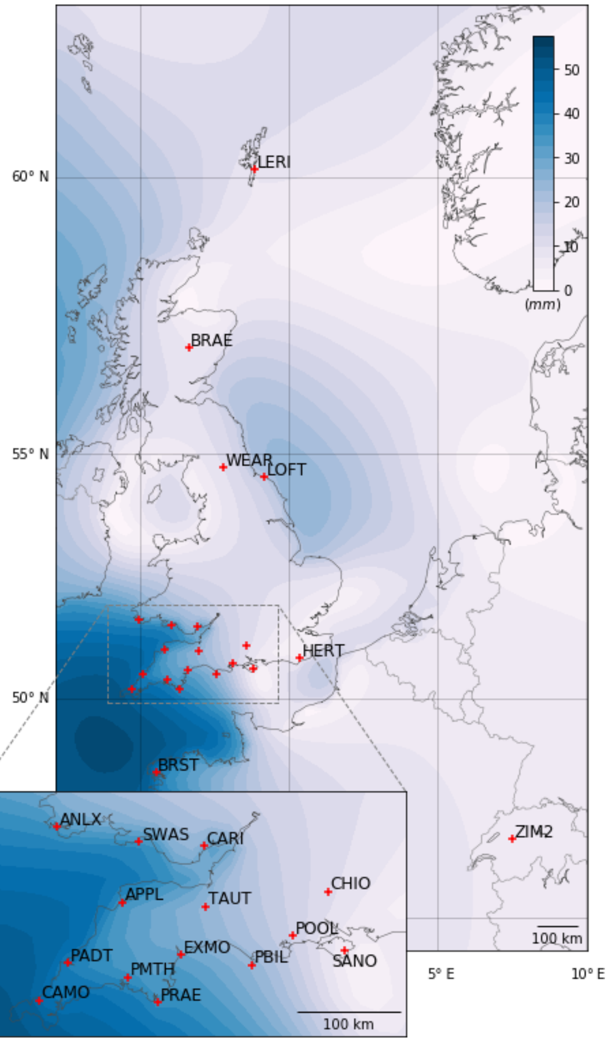

FIGURE 2.1: Map of the study area with GNSS site codes and M_2 up displacement amplitude in the background (TPXO7.2 ocean tide model and spherically symmetric Earth with PREM structure).

receivers. Note that sites CAMO, LERI and ZIM2 sites replace CAMB, LERW and ZIMM, respectively, which were used by Penna et al. (2015), to allow use of GLONASS data recorded at the former set of sites.

Aside from the addition of GLONASS data, an important difference to the study of Penna et al. (2015) is the shift in time period from 2007.0–2013.0 to 2010.0–2014.0. This shift provides sufficient GLONASS data following the upgrade of many receivers to track GLONASS from 2009 that followed the restoration of the GLONASS constellation that was finished in March 2010 (24 satellite vehicles; SVs). Despite this covering a shorter time span, the length of continuous observations at each site (minimum availability of 95 % through the dataset) exceeds the recommended $\sim$1000 d of continuous observations (4 years with 70 % availability) (Penna et al., 2015). The selected time period is fully covered by a complete and homogeneous set of reprocessed orbit and clock products.

The chosen sites experience a range of M_2 up OTLD amplitudes from $>$ 30 mm (ANLX, APPL, BRST, CAMO, PADT, PRAE), 15–30 mm (CARI, EXMO, LOFT, PBIL, SWAS, TAUT) and $<$ 15 mm (BRAE, CHIO, LERI, POOL, SANO, WEAR, ZIM2).

2.3 GNSS data processing strategy

The processing strategy was largely based on the GPS-only kinematic precise point positioning (PPP) approach (Zumberge et al., 1997) as per Penna et al. (2015) but with important modifications in terms of the software and to permit the inclusion of GLONASS data. We address PPP in three different modes here: GPS, GLONASS and combined GPS+GLONASS. In particular, we use NASA JPL's GipsyX (v1.3), which is a substantial rewrite of the now legacy GIPSY-OASIS code to allow for, amongst other things, multi-GNSS analysis. Penna et al. (2015) used GIPSY-OASIS v6.1.2. We adopted a PPP solution approach and estimated station positions every 5 min with a random walk model introducing estimated optimum between-epoch constraints on coordinate evolution. We used the VMF1 gridded troposphere mapping function, based on the European Centre for Medium-Range Weather Forecasts (ECMWF) numerical weather model (Boehm et al., 2006). Additionally, ECMWF values for the hydrostatic zenith delay and wet zenith delay were used as a priori values for stochastic estimation of the wet zenith delay as a random walk process with optimum process noise values (Sect. 2.5) and tropospheric gradients were estimated as a random walk process (Bar-Sever et al., 1998), with process noise at 0.005 mm/sqrt(s) (millimetres per square root second). An elevation cutoff angle of 7° was applied, sufficient to maximize the number of GLONASS observations at the respective site latitude as noted by Abbaszadeh et al. (2020), together with observation weights that were a function of the square root of the sine of the satellite elevation angle.

Earth body tide (EBT) and pole tides were modelled according to International Earth Rotation and Reference Systems Service (IERS) Conventions (Petit & Luzum, 2010). The OTLD within each processing run was modelled with the FES2004 tidal atlas (Lyard et al., 2006) and elastic Green functions based on the Gutenberg–Bullen Earth model (Farrell, 1972a) (referred to as FES2004_GBe), with centre-of-mass correction applied depending on the adopted orbit products. The FES2004-based OTLD values were computed using the free ocean tide loading provider that uses OLFG/OLMP software (http://holt.oso.chalmers.se/loading, last access: 1 October 2020), while the rest of OTLD values used in this chapter were computed with CARGA software (Bos & Baker, 2005). We did not model atmospheric S_2 tidal displacements.

PPP requires precomputed precise satellite orbit and clock products for each constellation processed, which should be solved for simultaneously within a single product's solution. Unfortunately, JPL's native clock and orbit products are not yet available for non-GPS constellations; hence, we adopted products from two IGS (Johnston et al., 2017) analysis centres (ACs): the European Space Agency (ESA) and Centre for Orbit Determination in Europe (CODE). The ESA combined GPS+GLONASS products from the IGS second reprocessing campaign (repro2) were used (Griffiths, 2019), while CODE's more recent REPRO_2015 campaign (Susnik et al., 2016) had to be used as CODE's repro2 is lacking separate 5 min GLONASS clocks.

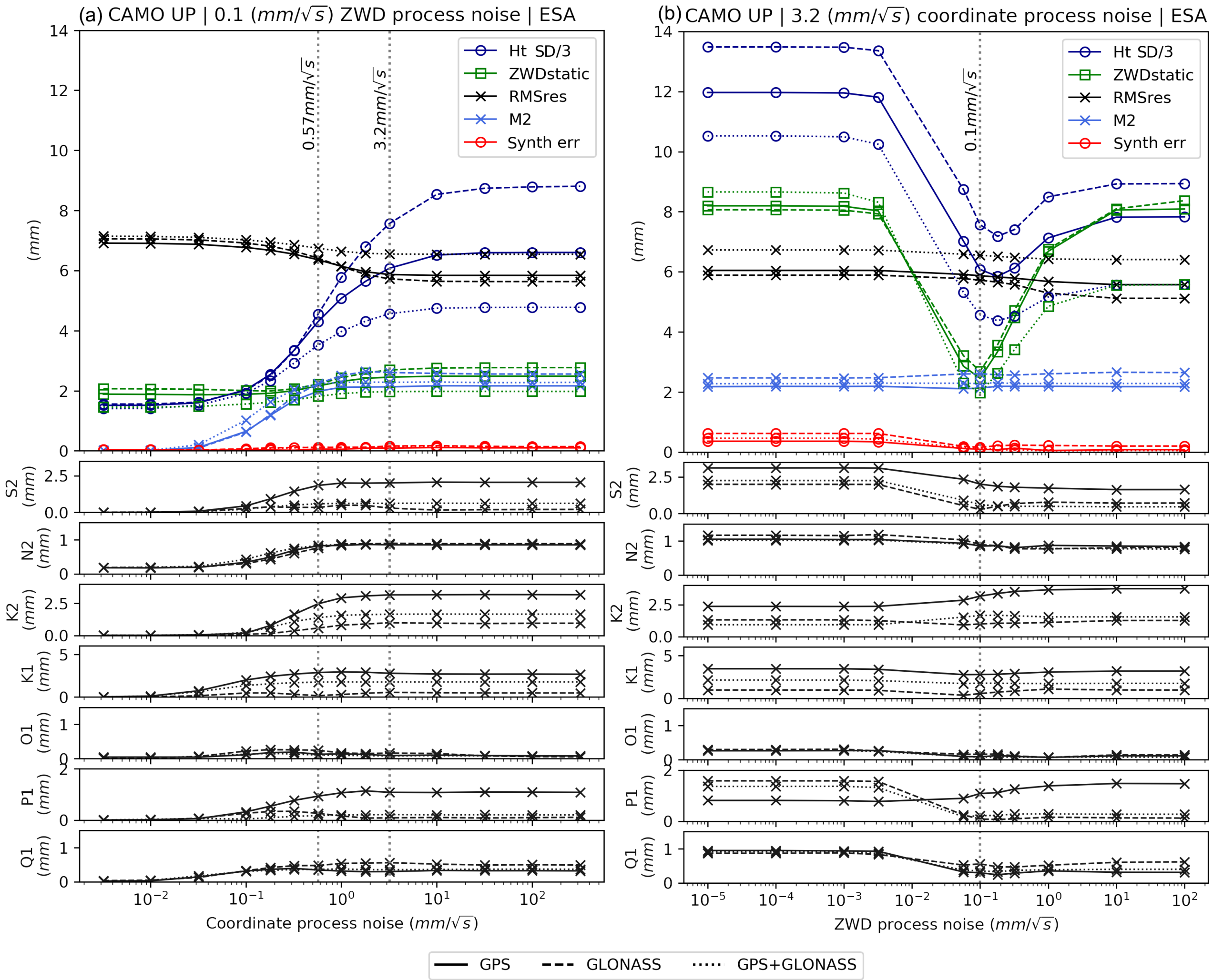

FIGURE 2.2: The effect of varying coordinate process noise **(a)** and zenith wet delay (ZWD) process noise **(b)** at test site CAMO for the up component (2010.0–2014.0), performed with ESA repro2 products. $\|Z_{\text{res}}\|$ is relative to FES2004_GBe. The different constellations' configurations: GPS, GLONASS and GPS+GLONASS are presented as solid, dashed and dotted lines, respectively. The colours pertain to the different metrics as described in the text and legend (note the same scheme is used as per Penna et al., 2015).

All three products consist of satellite orbits and clocks, sampled at 15 and 5 min, respectively, that were held fixed during our processing. The benefit of using JPL's native products, even though solely GPS, is the ability to perform PPP processing with integer ambiguity resolution (AR). PPP AR in GIPSY-OASIS/GipsyX software packages can be performed by using wide lane and phase bias tables which are part of JPL's native products (Bertiger et al., 2010). To provide comparison with previous studies, GPS was processed with JPL's native orbit and clock products from the repro2 campaign (JPL's internal name is repro2.1) with AR.

The CODE and ESA clock and orbit products were generated in different ways. CODE's REPRO_2015 orbit positions were computed using a 3 d data arc, while ESA used a 24 h data arc (Griffiths, 2019). Both ACs provided orbits in a terrestrial reference frame, namely IGS08 and IGb08, respectively, that are corrected for the centre-of-mass (geocentre) motion associated with OTLD (FES2004 centre-of-mass correction) and are in the CE frame, following Fu et al. (2012). Alternatively, JPL products were generated from a 30 h data arc and were computed with stations in a near-instantaneous frame realization; hence, the orbits are in the CM frame (we note that the JPL products distributed by the IGS are, by contrast, in CE). Considering the above, the modelled OTLD values for JPL's native products solutions were corrected for the effect of geocentre motion, while ESA/CODE products do not require this correction (Kouba, 2009).

It has been suggested that orbit arc length for a given product could potentially impact the estimated OTLD. In particular, Ito and Simons (2011) suggest that a 24 h data arc length (as per ESA products) may affect the P_1 constituent due to similarity of the periods. This is in addition to day-boundary edge effects given analysis of data in 24 h batches. We mitigate these effects to some extent by processing the ground stations in 30 h batches (allowing 3 h either side of the nominal 24 h day boundary).

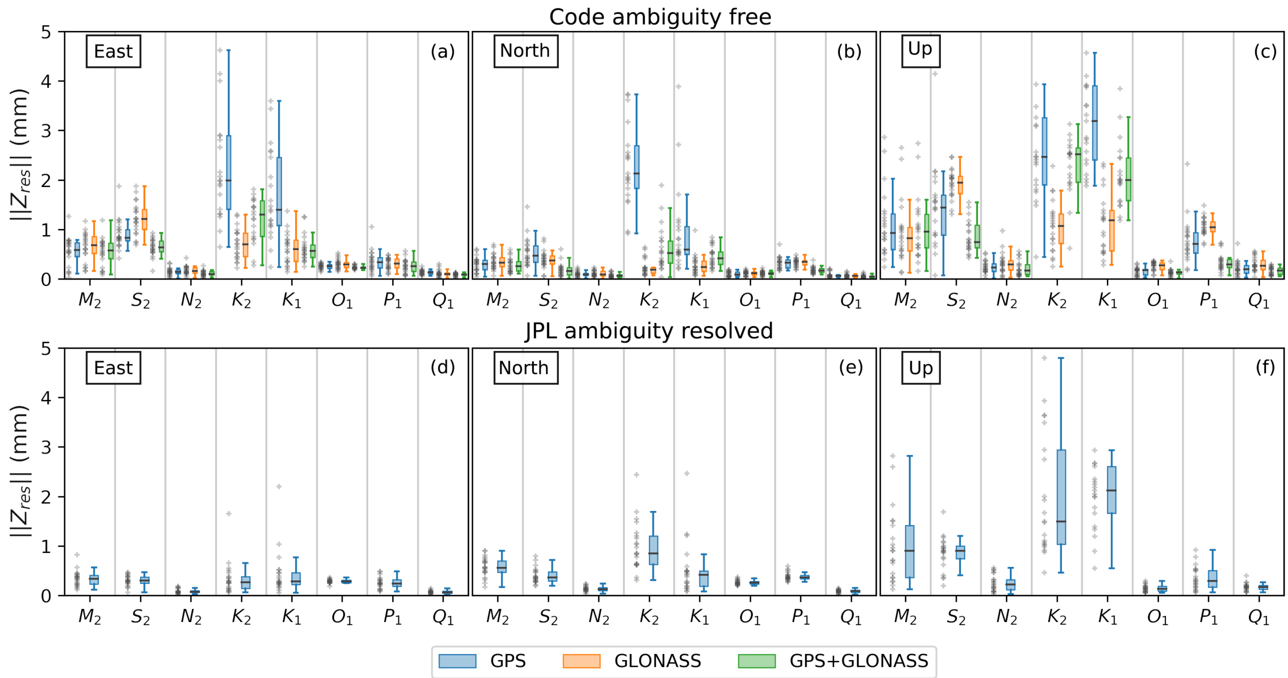

FIGURE 2.3: $\|Z_{\text{res}}\|$ per tidal constituent for east, north and up components (left, middle and right, respectively) relative to FES2014b_STW105d OTLD values with centre-of-mass correction (CMC) for JPL solutions. Grey crosses to the left of each boxplot represent sites' $\|Z_{\text{res}}\|$ values and are offset horizontally for clarity, while the horizontal line over each boxplot is a median of each constituent's $\|Z_{\text{res}}\|$. **(a–c)** $\|Z_{\text{res}}\|$ for GPS, GLONASS and GPS+GLONASS PPP solutions (blue, orange and green, respectively) computed using CODE products. **(d–f)** $\|Z_{\text{res}}\|$ of the GPS AR solution computed with JPL native products. The boxes show the interquartile range and the whiskers mark the limit of an additional $\pm 1.5 \times$ IQR, with the median as a horizontal line.

We post-processed the estimated coordinate time series as per Penna et al. (2015): the resulting 5 min sampled solutions were clipped to the respective 24 h window and merged together. Outliers were filtered from the raw 4-year time series using two consecutive outlier-detection strategies: rejecting epochs with extreme receiver clock bias values ($> 3 \times 10^3$ m) or where the XYZ σ was over 0.1 m and then rejecting epochs with residuals to a linear trend larger than 3 standard deviations per coordinate component. The XYZ time series were converted to a local east–north–up coordinate frame, detrended and resampled to

30 min sampling rate via a simple seven-point window average (seven samples – > one sample). The 30 min averaging reduces high-frequency noise (unrelated to OTLD) as well as the computational burden of further harmonic analysis.

Finally, OTLD modelled in GipsyX were added back using HARDISP (Petit & Luzum, 2010). HARDISP uses spline interpolation of the tidal admittance of 11 major constituents to infer values of 342 tidal constituents and generate a time series of tidal displacements. This approach almost eliminates the effect of companion constituents (Foreman & Henry, 1989) as they are modelled during the processing stage; small errors in the modelled major OTLD constituents will propagate into negligible errors in modelled companion tides. Thus, the analysed harmonic displacement parameters represent true displacement plus an indiscernible companion constituent error that is far below the measurement error. We tested the effect of the "remove–restore" OTLD procedure we adopted by solutions without modelling OTLD in GipsyX. The resulting differences in M_2 amplitudes were smaller than 0.1 mm, and this was reduced further when coordinate process noise was increased. This confirms that the results are independent of the prior FES2004_GBe OTLD values. The findings in the thesis are provided in the context of GipsyX software, and solutions derived using other software may produce different results especially if the underlying model choices differ.

The harmonic analysis of the reconstructed OTLD signal was performed using ETERNA software v.3.30 (Wenzel, 1996), resulting in amplitudes and local tidal potential phase lags negative which are suitable for solid Earth tide studies. OTLD phase lag, however, is defined with respect to the Greenwich meridian and phase lags are positive. Transforming to Greenwich-relative lags was done according to Boy et al. (2003) and Bos (2000). We then computed the vector difference between the reconstructed observed OTLD and that predicted by the model, following the notation of Yuan et al. (2013):

$$Z_{\mathrm{res}} = Z_{\mathrm{obs}} - Z_{\mathrm{th}}. \tag{2.1}$$

In Eq. (2.1), we assume body tide errors to be negligible; thus, Z_{obs} is simply an observed OTLD and Z_{th} is a theoretical OTLD, while Z_{res}, the residual OTLD, is their vector difference. Z_{res} presented in this chapter is, if not otherwise specified, relative to the theoretical OTLD values computed using the FES2014b ocean tide atlas, a successor of FES2012 used in Bos et al. (2015), and a Green function based on the STW105 Earth model additionally corrected for dissipation at the M_2 frequency which we call STW105d (referred to as FES2014b_STW105d). We utilize box-and-whisker plots to visualize the distribution of the estimates with the box and whiskers defined as the interquartile range (IQR) and an additional $\pm 1.5 \times$ IQR, respectively, with the median as a horizontal line.

2.4 Process noise optimization

Process noise settings within GipsyX need to be chosen to ensure optimal separation of site displacement, tropospheric zenith delays, noise, etc. For example, a tight coordinate process noise value, even the default value of 0.57 mm/sqrt(s), tends to clip OTL amplitudes, especially in coastal sites. Penna et al. (2015) developed a method of tuning process noise values for GPS PPP, which we expanded to accommodate the additional major diurnal/semi-diurnal constituents considered here, as well as the use of both GPS and GLONASS data.

To do this, we used the CAMO site, the successor of CAMB used by Penna et al. (2015), and tested a range of coordinate and zenith wet delay (ZWD) process noise settings exactly as described by Penna et al. (2015). We perform separate tests for GPS only, GLONASS only and GPS+GLONASS solutions. These tests focus on a range of metrics, namely the standard deviation of the height time series (shown as "Ht SD/3", as divided by 3), the standard deviation of kinematic ZWD normalized by ZWD values from a static solution ("ZWDstatic"), root mean square of the carrier phase residuals ("RMSres"), M_2 residual OTL magnitude, $\|Z_{\mathrm{res}}\|$, and $\|Z_{\mathrm{res}}\|$ of a synthetic ~13.96 h signal and its controlled, known input (designated "Synth err"). We focus on the results without the introduction of this synthetic signal here.

For each of the major constituents, both diurnal and semi-diurnal, and for each of the constellation choices, we found that 3.2 mm/sqrt(s) for coordinate process noise and 0.1 mm/sqrt(s) for tropospheric zenith delay process noise were optimal for our solutions, the same values as identified by Penna et al. (2015) for M_2 using GPS only. Figure 2.2 shows the results of the tests, with Fig. 2.2a showing the result of varying coordinate process noise, while ZWD process noise was held fixed (0.1 mm/sqrt(s), a default value) and Fig. 2.2b the result of varying the ZWD process noise with coordinate process noise equal to the optimum value of 3.2 mm/sqrt(s). The finding of identical optimal process noise settings for all constituents and constellations suggests that the different amplitudes and frequencies are less important than the data noise in the semi-diurnal and diurnal frequency bands and that the constellation-specific data noise does not substantially vary between constellations.

2.5 Results and discussion

Given the known accuracy of the ocean tide models in this region (Penna et al., 2015), and small effects of errors in solid Earth models, our assumption is that as $\|Z_{\mathrm{res}}\|$ approaches zero, the estimates increase in accuracy, also shown by Bos and Baker (2005). Based on previous studies (e.g. Yuan et al., 2013), we expected $\|Z_{\mathrm{res}}\|$ median values (up component) of ~2 mm for K_2 and K_1, ~1 mm for M_2, S_2 and P_1, and ~0.5 mm for N_2, O_1 and Q_1.

Figure 2.3a–c show GPS, GLONASS and GPS+GLONASS $\|Z_{\mathrm{res}}\|$ estimates for each of the east, north and up coordinate components. Over all components, the $\|Z_{\mathrm{res}}\|$ are uniformly small for N_2, O_1 and Q_1, with median around 0.1 mm. Residuals are slightly higher for M_2, P_1 and S_2, with the median being around 0.5–0.7 mm, and are often noticeably higher for K_1 and K_2, although there is substantial variation by constellation.

The combined GPS+GLONASS solutions perform either at the same level as GPS AR (M_2, O_1, Q_1) or better (N_2, P_1) for the up component. $\|Z_{\mathrm{res}}\|$ values are smaller and more consistent for the east (M_2, N_2, O_1) and north (M_2, N_2, P_1) components, respectively. The

GPS+GLONASS solution does not have $\|Z_{\text{res}}\|$ biases in the east and north components as is noticeable for the GPS AR solution (particularly for O_1 in the east and P_1 in the north, respectively). By $\|Z_{\text{res}}\|$ bias, we mean a noticeable gap between zero and the lower whisker.

Considering the problematic GPS K_2 and K_1 constituents, the GPS AR can reasonably reliably, in comparison to other types of solutions, extract $\|Z_{\text{res}}\|$ in the east component (Fig. 2.3d) which is smaller than that of GLONASS and GPS+GLONASS using ESA or CODE products. However, the smallest $\|Z_{\text{res}}\|$ in the up and north components is possible only using the GLONASS constellation solely which aligns with the conclusions of Abbaszadeh et al. (2020), who used ESA products and globally distributed GNSS network of sites.

Our results suggest that no single solution provides consistently better constituent estimates across all coordinate components. We suggest that optimum results are obtained using GPS+GLONASS for M_2, S_2, N_2, O_1, P_1 and Q_1, and GLONASS for K_2 and K_1, noting that GPS AR performs better for all constituents in the east component.

We now explore the sensitivity of our solutions to different products and analysis choices starting with elevation cutoff angle sensitivity, which particularly affects the amount of multipath influence on the coordinate time series. We pay particular attention to S_2, K_2, P_1 and K_1 given the large systematic errors evident in GPS-only solutions. We follow with an intercomparison of solutions using various products and then assess the impact of integer ambiguity resolution (GPS only). Finally, we test the stability of the constituent estimates to time series length.

2.5.1 Satellite orbit and clock product sensitivity tests

We assessed whether the solutions were sensitive to changes in satellite-elevation cutoff angle. Three additional cutoff angle scenarios were tested: 10°, 15° and 20° (in addition to the default 7° cutoff angle). Different elevation angle cutoffs will significantly alter the observation geometry as well as modulate the expression of signal multipath into solutions, decreasing the likely influence of multipath with higher cutoff values.

Figure 2.4a–c show the magnitude of vector difference, $\|\Delta Z_{\text{res}}\|$, between Z_{res} values estimated from the 7° and 20° solutions and CODE products in both cases. S_2, K_2, K_1 and P_1 constituents in the up coordinate component show larger mean magnitudes of vector differences in both GPS (0.56, 2.29, 2.88 and 0.54 mm, respectively) and GLONASS (0.82, 0.64, 1.01 and 0.58 mm, respectively) with the rest of constituents showing differences of less than 0.5 mm. GPS+GLONASS shows the smallest $\|\Delta Z_{\text{res}}\|$ between 7° and 20° cutoff estimates for S_2 and P_1 (0.31 and 0.23 mm, respectively) and an additional decrease in $\|\Delta Z_{\text{res}}\|$ for M_2, S_2,N_2, O_1 and Q_1 in the up component. The high agreement between OTLD values indicates the high stability of GPS+GLONASS estimates with changing cutoff angles.

The same comparison for GPS AR (7° and 20° cutoff, JPL native products) shows largely improved stability in comparison to all GPS-only ambiguity-free solutions (Fig. 2.4d–f). However, K_2 up and K_1 up show substantial differences between solutions: K_2 shows as

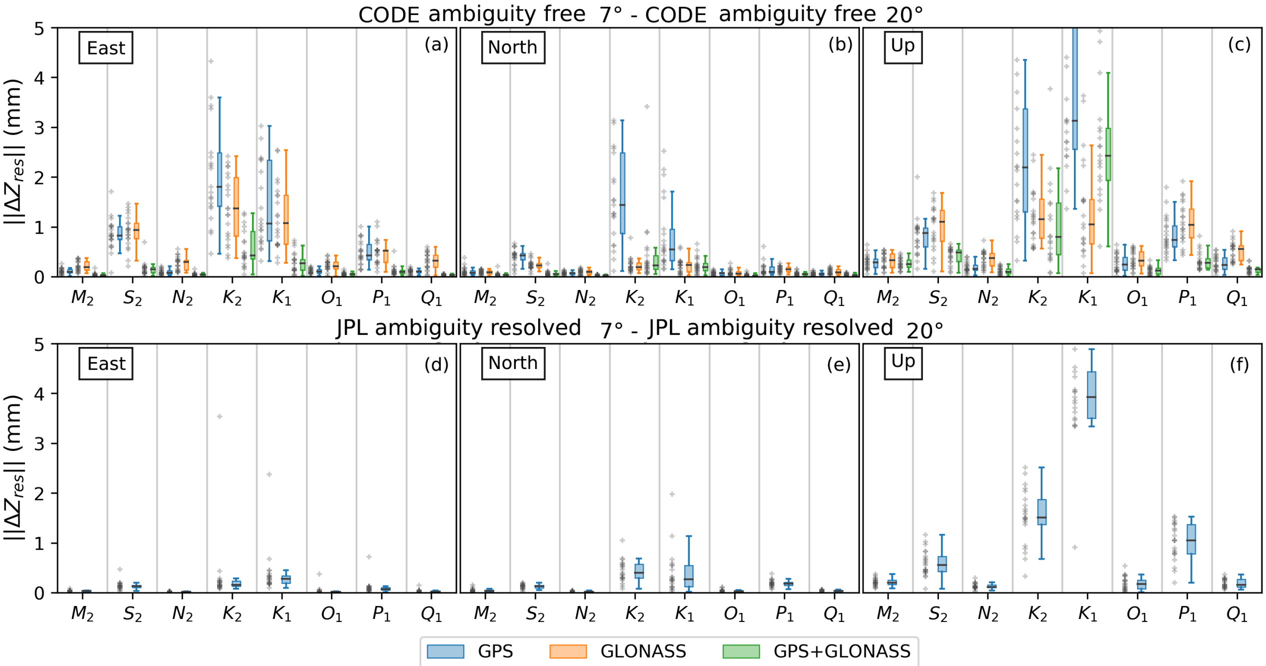

FIGURE 2.4: Magnitude of vector difference between estimated Z_{res} values computed with 7° and 20° elevation cutoff angles, $\|\Delta Z_{\text{res}}\|$, within the same set of orbits and clocks (**a–c** CODE; **d–f** JPL AR) for east, north and up coordinate components (left, middle and right, respectively). Grey crosses are as per Fig. 2.3. The smaller residuals using CODE products with GPS+GLONASS **(a–c)** are a result of improved OTLD stability as a function of cutoff angle using combined constellations (except K_1 up and K_2 up). JPL's GPS AR also shows great stability, with the exception of K_2 up and K_1 up. $\|\Delta Z_{\text{res}}\|$ for GPS, GLONASS and GPS+GLONASS PPP solutions is in blue, orange and green, respectively.

much smaller variance of $\|Z_{\text{res}}\|$ distribution in the 20° solution, possibly due to removal of multipath, and K_1 shows an increased variance and median of $\|Z_{\text{res}}\|$ at increased cutoff angle.

Following Yuan et al. (2013), we assessed the possible influence of inconsistencies in precomputed orbits or clocks on estimated OTLD. This was done by computing $\|\Delta Z_{\text{res}}\|$ between pairs of solutions with common constellation configurations: GPS (no AR here) solutions computed using ESA, CODE and JPL products; GLONASS/GPS+GLONASS solutions using ESA and CODE products. Figure 2.5a–c show the distribution of $\|\Delta Z_{\text{res}}\|$ between solutions computed with ESA and CODE products for all three constellation modes: GPS, GLONASS and GPS+GLONASS. The main differences are related to the S_2, K_2, K_1 and P_1 constituents. The maximum $\|\Delta Z_{\text{res}}\|$ between the observed OTLD for the rest of the constituents is less than ~0.3 mm.

Compared with GPS JPL, both CODE and ESA solutions (Fig. 2.5d–f and g–i, respectively) show $\|\Delta Z_{\text{res}}\|$ up to 0.5 mm in the horizontal components with respect to JPL solutions, which is also true for ESA in the up component with the exception of K_2 and K_1. CODE shows similar behaviour to ESA; however, significant divergence from JPL (Fig. 2.5d–f) is also observed for S_2 with even higher $\|\Delta Z_{\text{res}}\|$ for K_2 and K_1 in the up and the east.

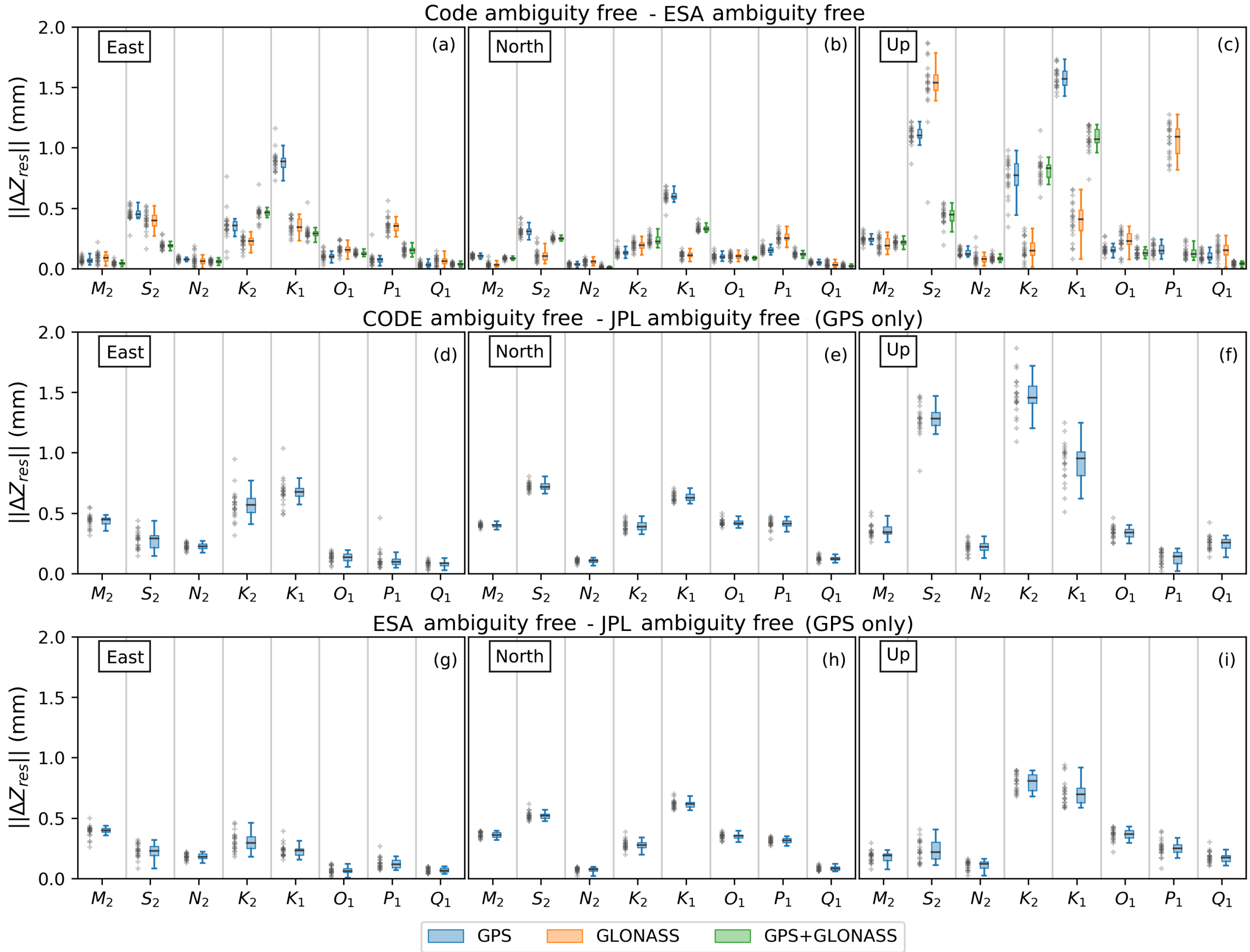

FIGURE 2.5: OTLD vector differences between CODE, ESA and JPL solutions (ambiguity free). **(a–c)** GPS, GLONASS and combined GPS+GLONASS differences between CODE and ESA solutions; **(d–f)** GPS difference between CODE and JPL solutions (ambiguity free); **(g–i)** GPS difference between ESA and JPL solutions (ambiguity free). Note the vertical scale of 2 mm. Grey crosses are as per Fig. 2.3.

2.5.2 S_2 constituent

Focusing on S_2, the GPS up residual shows ∼1 mm residual bias between solutions using CODE and ESA products (compare blue records between Fig. 2.6a and b). The GPS $\|Z_{\mathrm{res}}\|$ bias remains for solutions with a range of elevation cutoff angles (7°, 10°, 15° and 20°). GLONASS solutions (orange), however, show no $\|Z_{\mathrm{res}}\|$ bias for ESA and ∼1.5 mm bias for CODE, both with 7° elevation angle. GLONASS bias values with both products increase with elevation cutoff angle up to 15°. This GLONASS dependency with elevation cutoff is present to a lesser degree in both east and north components and is the same with ESA and CODE products (Fig. A.5).

GPS $\|Z_{\mathrm{res}}\|$ estimates show similar behaviour in terms of $\|Z_{\mathrm{res}}\|$ bias between ESA and CODE solutions in the up component (blue, Fig. 2.6) but ESA solutions' median $\|Z_{\mathrm{res}}\|$ values are ∼1 mm larger for all elevation cutoff angle solutions. Both ESA and CODE GPS+GLONASS S_2 results (green, Fig. 2.6) show a blend of the two patterns observed with GPS and GLONASS solutions. GPS+GLONASS S_2 shows less sensitivity to the cutoff angle

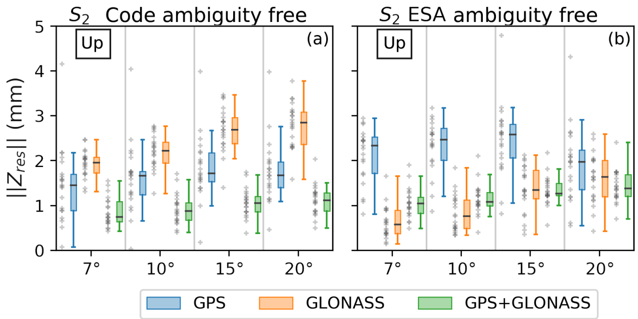

FIGURE 2.6: GPS, GLONASS and GPS+GLONASS $\|Z_{\mathrm{res}}\|$ for the S_2 constituent in the up component as a function of elevation cutoff angle, computed with ESA **(a)** and CODE products **(b)**. Note the inverse behaviour of GPS and GLONASS biases and the linear dependence of the GLONASS biases. Grey crosses are as per Fig. 2.3.

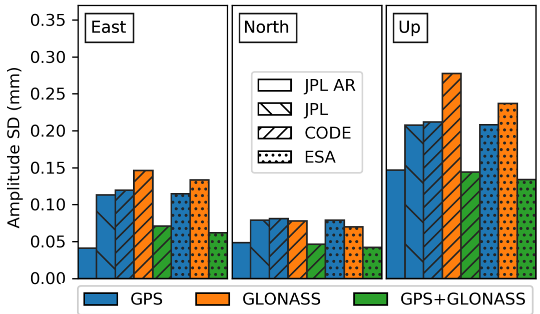

FIGURE 2.7: Average uncertainties (1σ) for OTLD amplitudes computed across eight constituents per products (stipple) and processing modes or constellation (colour): GLONASS (orange) and GPS (blue) modes show higher 1σ uncertainties, while GPS-only AR and combined GPS+GLONASS (green) show minimum 1σ uncertainties with the exception of east.

change than GLONASS or GPS solutions alone.

The substantial difference in S_2 between ESA and CODE (Fig. 2.6) suggests important differences in raw GNSS data analysis approaches within respective ACs. One relevant difference between products is in treatment of S_1 and S_2 atmospheric tides which were corrected for at the observation level in CODE products but not in ESA. However, the inverse behaviour of GPS and GLONASS between ESA and CODE solutions (orange, Fig. 2.6) cannot be explained with a single correction applied to both constellations. We expect that the differences in each solution are a function of satellite orbit modelling, although the exact origin is not clear and needs further investigation.

2.5.3 K_2 and K_1 constituents

As seen from Fig. 2.3, $\|Z_{\mathrm{res}}\|$ can be minimized if using GLONASS for the extraction of K_1 and K_2 constituents and GPS+GLONASS for the remainder of the constituents. In this case, $\|Z_{\mathrm{res}}\|$ will stay below 0.25 mm for north components and below 0.5 mm for the east and the up components.

GLONASS K_2 and K_1 estimates in the north have the lowest variance in $\|Z_{\mathrm{res}}\|$ and are most stable with different elevation cutoff angles and products. For the east component, CODE products with GLONASS have larger $\|Z_{\mathrm{res}}\|$ median and scatter than with

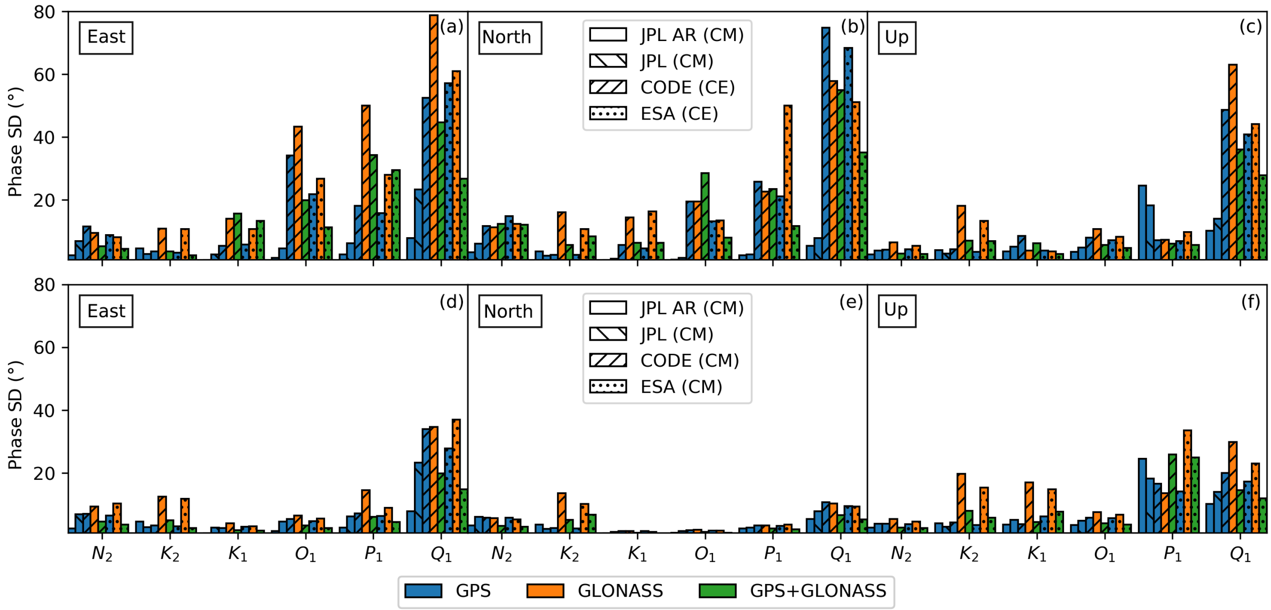

FIGURE 2.8: Average phase uncertainty per constituent for different products as returned by ETERNA. ESA and CODE products were in CE frame by default **(a–c)** and converted to CM **(d–f)**, while JPL products are in CM in both. M_2 and S_2 phase 1σ uncertainties are not shown here as values are too small to be seen with the scale specified.

GPS+GLONASS for K_1 and in terms of elevation cutoff stability (K_2 and K_1). Solutions using the ESA GLONASS products, however, perform better for K_1 east than the respective GPS+GLONASS in terms of $\|Z_{res}\|$ distribution consistency and median (Fig. A.2). Elevation cutoff stability of ESA K_2 and K_1 in the east component is best with GPS+GLONASS as also found when using CODE products.

The up component of K_2 and K_1 is the most problematic, showing high $\|Z_{res}\|$ values with all constellation modes. GLONASS OTLD values using either both ESA or CODE products have the smallest medians and variances of $\|Z_{res}\|$, outperforming JPL GPS AR. Note that GPS+GLONASS K_2 up has a marginally smaller median $\|\Delta Z_{res}\|$ in the elevation cutoff test than that of GLONASS only, possibly due to the larger number of total satellites; however, both K_2 and K_1 $\|Z_{res}\|$ suggest a $\sim$1.5 mm bias.

While we cannot definitively select a single constellation configuration optimal for all components of K_2 and K_1, we can conclude that based on our analysis, GLONASS solutions have smaller $\|Z_{res}\|$ in the K_2 and K_1 north and up components, while the east component shows better results with GPS+GLONASS (K_1, CODE). However, we recommend GLONASS-only solutions due to the higher level of agreement between solutions using ESA and CODE products. The only exception is the east component, where the preference is for JPL GPS AR (see Sect. 2.5.7).

2.5.4 P_1 constituent

GLONASS P_1 constituents show high $\|\Delta Z_{res}\|$ between CODE and ESA solutions over all coordinate components (orange, Fig. 2.5a–c). This was unexpected as ESA and CODE $\|Z_{res}\|$

boxplots show similar distributions of values (see Fig. A.2 in the Supplement for the equivalent ESA boxplots). This suggests a symmetrical deviation from the modelled values that produces a high $\|\Delta Z_{res}\|$. In all cases, however, GPS+GLONASS is preferred for P_1 estimation.

2.5.5 Effect of different orbit and clock products on noise and uncertainty

Changing orbit and clock products also changes the time series noise characteristics and hence influences the uncertainties of the estimated constituents (estimated separately by ETERNA for amplitude in Fig. 2.7 and phase in Fig. 2.8). Amplitude uncertainties are expressed here as an average across all constituents, as they do not differ much between analysed constituents. ETERNA assumes a white noise model in its analysis. We conclude that GLONASS solutions produce the highest amplitude uncertainties for east (0.15 mm CODE, 0.14 mm ESA) and up components (0.22 mm CODE, 0.27 mm ESA), while showing the same uncertainty as GPS for the north (0.07 mm, both CODE and ESA). GLONASS solutions using CODE products tend to have amplitude uncertainties that are marginally higher than those of ESA products. The amplitude uncertainties for combined GPS+GLONASS solutions are equal to those of JPL with ambiguities fixed (GPS AR), although the JPL GPS AR solution has slightly smaller uncertainty in the east component (smaller by $\sim$0.02 mm).

Considering the uncertainties of phase values, these are unsurprisingly dependent on the constituent's amplitude. Because JPL native products are in a CM frame, the constituent amplitudes are larger at the time of ETERNA analysis than those using ESA and CODE products which are both provided in a CE frame. For the ESA and CODE solution, this results in up to an order of magnitude increase in phase uncertainties for "weaker" diurnal constituents in the region: N_2, O_1, P_1, Q_1 (Fig. 2.8).

In general, this frame effect is directly related to centre-of-mass correction (CMC) specific to the constituent's CMC vector in comparison to the total theoretical OTLD vector. If applying a CMC correction to the constituent increases its amplitude, phase SD values will decrease in a CM frame solution. This is critically important for the constituents with amplitudes below 0.5 mm, as phase uncertainty increases significantly below this threshold. The most significant exception in our dataset is P_1 in the up component, which has a much larger amplitude in CE frame (Fig. 2.8c and f).

Converting CE products to CM (Fig. 2.8d–f) was done to demonstrate that the changes in phase uncertainty are indeed introduced by the smaller amplitudes in the CE frame. While this holds true, it is obvious that the P_1 up phase uncertainty increases, as was expected based on comparison with the JPL solutions. GLONASS K_1 up phase uncertainties show almost an order of magnitude increase in the CM frame while having unexpectedly small values in CE. This is a direct cause of GLONASS solution having larger K_1 up amplitudes in CE and smaller in CM with both CODE and ESA.

2.5.6 Impact of ambiguity resolution on GPS

The multi-GNSS products used here do not allow integer AR with PPP, and this is an active area of research and development within the IGS. However, assessing the impact of AR on GPS-only solutions provides some insight towards the future benefit of AR on GLONASS and GPS+GLONASS solutions once such products become available. We compared OTLD residuals from GPS and GPS AR using JPL native products that contain wide lane and phase bias tables (WLPB files) required for integer AR with PPP.

Figure 2.9 shows the effect on estimated constituents from enabling AR in a standard solution with 7° cutoff. Here, we observe decreased $\|Z_{\text{res}}\|$ over all coordinate components compared with the estimates from a non-AR solution. This is most visible in the K_2 and K_1 constituents and in the elimination of the S_2 $\|Z_{\text{res}}\|$ bias and with smaller improvements in M_2 and P_1.

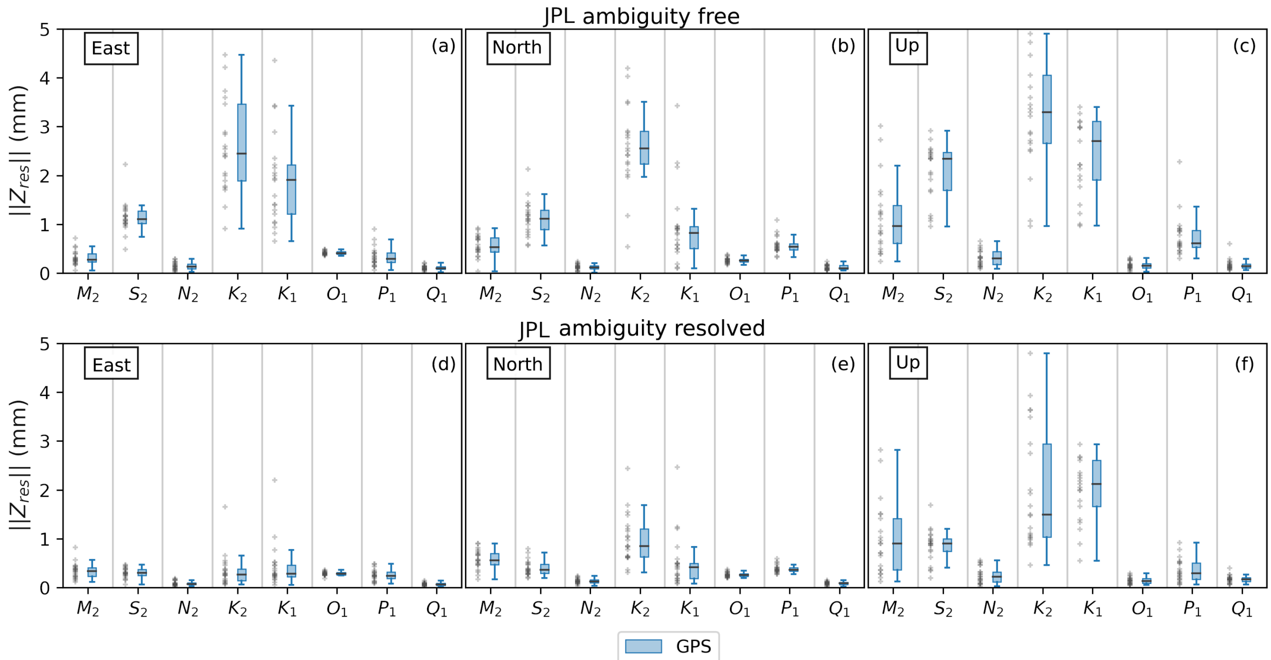

FIGURE 2.9: Comparison of residual constituents' estimates from GPS **(a–c)** and GPS AR **(d–f)** JPL native solutions. Grey crosses are as per Fig. 2.3. As seen, most of constituents' $\|Z_{\text{res}}\|$ distribution variances and medians are smaller, while S_2 $\|Z_{\text{res}}\|$ bias is removed with AR solutions.

Importantly, Fig. 2.9 shows that enabling AR eliminates $\|Z_{\text{res}}\|$ bias in GPS and aligns the residual vectors with ESA/CODE GPS+GLONASS (Fig. 2.3). This is a clearer improvement than reported by Thomas et al. (2007).

Given this effect, the S_2 $\|Z_{\text{res}}\|$ bias was once again assessed with various elevation cutoff angles solutions. JPL GPS solutions (floating AR), in the up component (Fig. 2.10a), show the S_2 $\|Z_{\text{res}}\|$ bias to be constant with cutoff angle, being about 1 mm, and with the $\|Z_{\text{res}}\|$ variance of around 3 mm. Similar behaviour was previously observed with solutions using ESA products (Fig. 2.6).

Enabling integer ambiguity resolution (GPS AR) removes the ~1 mm S_2 $\|Z_{\text{res}}\|$ bias completely at 7° and 10° elevation cutoff angles while leaving ~0.4 mm bias at 15° and 20° in

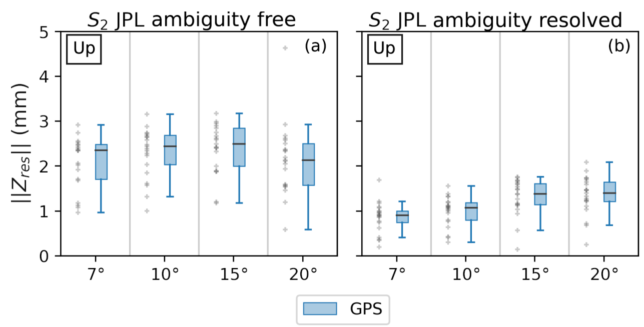

FIGURE 2.10: GPS S_2 up constituent's $\|Z_{\mathrm{res}}\|$ change with elevation cutoff angle computed with JPL products floating AR **(a)** and integer AR **(b)**. Grey crosses are as per Fig. 2.3. As seen, AR helps in removing the bias and decreases the $\|Z_{\mathrm{res}}\|$ distribution variance.

the up component. Consequently, up $\|Z_{\mathrm{res}}\|$ medians change by 1–2 mm depending on elevation cutoff angle. Based on this observation, we expect that resolving ambiguities within PPP might help in solving, or at least minimizing, the S_2 $\|Z_{\mathrm{res}}\|$ present in ESA GPS and CODE GLONASS solutions. Eliminating biases in GPS and GLONASS separately should increase the stability and consistency of GPS+GLONASS S_2 $\|Z_{\mathrm{res}}\|$.

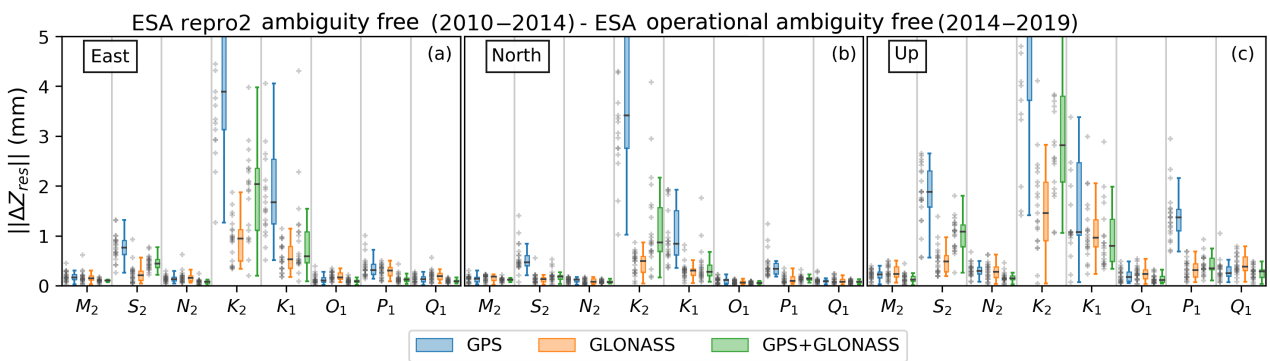

FIGURE 2.11: OTLD vector differences between ESA repro2 (2010.0–2014.0) and ESA operational (2014.0–2019.0) OTLD estimates: GPS (blue), GLONASS (orange) and GPS+GLONASS (green) constellation modes present. Grey crosses are as per Fig. 2.3.

2.5.7 Impact of time series length

Yuan et al. (2013) used a filter-based harmonic parameter estimation approach and examined the dependence of Kalman filter convergence on time series length for each of the eight major constituents. Yuan et al. (2013) concluded that, after 1000 daily solutions, convergence (minimized $\|Z_{\mathrm{res}}\|$) was reached for lunar-only constituents (M_2, N_2, O_1, Q_1), while reporting solar-related constituents (S_2, K_2, K_1, P_1) were not fully converged even after 3000 daily solutions.

We assessed how $\|Z_{\mathrm{res}}\|$ of each of eight major constituents varies as a function of the time series length with kinematic estimation approach. The duration of the series varied by integer years and, to enable a complete analysis, we expanded the candidate solutions to 2019.0 and processed additional data with operational products: JPL repro3.0, ESA operational, CODE MGEX (CODE operational lacks GLONASS clock corrections). While the goal of a reprocessing campaign is to preserve consistency with operational products (Griffiths,

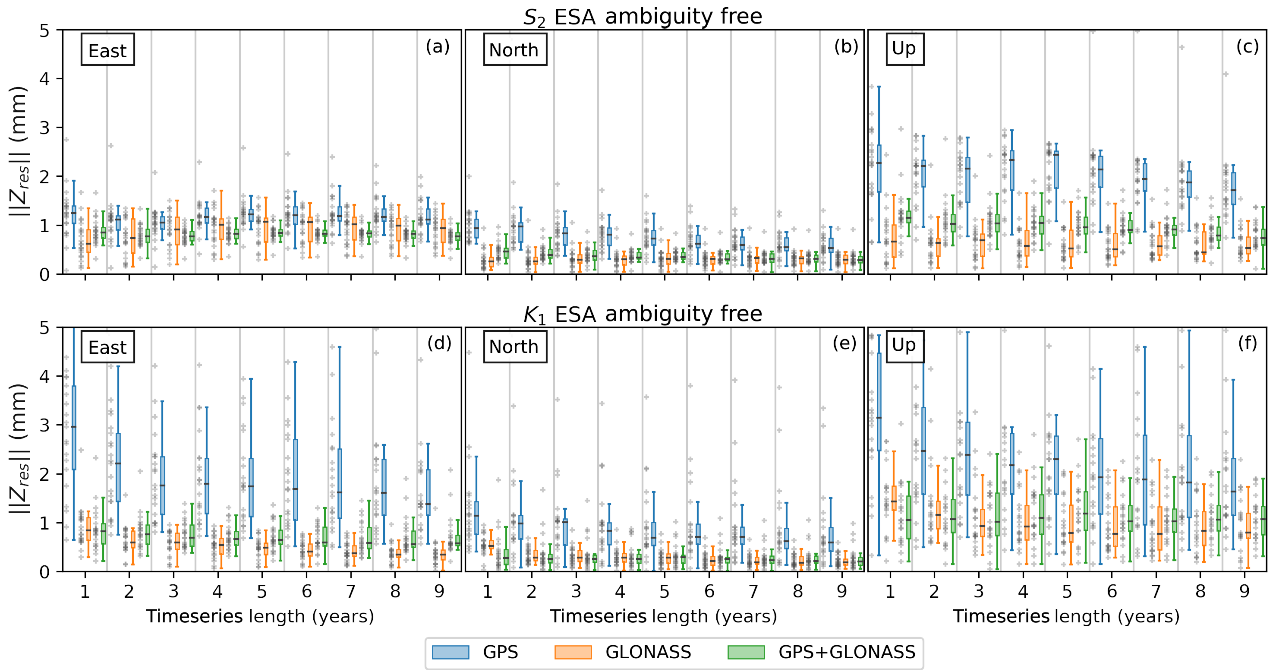

FIGURE 2.12: Dependency of estimated $||Z_{\text{res}}||$ and time series' length in years for two solar-related constituents: S_2 **(a–c)** and K_1 **(d–f)**. GPS, GLONASS and GPS+GLONASS PPP solutions are in blue, orange and green, respectively, using ESA products. Grey crosses are as per Fig. 2.3. Note that 1–4 years of time series length use ESA repro2, while the rest use a combination of ESA repro2 and ESA operational products.

2019), based on previous results, we assumed that changing satellite orbit and clock products may produce substantial differences in problematic solar-related constituents (S_2, K_2, K_1, P_1). Thus, we first performed a comparison of ESA repro2 solutions (2010.0–2014.0) with the ESA operational product (2014.0–2019.0) which confirmed the hypothesis (Fig. 2.11). GLONASS $||\Delta Z_{\text{res}}||$ show the smallest variance for K_1 and K_2 compared with GPS and GPS+GLONASS but are significant, up particularly, which might be related to the changes in the analysis used to produce GLONASS orbits and clocks. Considering S_2, the very same form of bias remains as previously seen in the 2010.0–2014.0 dataset. This suggests a symmetric deviation of repro2 and operational products solutions from the modelled value. The same explanation can be applied to the GPS-only P_1 $||\Delta Z_{\text{res}}||$ bias in the up component of 0.5 mm.

The results shown in Fig. 2.12 are produced from a composition of reprocessed products and operational products (years 5 to 9). We focus on S_2 up and K_1 up, as the most problematic diurnal constituents. The results align with general conclusions of Yuan et al. (2013) suggesting a weak relationship between time series length and $||Z_{\text{res}}||$ for solar-related constituents. However, if constituents are examined according to our recommended optimum constellation strategy, $||Z_{\text{res}}||$ appears (see Fig. A.4.1-A.4.2) stable over time, which suggests that even if there are changes in the products, they are not having an impact with this methodology.

2.6 Conclusion

We expand the GPS-only methodology of ocean tide loading displacement estimation described in Penna et al. (2015) with data from the GLONASS constellation. We assess the performance of GPS and GLONASS for the estimation of eight major ocean tide loading constituents in stand-alone modes and in a combined GPS+GLONASS mode. We examine data from 21 sites from the UK and western Europe over the period of 2010.0–2014.0 through processing data in kinematic PPP using products from three different analysis centres: CODE, ESA and JPL. The latter was also used to assess the effect of GPS ambiguity fixing on estimated ocean tide loading displacements. All solutions were intercompared to gain an insight into the sensitivities of the constituent estimates to different choices of satellite orbit and clock products, satellite elevation cutoff and constellation configurations.

We find that the optimal constellation mode varies across all eight major tidal constituents and components. We show that ambiguity-free GPS+GLONASS solutions show a similar level of precision as GPS with ambiguities resolved (GPS AR), with P_1 estimates using GPS+GLONASS showing improved precision and stability. The K_2 and K_1 constituents, which are known to be problematic in GPS solutions, are still unusable in GPS+GLONASS solutions, presumably due to the propagation of GPS related errors. The S_2 constituent also cannot be reliably recovered with GPS+GLONASS, as GLONASS shows dependency between the estimates and the chosen elevation cutoff angle. GPS-based estimates of S_2 show a constant bias in absolute residuals when ambiguity resolution is not implemented, but this is substantially reduced by resolving the ambiguities to integers. GLONASS-based estimates show a comparable level of performance to ambiguity-free GPS for M_2, N_2, O_1, P_1 and Q_1, while showing improved results for K_2 and K_1.

Additional comparison of OTLD estimates from reprocessed and operational products shows that GLONASS estimates of K_2 and K_1 show differences in the up and, to a lesser extent, in the east components when using different products.

Considering the above information, we suggest that estimation of K_1 and K_2 constituents is best undertaken using GLONASS only solutions with an emphasis towards the north component where it is most stable. M_2, S_2, N_2, O_1 and Q_1 can be reliably estimated from combined GPS+GLONASS or GPS AR solutions, while P_1 is best with GPS+GLONASS.

Integer ambiguity resolution was not possible in the GLONASS or GPS+GLONASS solutions tested here due to limitations in the products available. However, evidence from our GPS AR testing suggests that further increases in precision and stability will be seen when AR fixing can be performed using GLONASS, and this should have a positive impact on estimates of solar-related constituents.

2.7 Thesis Context

The study presented in this chapter contributes to addressing RQ1, providing one of the first assessments of GPS, GLONASS and combination solutions for the determination of

OTLD. The analysis, validated relative to the previous studies, were expanded with an additional GNSS constellation, and additional tidal constituents. The described work shows the first estimates of each of the eight constituents from a combined GPS+GLONASS solution that uses CODE and ESA orbit and clock products, addressing a specific gap that has been identified. The work shows that GLONASS adds important new information on tidal displacements of Earth and complements GPS, especially with regard to solar-related constituents M_2, K_2, K_1 and P_1. This provides a new opportunity for GNSS measurements to be used to further understand the geophysical properties of Earth at tidal frequencies. The thesis follows with an investigation into sensitivities of the derived OTLD estimates to the Earth's interior processes. In chapter 3 that follows, this question is approached with an analysis of the sites across New Zealand with a focus on sites close to the Hikurangi subduction zone.

Chapter 3

OTLD in the vicinity of the active tectonic margin

Summary

GPS observations of ocean tide loading displacements can help infer the regional anelastic properties of the asthenosphere. We estimate M_2 ocean tide loading displacements at 170 GPS sites in New Zealand and compare these to modelled values using a range of numerical tide and radially symmetric (1D) elastic and anelastic Earth models. Regardless of the model combination we are unable to reduce the strong spatial coherence of the M_2 residuals across the North Island where they reach 0.4 mm (2 %). The best fit in the North Island is obtained when combining the FES2014b tide model with spatially-variable ocean density and water compressibility, and the STW105 Earth model. The residuals exhibit a change of $\sim$0.3 mm in magnitude between the Taupo Volcanic Zone and the east coast ($\sim$100 km), suggesting that this region's laterally-varying, shallow rheological structure may need to be considered to explain these observations.

This chapter has been published as: Matviichuk, B., King, M. A., Watson, C. S., & Bos, M. S. (2021b). Limitations in One-Dimensional (an)Elastic Earth Models for Explaining GPS-Observed M2 Ocean Tide Loading Displacements in New Zealand. *Journal of Geophysical Research: Solid Earth*, *126*(6). https://doi.org/10.1029/2021JB021992. Minor changes have been made to the original published article for consistency in this thesis. This includes general terminology and grammar.

3.1 Introduction

The asthenosphere, the weak viscoelastic substrate beneath the lithosphere, is fundamental to the concept of plate tectonics and the earthquake cycle (Hu et al., 2016). The rheological properties of the asthenosphere are, however, not well understood (Karato, 2012). The importance of the asthenosphere is amplified at active convergent boundaries of tectonic plates, specifically subduction systems that initiate forces principal in driving plate tectonics and mantle convection (Stern, 2004). New Zealand is split by the transform Alpine Fault and is locked between two subduction systems: the Hikurangi in the north and Puysegur in the south (Lamarche & Lebrun, 2000). These lithospheric discontinuities should produce the large perturbations observable in the earth tide and perhaps the ocean load tide displacements (Zürn et al., 1976).

Analysis of Ocean Tide Loading, a phenomenon created by the solid Earth's response to tidal-water mass redistribution, can be used to validate ocean tide models and elastic Earth models at tidal periods (e.g. Farrell, 1972b; Martens et al., 2016; Yuan & Chao, 2012; Yuan et al., 2013). More recently GPS-derived Ocean Tide Loading Displacements (OTLD) have been used to constrain the asthenosphere's anelasticity at the period of the major M_2 tidal constituent (period of 12.42 h) by showing improved agreement with deformation modelled using anelastic Earth models. To date, studies of asthenosphere anelasticity have focused on continental settings such as western Europe, western USA, South America, the eastern China Sea region and Alaska (Bos et al., 2015; Ito & Simons, 2011; Martens & Simons, 2020; Wang et al., 2020).

In this chapter, we examine the tidal deformation of New Zealand, at the dominant M_2 tidal period, using an array of continuous GPS stations. We combine recent ocean tide models with a range of purely elastic and anelastic 1D Earth models and compare modelled deformation with GPS observed estimates to further understand the anelastic properties of the asthenosphere beneath New Zealand.

3.2 Methods

3.2.1 GPS Data and Analysis

We analyzed all available continuously operating GNSS stations in New Zealand over the period from the beginning of 2013 to mid-2020 (DOY 153), chosen to maximize the number of stations with overlapping data and minimize data gaps in individual stations. Over this seven-year period, data are available from 170 stations, with all but two (CHTI and RAUL) located on mainland New Zealand (see Table B.1 for a full list of sites). These stations were designed for nationwide coverage with station spacing in the range 80–100 km to monitor and control the national datum and for geophysical studies (Gale et al., 2015). As shown in Fig. 3.1, the network provides approximately uniform (but sparse) coverage in the South Island with a substantially higher spatial density of coverage across much of the North Island.

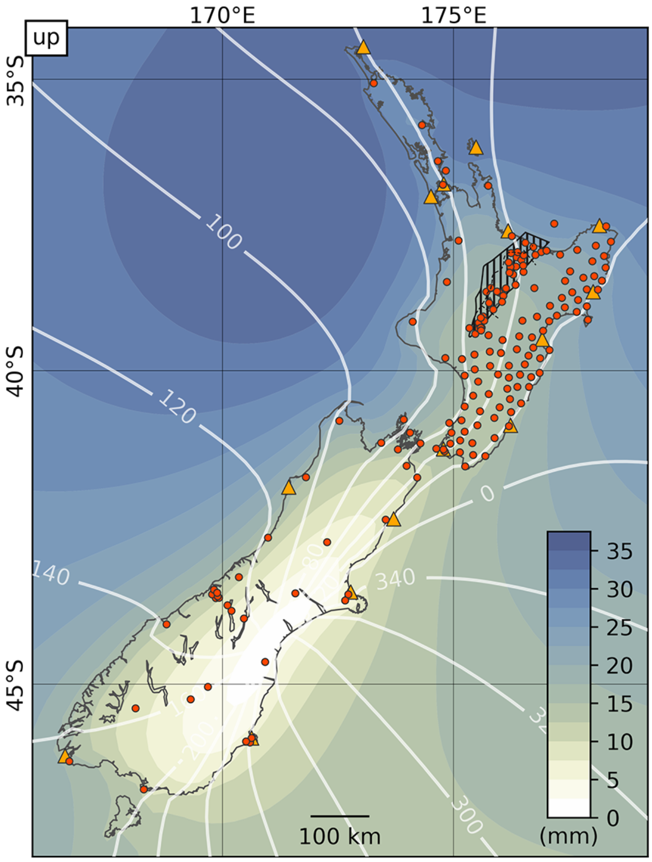

FIGURE 3.1: Map of New Zealand showing modelled M_2 Up OTLD amplitude and phase (relative to Greenwich) computed with TPXO7.2 ocean tide model and PREM Green's function. GPS sites and tide gauge locations are represented by red circles and orange triangles, respectively. The hatched area in the North Island represents the approximate region of the Taupo Volcanic Zone.

These data were analyzed using GipsyX v1.3 software (Bertiger et al., 2020) using a kinematic Precise Point Positioning (PPP) approach (Zumberge et al., 1997). The dataset processing was fascilitated by a custom wrapper (Matviichuk, 2020). Our approach was described in full by Matviichuk et al. (2020) with the main difference being that here we used only the GPS data. Data from other GNSS (e.g. GLONASS) were not logged at all sites over this period hence was excluded from this analysis. We used NASA JPL's orbit and clock products from their third internal reprocessing campaign (repro 3.0, released March 2018). Ambiguities were fixed to integers where possible (Bertiger et al., 2010). Earth body tides were modelled within GipsyX according to IERS 2010 Conventions (Petit & Luzum, 2010).A priori OTLD values were removed based on the FES2004 ocean tide model (Lyard et al., 2006) and Gutenberg-Bullen purely-elastic Earth model (Farrell, 1972a) in a centre-of-mass of the whole Earth system frame (holt.oso.chalmers.se/loading) – we later restored the OTLD component at the coordinate time series level for further study; this remove-restore approach is done to reduce the magnitude of companion tides and follows approaches adopted previously (e.g. Abbaszadeh et al., 2020; Matviichuk et al., 2020; Penna et al., 2015).

The GipsyX coordinate and zenith-wet-delay process noise values were chosen based on the tests of Penna et al. (2015), Wang et al. (2020) and Matviichuk et al. (2020), using values of 3.2 mm/sqrt(s) and 0.1 mm/sqrt(s), respectively. Our parameterization produces coordinate estimates every 300 s from which we remove large outliers identified with clock bias estimates larger than 3×10^3 meters and residuals to a detrended timeseries that are larger than $\pm 3\sigma$ of each global cartesian coordinate component. These timeseries were converted to local topocentric east, north and up components which were then further analyzed.

3.2.2 OTLD Models

We focus here on the difference between the GPS-derived OTLD and those modelled based on ocean tide models and elastic and anelastic Earth models. For the tides we mainly consider three relatively recent global ocean tide models: GOT4.10c (Ray, 2013), TPXO9.v1 (Egbert & Erofeeva, 2002) and FES2014b (Lyard et al., 2021), although we also explore FES2012 (Carrere et al., 2012) and FES2004 (Lyard et al., 2006). We also consider one regional New Zealand tide model (Walters et al., 2001), EEZ, which we combine with FES2014b outside the model's domain for loading computations. We used bi-cubic interpolation to resample the models to a common $0.05 \times 0.05°$grid. We note that the TPXO9.v2a model was also later analyzed but we found no improvement relative to TPXO9.v1 model present in the analysis.

The amplitude of the M_2 tide reaches over 1 m near the coast of New Zealand, due to the shallow bathymetry, and decreases to 10-20 cm in the open ocean (Stammer et al., 2014). The pattern of M_2 between the two islands of New Zealand is similar to an amphidromic point although the amplitudes are not zero. As a result, the tides to the east and west of New Zealand are out of phase and partly cancel out each other's contribution to the total OTLD value in the up component.

All modelled OTLD values were computed using the CARGA software (Bos & Baker, 2005). The coastline was taken from the GMT database (Wessel & Smith, 1996) and has a resolution of around 150 m. In most studies a constant sea water density is assumed, for example 1030 kg/m^3. Ray (2013) advocated to take the spatial variation of the density into account, and even the fact that water is slightly compressible, which means that the mean density of a water column should increase due to the extra density at the bottom of the column. For the ocean around New Zealand the effect on the resultant deformation is around 1-3 %. Assuming a mean 2 % effect and a mean OTLD amplitude of 20 mm, this corresponds to a potential error of 0.4 mm which is too large to be ignored. We have implemented the equations of Ray (2013) and obtained mean density values from the World Ocean Atlas 2013 - WOA13 (Zweng et al., 2013) based on a $0.25 \times 0.25°$ grid.

Three Green's functions were assessed with this set of ocean tide models: PREM (Dziewonski & Anderson, 1981), STW105 (Kustowski et al., 2008) and S362ANI (Kustowski et al., 2008). PREM and STW105 provide radial (1D) profiles for the density, and seismic velocities Vp and Vs. These profiles were used to compute load Love numbers which were converted into Green's functions (Bos & Scherneck, 2013). The method is based on Alterman et al. (1959) but uses the more recent Chebyshev collocation method to solve the differential equations (Guo et al., 2001). These profiles are based on seismic data and are only valid at a period of 1 s. To convert them to the period of the M_2 constituent, a constant absorption band (Q=constant, see Table B.3) is assumed between these two periods (Bos et al., 2015).

S362ANI is based on STW105 but has a shear velocity that varies horizontally, not just by depth. Given our focus on 1D radially symmetric models, we averaged the values in a rectangular region between 48° S and 33° S and 165° E and 180° E to yield a model representative of the average values over the study region. Once converted into a radially symmetric model, the Green's function for S362ANI was computed in similar manner as PREM and STW105.

3.2.3 OTLD Analysis

Amplitudes and phases of tidal constituents, and their uncertainties, were estimated from the GPS coordinate timeseries using the ETERNA software v.3.30 (Wenzel, 1996) for 17 tidal constituents, with local phases converted to Greenwich phases with lags positive to enable comparison with the models of OTLD. Our focus is solely on the largest loading constituent in New Zealand, M_2, the major semi-diurnal lunar constituent. To decrease the computation time and measurement noise, the timeseries were first downsampled to 30-min through window averaging.
Before computing the residuals, we assessed the impact from the differences in the ocean tide models on the modelled OTLD values. For this we computed errors associated with differences between the three global ocean tide models: FES2014b, GOT4.10c and TPXO9.v1 (Fig. B.3). The errors are consistent over most sites with a mean error value of $\sim$0.1 mm in all three components. We follow the naming conventions of Yuan and Chao (2012) with observed and modelled OTLD referred to as Z_{obs} and Z_{OTL} respectively with Z_{res} being their vector difference. We refer to the magnitude of the vector difference as $\|Z_{\text{res}}\|$.

3.3 Results

3.3.1 Preliminary analysis of the ocean tide models

We expected local EEZ ocean tide model to perform similarly to the most recent global tide models at the M_2 period. We computed an average of the three most recent ocean tide models: FES2014b, GOT4.10c, and TPXO9.v1 (Fig. 3.2a) to provide a baseline for the assessment of the EEZ model. We added the FES2004 global model to the comparison to assess the performance of global model recommended within the IERS 2010 Conventions for geodetic analysis (Petit & Luzum, 2010). Compared with the newer global models, FES2004 demonstrated higher discrepancies (up to 1 m) in the semi-closed water bodies and shallow bights (Fig. B.1a), while the EEZ regional tide model shows an approximately constant vector difference in the shallow sea waters (<1000 m depth) of around 0.1 m (Fig. B.1b).

We assess the tide models further by comparing modelled M_2 tide values with those from 15 tide gauges, shown in Fig. 3.1. The mean of the M_2 amplitude differences are shown in Table 3.1 demonstrating that the EEZ model exhibits over 5-7 cm amplitude difference relative to tide gauges. The other global models have mean amplitude differences of 1.13-3.05 cm, with the GOT4.10c model in closest agreement in terms of mean amplitude difference at the tide gauges (see Table B.3 for details).

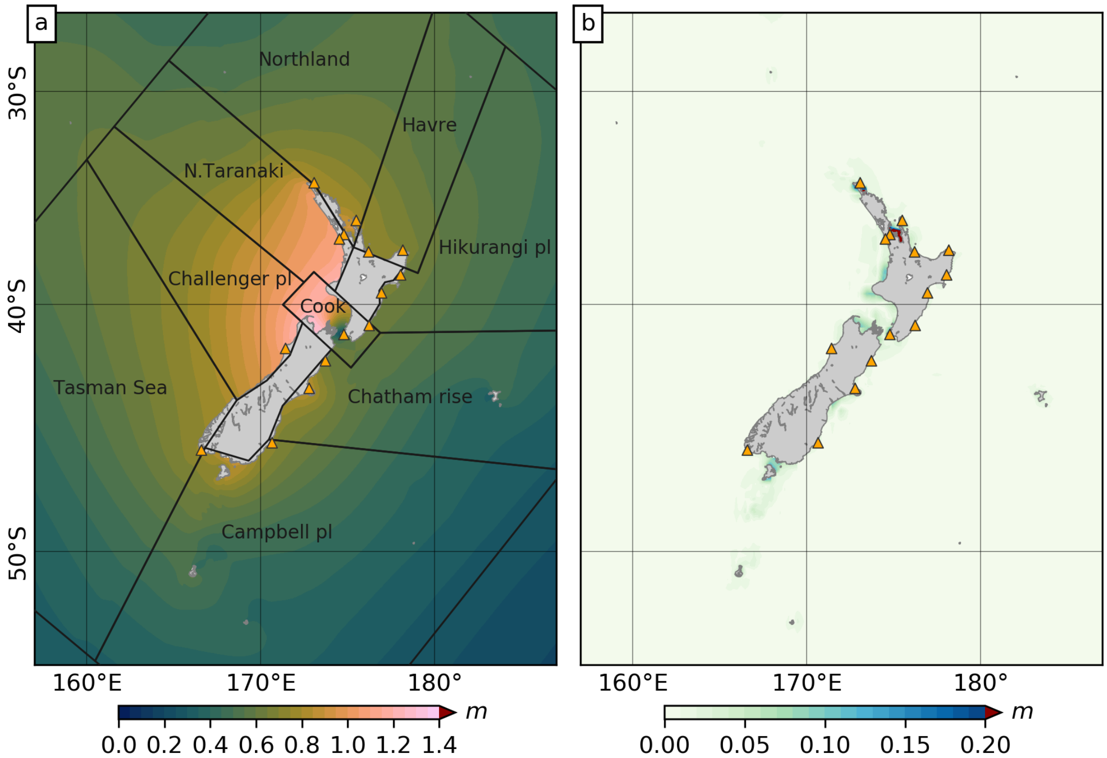

FIGURE 3.2: Comparison of recent global ocean tide models (FES2014b, GOT4.10c, TPXO9.v1) around New Zealand: (a) M_2 tidal amplitudes computed as a mean of the ocean tide models. (b) Standard deviation (SD) of the vector differences between the global ocean tide models. The grey labeled polygons in (a) represent the areas used for OTLD phasor reconstruction. Note the scale extension above 0.2 m in (b) to demonstrate the high degree of agreement between these models with exception for ∼1 m SD on one small section of the north coast. Orange triangles represent tide gauges used in the analysis.

To assess the variation between recent global ocean tide models at the M_2 period we computed the inter-model standard deviation (Fig. 3.2b). We found M_2 standard deviation (SD) values of 0.18 cm and 2.68 cm for the deep ocean (>1000 m depth) and the shallow sea (< 1000 m depth) respectively. These values are smaller by 40 % and 20 % than globally derived values reported by Stammer et al. (2014) for M_2. The largest SD values of up to 0.6 m are located in the Hauraki Gulf in the north-west of North Island, which indicates the region where the largest ocean tides errors are expected. We note however that this is a very small region and hence will likely have negligible impact on most modelled displacements considered here.

3.3.2 Comparison of GPS and PREM-based Models

The GPS-estimated M_2 up OTLD (with the a priori model restored) are shown in Fig. 3.3 with horizontal components shown in Fig. B.2. These show a spatially coherent signal across New Zealand with the amplitude ranging from 2 to 32 mm (sites WAIM and KTIA, respectively). Using these observations and the modelled Z_{OTL} based on FES2014b and PREM we computed Z_{res} as shown in Fig. 3.4 for each of the east, north and up coordinate components. M_2 up residuals in the North Island are significant and demonstrate a spatially coherent amplitude of ∼1 mm and phase residual of ∼-10 °, while residuals in the South Island are small but harder to interpret due to the lower station density and the low OTLD

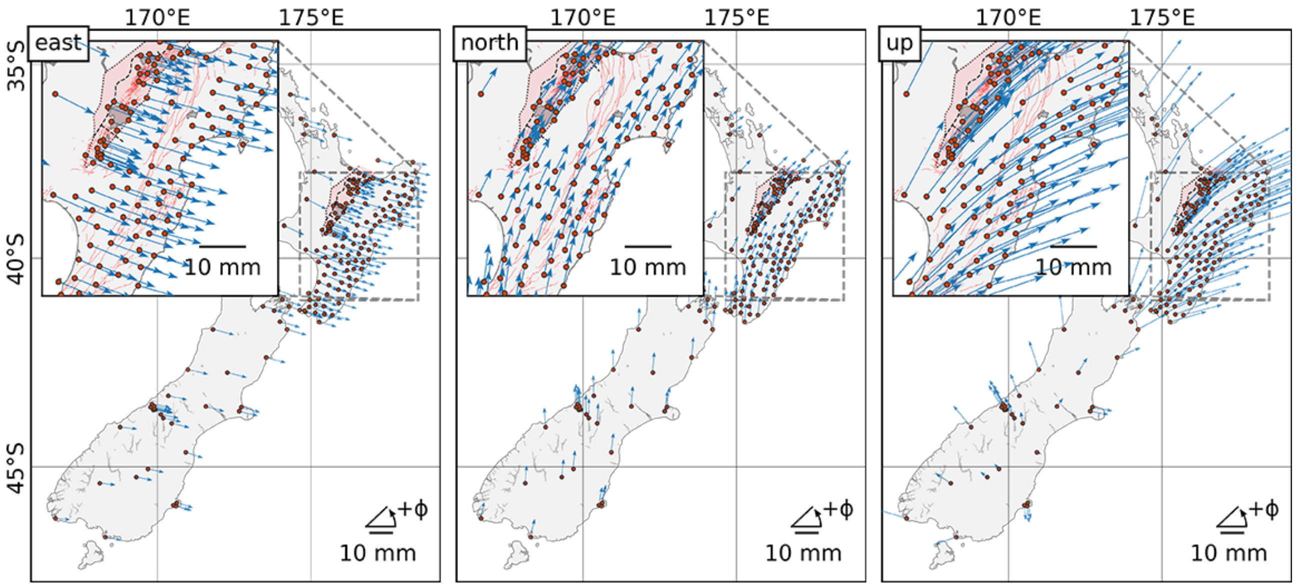

FIGURE 3.3: GPS-derived M_2 ocean tide loading displacements in the in the east, north and up coordinate components.

amplitude (Fig. 3.1). This is consistent across different global ocean tide models as indicated by the $\|Z_{res}\|$ values summarized in the boxplots (Fig. 3.5c, B.4-B.5). $\|Z_{res}\|$ variation over the range of tide models with PREM has median value of around 0.7 mm for any of the global tide models while the median for the EEZ model is ∼2 mm. This bias within the EEZ model results in a spatially coherent signal evident from the phasor maps (Fig. B.6.2, up component), especially in the North Island.

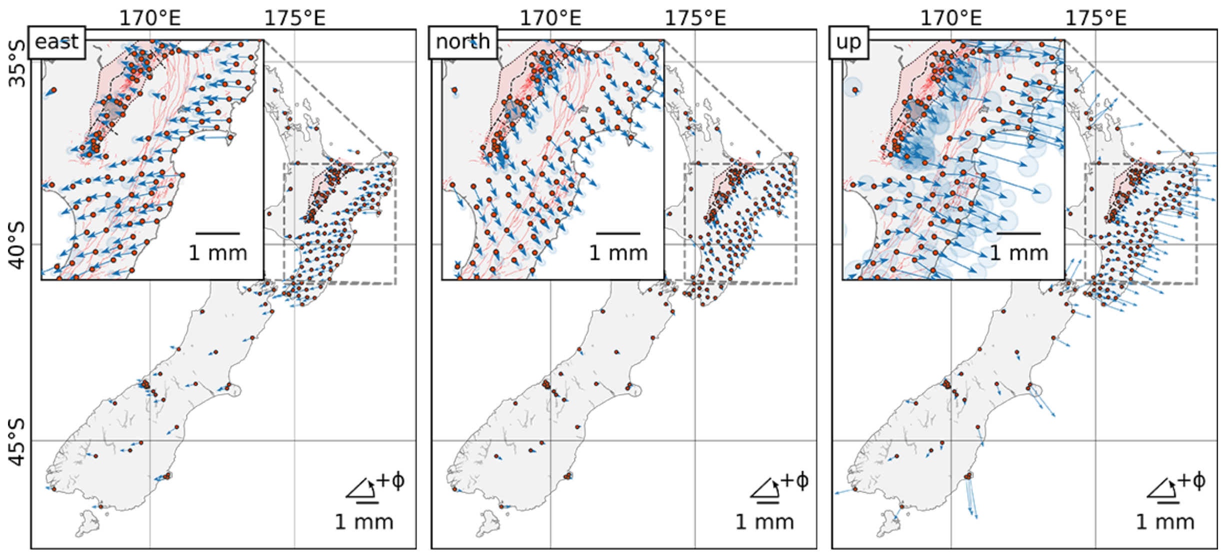

FIGURE 3.4: M_2 residual OTLD, Z_{res}, relative to FES2014b ocean tide model and PREM Green's function in the east, north and up components which can be treated as a baseline residuals present in the majority of GPS studies

While all the recent global ocean tide models perform similarly in the horizontal components, FES2014b demonstrates the largest reduction of $\|Z_{res}\|$ over the set of Green's functions in the up component (Fig. B.5). Note that the JPL products were generated using an analysis that used GOT4.8ac ocean tide model (Desai & Ray, 2014), which explicitly states

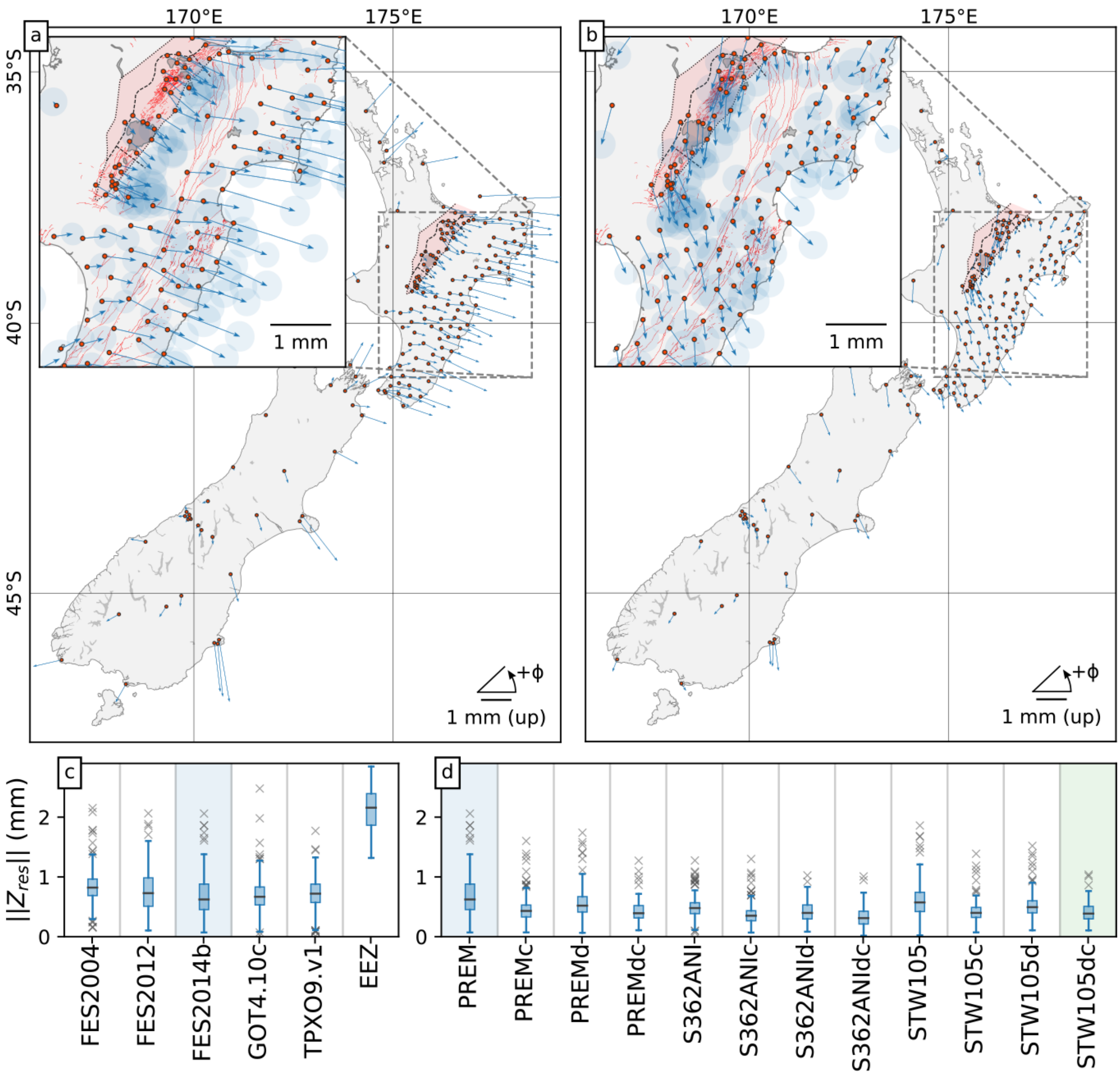

FIGURE 3.5: M_2 OTLD residuals relative to FES2014b_PREM (a), FES2014_STW105dc (b) with circles on the ends of phasors representing 95 % confidence interval of the derived OTLD values. M_2 OTLD residual magnitude ($\|Z_{res}\|$) boxplots for different model setups (c, d). The horizontal line on each box is the median value, the box represents the inter-quartile range (IQR) and the whiskers show an additional 1.5×IQR. Blue and green shading highlights boxplots of (a) and (b) maps, respectively. The Earth model suffixes 'd' and 'c' in panel (d) refer to the additional treatment of dissipation and compressibility, respectively.

that the altimeter data the model is based on, were corrected for the center-of-mass (CoM) motion of the Earth, hence the "c" suffix in the name. This may create inconsistency producing residuals relative to the other models tested here associated with CoM modeling (see Chapter 4 for more detail on CoM). Thus, we compared modelled results using FES2014b and GOT4.8c and found CoM differences values to be negligible ($\leq$0.01 mm) which suggest the presence of the similar CoM correction in FES2014b. We continue with FES2014b (Fig. 3.5c) as a baseline ocean tide model for the subsequent tests.

We considered the impact on the total OTLD of specific water bodies by dividing the global oceans into nine separate water areas surrounding New Zealand (Fig. 3.2). To illustrate the influence of different regions, we selected three sites that experience high, moderate and low M_2 OTLD: KTIA, RGMT and MQZG, respectively (Fig. 3.6). The set of ocean tide models considered consists of the three recent global atlases (FES2014b, TPXO9.v1 and GOT4.10c), FES2012 and EEZ. The latter produces $\sim$2 mm residual amplitude (purple symbols in Fig. 3.6) and is, due also to the tide gauge comparison (Table 3.1), excluded from further analysis. The other models show closer agreement but in general the residuals are larger than the estimated 2-sigma uncertainties of the observed OTLD when using PREM (Fig. 3.6, bottom panels). However, we note the similar magnitude of the variance in $\|Z_{\text{res}}\|$ for all models including EEZ (when the bias is ignored) in the up component and complete absence of a $\|Z_{\text{res}}\|$ bias in the horizontal components (Fig. B.5).

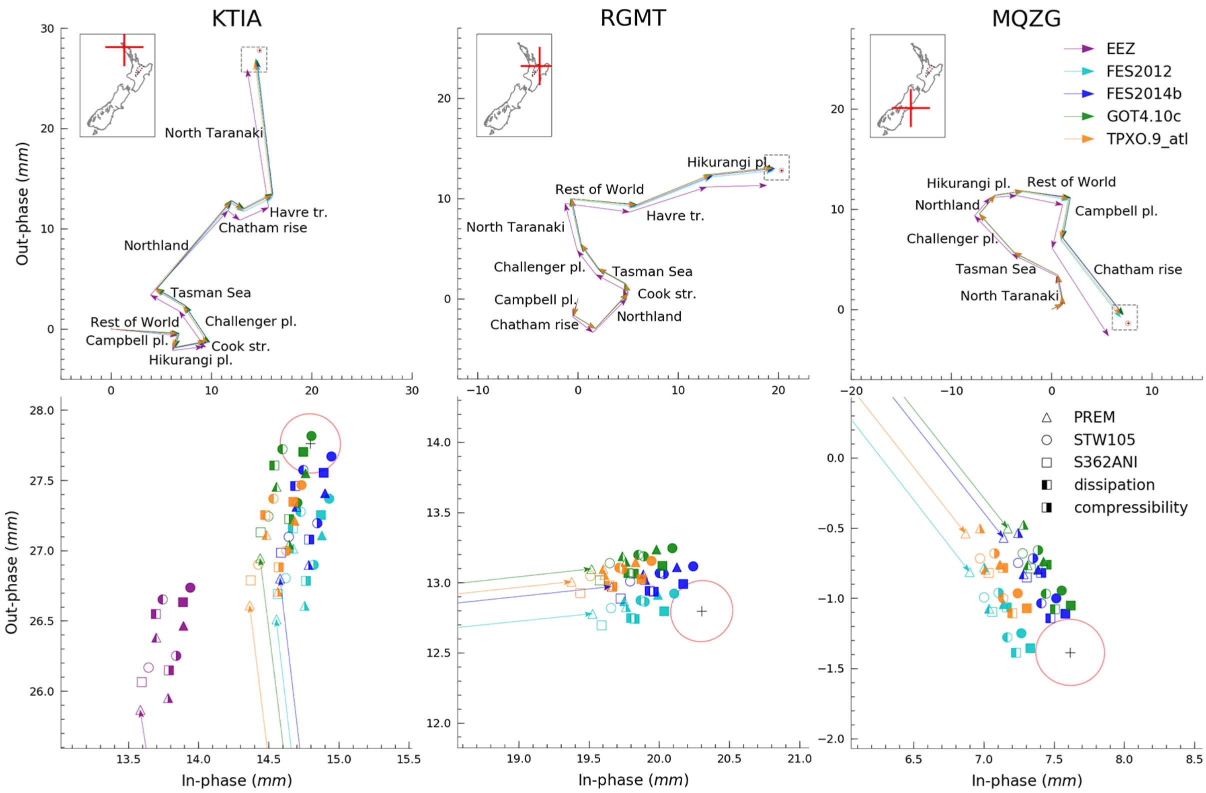

FIGURE 3.6: Phasor plots of the OTLD contributions from different oceanic regions (see Fig. 3.2a) for M_2 Up displacements computed with various Green's functions and ocean tide models. The bottom panels show the detail for the vector tip area shown enclosed by a square in the respective top panels. GPS observations are shown with a black "+" and 95 % confidence interval as a red circle. OTLD produced by the area outside the polygons shown in Fig. 3.2a is titled as "rest of the world".

Residuals using the purely elastic (original with no corrections) STW105 show a similar level of variance and median as PREM (Fig. 3.5d) while S362ANI shows 50 % reduced variance and slightly reduced median (0.48 mm compared with 0.61 mm for PREM). However, neither model produces consistent agreement within the GPS uncertainty as shown, for example, with the three sites presented in Fig. 3.6. We next explore the sensitivity of the modelled OTLD to anelastic dissipation (denoted suffix "d"), and spatially-varying ocean density and compressibility ("c").

TABLE 3.1: Average M_2 amplitude differences computed over 15 tide gauges relative to a set of ocean tide models.

	FES2004	FES2012	FES2014b	GOT4.10c	TPXO.9_atl	EEZ
Avg. difference (cm)	-0.81	2.95	3.05	1.13	2.32	8.41

3.3.3 Effect of Considering Anelasticity (Dissipation)

Bos et al. (2015) demonstrated that accounting for some of the effects of M_2 mantle anelasticity by modifying the Green's functions to include dissipation, decreased OTLD residuals in western Europe by up to 0.2 mm. Matviichuk et al. (2020) confirmed these results for the same region but using a different time frame, while similar results have been found by Wang et al. (2020) and Martens and Simons (2020) for south-east Asia and Alaska, respectively.

For New Zealand, we find a reduction of $\|Z_{\text{res}}\|$ variance and median for all Earth models when dissipation is included (Fig. 3.5d). The effect is illustrated in Fig. 3.6 where the models including dissipation (squares with left side only filled) are shown to be closer to the GPS estimates. These do, however, remain outside the GPS 95 % confidence interval. At the same time as this improvement, we noticed the introduction of up to 0.2 mm $\|Z_{\text{res}}\|$ bias into the north component with dissipation enabled, independent of the Green's function used; the east component also shows this effect but only with S362ANI (Fig. B.4). Enabling sea water compressibility correction partially suppresses the bias. We discuss this further below.

3.3.4 Assessment of Water Density and Compressibility Correction

Enabling the seawater compressibility correction decreases the median $\|Z_{\text{res}}\|$ by a further $\sim$0.2 mm in the up component, as shown in Fig. 3.5d and by example in Fig. 3.6 (fully filled symbols). In some cases, the application of both dissipation and compressibility eliminates the residual in the up component, although as we discuss in the next section, large, regionally coherent residuals persist. Horizontal components show an increase in variance (Fig. B.4) with only compressibility considered. The dissipation-introduced $\|Z_{\text{res}}\|$ bias in the north component can be partially (S362ANIdc) or completely (PREMdc, STW105dc) removed by additionally applying the compressibilty correction (Fig. B.4-B.5, FES2014b). The east component shows a marginal (less than 0.1 mm) increase in both $\|Z_{\text{res}}\|$ median and variance over the solutions with just dissipation included for PREM and STW105, while S362ANI shows further dissipation-introduced increase in $\|Z_{\text{res}}\|$ bias by another 0.1 mm (Fig. B.4).

Following Martens and Simons (2020), we constructed Empirical Cumulative Distribution Function (ECDF) plots (Fig. B.7.1) to investigate the impact of corrections on the distribution of $\|Z_{\text{res}}\|$. The ECDF analysis shows the expected behavior of the corrections in the up component: each correction increases the slope of the ECDF indicating successive improvement with each correction. This is not the case for the horizontal components where both corrections introduce biases using S362ANI, which otherwise demonstrates performance comparable to other models without the corrections. The optimum correction of PREM and

STW105 in the north component very much relies on the selection of ocean tide model. The dissipation-introduced bias is suppressed by the compressibility correction in the case of FES2014b and GOT4.10c, which suggests the best performance with both dissipation and compressibility corrections enabled. In the case of TPXO9.v1, the bias is too large for compressibility to overcome, effectively repeating the trend as observed for S362ANI.

Removing the respective mean Z_{res} values from each set of residuals (Fig. B.7.2) aligns the ECDFs over all components, fully removing the differences in the horizontal components with exception for S362ANI-based values in the north component. Removing mean Z_{res} also absorbs any long-wavelength errors incurred through any mismodeling of the solid Earth body tide.

3.4 Discussion

Following these tests, the optimal agreement between the observed and modelled OTLD in all three components occurs when using FES2014b and STW105dc. The spatial distribution of Z_{res} shows a spatially coherent signal with amplitude of $\sim$0.5 mm over the Taupo Volcanic Zone (TVZ) in the North Island, as shown in Fig. 3.4. The dense coverage of stations in these regions reveals a distinct change of Z_{res} between sites in the East Coast (EC) and TVZ that experience the same M_2 OTLD (Fig. 3.1).

To aid discussion, we consider four different regions (blocks) within this region as illustrated by the symbols in Fig. 3.7: TVZc, TVZs, ECc, ECs, with “c” and “s” subscripts identifying central and southern subareas, respectively. Residual OTLD in each block was averaged to provide Z_{res} summary metrics (per component) relevant to each region (Table B.4). Note that several coastal sites along the EC were removed (e.g. Hawke Bay) as they experience a localized signal caused mainly by the unmodelled ocean tides (Fig. 3.7, black symbols) which is independent of the ocean tide model or Green’s function used. The sites in both TVZ regions show residual amplitudes of $\sim$0.5 mm with phase changing sharply from -102°to -70°between TVZc and TVZs. The relative phase change between TVZ and EC within the same central or south area (TVZc/ECc and TVZs/ECs) is found to be approximately constant ($\sim$35°) while revealing 0.25 mm and 0.15 mm larger amplitudes for TVZc and TVZs, respectively.

The sharp change in residual phase between TVZc and TVZs, and the strong spatial variation in residual amplitude between respective EC and TVZ sub-regions over length-scales of the order of $\sim$100 km suggests that the variations are due to localized effects. We discount errors in ocean tides given our previous tests and the spatial distribution of the residuals. Also, biases in the adopted deep Earth rheological structure (Lau et al., 2017) would be effectively constant over this spatial scale.

Instead, our assumption is that the spatial pattern in the residuals result from mismodeled shallow-Earth rheological structure. To explore this further, we iterate through a range of alternative Earth models, all one-dimensional but with different rheological structure in the

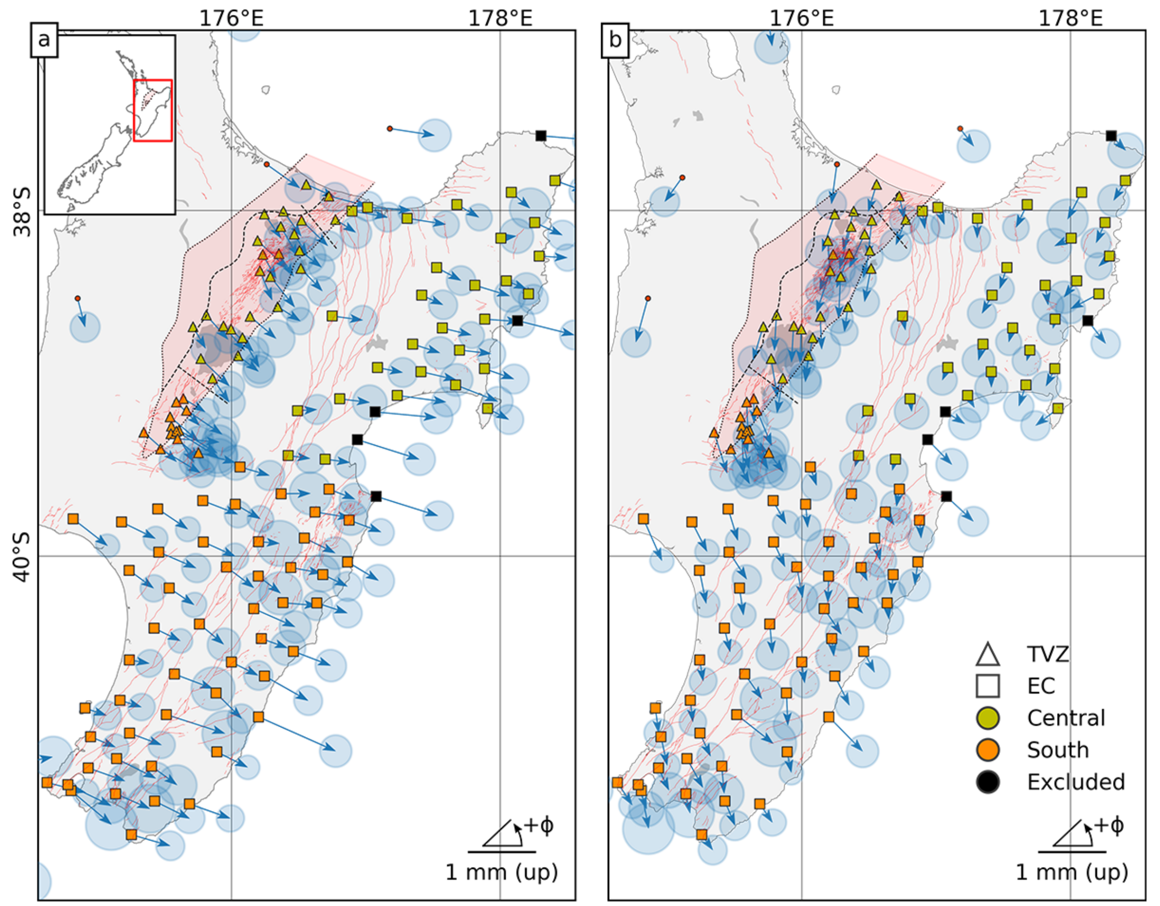

FIGURE 3.7: GPS-derived M_2 OTLD residuals for a section of the North Island relative to FES2014b ocean tide model combined with dissipation corrected STW105d (a) and STW105dc (b). "d" and "c" suffixes stand for dissipation and compressibility corrections. Sites are categorized into Taupo Volcanic Zone (TVZ) and East Coast (EC) regions (symbol shape) with subdivision of each into central and south along the TVZ central/south boundary (symbol color). Circles on the ends of phasors represent 95 % confidence interval of the derived OTLD residuals

upper tens of kilometers based on seismic tomography inversions (Eberhart-Phillips & Bannister, 2015; Eberhart-Phillips & Fry, 2018). No single one-dimensional (radially-varying) Earth model could explain the regional pattern of residuals, with changes generally producing changes that were spatially uniform across the region of Fig. 3.7.

Deviations in the shallow rheological structure from that used to compute the Earth body tides could produce spatial patterns in localized residuals. Zürn et al. (1976) developed a 2D finite-element model of a subduction zone in Alaska, and showed that the subduction zone structure can produce an effect up to 0.8 % on the solid Earth body tide in the radial direction directly above the asthenospheric slab. For the M_2 body tide at the latitude of the North Island, this equates to 0.7 mm. However, their modeling also showed that the maximum gradient in the body tide over the distance from East coast to the TVZ (up to 150 km) should not exceed 0.25 % Zürn et al., 1976, Fig. 5. We note that the effect on phase is not described in their work. However, if we consider the relative location of the TVZ over the subduction slab (observed by the Vp anomaly at 100-130 km depth (Eberhart-Phillips & Fry, 2018)), the maximum expected change becomes close to 0.15 %, or 0.13 mm for M_2 at these latitudes. As such, this is well below the magnitude of the variations seen in Fig. 3.7.

The effect of lateral rheological structure on modelled OTLD is unclear to us as it has not been modeled in the thesis. However, modeling of elastic deformation due to longer-period surface mass displacement indicates that consideration of localized Earth structure produced differences of the order 10 % in the vertical and 20 % in the horizontal over distances of 10-50 km (Dill et al., 2015). The average M_2 OTLD in the region of the TVZ shown in Fig. 3.7 is $\sim$19 mm and so even a 2 % effect due to lateral variation may be relevant to explaining the observed residuals. Given the minor, but non-negligible effect of lateral variation on Earth body tides, and likely effects on OTLD, our analysis suggests that one-dimensional models of this region are unlikely to fully explain GPS observations of OTLD at M_2.

To check for potential long-wavelength errors that could introduce the observed dissipation-introduced biases in the horizontal components, we repeated our analyses for a set of 15 stations in inland Australia (see Table B.2 for site list) where the geological setting is simpler and where a 1D model should produce accurate results. For this dataset we needed to adopt a different time period (2015-2018 inclusive) due to data availability but checking a subset of sites in New Zealand found that the time-period was inconsequential. Figures B.9 and B.10 demonstrate that, although the magnitude of the OTLD is still several mm, for these stations the residuals (observed minus predicted OTLD) are indeed small and within the uncertainty of the observations. This validates the robustness of our analyses and suggests that tidal centre-of-mass errors in this region are small, specifically for FES2014b and GOT4.10c ocean tide models.

Figures B.7.1 and B.7.2 show that the OTLD residuals for the horizontal components suffer from a common mode issue that modification of the Green's function cannot overcome. For the up component, the influence of the dissipation effect within asthenosphere that requires us to modify the elastic properties of the Earth model from the reference period of 1 s to tidal periods is noticeable. Furthermore, including spatially varying seawater density and compressibility results in an additional reduction of the misfit. These two figures also demonstrate that the difference between the ocean tide models used in the loading computations is small. Therefore, the most likely candidate to reduce the misfit further is to use an advanced (3D) (an)elastic model of the region.

Similar problems using a 1D Earth modeling OTLD in Alaska were recently described by (Martens & Simons, 2020). We are unaware of three-dimensional models being in use for the computation of OTLD, however Latychev et al. (2009) have computed Earth body tides with a three-dimensional model. One practical consequence of this is that mismodelled tidal deformations in this region will propagate into conventional 24 hr coordinate solutions (Penna et al., 2007). Such propagation will introduce long-period noise in GPS coordinate time series in New Zealand and impact subsequent geophysical interpretation.

3.5 Conclusions

We estimate M_2 ocean tide loading displacements (OTLD) at 170 GPS sites in New Zealand from the beginning of 2013 to mid-2020 (DOY 153). Comparison with modelled OTLD displacements using a range of global tide models and elastic PREM shows sub-mm agreement, with much larger disagreements when using a local New Zealand tide model.

But on close inspection we find that no single one-dimensional elastic Earth model, when combined with modern global tide models, can consistently explain the GPS-derived OTLD within uncertainties. Of the tested ocean tide models, FES2014b produced the best results. However, application of an anelastic dissipation correction, and varying water density and compressibility substantially improves the agreement between the various models and observed OTLD. Despite this, some regional spatially-coherent unmodelled residual signals remain in the North Island with magnitudes of up to 0.3 mm. These show substantial variation in phase over $\sim$100 km in the region between the Taupo Volcanic Zone and the East coast. We attempted to reproduce the observed signal using a range of 1D Earth models with varying shallow Earth structures, including the effects of anelasticity, however no single model could explain the residuals. We anticipate that these residuals are a result of unmodelled lateral variations in Earth rheological structure forced largely by ocean tide loading but with a smaller component likely from mismodelled Earth body tides.

This analysis of residual OTLD demonstrates the deficiencies of the 1D Earth modeling approach that is currently standard practice. This is particularly relevant to GPS analysis using 24 hr coordinate solutions, given mismodelled tidal displacements propagate into long-period signal. Utilizing 3D Earth modeling to compute tidal phenomena is likely required to explain the observations in regions with major discontinuities in Earth's lateral structure (e.g. subduction margins). Such models, combined with these observations, could provide new insights into the shallow rheological structure of these regions.

3.6 Thesis Context

This chapter focused on the geophysical interpretation of the residual OTLD across the the area in the vicinity of the active tectonic margin – the Hikurangi subduction zone in an effort to address RQ2 using the previously acquired knowledge from achieving the objectives associated with RQ1. The GLONASS-capable sites were found to be spatially sparse, especially in the area of geophysical interest hence only GPS observations were analysed. The chapter demonstrated the sensitivity of the OTLD estimates to the elastic properties of the asthenosphere across the Taupo Volcanic Zone. The results across Taupo Volcanic Zone clearly show OTLD residuals of a geophysical nature that are characterised by a sharp change in the elastic properties over a short distance. This chapter provides an initial assessment of the residual OTLD sensitivities to the Mantle properties. On demonstrating the possibility of identifying signals of geophysical interest, the following chapter explores the OTLD variations away from zones of complicated tectonics, switching to the large and relatively stable block of continental crust – the Australian plate. The derived OTLD, especially in the very inland Australia, should bear negligible unmodelled geophysical effects, highlighting purely geodetic deficiencies of the solution which are the focus of RQ3.

Chapter 4

High-resolution OTLD over a large and stable block of continental crust

Summary

We seek to understand the residual signal in GPS and GLONASS estimates of ocean tide loading displacements (OTLD) after removing state-of-the-art model estimates. We estimate OTLD over Australia using GPS and/or GLONASS data from 360 sites and compare them with model estimates, with a focus on the lunar semidiurnal M_2 and diurnal O_1 constituents. We observe coherent spatial patterns of residual OTLD in each of the east, north, and up coordinate components after the removal of models of elastic deformation. We subsequently model the impact of anelastic dissipation on the M_2 signal and show a 0.2 mm reduction of the up component residuals only at coastal sites compared with a purely elastic model, with a similar reduction at all sites in the east and north components. Of the seven tide models we use in the OTLD modeling, we find the best agreement with FES2014b. We find OTLD estimates are sensitive to the chosen orbit and clock products used in our analysis, with differences of up to 0.5 mm in the east component between solutions using the JPL or ESA/CODE products (GPS-only) but consistent at the level of 0.1 and 0.2 mm in the north and up components, respectively. We find biases in the center of mass (CoM) estimates computed from the TPXO9.v1 model of up to 0.2 mm and 0.5 mm for M_2 and O_1, respectively, relative to other models and the GNSS data. We could not identify a regional ocean source for this bias but provide an assessment of contributions from global oceanic regions. Our analysis shows that current GNSS estimates of OTLD, ignoring the regional anomalies due to orbit and clock products, can be explained down to $\sim$0.2 mm but with unexplained spatially coherent residuals that could depend on the appropriate treatment of the CoM variation, anelasticity and/or three-dimensional Earth structure.

This chapter has been submitted and is under review with Journal of Geodesy, 28 May 2021.

4.1 Introduction

Data from continuous GPS sites has been used to estimate solid Earth displacements due to ocean tide loading (OTLD) since the early 2000s (Allinson, 2004; Khan & Tscherning, 2001; Schenewerk et al., 2001). This has been used to yield insights into ocean tide models (King, 2005; Penna et al., 2008) and solid Earth rheology, notably asthenosphere anelasticity (Bos et al., 2015; Martens & Simons, 2020; Martens et al., 2016; Wang et al., 2020) and Lower Mantle buoyancy (Lau et al., 2017). The use of satellite geodesy to derive OTLD has mainly been limited to the GPS constellation as it was the only complete global satellite navigation system from the late 1990s until 2010 when the GLONASS constellation was fully restored. Since that time, many GNSS networks started migrating to multi GNSS receivers and antennas, deploying new sites with GPS+GLONASS or multi-GNSS capable receivers. As such, there is now often one decade of both GPS and GLONASS data available at thousands of sites globally. Besides providing additional data to assist in observing millimeter or sub-millimeter level displacements, GLONASS has some advantages over GPS in terms of the absence or reduction of systematic errors at tidal frequencies (Abbaszadeh et al., 2020; Bos et al., 2015; Ito & Simons, 2011; Martens & Simons, 2020; Martens et al., 2016; Matviichuk et al., 2020; Wang et al., 2020).

Most previous studies related to OTLD have focused on regions over the scale of a few hundred km which makes it difficult to separate widespread GNSS systematic errors from more localized OTLD model error. We focus here on the tidal deformation of Australia, making use of GPS and GLONASS from a continental array of multi-GNSS receivers. Assessing displacements over a large continental region such as Australia provides insights into not only into the ocean tides and solid Earth rheology but also potential systematic errors in the estimates themselves – something which is hard to detect over small coastal areas. As such, we consider site displacement time series based on a range of satellite orbit and clock products.

Following previous studies, we focus on the major lunar semidiurnal and diurnal constituents M_2 and O_1 which are thought to be free from major GNSS systematic errors (e.g. Yuan et al., 2013). We do so using GPS+GLONASS sites on the Australian continent. In our study, we remove from the site's observed displacements the modelled solid Earth body tides and OTLD based on purely elastic Earth models and focus our investigation on the determination of the source of the residual signal.

4.2 Dataset and Methods

After a preliminary quality assessment of the dataset, 360 Australian continuous GNSS sites were selected for processing from 2015 to mid-2020. Sites were mainly located on bedrock but some sites were located in sedimentary areas or, in a few cases, on buildings. The site locations are shown in Fig. 4.1 (see Table C.1 for sites' coordinates). There were two selection criteria: a GLONASS-capable receiver with both GPS and GLONASS data availability and near-continuous recording since around 2015 DOY 001. The total data span is close to 2000

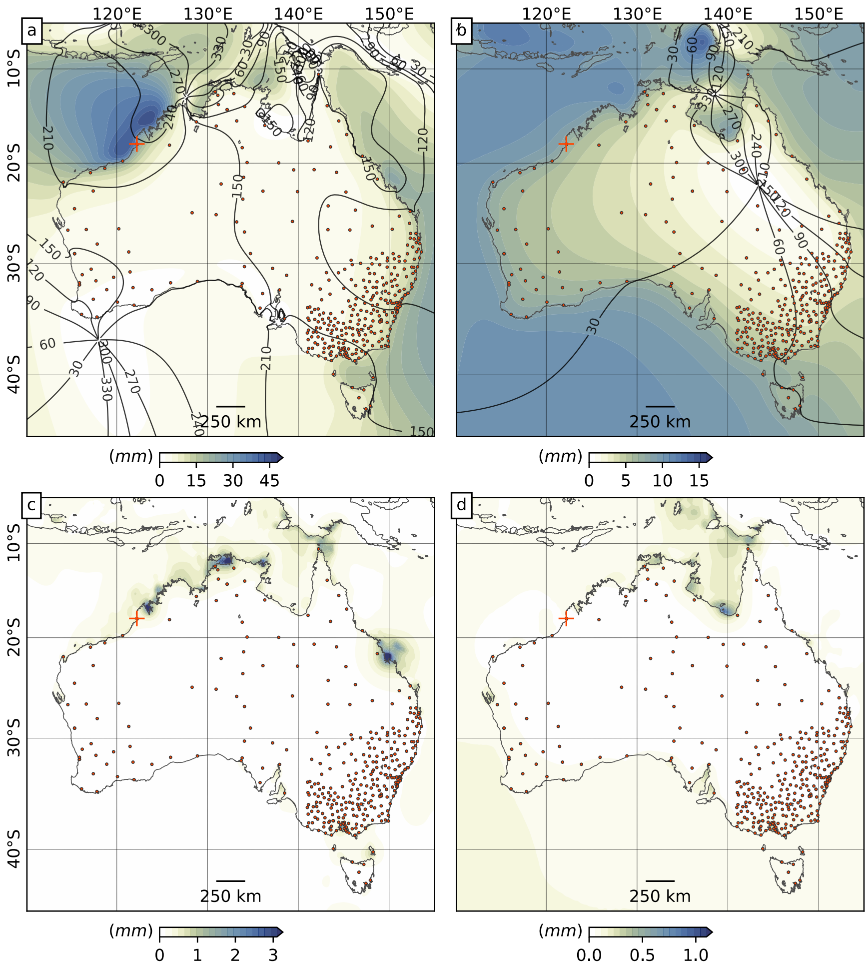

FIGURE 4.1: M_2 (a) and O_1 (b) OTLD maps of the up coordinate component computed as average over seven OTLD grids based on FES2012, FES2014b, GOT4.10c, GOT4.8, TPXO8, TPXO9, TPXO9.v2a global ocean tide models and S362ANI adjusted for dissipation at M2; and standard deviation maps between modelled grids at M_2 (c) and O_1 (d). Red dots represent site locations. Note the different color bar ranges between panels. The phase shown with black contour lines is relative to Greenwich. The site 'BRO1' used in process noise optimization tests, is marked with a red cross.

days, compatible with the findings of Penna et al. (2015) and Matviichuk et al. (2020) that demonstrated 1000 days to be sufficient span for reliable OTLD estimates. Average data availability is 95 % over all sites with most experiencing a 1-month gap in the December of 2017 likely due to a system issue in the Geoscience Australia data server. This gap should not impact the results (see Bos et al., 2015).

We use the kinematic precise point positioning (PPP) technique (Zumberge et al., 1997) using NASA JPL's GipsyX software suite v1.3 (Bertiger et al., 2020) to process daily 30 s RINEX files according to the approach of Matviichuk et al. (2020). The analysis involves estimating 5-min coordinates and Zenith Wet Delay (ZWD) estimates as random walk processes, with process noise settings discussed below, and receiver clock terms estimated as a white noise process. ZWD were mapped to the elevation angle of the satellites using the VMF1 mapping function and using a priori zenith wet and hydrostatic delays derived from the European Centre for Medium-range Weather Forecasts (ECMWF) datasets (Boehm et al., 2006). We modelled solid Earth and pole tides according to the IERS2010 Conventions and discuss below our approach to modeling OTLD (Petit & Luzum, 2010).

A range of satellite orbit and clock products were used. Final CODE MGEX (Dach et al., 2020) and ESA operational products were held fixed in the GPS, GLONASS and GPS+GLONASS solutions in which ambiguities were kept as non-integer estimates, while JPL repro3.0 products (NASA Jet Propulsion Laboratory (JPL), 2020) were used to provide GPS solutions with both floating and integer-fixed ambiguities. The ambiguities were fixed using GPS wide lane and phase bias tables that are disseminated as part of JPL's native product format (Bertiger et al., 2010). The elevation cutoff angle was set to 7° for both GPS and GLONASS constellations. Abbaszadeh et al. (2020) reported that solutions using GLONASS constellation may benefit from decreased cutoff angle for sites at latitudes less than 50 degrees but our additional tests tests using these sites with elevation cutoff angles of 3° and 5° demonstrated negligible difference between GLONASS-derived OTLD estimates. We did not closely examine the amount of data at these low elevation angles as our solutions were stable.

The resulting kinematic timeseries at 5-min sampling were then resampled to 30 minutes and analyzed with ETERNA v3.30 with settings recommended for timeseries of over 1 year in length (Wenzel, 1996). We followed previous studies (Abbaszadeh et al., 2020; Matviichuk et al., 2020; Penna et al., 2015) and used a remove-restore procedure of a priori OTLD values computed using the FES2004 ocean tide model and the Gutenberg-Bullen Earth model. This allows computation of positioning timeseries with only the residual OTLD signal present and thus decreases the values of the optimal coordinate process noise, slightly suppressing noise.

We focus on M_2 and O_1 tidal constituents, avoiding the complexities of solar-related constituents, S_2, K_2, K_1, P_1 that possess additional unmodelled effects: S_2 is demanding to satellite modeling and has been shown to have biases in both GPS (King, 2006; Thomas et al., 2007) and GLONASS estimates (Abbaszadeh et al., 2020; Matviichuk et al., 2020), also it has atmospheric component which can be modelled (Tregoning & Dam, 2005) but models are unable to fully explain the observed residuals. The K_2 and K_1 constituents are known to be problematic with GPS due to the closeness of orbital and constellation repeat periods, thus absorbing the multipath signals (Urschl et al., 2005). GLONASS-only was found to perform better with K_2 and K_1 but the recovered residuals were far larger than the values at other major constituents. (Matviichuk et al., 2020). The displacements at lunar N_2 and Q_1 constituents are relatively small which may limit the accuracy of the recovered phase values (Matviichuk et al., 2020). Assessment of the M_2 and O_1 combination has been done previously through gravimetric (Bos & Baker, 2005) and GPS observations (Martens & Simons, 2020; Martens et al., 2016).

The residual OTLD is computed via vector differencing the observed and modelled OTLD, i.e. Z_{res} = Z_{obs} - Z_{otl}, according to the naming conventions of Yuan and Chao (2012) and where Z_{obs} is the estimates after restoration of the FES2004 model OTLD removed previously. Note that since Z_{obs} has been corrected for solid Earth body tides at the PPP processing stage, Z_{res} consists mainly of residual OTLD, noting that the body tides can be modelled with an accuracy of around 1 % (Yuan & Chao, 2012) away from regions of substantial lateral variation in Earth's structure such as subduction zones (Zürn et al., 1976).

A set of seven global ocean tide models was used in the analysis, excluding FES2004 used in the initial processing: FES2012 (Carrere et al., 2012), FES2014b (Lyard et al., 2021), GOT4.8 and GOT4.10c (Ray, 2013), TPXO8, TPXO9.v1 and TPXO9.v2a (Egbert & Erofeeva, 2002). These were used together with Green's f unctions for the PREM (Dziewonski & Anderson, 1981), STW105 and S362ANI (Kustowski et al., 2008) Earth models to compute OTLD predictions (Farrell, 1972b) with CARGA software (Bos & Baker, 2005) using the free ocean tide loading provider (http://holt.oso.chalmers.se/loading).

In addition to purely elastic Earth models, we also consider the effects of mantle and asthenosphere anelasticity. We do this following the approach of Bos et al. (2015) by accounting for the frequency-dependence of the shear modulus as the period of the stress cycle is increased at tidal frequencies relative to the 1 Hz reference frequency of seismic Earth models that results in greater energy absorption. The single M_2 constituent was selected to represent the tidal frequency band as the shear modulus difference between the diurnal and semidirnal frequency bands was found to be negligible. The Q quality factor provided with reference Earth models was assumed constant - independent of frequency (Bos et al., 2015; Lambeck, 1988). For the values of Q we use the values from the one-dimensional models (Table B.4 shows PREM and STW105 Q values by depth). In all cases we use radially symmetrical Earth models.

We also considered the effects of spatial water density and water compressibility (Ray, 2013). Spatial water density and compressibility corrections were demonstrated to decrease the M_2 Z_{res} in New Zealand at the same level as the dissipation correction – $\sim$0.2 mm in the up component (Matviichuk et al., 2021b). The spatial water density values were extracted from $0.25\times0.25°$grid of the World Ocean Atlas 2013 (Zweng et al., 2013) and included using the method of Ray (2013). We add 'd' and 'c' suffixes to the Green's function name (e.g., STW105dc) to reflect when anelastic dissipation (d) and/or spatial water density and compressibility corrections (c), were applied in CARGA. The OTLD is modelled in the center-of-mass frame that is consistent with each of the orbit and clocks products (Fu et al., 2012): CM for JPL and CE for ESA and CODE.

4.3 Results and Discussion

We first discuss the results based on each of ESA, CODE and JPL products in terms of optimal process noise computation and their intercomparison relative to the FES2014b and STW105dc OTLD modelled values. Second, we compare the results with the OTLD based on the different ocean tide models. Finally, we explore the computed sub-daily center of mass (CoM) tidal variations values and assess inter-model differences, and the effects of spatial water density and water compressibility corrections.

4.3.1 Parameter sensitivity tests

4.3.1.1 Process noise sensitivity tests

Our first step was to establish the optimum process noise settings for the coordinate and ZWD parameters. While this has been done for the UK (Matviichuk et al., 2020; Penna et al., 2015), these findings may not extrapolate to Australian environmental conditions. BRO1, a site with the maximum OTL amplitude experienced in the chosen Australian network, was selected for the assessment of solution sensitivity to different process noise values. It is marked with a red '+' in Fig. 4.1. We repeated and extended the tests of Penna et al. (2015) according to Matviichuk et al. (2020) and these confirmed the optimum coordinate and ZWD process noise values of 3.2 and 0.1 mm/sqrt(s) respectively (Fig. C.1.1). These values are exactly the same as previously estimated by Penna et al. (2015) for western Europe. The tests were repeated using JPL, ESA and CODE products and the conclusions remained the same giving confidence that the process noise settings were robust. These values were used for all further tests.

4.3.1.2 OTLD absorption by tropospheric parameters

We expanded the above test assessing the signals at tidal frequencies in ZWD estimates, that could potentially be an absorbed OTLD from coordinate timeseries. This was done by vector differencing signals at tidal frequencies extracted from a priori ECMWF-derived ZWD timeseries and that derived from the resulting adjusted ZWD at site BRO1 (Fig. C.1.2). We found that tidal frequency signals in estimated ZWD are insensitive to variations of coordinate process noise assessed in Penna et al. (2015) and Matviichuk et al. (2020). Iterating over ZWD process noise values shows very low propagation of tidal signal into resulting ZWD when using process noise values below the default value of 0.1 mm/sqrt(s). Tidal signals in parameter estimates do not change with higher process noise values and this holds for all eight constituents assessed.

4.3.2 Comparison of ocean tide models in Australia

Following Bos et al. (2015), we computed the mean ocean tide models and standard deviation (SD) maps for both M_2 and O_1 constituents (Fig. C.2) after resampling all ocean tide models to a consistent $0.05 \times 0.05°$grid. By way of example for the amplitudes of OTLD for M_2 and O_1, these are shown in Fig. 4.1 based on the mean of seven most recent global ocean tide models and S362ANI Green's function corrected for dissipation at M_2. The OTLD amplitudes range from 0.1 to 31 mm for M_2 and from 0.15 to 8.5 mm for O_1 (Fig. 4.1a, b), with maximum OTLD for both constituents in the north west and west of Australia.

The high SD areas of ocean tide models may indicate regions where errors exist in the ocean tide models that may impact the estimated OTLD. While the mean SD over the total area is less than 0.01 m, some shallow shelf areas demonstrate localized SD anomalies. Regarding M_2, high SD values (over 0.2 m) are observed in the north and north-east of Australia (Fig. C.2c). modelled O_1 has large, highly-localized SD of up to 0.15 m in the north (Fig. C.2d) but is generally otherwise small. Thus, we treat modelled OTLD values for sites close to the respective areas as being potentially impacted by errors in the ocean tide models. We regard agreement between models as an indication of relative model robustness. Considering the SD between OTLD grids at M_2 and O_1, these are negligible for the most of the continent but reach over 3 mm in localized areas that correspond to the areas of high SD between ocean tide models (comparing Fig. 4.1c, d and Fig. C.2c, d).

4.3.3 Observed OTLD

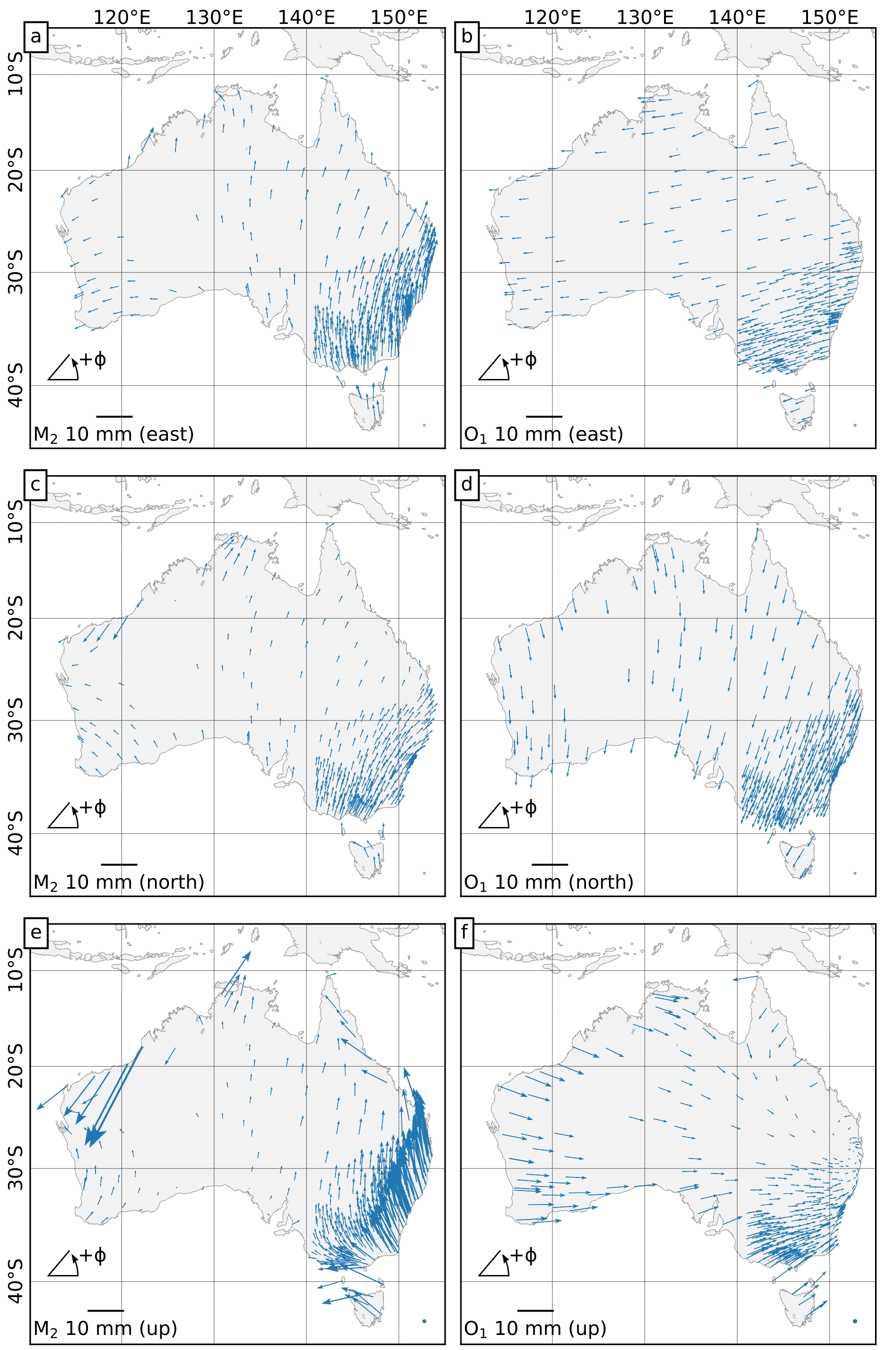

FIGURE 4.2: Observed OTLD (FES2004-restored) in the up component derived from ambiguity resolved GPS using JPL products at M_2 (a, c, e) and O_1 (b, d, f) tidal constituents in the east, north and up components. The grey dot in the right bottom corner of each plot represents average error ellipse over all sites.

The JPL GPS AR estimated OTLD is shown in Fig. 4.2, for M_2 (left) and O_1 (right) for each of east, north and up components after the restoration of the signal. Each panel shows strong spatial coherence giving immediate confidence in the robustness of the estimates, unsurprising given the amplitudes regularly exceed 10 mm in all coordinate components for both M_2 and O_1. As expected, signals are generally largest nearest the coast and decay inland, although substantial signal exists in the interior for various constituents and components (e.g., O_1 north, M_2 east). Particularly striking spatial patterns are evident along the densely observed east coast. Largest signals at M_2 are found in the Broome region of north-west Australia where site BRO1 shows the maximum M_2 OTLD in the up component of 30 mm following by 15 mm over the Australian east coast. These particular displacements reflect larger tides in the region (Fig. C.2a).

For M_2 up, the phase of the signal is shown to rotate along the east coast and for several hundreds of km inland, with signal of ~3 mm amplitude in central Australia. This distribution of displacement that decays into central Australia is also true for the east and north components of M_2 though with smaller amplitudes.

The observed O_1 displacements in the up component decay towards the east coast, aligning approximately uniformly in phase to 0°and -90°in the east and north components respectively (Fig. 4.2 d-f). Central Australian sites experience displacements of ~4 mm in amplitude compared to the small signal at M_2 in all coordinate components.

While the OTLD field in Fig. 4.2 is limited to GPS AR, results from any constellation are broadly similar when plotted at this scale. Thus, we proceed with analysis of the differences with modelled OTLD and discuss potential systematic errors.

4.3.4 Comparison of modelled and observed OTLD

4.3.4.1 Comparison of solutions based on different orbit and clock products

In Fig. 4.3a and b, we show the difference, Z_{res}, between the JPL AR GPS-only derived OTLD estimates of M_2 and O_1 (Fig. 4.2a, b) and modelled OTLD, based on FES2014b and STW105dc Green's function. M_2 Z_{res} are largest along the south-east coast and extending several hundred kilometers inland, with amplitudes reaching ~1.5 mm but generally smaller than 0.5 mm in the interior. For O_1, the residuals remain on the level of ~0.3 mm over much of the continent.

The middle and bottom rows of Fig. 4.3 show Z_{res} but for GPS+GLONASS solutions using ESA (Fig. 4.3c, d) and CODE (Fig. 4.3e, f) products. M_2 panels (Fig. 4.3a, c, e) demonstrate a high degree of similarity in the Z_{res} between solutions. M_2 ESA Z_{res} are rotated along the east coast (see also Fig.4.4c) and are much larger in northern Australia than JPL or CODE, while CODE M_2 Z_{res} is larger in the western Australia. M_2 Z_{res} in horizontal components is also close between solutions (Fig. C.4.1). The mean M_2 Z_{res} magnitude values, $\overline{\|\Delta Z_{\text{res}}\|}$, are ~0.22, ~0.23 and ~0.40 mm in the east, north and up components, respectively, independent of which products were used in generating the solution with either GPS AR or GPS+GLONASS constellation modes. The M_2 up value is slightly smaller for the two sets

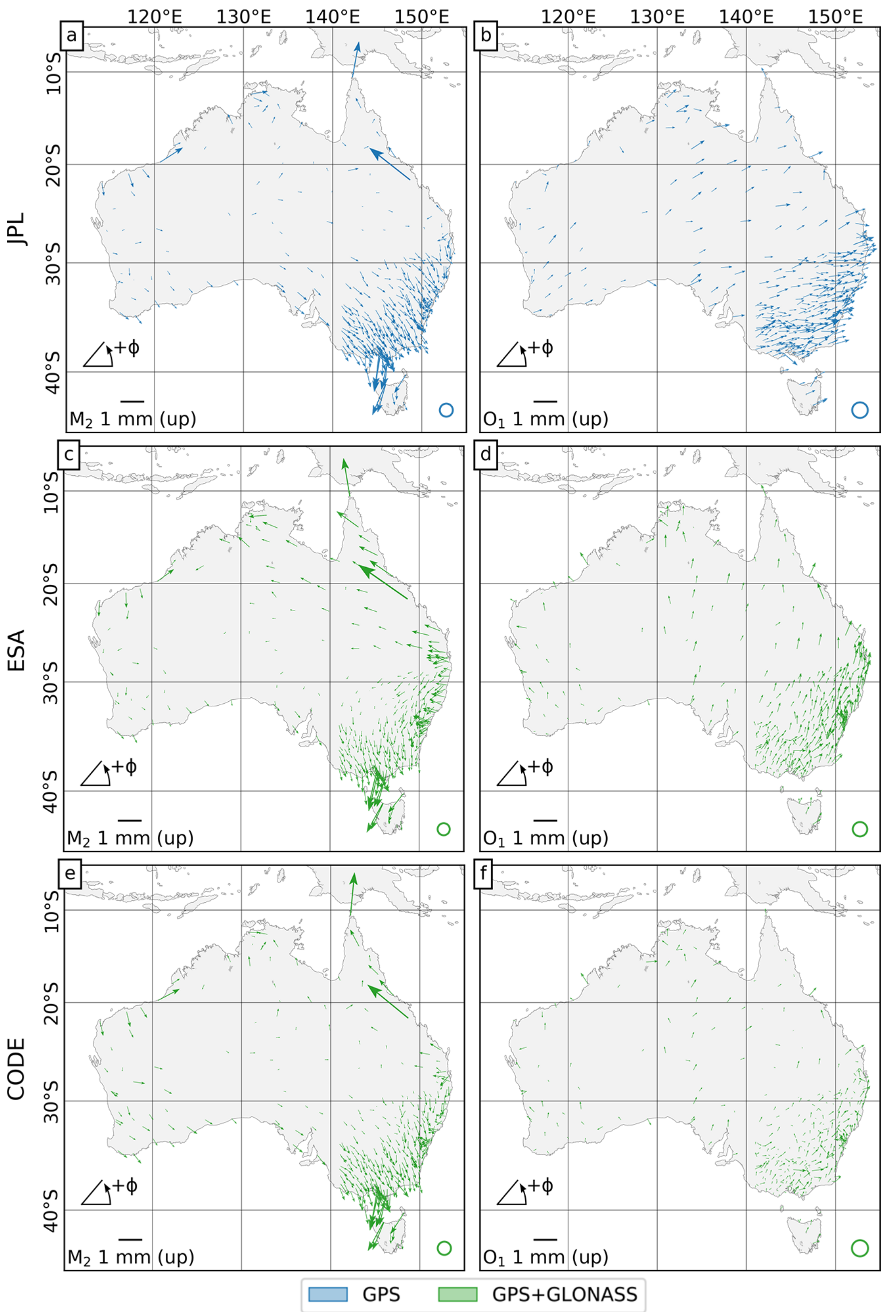

FIGURE 4.3: Residual OTLD, Z_{res}, in the up component for M_2 and O_1 constituents derived from GPS-only JPL AR (a, b) and GPS+GLONASS ESA (c, d) and CODE (e, f) products solutions relative to modelled OTLD computed with FES2014b ocean tide model and STW105dc Green's function. The circle in the bottom right represents the mean 95 % confidence ellipsoid over all sites.

of GPS+GLONASS solutions compared to GPS AR adding further to evidence that adding multiple constellations improves estimates of tidal displacements. M_2 $\|Z_{res}\|$ values of solutions based on non-integer ambiguity GPS-only and GLONASS-only solutions are mostly larger than the above GPS AR or GPS+GLONASS values independent of the products and component (see Table 4.1). Despite the inter-solution similarity, the estimates based on JPL products (independent of AR) in the east component (Fig. C.4.1a) show lateral change of $\|Z_{res}\|$ between eastern and western Australia relative to both ESA (Fig. C.4.1d) and CODE (Fig. C.4.1g) GPS+GLONASS residuals. We do not understand the origin of this signal, although it must originate in the orbit and clock products.

TABLE 4.1: Mean of M_2 and O_1 residual magnitudes, $\overline{\|Z_{res}\|}$, derived from solutions using JPL (GPS only), ESA and CODE products and GPS, GLONASS, GPS+GLONASS constellation modes. JPL products were also used to compute solutions with integer ambiguity resolution (AR). Z_{res} was computed relative to modelled OTLD values with FES2014b ocean tide model and STW105dc Green's function with CoM correction in case of JPL.

$\overline{\|Z_{res}\|}$, mm		JPL GPS	JPL GPS AR	ESA GPS	ESA GLO	ESA GPS+GLO	CODE GPS	CODE GLO	CODE GPS+GLO
M_2	east	0.33	0.21	0.26	0.32	0.22	0.21	0.24	0.19
	north	0.18	0.22	0.25	0.21	0.22	0.21	0.23	0.22
	up	0.37	0.38	0.39	0.41	0.34	0.42	0.32	0.34
O_1	east	0.21	0.26	0.16	0.20	0.14	0.32	0.32	0.24
	north	0.34	0.35	0.16	0.16	0.14	0.21	0.25	0.24
	up	0.44	0.39	0.30	0.34	0.31	0.27	0.31	0.19

We also directly compared Z_{res} estimates derived from GPS+GLONASS and GPS AR by computing a mean of the respective Z_{res} vector difference magnitudes, $\overline{\|\Delta Z_{res}\|}$. CODE GPS+GLONASS Z_{res} in the north and up components are close to that of JPL GPS AR with $\overline{\|\Delta Z_{res}\|}$ of ~0.1 mm while ESA GPS+GLONASS Z_{res} is close to JPL GPS AR only in the north component ($\overline{\|\Delta Z_{res}\|}$ <0.02 mm). This is different to the results reported in Matviichuk et al. (2020) where ESA GPS+GLONASS derived Z_{res} were found to be closer than that of CODE to Z_{res} derived from JPL GPS AR over all components. This change may be related to the differences in products used - operational products in this study and reprocessed products (repro2) in Matviichuk et al. (2020)", but the quantification of this would require a dedicated experiment.

Regarding the O_1 constituent, the Z_{res} phasors show rotations and magnitude variations over JPL, ESA and CODE products (Fig. 4.3b, d, f). In particular, JPL AR and ESA residuals appear rotated by about 90 ° over the east coast (comparing Fig. 4.4d and Fig. 4.4e). Visually, estimates based on CODE products have the smallest O_1 Z_{res} in the up component (Fig. 4.3f and 4.4f). As shown in Table 2, CODE products solutions demonstrate the smallest $\overline{\|\Delta Z_{res}\|}$ in the up component and ESA in the horizontal components; JPL AR solutions have the largest $\overline{\|\Delta Z_{res}\|}$ in the north and up while CODE $\overline{\|\Delta Z_{res}\|}$ are the largest in the east component across all three constellation modes. However, these summary statistics hide that regional variations exist in the magnitude of the residuals, for example the east component CODE GPS+GLONASS Z_{res} anomaly in the western Australia (comparing Figs C.4.2a and g).

4.3.4.2 Sensitivity of modelled OTLD to different ocean tide models

Now considering different ocean tide models used in the modeling, OTLD computed relative to GOT4.10c are generally comparable to those computed with FES2014b, as described above. There are, however, localized differences between modelled OTLD values in the up component. These are concentrated in M_2 and mostly in Bass Strait and several areas in the north and north west of Australia with $\|\Delta Z_{res}\|$ reaching 1.5 mm in the very north, at the Thursday Island site (TITG) in the Torres Strait (see Fig. C.6.1a-c). In terms of O_1, the

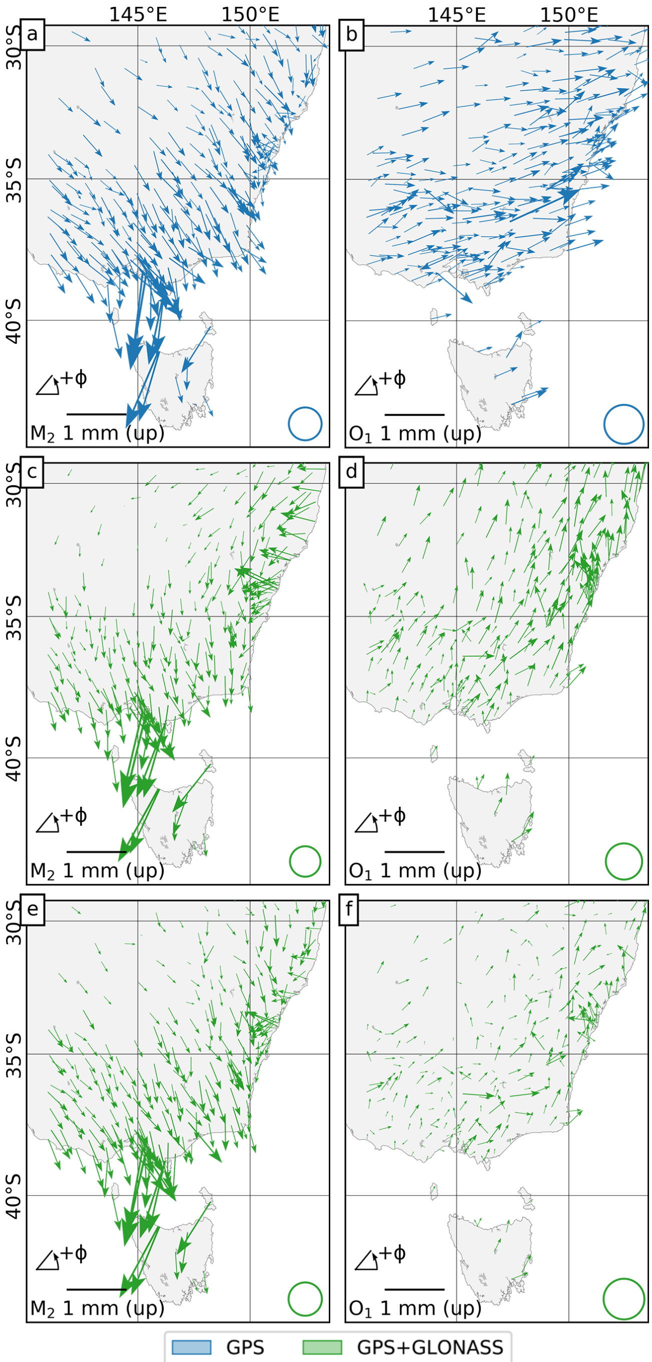

FIGURE 4.4: M_2 (left panels: a, c, e) and O_1 (right panels: b, d, f) Z_{res} in the up component over south-east Australia computed with JPL , ESA and CODE (top, middle and bottom respectively) relative to FES2014b ocean tide models and STW105dc Green's function. JPL solutions are GPS-only AR (CM), ESA and CODE are GPS+GLONASS (CE). The circles in the bottom right represent the mean 95 % confidence ellipsoid over all sites.

differences in modelled displacements between the two tide models do not exceed 0.1 mm and are usually half of that, with $\overline{\|\Delta Z_{res}\|}$ of 0.04 mm (Fig. C.6.2a-c).

Both TPXO9.v1 and TPXO9.v2a models (we focus on TPXO9.v1 but the difference with TPXO9.v2a is negligible) also produce similar M_2 up results to FES2014b and GOT4.10c with improvement in the Bass Strait and the East coast (comparing GPS+GLONASS Z_{res} in Fig. C.4.1 and C.5.1), although residuals are still larger in Bass Strait than in other locations pointing to residual tide model errors in TPXO9.v1 variants. No noticeable difference is present in the horizontal components of M_2 (Fig. C.6.1d-f). The O_1 TPXO9.v1 OTLD values are very close to those computed with FES2014b (mean difference of 0.03 mm) with marginal increase of the $\overline{\|\Delta Z_{res}\|}$ in the up (0.08 mm) as demonstrated in Fig. C.6.2d-f.

Interestingly, JPL Z_{res} shows significant differences between TPXO9.v1 and either FES2014b and GOT4.10c. This is evident in all components and of both constituents but most noticeable in the up for M_2 (Fig. C.5.1a-c) and in the north for O_1 (Fig. C.5.2a-c) where $\|\Delta Z_{res}\|$ values increase by up to 0.2 and 0.4 mm, respectively, relative to FES2014b and GOT4.10c. We discuss the source of this signals in section 4.3.6.

4.3.4.3 Sensitivity of modelled OTLD to Green's functions and corrections

The three Green's functions used in the analysis, PREM, STW105 and S362ANI, do not produce a noticeable difference in terms of residuals distribution over a set of ocean tide models (Fig. C.9.1-C.9.3). One of the explanations for this is the high number of inland stations, away from the coast, where OTLD is small, thus the cumulative effect from changing Green's function is insignificant. The analysis of 50 coastal sites (marked with * in Table C.1) revealed a marginal advantage of S362ANI Green's function in the up component but it produces larger Z_{res} in the east component.

We now assess, in turn, the effects of considering the corrections to the previously defined Green's function: anelastic dissipation correction at M_2, and the correction for spatial water density and compressibility correction. Fig. 4.5 shows the cumulative effect from corrections at M_2 (a, c, e) and O_1 (b, d, f) in the up component. These tests were conducted using FES2014b and STW105 and have very similar impacts for the other tide models and one dimensional Earth models.

For anelastic dissipation, the effect for M_2 in the up component is generally negligible, due to the large number of sites away from the coast where the effect is largest (Fig. C.8.1a, C.9.1-C.9.3). The dissipation correction is only significant in up at the very same 50 coastal sites located right along the east and north-west coasts of Australia, but less uniform than in the previous studies of western Europe (Bos et al., 2015; Matviichuk et al., 2020). The coastal dataset demonstrates the previously reported 0.2 mm improvement of the mean $\|Z_{res}\|$ and reduces the variance regardless of the underlying Earth or ocean tide model(Fig. C.9.4-C.9.6). The effect from dissipation correction in the east component is strong in the south-east and north Australia (Fig. C.8.1a). North component shows the rotation of the correction's phasors in the south-east Australia close to Bass Strait and strong signals at stations in the west (Fig. C.8.1b).

Altering the elastic constants of the Earth model from 1 Hz to the M_2 period due to dissipation also affects other tidal constituents including O_1. The dissipation correction at O_1 is usually negligible ($\sim$0.03 mm) over all components, reaching 0.2 mm in the up component in the very north close to Torres Strait (Fig. C.8.2a-c,C.10.1-C.10.3). We also tested altering elastic constant from 1Hz to O_1 constituent period, but the impact from the correction on O_1 and other constituents was found to be negligible ($<$0.1 mm) .

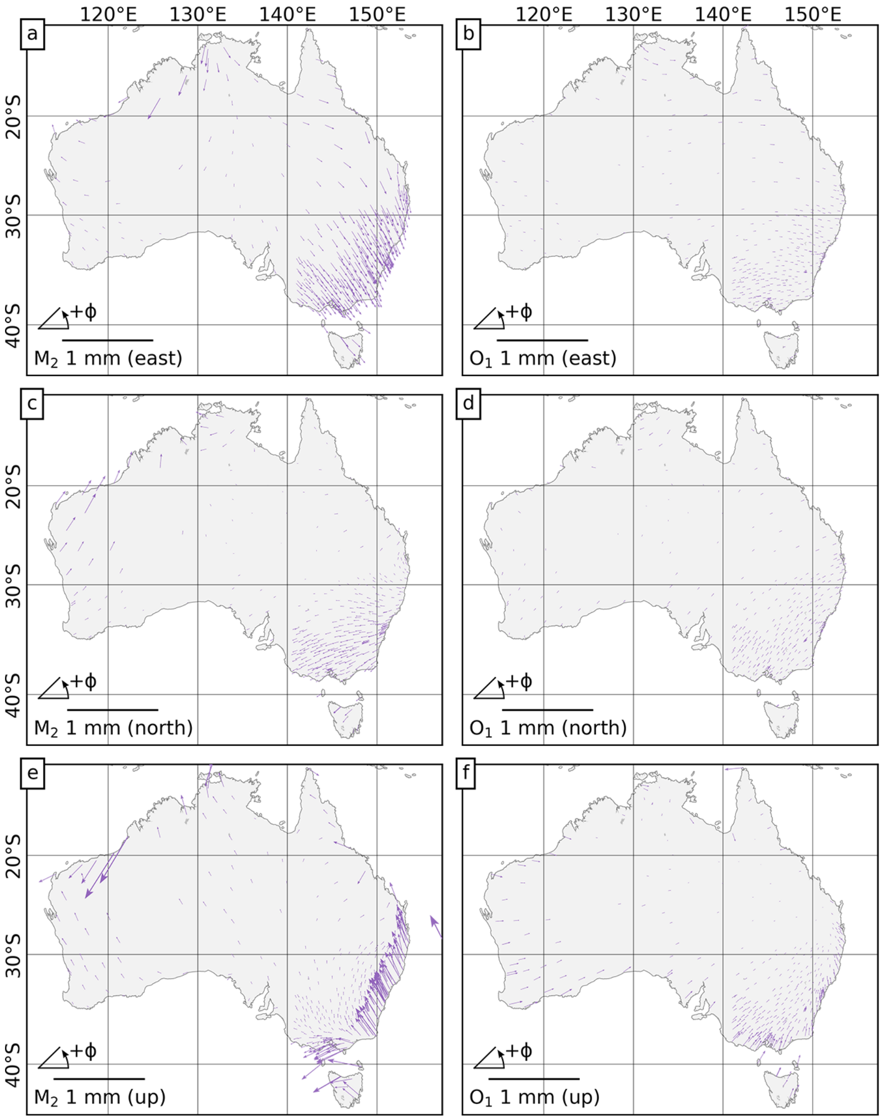

FIGURE 4.5: The modelled effect due to considering dissipation and spatial water density and compressibility corrections for the east (top), north (middle) and up (bottom) components at M_2 (left panels) and O_1 (right panels).

The spatial water density and compressibility corrections demonstrate uniform effect over both inland and coastal sites, but the average effect is small. For M_2, the average magnitude of the correction effect is 0.1 mm in the up and east, and negligible (~0.04 mm) in the north (see Fig. C.8.1d-f), reaching 0.2 mm in the up component at the sites that experience maximum OTLD. At O_1, average correction magnitude is half of that of M_2 but shows strong 0.1 mm residual magnitude in the up component at the sites in western Australia (Fig. C.8.2d-f).

4.3.5 Comparison of solutions using GPS, GLONASS or GPS+GLONASS

We now provide an assessment of the impact of the choice of constellation configuration on the derived OTLD at M_2 and O_1. For this we fixed the OTLD model predictions to the combination of FES2014b tidal model and STW105dc Green's function. Previous analysis done across western Europe and New Zealand has shown that GPS+GLONASS performs close to GPS AR at lunar constituents, especially the M_2 while GPS AR performs better in the east component, in which integer ambiguity resolution has greatest impact. No apparent systematic differences were detected, possibly due to limitations of the spatial scale.

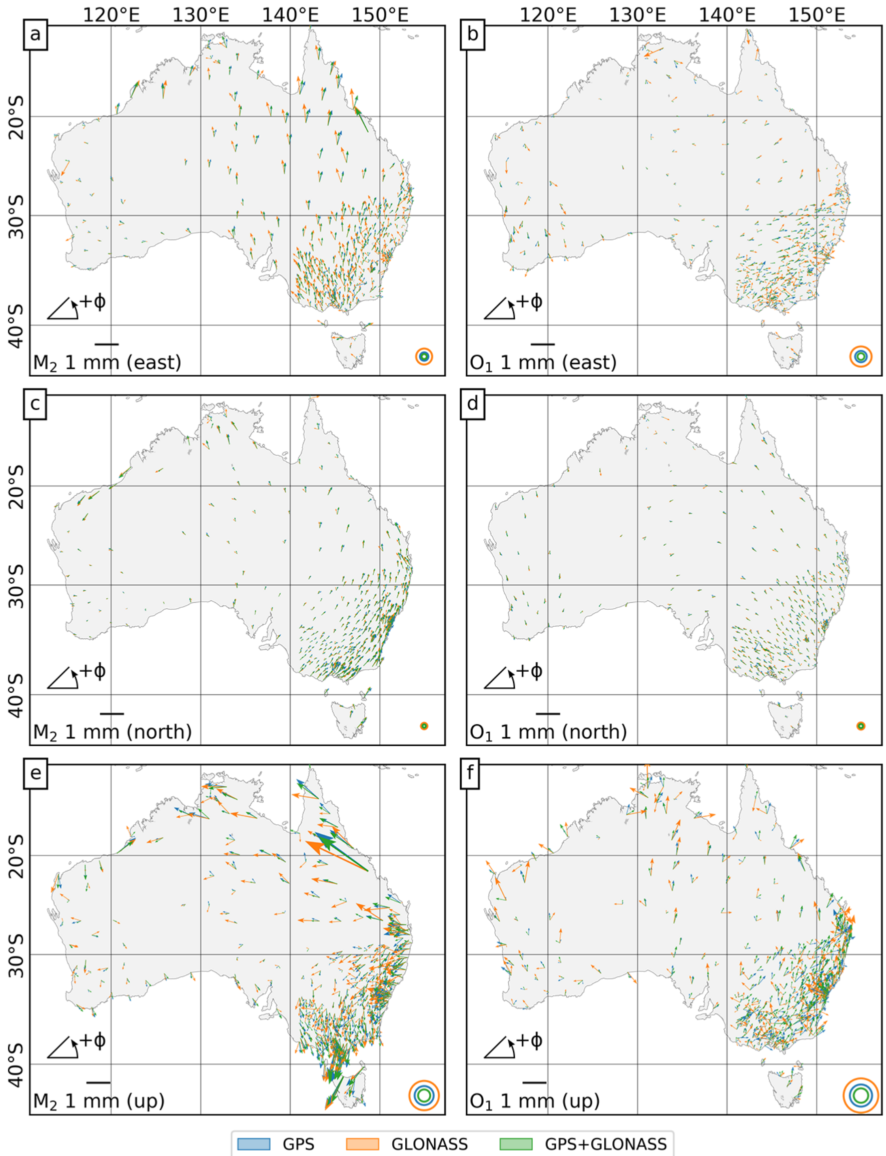

FIGURE 4.6: M_2 (a-c) and O_1 (d-f) OTLD residual displacements derived from GPS, GLONASS and GPS+GLONASS solutions using ESA products for the east, north and up components. The circles in the bottom right represent the mean 95 % confidence ellipsoid for all sites with constellation configuration used according to the legend.

Fig. 4.6 shows residual phasors derived from each of GPS-only (blue), GLONASS-only (orange) and GPS+GLONASS (green) solutions using ESA products. All constellation modes perform similarly in the north component at both M_2 and O_1 (Fig. 4.6c, d) with most visible difference in the east component (Fig. 4.6a, b). ΔZ_{res}, a Z_{res} vector difference computed at each site between different constellation modes solutions reveals that GPS-only and GPS+GLONASS OTLD estimates are close: in the up component, M_2 mean $\|\Delta Z_{res}\|$ between GPS and GPS+GLONASS is $\sim$0.13 mm with both ESA and CODE products while for O_1 it is 0.15 mm and 0.2 mm with ESA and CODE, respectively. Mean $\|\Delta Z_{res}\|$ between GLONASS and GPS+GLONASS is twice the values derived from GPS and GPS+GLONASS

TABLE 4.2: Mean of M_2 and O_1 phase standard deviations, $\overline{\sigma(\phi)}$, derived with ETERNA from JPL (GPS only), ESA and CODE products solutions (GPS, GLONASS, GPS+GLONASS). JPL products were also used to compute solutions with integer ambiguity resolution (AR).

		JPL		ESA			CODE		
$\overline{\sigma(\phi)}$, °		GPS	GPS AR	GPS	GLO	GPS+GLO	GPS	GLO	GPS+GLO
M_2	east	1.43	0.60	1.60	3.08	1.00	2.05	3.28	1.26
	north	1.29	0.90	3.59	4.81	2.39	4.12	4.42	2.46
	up	2.56	2.57	2.10	3.23	1.38	2.45	3.38	1.56
O_1	east	2.56	1.17	10.66	18.13	6.43	9.05	13.00	5.32
	north	0.92	0.72	3.18	4.10	2.20	4.16	4.04	2.77
	up	9.60	5.02	4.35	6.97	2.78	5.66	7.52	3.29

difference ($\sim$0.28 and $\sim$0.3 mm for M_2 and O_1) in the up. East component comparisons show the same distribution but with magnitudes half of what is seen in the up while the differences in the north component shows negligible magnitudes for both constituents, independent of constellation modes (<0.05 mm). The increase of GLONASS Z_{res} in the east and up components, relative to the GPS and GPS+GLONASS, may be related to the larger number of satellites in the GPS constellation producing a combined solution weighted towards GPS (Matviichuk et al., 2020).

ESA/CODE GPS+GLONASS Z_{res} estimates have the smallest uncertainties (SD) at both M_2 and O_1 producing smallest mean confidence ellipsoid over all components (Fig. 4.6). The confidence ellipsoids were estimated from amplitude and phase uncertainties derived from ETERNA. GPS AR, however, has smaller uncertainty than GPS+GLONASS in the east component at M_2 and O_1 (Figs C.4.1, C.4.2) presumably due to the impact of GPS ambiguity fixing on the east component (Blewitt, 1989). The GLONASS mean uncertainty is the largest independent of the component. Note that uncertainties here are derived from ETERNA, reflecting time series noise, and are not reliant on the formal uncertainties of the coordinate time series. The average uncertainty of the estimated amplitude values for both constituents is less than 0.01 mm, while phase values average while the average uncertainty of the phase values is on the level of 2-5 ° for JPL GPS AR and ESA/CODE GPS+GLONASS solutions depending on the constituent and coordinate component. The mean amplitude uncertainty values are thus excluded from the analysis as the confidence ellipsoids are mostly controlled by the uncertainty of phase the values (Table 4.2).

We further illustrate the variations in the OTLD residuals as the constellations and products are varied using a modified empirical cumulative distribution functions (ECDFs) as per Martens and Simons (2020) (Fig. 4.7). Curves that rise most quickly to 1.0 reflect a relatively better overall fit of the modelled values with the observations. Note that each ECDF curve had respective mean Z_{res} value subtracted (normalized). This excludes the possible common mode errors/biases showing the pure distribution of fit (see Fig. C.11 for unmodified ECDF curves).

The horizontal components of M_2 and O_1 demonstrate close agreement to models, converging to 1.0 at 0.3 mm with the only exception being GLONASS that reaches 1.0 at 0.5 mm

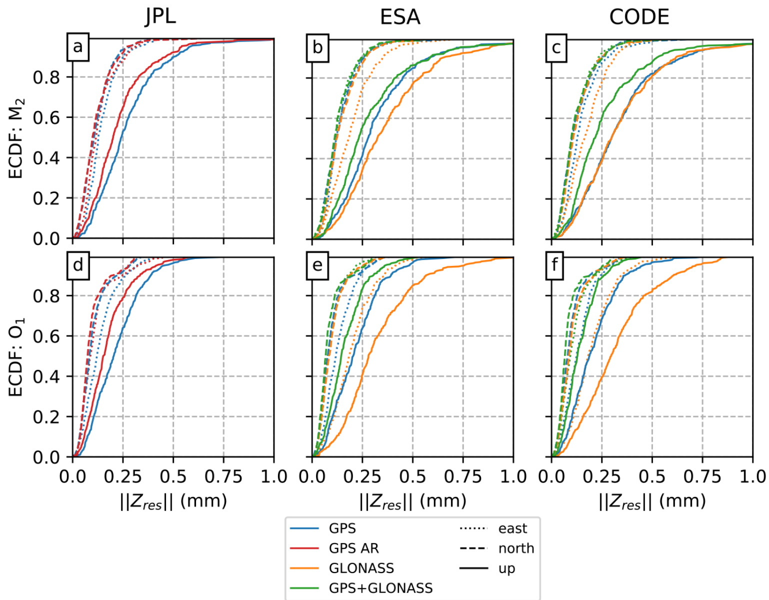

FIGURE 4.7: Empirical cumulative distribution functions (ECDFs) of OTLD residuals (east, north, up) relative to the FES2014b ocean tide model and STW105dc Green's function for JPL, ESA and CODE solutions for M_2 (top panels) and O_1 (bottom panels) constituents. The mean OTLD residual vector has been subtracted. "GPS AR" stands for integer ambiguity resolution only available with JPL products.

in case of M_2 (ESA) and O_1 (both ESA and CODE). Note that with the mean Z_{res} removed no obvious difference between GPS AR and GPS+GLONASS fit in the east component is present (as reported in Sect. 4.3.5). This can be explained by the common signal in the east component experienced by all sites in the case of GPS+GLONASS solutions.

For the up component, normalized Z_{res} magnitude of JPL GPS AR shows better fit (ECDF is 1 at ∼0.8 mm) than CODE/ESA GPS+GLONASS (ECDF is 1 at ∼1 mm) at M_2, performing the same at O_1 (Fig.4.7). GPS-only (non-AR, solid blue lines) M_2 ECDFs are similar across ESA and JPL products (Fig. 4.7a, b), as reported previously in Matviichuk et al. (2020) for western Europe. However, there is a slightly reduced agreement with CODE that demonstrates GPS-only performance similar to that of GLONASS. At the O_1, up component, GPS-only demonstrates far better fit than GLONASS independent of the satellite products. GLONASS demonstrates the worst performance at both M_2 and O_1 performing in east component same as GPS in the up at O_1.

4.3.6 Large-scale bias in TPXO9

Next, we fix the Green's function to STW105dc while iterating through the ocean tide models. Both TPXO9.v1 and TPXO9.v2a ocean tide models show improvements at M_2 relative to FES2014b and GOT4.10c with ESA and CODE solutions (Fig. C.9.2 and C.9.3). JPL products solution show Z_{res} of constantly higher magnitude (bias, for simplicity) with TPXO9.v1 and TPXO9.v2a ocean tide models at M_2 and O_1 of ∼0.2 and ∼0.3 mm respectively at all sites (Fig. C.9.1a-c and Fig. C.9.2a-c). We use TPXO9.v1 in all further analysis as the difference with TPXO.v2a was found to be negligible in the region. To illustrates the issue, we computed a vector difference between FES2014b and TPXO9.v1 modelled values (CM) at

M_2 and O_1 (Fig. 4.8a, d). We next explore potential contributors to the biases evident with TPXO9-based models.

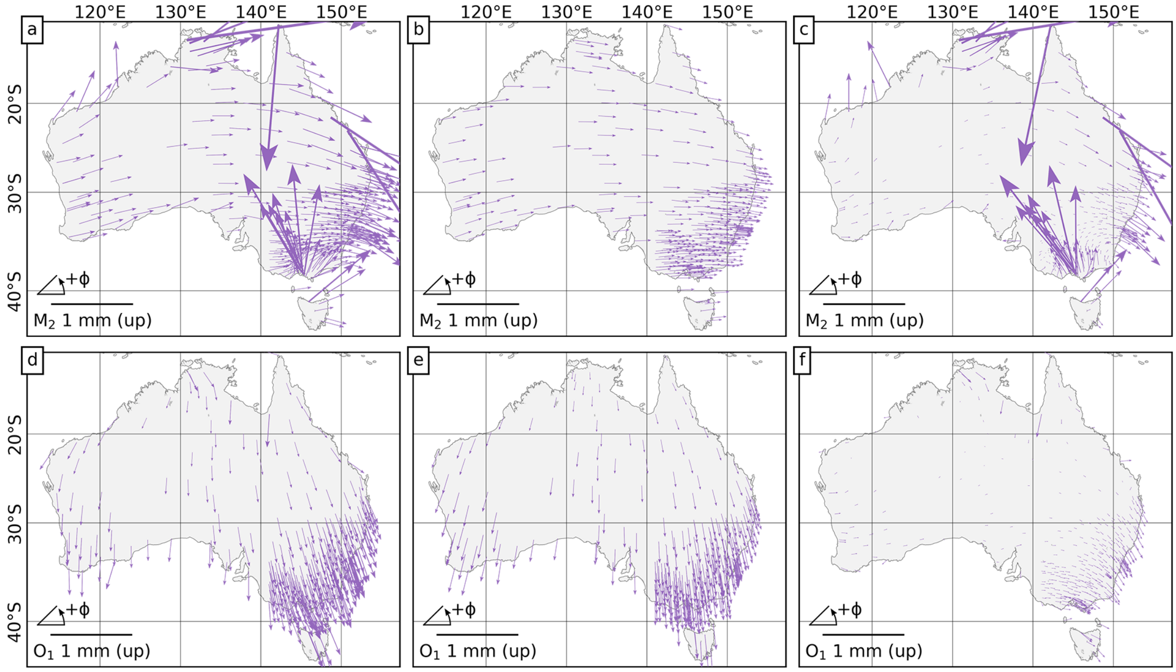

FIGURE 4.8: Site vector differences for the up component between CM OTLD values for M_2 (top) and O_1 (bottom) based on the FES2014b and TPXO9.v1 loading field (a, d) and the vector difference between the respective CoM values only (b, e). The phasor fields shown in a and b are very similar except for local anomalies associated with the Bass Strait (south east) and Timor Sea (north) that are related to the differences in the models. (c, f) show the vector difference between OTLD residuals (a, b) and CoM residuals (d, e).

4.3.6.1 Assessment of CoM values

The absence of this effect in the CE modelled values used with ESA and CODE solutions, its similarity between stations, and considering the results from local ocean tide models grids comparison (Fig. C.2), suggest that the difference is related to the CoM correction associated with far-field differences between the TPXO9.v1 and both of FES2014b and GOT4.10c. First, we computed a vector difference between CoM-corrected FES2014 and TPXO9.v1 modelled OTLD values (Fig. 4.8a, d). Next, we computed CoM values by subtracting CE OTLD values from respective CM for M_2 and O_1 (Fig. 4.8b, e). The alignment of both phasor maps strongly suggests that observed difference between modelled values is in the CoM correction. Note that both CM and CE OTLD are computed through convolution of the modelled tidal mass with respective CM/CE Green's function. As such, differences between resulting CoM values are related purely to the ocean tide models.

Correcting the TPXO9-related bias by subtracting it from the modelled OTLD difference makes the resulting TPXO9/FES2014b vector difference close to that using solutions computed with CE satellite products with localized differences in the up component related to the Bass Strait, Timor Sea and the Great Barrier Reef at M_2 and to the East coast at O_1 (Fig. 4.8c, f). The observed CoM-related bias reflects global-scale mass changes as opposed to the more regional or local-scale variations that dominate the loading deformations. The

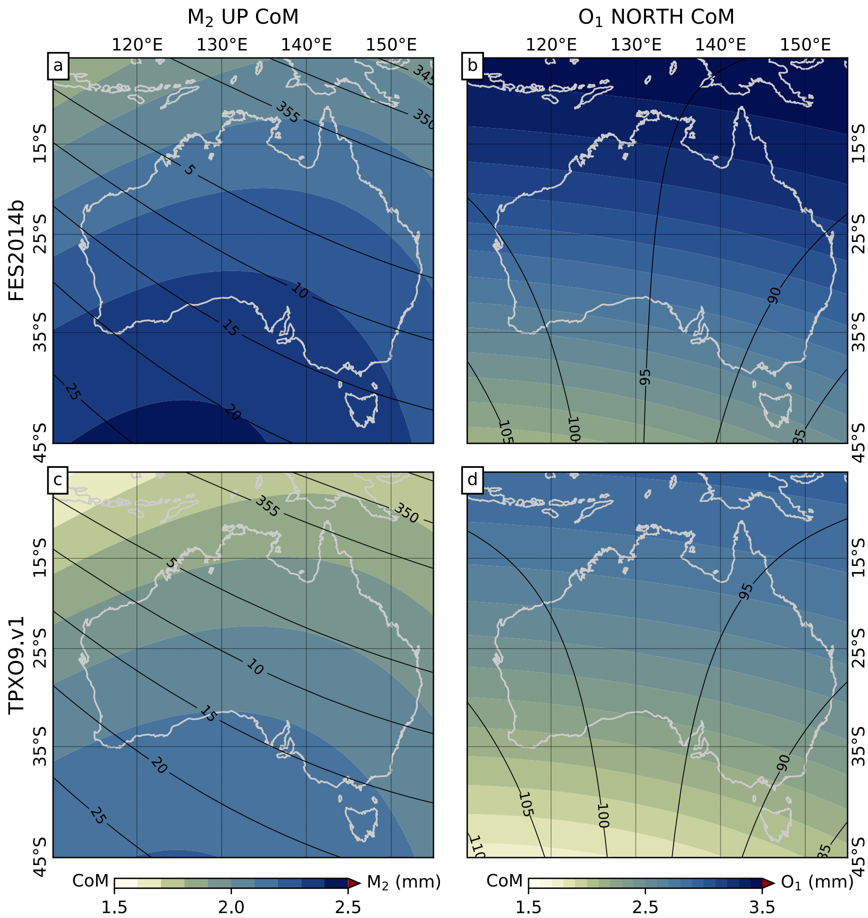

FIGURE 4.9: M_2 CoM in the up and O_1 CoM in the north component computed with FES2014b (a, b) and TPXO9.v1 (c, d) ocean tide models. Note the constantly larger CoM amplitudes in case of FES2014b.

CoM bias in the east and north components at M_2 and O_1 is presented in Fig. C.12.1 and C.12.2, respectively.

We generated OTLD grids using the same set of ocean tide models and fixed Green's function in CE and CM frame. The vector differences between CM and CE grids is effectively a CoM grid showing the CoM distribution over the region. We focus on components with most significant CoM bias in TPXO9: the up component for M_2 and north component for O_1 (Fig. 4.9). While the distribution in ENU varies, the result of ENU to XYZ conversion should be equal to a single set of XYZ values constant to each ocean tide model.

We then converted CoM values from ENU to XYZ frame through transformation of in-phase and out-phase components separately. The observed noise associated with numerical precision on the level of <0.05 mm was removed with averaging of values over sites. Also, we observed negligible CoM biases created by introducing spatial water density and compressibility corrections (~0.05 mm for M_2 and ~0.02 mm for O_1) in each of X, Y and Z components (Fig. C.14.1). We also explored the effect of water mass conservation but we found it to be negligible as well (see Supplementary Information).

TABLE 4.3: M_2 and O_1 CoM amplitude (A) and phase (ϕ) values, computed with FES2014b, GOT4.10c and TPXO9.v1.

		A, mm			ϕ, °		
		X	Y	Z	X	Y	Z
M_2	FES2014b	1.590	1.275	2.099	-33.806	-171.550	53.205
	GOT4.10c	1.579	1.298	2.211	-33.398	-171.735	54.095
	TPXO9.v1	1.383	1.095	1.959	-31.296	-173.348	51.738
O_1	FES2014b	1.485	1.392	3.451	15.264	35.162	-84.183
	GOT4.10c	1.473	1.374	3.522	15.981	38.077	-84.855
	TPXO9.v1	1.275	1.226	2.922	13.688	37.765	-82.351

4.3.6.2 Regional sources of the CoM differences

We assess the OTLD contribution of distant tides to the CoM bias observed with TPXO9.v1 focusing on five ocean tide models of which three are most recent: FES2014b, GOT4.10c with their previous version FES2012 and GOT00.2, and TPXO9.v1. We divided the global tide models into seven polygons covering the main ocean areas (Fig. C.15). The resulting CM and CE values, in ENU, were vector differenced to get CoM values and rotated to XYZ. CoM values from each global water region were then used to construct full CoM phasors (Fig. C.13). The Pacific region has the largest impact on the CoM but the Atlantic and Indian regions can demonstrate the same amount of CoM motion as the Pacific in the Y and Z components of M_2 (Fig. C.13b, c). The effect from Pacific is also the largest in O_1 with exception for X component where Indian and Atlantic water regions are equally large to that of Pacific (Fig. C.13d).

All reconstructed CoM phasors are very similar at M_2 while showing minor differences at O_1 (Fig. C.13), specifically O_1 in the Z component where TPXO9.v1 and two preceding models do diverge from FES2014b and GOT4.10c (Fig. C.13f).

We next compare TPXO9.v1 with the other four selected ocean tide models by vector differencing with each regional phasors to better study the region-specific differences. If the CoM bias is concentrated in a single area, we should see it as a single phasor in the vector difference test. Fig. 4.10 clearly demonstrates that the TPXO9.v1 CoM deficiency relative to the two global ocean tide models CoM, FES2014b and GOT4.10c, is distributed over multiple regions of the globe. Both FES2012 and GOT00.2 CoM show smallest variations relative to TPXO9.v1 except for M_2 in the X component where GOT00.2 shows 0.15 mm divergence similar to FES2014b and GOT4.10c (Fig. 4.10). In addition, one can observe how FES2014b and GOT4.10c are similar at M_2 and O_1 in all components with exception of M_2 in Z component, presumably associated with the Antarctic, Arctic, and Atlantic regions. In all other cases, closer agreement can be inferred between FES2014b and GOT4.10c than between TPXO9.v1 and either other model.

GOT4.10c model was explicitly corrected for the effect of altimeter observations being in the CM frame (hence the 'c') (Desai & Ray, 2014) while FES2014b loading tide is based on GOT4.8ac, another explicitly geocenter-corrected model (Lyard et al., 2021). We are not aware if an altimeter geocenter correction was included in TPXO9.v1, and if not then this may be the reason for the observed difference especially considering the similarity between TPXO9.v1 and the preceding models.

Overall, the exact source of the CoM bias in TPXO9.v1 is not certain. The bias is also present with TPXO9.v2a and we have not examined earlier versions of the TPXO tide model series. While both TPXO9 variants can safely be used for OTLD modeling in CE frame, the CM correction computed with this models should ignored in favour of FES2014b or GOT4.10c. Example of such a use-case is processing PPP solutions with using orbits and clocks in CM frame as in the case of native JPL products.

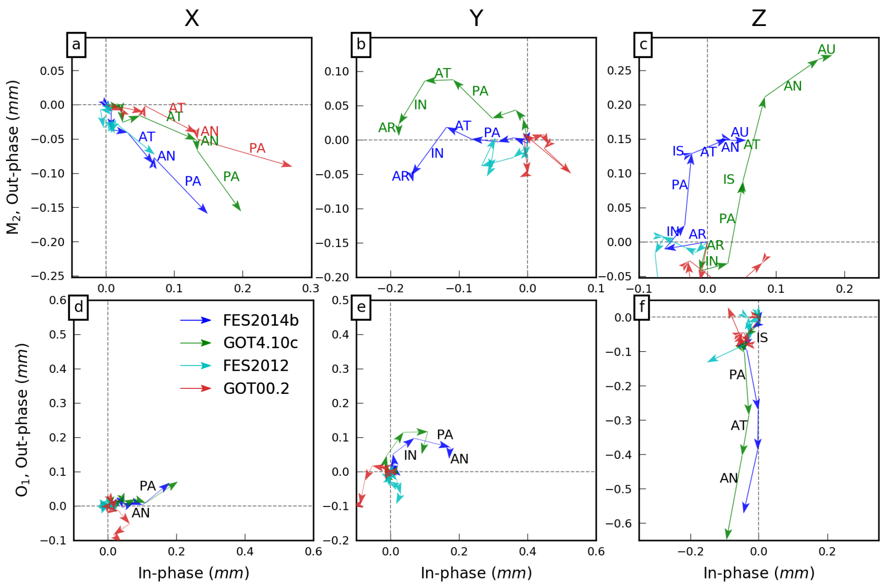

FIGURE 4.10: Reconstructed from global regions FES2014b, GOT4.10c and their respective predecessors, FES2012 and GOT00.2, phasors vector differenced with TPXO9.v1 phasors for M_2 (a-c) and O_1 (d-f) over X, Y and Z components. Alignment of both phasors demonstrates that both models are a lot closer between them-selves than with TPXO9.v1. The two-letter indices represent regions of global ocean: AN – Antarctic, AR – Arctic, AT- Atlantic, AU – Australia (local), PA – Pacific, IN – Indian and IS – Indonesian.

4.3.6.3 Further Discussion

This chapter studies OTLD across a Australia demonstrating the deficiencies that could be associated with differences in satellite products and ocean tide models in greater detail. The selected dataset reveals large scale biases, in particular biases in JPL GPS-derived in the east coordinate component across western Australia, and high-resolution coherent residual OTLD variations over a dense network of sites adjacent to the Bass Strait. The study fits in between local regional studies of OTLD areas with complicated tides (e.g., King, 2006; Penna et al., 2015; Wang et al., 2020; Yuan et al., 2009) or tectonics (Ito & Simons, 2011; Matviichuk et al., 2021b) and global studies (e.g., Yuan et al., 2013). Our work fills a gap in our knowledge of OTLD interpretation over regional scales in a similar way to Yuan and Chao (2012) in the western United States.

Accounting for their study of the effect of anelasticity, in the form of dissipation correction, and for the effect of the spatial water density and compressibility can explain 0.2-0.5 mm of unmodelled signal depending on site's distance from the coast which otherwise can propagate into observations. Accounting for these effects should contribute to enhancement of satellite products, prompt further studies of Earth's anelastic response and increased inclusion of GNSS-derived tidal estimates into the ocean tide models computation and assessment.

The deficiencies of modern ocean tide models are very much localized and there is a strong confidence that the observed CoM bias of TPXO9 models was fully explained in this publication, which gives confidence to the residual OTLD values not being related to the systematic errors in the ocean tide models.

However, there is a limitation which prevents accurate geophysical interpretation of the derived residual OTLD related to the differences between OTLD estimates derived from different products solutions. These differences also vary through constituents and constellation modes, producing rotations in residual phasors specific to analysis center and constellation mode. The differences between analysis centers products suggest using residual OTLD estimates as additional quality control tool for these products.

4.4 Conclusions

We studied ocean tide loading displacements (OTLD) of semidiurnal M_2 and diurnal O_1 lunar constituents in order to extract reliable geophysical signals that could be used to infer an(elastic) properties of the Earth, related mainly to the asthenosphere. We also assessed ocean tide models and Green's functions used for theoretical modeling of the OTLD to understand the accuracy of the observed OTLD residuals. We processed 360 GNSS sites over Australia assessing timeseries estimated with GPS, GLONASS and GPS+GLONASS using ESA, CODE and JPL orbit and clock products.

We found that the OTLD values extracted from the solutions using ETERNA, demonstrate negligible differences due to change in products and/or constellation modes in the north component, increasing for the east and up, respectively. We, however, noticed a regional change in M_2 residual amplitude in the east component from east to west of Australia between JPL and ESA/CODE products solutions.

Addition of dissipation correction to the OTLD models reduced the residual OTLD amplitude of M_2 by 0.2 mm in the up component at the coastal sites and in the east component at inland and coastal sites. Spatial water density and compressibility corrections demonstrated a further 0.2 mm reduction of residuals at the coastal sites in the up component.

While most ocean tide models and Green's functions resulted in similar modelled displacement values, TPXO9.v1 models resulted in a noticeable bias at all sites when using products in the CM frame. This bias was found to be located in the center-of-mass (CoM) variation values used for converting the OTLD values to CM frame. Studying the region-by-region contribution of the tide model to the modelled CoM revealed that TPXO9.v1 CoM bias is not produced by a single ocean region but is spread in complex way through the global ocean.

Overall, our results show that while GNSS-derived estimates of ocean tide loading displacements show generally close agreement with models in Australia, important differences remain that depend on both the GNSS products and the ocean tide models in addition to uncertainties in elastic and anelastic Earth properties and body tides. These systematic differences are evident in continental scale observations that may not otherwise be clear in smaller-scale networks most commonly studied to date and motivate further research into their origin. The study also provides strong evidence for the inclusion of dissipation and spatial water density and compressibility corrections into modelled OTLD.

4.5 Thesis Context

This chapter focused on addressing RQ3 in an attempt to analyse OTLD across a large block of stable continental crust, highlighting the purely geodetic effects present in the results. The chapter focused only on the most reliable constituents M_2 and O_1, as demonstrated in chapter 2, for the further assessment of the benefits of adding the GLONASS constellation in combination with GPS. This and the assessment of the ocean tide models in the region contribute to the two last objectives of RQ1. The chapter also highlighted limitations in the GPS and GLONASS estimates, associated with orbit and clock products. The methods used in the chapter were based on those from chapter 2, while the OTLD modelling benefitted from the advancements made in chapter 3, i.e., the inclusion of the spatial water density and compressibility corrections. This chapter is now followed by a conclusions chapter to summarise the contribution to knowledge from this thesis.

Chapter 5

Conclusions, Contributions and Future Research

5.1 General Conclusions

This thesis sets out to advance the methodology of probing the elastic parameters of the Earth at frequencies much lower than seismic frequencies (from periods of first minutes to 1Hz and higher) – by observing the daily and sub-daily displacements of the Earth's crust due to the varying weight of ocean tides. The thesis demonstrates developments in two areas in parallel: geodesy and geophysics.

The thesis addresses specific knowledge gaps associated with accuracy of the derived tidal displacements with GNSS and the elastic structure/response of the Earth at tidal frequencies. To address the knowledge gaps, a set of Research Questions (RQs) has been created, namely:

RQ 1. What are the benefits from the addition of observations from the GLONASS constellation to GPS when estimating OTLD?

RQ 2. Are the derived OTLD estimates sensitive enough to detect the properties of the Earth's interior?

RQ 3. Are there variations of the residual OTLD field over a large blocks of stable continental crust and what are the possible sources of these variations?

The thesis objectives were achieved progressively per chapter, with each chapter contributing to the general idea of enhancement of derived OTLD estimates and the sensitivity of the method in general. Three regions were studied, each to answer one of three research questions - the United Kingdom, New Zealand and Australia.

The thesis started with addressing the RQ1 through calibration of the GPS and GLONASS constellations and process noise values in chapter 2 as per the technique of Penna et al. (2015) who studied optimal settings for M_2 but only with GPS constellation. Process noise settings for GPS and GLONASS data analysis were tuned to cover all eight major tidal constituents: four diurnal and four semi-diurnal. No single constellation mode was found to return the smallest residuals over all eight constituents, rather optimal constituent-constellation mode pairs were identified. Constituent estimates using the GLONASS constellation, while demonstrating the best performance at K_2 and K_1, varied substantially between different orbit and clock products and thus are presently unreliable. As previously identified for M_2 with GPS only, the application of an anelastic dissipation correction resulted in improved agreement between models and our observations, with a reduction in misfit of up to 0.2 mm in the up component.

Chapter 3 addresses RQ2, providing an assessment of the sensitivity of the OTLD to the Earth's processes by analysing a network of continuously running GPS stations in New Zealand focusing on the semi-diurnal M_2 constituent. In addition, it advances the last objective of RQ1 by assessing the global and local ocean tide atlases over the studied region. It has demonstrated the unexpected deficiencies of the local tide model – EEZ, which were confirmed by the revealed 8 cm difference at the coastal tide gauges while the average difference over a set of global ocean tide models was found to be $\sim$2-3 cm.

The closeness of the active tectonic margin, the Hikurangi subduction zone, to this network helped reveal the limitations of one-dimensional Green's functions in the Taupo Volcanic Zone, which could be extrapolated to other regions of complex tectonics. This assessment was based on GPS-only data as the coverage of multi-GNSS stations was not sufficiently dense in the areas of maximum geophysical signal. In addition to applying an anelastic dissipation correction, corrections were also developed and applied for spatial variations in water density and ocean compressibility. While these were effective, no correction or Green's function was able to change the sharp phasor rotation in the North Island. This led to the conclusion that the effects of lateral variations in (an)elastic Earth structure on OTLD are likely being detected.

Chapter 4 addresses RQ3 and is built on top of findings from achieving the objectives associated with RQ1 and RQ2. This chapter also advances the two last objectives of RQ1 as it continues the assessment of the GLONASS-related constellation modes sensitivities but over a large stable region with very limited presence of unmodeled OTLD of geophysical nature. The chapter focused on the most stable lunar semi-diurnal M_2 and diurnal O_1 constituents, as concluded from chapter 2. The densely covered coastline provided an opportunity for the assessment of global tide models and the corrections introduced in chapters 2 and 3. The dissipation correction was confirmed to be effective only at the coastal sites at M_2 in the up component. All sites, however, were affected in the horizontal components. Spatial water density and compressibility corrections were demonstrated to substantially impact only the up component, affecting sites up to several hundred kilometers from the coast. The large inland regions, far from the ocean, allowed the study of geodesy-related OTLD deficiencies ignoring the small-scale anomalies possibly related to geophysics.

Chapter 4 revealed, however, several systematic differences that limit accurate geophysical interpretation. First, a bias in OTLD estimates was found that was distributed equally through all sites when using modeled OTLD values based on TPXO9 models in CM frame. This bias was later found to be related to the center-of-mass inconsistencies in the TPXO9 models. Second, the differences were found between derived OTLD values estimated with different satellite products and constellation modes. These may may not otherwise be clear in smaller-scale networks most commonly studied to date but their origin is of great importance for all GNSS-related tasks.

5.2 Contributions to the body of knowledge

1. The thesis presents an early contribution to the assessment of the advantages of GPS+GLONASS combination for estimation of ocean tide loading displacement and its sensitivity to eight major constituents.

2. The thesis contains the first published results of a GNSS-estimated ocean tide loading displacement field across New Zealand (Chapter 3) demonstrating sensitivities of the residual tidal displacements to the areas of increased tectonic complexity, and the limitations of one-dimensional Green's functions in the areas of such complicated structure.

3. All recent ocean tide models were assessed in three different regions of the globe: United Kingdom, New Zealand and Australia.

4. The thesis demonstrates deficiencies of outdated global and local ocean tide models (e.g., FES2004, local NZ ocean tide model EEZ).

5. The thesis highlights that an anelasticity correction should be included in forward models in conventional GNSS (e.g., 24 hr positioning) to mitigate propagation of tidal signals into GPS time series.

6. The importance of the spatial water density and compressibility correction was demonstrated, highlighting noticeable improvements at the coastal GNSS sites.

7. The thesis contributes to the comparison and quality control of orbits and clock products from different analysis centres, namely, ESA, CODE and JPL. The derived tidal displacements were demonstrated to be sensitive not only to the orbits and clocks provided but also to the constellation configuration. In addition, some spatially coherent artifacts were discovered (see chapter 4, JPL GPS anomaly in the east component).

8. The thesis demonstrated the inconsistency within the TPXO9 family of ocean tide models that resulted in a centre-of mass bias. This is of importance because of the high reported accuracy of the modern ocean tide models and thus large errors are not expected.

9. The thesis shows the importance of the legacy multi-GNSS datasets starting from 2010 as the needed processing window for the methodology should be over 1000 days or longer in the case of data gaps.

5.3 Limitations and future research

Integer ambiguity resolution was only possible for GPS constellation using GipsyX native products, while solutions based on ESA and CODE products were computed with float ambiguities. Enabling GPS integer ambiguity resolution has previously been demonstrated to increase the spatial consistency of the OTLD and reduce the residual OTLD at GPS-problematic frequencies in the east and up components. Assessment of ambiguity resolved solutions of other constellations and ambiguity resolved Multi GNSS combinations is of particular interest, especially considering the recent completion of BeiDou and the final stages of GALILEO GNSS constellation completion. Multi-GNSS ambiguity resolved solutions should have far better repeatability between various orbit and clock products, resulting in higher confidence of the residual displacement fields being unrelated to the geodetic solution.

Observations of GALILEO, GLONASS and BeiDou constellations in standalone mode and in various combinations should be beneficial for solar-related constituents. These GNSS have orbital and constellation periods away from solar periods unlike GPS, which has been demonstrated to degrade the performance of GPS+GLONASS solutions at solar-related constituents. Standalone GLONASS-derived OTLD estimates are very different between ESA and CODE products solutions thus could not be used for interpretation either, highlighting the importance of multi-GNSS combinations without GPS.

Results focusing on New Zealand were produced based on GPS data only, but accumulated data from upgraded multi-GNSS receivers should become available in the upcoming years. Multi-GNSS data from Taupo Volcanic Zone should further advance the understanding of relation between ocean tide loading and response of the active tectonic margins to the periodical displacements and, most importantly, its change in time if any. In addition, post-seismic effects from large earthquake events may become visible. This however requires similar, preferably multi-GNSS, data accumulation before and after the event (>1000 days) effectively increasing the requirements to data length by a factor of two. The preliminary GPS-only tests centred at Kaikoura earthquake in New Zealand (14/11/2016, 7.8 magnitude) have not revealed any noticeable change in OTLD. The expected OTLD change is thought be small and may affect a wide range of constituents thus increased accuracy and precision of multi-GNSS could be beneficial in studies of the earthquake cycle.

The observed variations of the residual OTLD field related to the limitations of the one-dimensional Green's functions could be further studied using the three-dimensional modelling approach of Latychev et al. (2009) to account for variable elastic properties of the media. This could be applied to explanation of localized anomalies as that in New Zealand (Chapter 3).

Further development of tidal tomography techniques as in Lau et al. (2017) could be expanded to eight major constituents if non-GPS constellations combinations prove reliable at solar-related constituents. Tomography-based inversion of M_2 residual displacements was shown to reveal the low velocity zones in the Earth's Mantle while simultaneous inversion of multiple constituents could lead to greater detail and accuracy of the Earth model. This, however, may require introduction of the atmospheric tide loading displacement, widening the area of OTLD application to the atmosphere modelling. Aside from better understanding of the Earth's interior, observing tidal deformations of Earth may provide a new way of monitoring of subduction margins and better prediction of tectonic events.

5.4 Final remarks

This thesis advances our understanding of ocean tide loading displacements and limitations of modern modelling techniques that have became possible with increased precision and accuracy of geodetic timeseries. The deficiencies in geodetic techniques were summarised with possible future advancements that could mitigate them. The thesis raises the value of combining data from different GNSS constellations and highlights the need for integer ambiguity resolution in multi-GNSS geodetic coordinate solutions.

The results from ocean tide and Earth models assessments provided in three different regions of the globe demonstrate that dissipation of tidal energy is a phenomena that needs addressing especially in the coastal stations. Also, the effect of spatial variations in water density and compressibility should be taken in to account when modelling the ocean tide loading displacement.

The limitation of widely used (in geodesy) one dimensional Earth models were demonstrated in the conditions of a complicated active tectonic margin in New Zealand, specifically a subduction zone. However, additional sources of inconsistency were demonstrated such as difference in the estimated OTLD between solutions computed with different orbit and clock products, a deficient local ocean tide model and a deficient center-of-mass correction due to issues in an ocean tide model. The OTLD differences associated with orbit and clock product differences highlight the need to improve modelling of orbits and clocks of the different constellations as such deficiencies are currently limiting factors holding back geophysical studies of tidal deformations.

Additional information on the Earth's elastic properties specifically in the regions of high tectonic activity will provide better understanding of seismic hazards such as earthquakes and tsunamis, and enable better monitoring of faults and zones of volcanic activity.

References

Abbaszadeh, M., Clarke, P. J., & Penna, N. T. (2020). Benefits of combining GPS and GLONASS for measuring ocean tide loading displacement. *Journal of Geodesy*, *94*(7), 63. https://doi.org/10.1007/s00190-020-01393-5

Agnew, D. (2015). Earth Tides. *Treatise on Geophysics* (pp. 151–178). Elsevier. https://doi.org/10.1016/B978-0-444-53802-4.00058-0

Airy, G. B. (1855). On the Computation of the Effect of the Attraction of Mountain-Masses, as Disturbing the Apparent Astronomical Latitude of Stations in Geodetic Surveys. *Philosophical Transactions of the Royal Society of London*, *14*, 101–104.

Allinson, C. R. (2004). Stability of direct GPS estimates of ocean tide loading. *Geophysical Research Letters*, *31*(15), L15603. https://doi.org/10.1029/2004GL020588

Alterman, Z., Jarosch, H., Pekeris, C. L., & Jeffreys, H. (1959). Oscillations of the earth. *Proceedings of the Royal Society of London*, *252*(1268), 80–95. https://doi.org/10.1098/rspa.1959.0138

Baker, T. F. (1984). Tidal deformations of the Earth. *Science Progress (1933-)*, *69*(274), 197–233.

Barrell, J. (1914). The Strength of the Earth's Crust [Publisher: The University of Chicago Press]. *The Journal of Geology*, *22*(8), 729–741.

Bar-Sever, Y. E., Kroger, P. M., & Borjesson, J. A. (1998). Estimating horizontal gradients of tropospheric path delay with a single GPS receiver. *Journal of Geophysical Research: Solid Earth*, *103*(B3), 5019–5035. https://doi.org/10.1029/97JB03534

Bertiger, W., Bar-Sever, Y., Dorsey, A., Haines, B., Harvey, N., Hemberger, D., Heflin, M., Lu, W., Miller, M., Moore, A. W., Murphy, D., Ries, P., Romans, L., Sibois, A., Sibthorpe, A., Szilagyi, B., Vallisneri, M., & Willis, P. (2020). GipsyX/RTGx, a new tool set for space geodetic operations and research. *Advances in Space Research*, *66*(3), 469–489. https://doi.org/10.1016/j.asr.2020.04.015

Bertiger, W., Desai, S. D., Haines, B., Harvey, N., Moore, A. W., Owen, S., & Weiss, J. P. (2010). Single receiver phase ambiguity resolution with GPS data. *Journal of Geodesy*, *84*(5), 327–337. https://doi.org/10.1007/s00190-010-0371-9

Blewitt, G. (1989). Carrier phase ambiguity resolution for the Global Positioning System applied to geodetic baselines up to 2000 km. *Journal of Geophysical Research: Solid Earth*, *94*(B8), 10187–10203. https://doi.org/10.1029/JB094iB08p10187

Bo Pedersen, F. (2011). *On the History of the Continents: A Story of Plate Tectonics and Earth Tides*. LICengineering A/S.

Boehm, J., Werl, B., & Schuh, H. (2006). Troposphere mapping functions for GPS and very long baseline interferometry from European Centre for Medium-Range Weather Forecasts operational analysis data. *Journal of Geophysical Research: Solid Earth*, *111*(B2). https://doi.org/10.1029/2005JB003629

Bos, M. S. (2000). *Ocean tide loading using improved ocean tide models* (Thesis). University of Liverpool.

Bos, M. S., & Baker, T. F. (2005). An estimate of the errors in gravity ocean tide loading computations. *Journal of Geodesy*, *79*(1), 50–63. https://doi.org/10.1007/s00190-005-0442-5

Bos, M. S., Penna, N. T., Baker, T. F., & Clarke, P. J. (2015). Ocean tide loading displacements in western Europe: 2. GPS-observed anelastic dispersion in the asthenosphere. *Journal of Geophysical Research: Solid Earth*, *120*(9), 6540–6557. https://doi.org/10.1002/2015JB011884

Bos, M. S., & Scherneck, H.-G. (2013). Computation of Green's Functions for Ocean Tide Loading. In G. Xu (Ed.), *Sciences of Geodesy - II* (pp. 1–52). Springer Berlin Heidelberg. https://doi.org/10.1007/978-3-642-28000-9_1

Boy, J.-P., Llubes, M., Hinderer, J., & Florsch, N. (2003). A comparison of tidal ocean loading models using superconducting gravimeter data. *Journal of Geophysical Research: Solid Earth*, *108*(B4). https://doi.org/10.1029/2002JB002050

Carrere, L., Lyard, F., Cancet, M., Guillot, A., & Roblou, L. (2012–September 29). FES 2012: A New Global Tidal Model Taking Advantage of Nearly 20 Years of Altimetry. *20 Years of Progress in Radar Altimetry*, *710*, Article 13, 13.

Colli, L., Fichtner, A., & Bunge, H.-P. (2013). Full waveform tomography of the upper mantle in the South Atlantic region: Imaging a westward fluxing shallow asthenosphere? *Tectonophysics*, *604*, 26–40. https://doi.org/10.1016/j.tecto.2013.06.015

Condie, K. C. (2016). The Mantle. *Earth as an Evolving Planetary System* (pp. 89–133). Elsevier. https://doi.org/10.1016/B978-0-12-803689-1.00004-3

Dach, R., Schaer, S., Arnold, D., Kalarus, M., Prange, L., Stebler, P., Villiger, A., & Jaeggi, A. (2020). CODE final product series for the igs. https://doi.org/10.7892/boris.75876.4

Desai, S. D., & Ray, R. D. (2014). Consideration of tidal variations in the geocenter on satellite altimeter observations of ocean tides. *Geophysical Research Letters*, *41*(7), 2454–2459. https://doi.org/10.1002/2014GL059614

Dill, R., Klemann, V., Martinec, Z., & Tesauro, M. (2015). Applying local Green's functions to study the influence of the crustal structure on hydrological loading displacements. *Journal of Geodynamics*, *88*, 14–22. https://doi.org/10.1016/j.jog.2015.04.005

Dziewonski, A. M., & Anderson, D. L. (1981). Preliminary reference Earth model. *Physics of the Earth and Planetary Interiors*, *25*(4), 297–356. https://doi.org/10.1016/0031-9201(81)90046-7

Eberhart-Phillips, D., & Bannister, S. (2015). 3-D imaging of the northern Hikurangi subduction zone, New Zealand: variations in subducted sediment, slab fluids and slow slip. *Geophysical Journal International*, *201*(2), 838–855. https://doi.org/10.1093/gji/ggv057

Eberhart-Phillips, D., & Fry, B. (2018). Joint local earthquake and teleseismic inversion for 3-D velocity and Q in New Zealand. *Physics of the Earth and Planetary Interiors*, *283*, 48–66. https://doi.org/10.1016/j.pepi.2018.08.005

Egbert, G. D., & Erofeeva, S. Y. (2002). Efficient Inverse Modeling of Barotropic Ocean Tides. *Journal of Atmospheric and Oceanic Technology*, *19*(2), 183–204. https://doi.org/10.1175/1520-0426(2002)019<0183:EIMOBO>2.0.CO;2

Everest, G., & East India Company. (1847). *An account of the measurement of two sections of the meridional arc of India, bounded by the parallels of 18° 3′ 15″; 24° 7′ 11″; & 29° 30′ 48″*. Printed by order of the Court of directors of the Hon. East-India Co., by J. & H. Cox.

Farrell, W. E. (1972a). Deformation of the Earth by surface loads. *Reviews of Geophysics*, *10*(3), 761–797. https://doi.org/10.1029/RG010i003p00761

Farrell, W. E. (1972b). Global Calculations of Tidal Loading. *Nature Physical Science*, *238*(81), 43–44. https://doi.org/10.1038/physci238043a0

Fichtner, A., Kennett, B. L. N., Igel, H., & Bunge, H.-P. (2009). Full seismic waveform tomography for upper-mantle structure in the Australasian region using adjoint methods. *Geophysical Journal International*, *179*(3), 1703–1725. https://doi.org/10.1111/j.1365-246X.2009.04368.x

Foreman, M., & Henry, R. (1989). The harmonic analysis of tidal model time series. *Advances in Water Resources*, *12*(3), 109–120. https://doi.org/10.1016/0309-1708(89)90017-1

French, S., Lekic, V., & Romanowicz, B. (2013). Waveform Tomography Reveals Channeled Flow at the Base of the Oceanic Asthenosphere. *Science*, *342*(6155), 227–230. https://doi.org/10.1126/science.1241514

Fu, Y., Freymueller, J. T., & van Dam, T. (2012). The effect of using inconsistent ocean tidal loading models on GPS coordinate solutions. *Journal of Geodesy*, *86*(6), 409–421. https://doi.org/10.1007/s00190-011-0528-1

Gale, N., Gledhill, K., Chadwick, M., & Wallace, L. (2015). The Hikurangi Margin Continuous GNSS and Seismograph Network of New Zealand. *Seismological Research Letters*, *86*(1), 101–108. https://doi.org/10.1785/0220130181

Griffiths, J. (2019). Combined orbits and clocks from IGS second reprocessing. *Journal of Geodesy*, *93*(2), 177–195. https://doi.org/10.1007/s00190-018-1149-8

Griffiths, J., & Ray, J. R. (2009). On the precision and accuracy of IGS orbits. *Journal of Geodesy*, *83*(3-4), 277–287. https://doi.org/10.1007/s00190-008-0237-6

Guo, J.-Y., Ning, J.-S., & Zhang, F.-P. (2001). Chebyshev-collocation method applied to solve ODEs in geophysics singular at the earth center. *Geophysical Research Letters*, *28*(15), 3027–3030. https://doi.org/10.1029/2001GL012886

Hager, B. H., Richards, M. A., O'Nions, R. K., Clayton, R., & Parsons, B. (1989). Long-wavelength variations in Earth's geoid: Physical models and dynamical implications [Publisher: Royal Society]. *Philosophical Transactions of the Royal Society of London. Series A, Mathematical and Physical Sciences*, *328*(1599), 309–327. https://doi.org/10.1098/rsta.1989.0038

Hu, Y., Bürgmann, R., Banerjee, P., Feng, L., Hill, E. M., Ito, T., Tabei, T., & Wang, K. (2016). Asthenosphere rheology inferred from observations of the 2012 Indian Ocean earthquake. *Nature*, *538*(7625), 368–372. https://doi.org/10.1038/nature19787

Ito, T., & Simons, M. (2011). Probing Asthenospheric Density, Temperature, and Elastic Moduli Below the Western United States. *Science*, *332*(6032), 947–951. https://doi.org/10.1126/science.1202584

Jentzsch, G. (1997). Earth tides and ocean tidal loading. In H. Wilhelm, W. Zürn, & H.-G. Wenzel (Eds.), *Tidal Phenomena* (pp. 145–171). Springer Berlin Heidelberg. https://doi.org/10.1007/BFb0011461

Johnston, G., Riddell, A., & Hausler, G. (2017). The International GNSS Service. In P. J. Teunissen & O. Montenbruck (Eds.), *Springer Handbook of Global Navigation Satellite Systems* (pp. 967–982). Springer International Publishing. https://doi.org/10.1007/978-3-319-42928-1_33

Karato, S.-i. (2012). On the origin of the asthenosphere. *Earth and Planetary Science Letters*, *321-322*, 95–103. https://doi.org/10.1016/j.epsl.2012.01.001

Khan, S. A., & Tscherning, C. C. (2001). Determination of semi-diurnal ocean tide loading constituents using GPS in Alaska. *Geophysical Research Letters*, *28*(11), 2249–2252. https://doi.org/10.1029/2000GL011890

King, M. A. (2005). Validation of ocean tide models around Antarctica using onshore GPS and gravity data. *Journal of Geophysical Research*, *110*(B8), B08401. https://doi.org/10.1029/2004JB003390

King, M. A. (2006). Kinematic and static GPS techniques for estimating tidal displacements with application to Antarctica. *Journal of Geodynamics*, *41*(1-3), 77–86. https://doi.org/10.1016/j.jog.2005.08.019

Kouba, J. (2009). *A guide to using international gnss service (igs) products* (Report). Geodetic Survey Division, Natural Resources Canada.

Kustowski, B., Ekström, G., & Dziewoński, A. M. (2008). Anisotropic shear-wave velocity structure of the Earth's mantle: A global model. *Journal of Geophysical Research: Solid Earth*, *113*(B6). https://doi.org/10.1029/2007JB005169

Lamarche, G., & Lebrun, J.-F. (2000). Transition from strike-slip faulting to oblique subduction: Active tectonics at the Puysegur Margin, South New Zealand. *Tectonophysics*, *316*(1), 67–89. https://doi.org/10.1016/S0040-1951(99)00232-2

Lambeck, K. (1988). *Geophysical geodesy : The slow deformations of the earth*. Oxford : Clarendon press.

Latychev, K., Mitrovica, J. X., Ishii, M., Chan, N.-H., & Davis, J. L. (2009). Body tides on a 3-D elastic earth: Toward a tidal tomography. *Earth and Planetary Science Letters*, *277*(1), 86–90. https://doi.org/10.1016/j.epsl.2008.10.008

Lau, H. C. P., Mitrovica, J. X., Davis, J. L., Tromp, J., Yang, H.-Y., & Al-Attar, D. (2017). Tidal tomography constrains Earth's deep-mantle buoyancy. *Nature*, *551*(7680), 321–326. https://doi.org/10.1038/nature24452

Lyard, F., Lefevre, F., Letellier, T., & Francis, O. (2006). Modelling the global ocean tides: Modern insights from FES2004. *Ocean Dynamics*, *56*(5-6), 394–415. https://doi.org/10.1007/s10236-006-0086-x

Lyard, F. H., Allain, D. J., Cancet, M., Carrère, L., & Picot, N. (2021). FES2014 global ocean tide atlas: Design and performance. *Ocean Science*, *17*(3), 615–649. https://doi.org/10.5194/os-17-615-2021

Martens, H. R., & Simons, M. (2020). A comparison of predicted and observed ocean tidal loading in Alaska. *Geophysical Journal International*, ggaa323. https://doi.org/10.1093/gji/ggaa323

Martens, H. R., Simons, M., Owen, S., & Rivera, L. (2016). Observations of ocean tidal load response in South America from subdaily GPS positions. *Geophysical Journal International*, *205*(3), 1637–1664. https://doi.org/10.1093/gji/ggw087

Matviichuk, B. (2020). *GipsyX_Wrapper* (Version v0.1.0). Zenodo. https://doi.org/10.5281/zenodo.4001166

Matviichuk, B., King, M. A., & Watson, C. S. (2020). Estimating ocean tide loading displacements with GPS and GLONASS. *Solid Earth*, *11*(5), 1849–1863. https://doi.org/10.5194/se-11-1849-2020

Matviichuk, B., King, M. A., Watson, C. S., & Bos, M. S. (2021a). Comparison of state of the art observed and predicted OTL displacements across the Australian continent. *Journal of Geodesy*,

Matviichuk, B., King, M. A., Watson, C. S., & Bos, M. S. (2021b). Limitations in One-Dimensional (an)Elastic Earth Models for Explaining GPS-Observed M2 Ocean Tide Loading Displacements in New Zealand. *Journal of Geophysical Research: Solid Earth*, *126*(6). https://doi.org/10.1029/2021JB021992

NASA Jet Propulsion Laboratory (JPL). (2020). Repro 3.0 final products.

Penna, N. T., Bos, M. S., Baker, T. F., & Scherneck, H.-G. (2008). Assessing the accuracy of predicted ocean tide loading displacement values. *Journal of Geodesy*, *82*(12), 893–907. https://doi.org/10.1007/s00190-008-0220-2

Penna, N. T., Clarke, P. J., Bos, M. S., & Baker, T. F. (2015). Ocean tide loading displacements in western Europe: 1. Validation of kinematic GPS estimates. *Journal of Geophysical Research: Solid Earth*, *120*(9), 6523–6539. https://doi.org/10.1002/2015JB011882

Penna, N. T., King, M. A., & Stewart, M. P. (2007). GPS height time series: Short-period origins of spurious long-period signals. *Journal of Geophysical Research: Solid Earth*, *112*(B2). https://doi.org/10.1029/2005JB004047

Petit, G., & Luzum, B. (2010). IERS Conventions (2010). (36), 179.

Pratt, J. H. (1854). On the Attraction of the Himalaya Mountains, and of the Elevated Region beyond Them, upon the Plumb-Line in India [Publisher: The Royal Society]. *Proceedings of the Royal Society of London*, *7*, 175–182.

Pratt, V. A. (1855). On the Effect of Local Attraction upon the Plumb-Line at Stations on the English Arc of the Meridian, between Dunnose and Burleigh Moor; and a Method of Computing Its Amount. *Proceedings of the Royal Society of London*, 440–443.

Ray, R. D. (2013). Precise comparisons of bottom-pressure and altimetric ocean tides. *Journal of Geophysical Research: Oceans*, *118*(9), 4570–4584. https://doi.org/10.1002/jgrc.20336

Schenewerk, M. S., Marshall, J., & Dillinger, W. (2001). Vertical Ocean-loading Deformations Derived from a Global GPS Network. *Journal of the Geodetic Society of Japan*, *47*(1), 237–242. https://doi.org/10.11366/sokuchi1954.47.237

Stammer, D., Ray, R. D., Andersen, O. B., Arbic, B. K., Bosch, W., Carrère, L., Cheng, Y., Chinn, D. S., Dushaw, B. D., Egbert, G. D., Erofeeva, S. Y., Fok, H. S., Green, J. A. M., Griffiths, S., King, M. A., Lapin, V., Lemoine, F. G., Luthcke, S. B., Lyard, F., … Yi, Y. (2014). Accuracy assessment of global barotropic ocean tide models. *Reviews of Geophysics*, *52*(3), 243–282. https://doi.org/10.1002/2014RG000450

Stern, R. (2004). Subduction initiation: Spontaneous and induced. *Earth and Planetary Science Letters*, *226*(3-4), 275–292. https://doi.org/10.1016/S0012-821X(04)00498-4

Susnik, A., Dach, R., Villiger, A., Maier, A., Arnold, D., Schaer, S., & Jaeggi, A. (2016). CODE reprocessing product series.

Thomas, I. D., King, M. A., & Clarke, P. J. (2007). A comparison of GPS, VLBI and model estimates of ocean tide loading displacements. *Journal of Geodesy*, *81*(5), 359–368. https://doi.org/10.1007/s00190-006-0118-9

Tregoning, P., & Dam, T. v. (2005). Atmospheric pressure loading corrections applied to GPS data at the observation level. *Geophysical Research Letters*, *32*(22). https://doi.org/10.1029/2005GL024104

Urschl, C., Dach, R., Hugentobler, U., Schaer, S., & Beutler, G. (2005). Validating ocean tide loading models using GPS. *Journal of Geodesy*, *78*(10), 616–625. https://doi.org/10.1007/s00190-004-0427-9

Walters, R. A., Goring, D. G., & Bell, R. G. (2001). Ocean tides around New Zealand. *New Zealand Journal of Marine and Freshwater Research*, *35*(3), 567–579. https://doi.org/10.1080/00288330.2001.9517023

Wang, J., Penna, N. T., Clarke, P. J., & Bos, M. S. (2020). Asthenospheric anelasticity effects on ocean tide loading around the East China Sea observed with GPS. *Solid Earth*, *11*(1), 185–197. https://doi.org/10.5194/se-11-185-2020

Wegener, A. (1912). Die Entstehung der Kontinente. *Geologische Rundschau*, *3*(4), 276–292. https://doi.org/10.1007/BF02202896

Weismüller, J., Gmeiner, B., Ghelichkhan, S., Huber, M., John, L., Wohlmuth, B., Rüde, U., & Bunge, H.-P. (2015). Fast asthenosphere motion in high-resolution global mantle flow models. *Geophysical Research Letters*, *42*(18), 7429–7435. https://doi.org/10.1002/2015GL063727

Wenzel, H.-G. (1996). The nanogal software : Earth tide data processing package ETERNA 3.30. *Bull. Inf. Marées Terrestres*, *124*, 9425–9439.

Wessel, P., & Smith, W. H. F. (1996). A global, self-consistent, hierarchical, high-resolution shoreline database. *Journal of Geophysical Research: Solid Earth*, *101*(B4), 8741–8743. https://doi.org/10.1029/96JB00104

Yuan, L. G., Ding, X. L., Zhong, P., Chen, W., & Huang, D. F. (2009). Estimates of ocean tide loading displacements and its impact on position time series in Hong Kong using a dense continuous GPS network. *Journal of Geodesy*, *83*(11), 999–1015. https://doi.org/10.1007/s00190-009-0319-0

Yuan, L., & Chao, B. F. (2012). Analysis of tidal signals in surface displacement measured by a dense continuous GPS array. *Earth and Planetary Science Letters*, *355-356*, 255–261. https://doi.org/10.1016/j.epsl.2012.08.035

Yuan, L., Chao, B. F., Ding, X., & Zhong, P. (2013). The tidal displacement field at Earth's surface determined using global GPS observations. *Journal of Geophysical Research: Solid Earth*, *118*(5), 2618–2632. https://doi.org/10.1002/jgrb.50159

Zschau, J. (1978). Tidal Friction in the Solid Earth: Loading Tides Versus Body Tides. In P. Brosche & J. Sündermann (Eds.), *Tidal Friction and the Earth's Rotation* (pp. 62–94). Springer Berlin Heidelberg. https://doi.org/10.1007/978-3-642-67097-8_7

Zumberge, J. F., Heflin, M. B., Jefferson, D. C., Watkins, M. M., & Webb, F. H. (1997). Precise point positioning for the efficient and robust analysis of GPS data from large networks. *Journal of Geophysical Research: Solid Earth*, *102*(B3), 5005–5017. https://doi.org/10.1029/96JB03860

Zürn, W., Beaumont, C., & Slichter, L. B. (1976). Gravity tides and ocean loading in southern Alaska. *Journal of Geophysical Research (1896-1977)*, *81*(26), 4923–4932. https://doi.org/10.1029/JB081i026p04923

Zweng, M. M., Reagan, J. R., Antonov, J. I., Locarnini, R. A., Mishonov, A. V., Boyer, T. P., Garcia, H. E., Baranova, O. K., Johnson, D. R., Seidov, D., Biddle, M. M., & Levitus, S. (2013). World ocean atlas 2013. Volume 2, Salinity. https://doi.org/10.7289/V5251G4D

Appendix A

Supporting Information for Chapter 2

A.1 Supporting figures

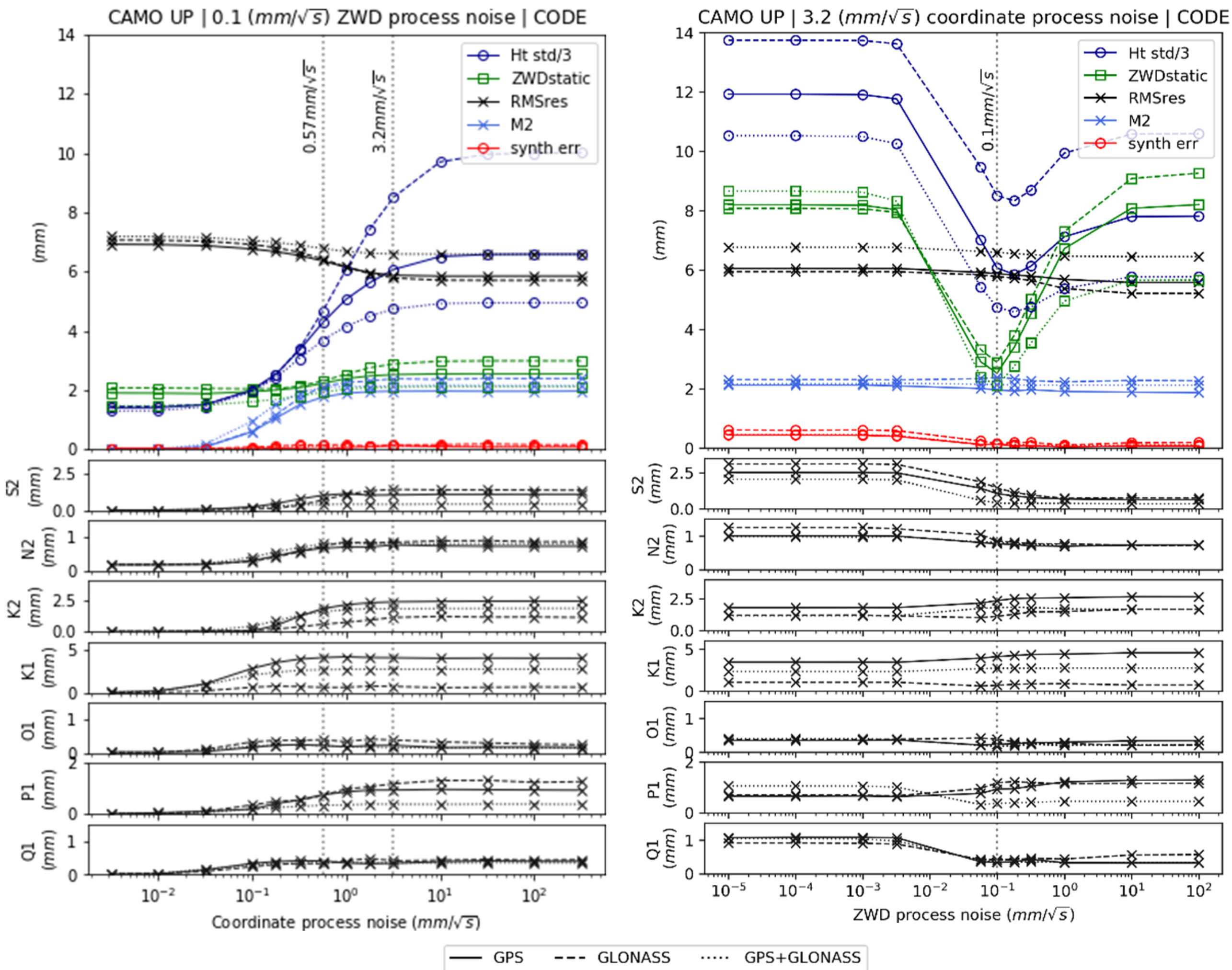

FIGURE A.1.1: The effect of varying coordinate process noise (left) and ZWD process noise (right) at test site CAMO for the up component (2010.0 – 2014.0). This test was performed for all three constellation modes: GPS, GLONASS, GPS+GLONASS using CODE REPRO_2015 products.

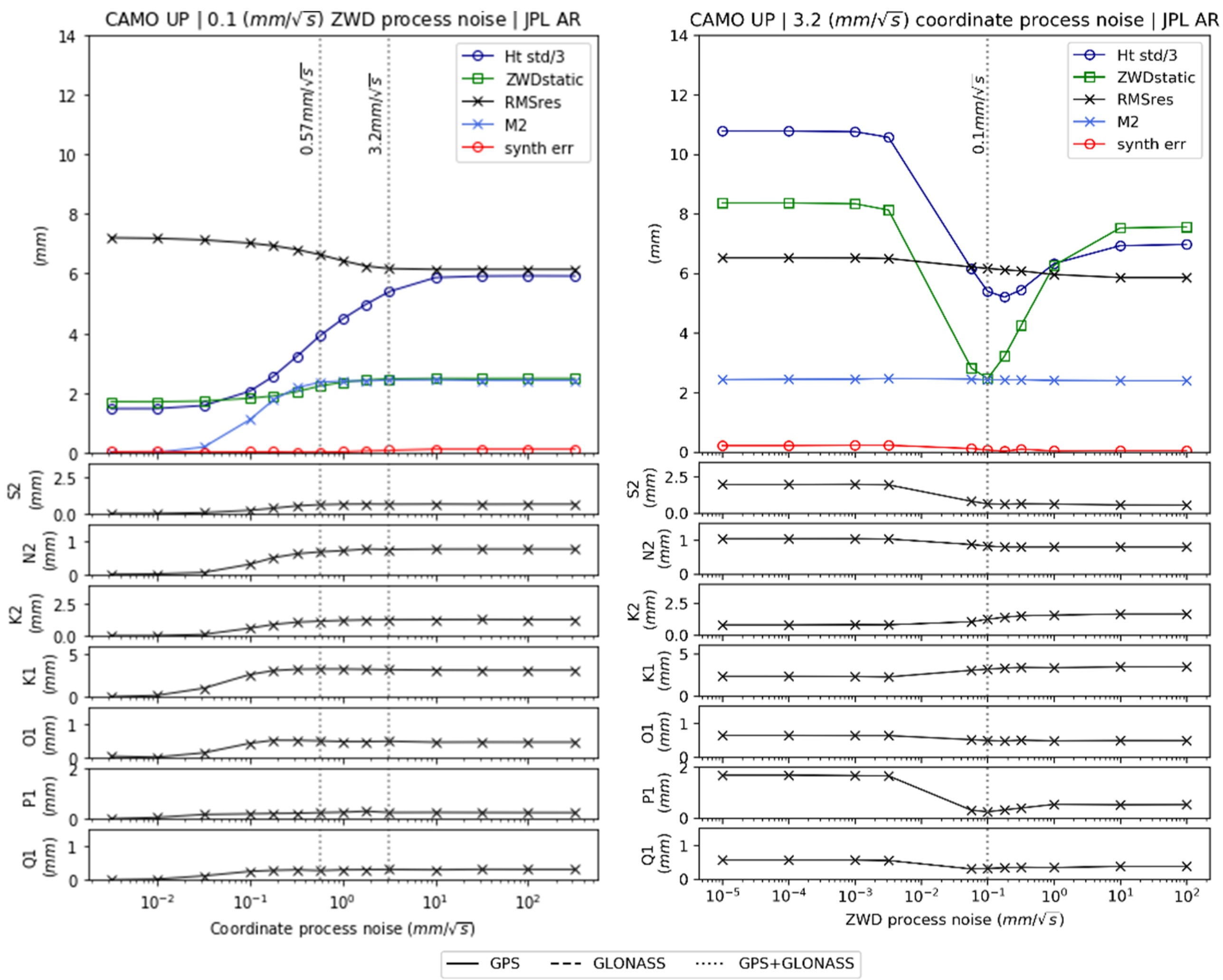

FIGURE A.1.2: Same as Fig. A.1.1 but for GPS-only AR using JPL products.

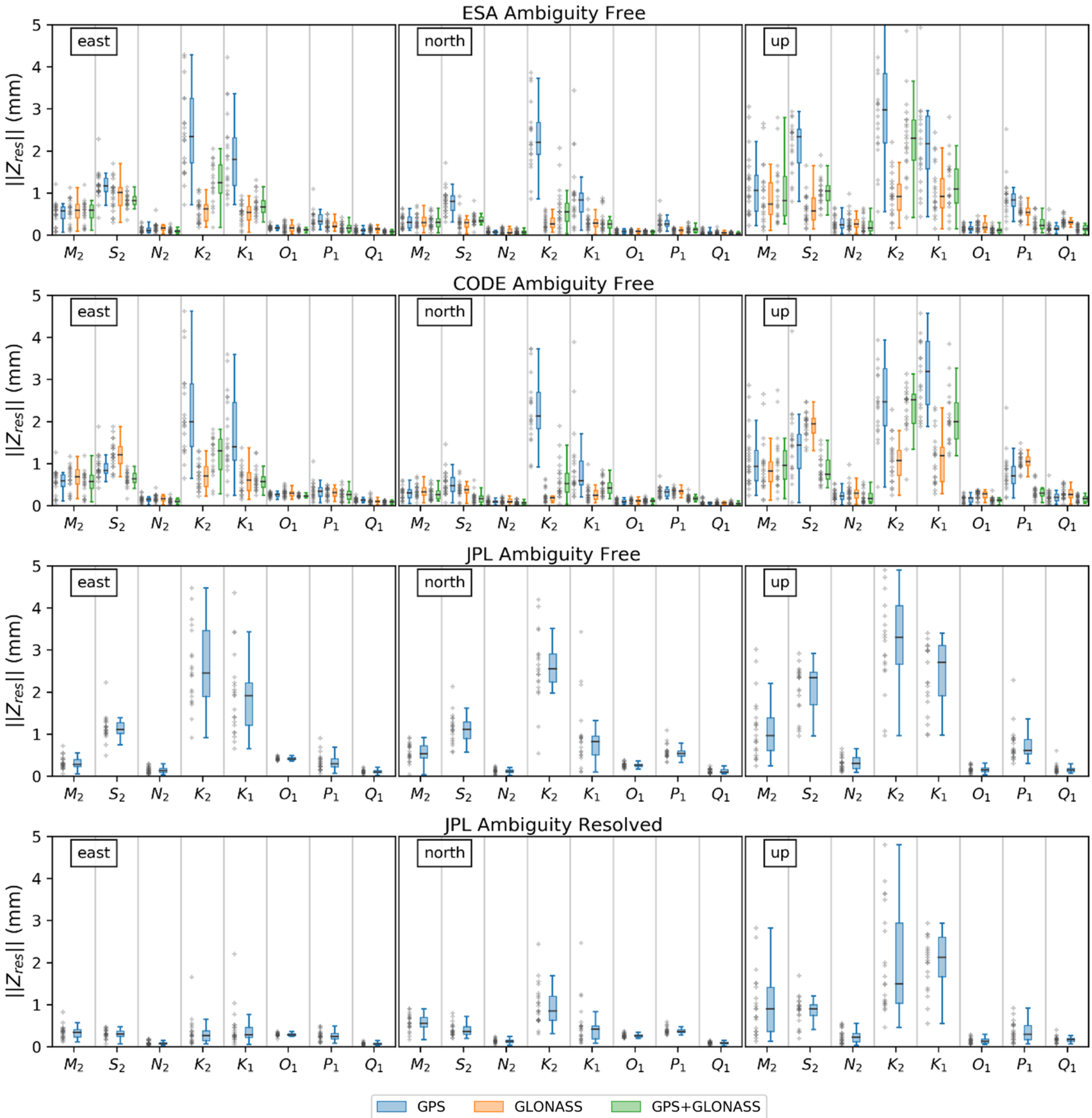

FIGURE A.2: $\|Z_{res}\|$ per tidal constituent for the east, north and up components (left, middle and right, respectively) relative to FES2014b_STW105d OTL values with CMC correction for JPL solutions. Grey crosses as per Figure 2.3. Top to bottom: ESA (GPS, GLONASS, GPS+GLONASS), CODE (GPS, GLONASS, GPS+GLONASS), JPL (GPS), JPL AR (GPS). Elevation cutoff angle of 7 °was used for all solutions.

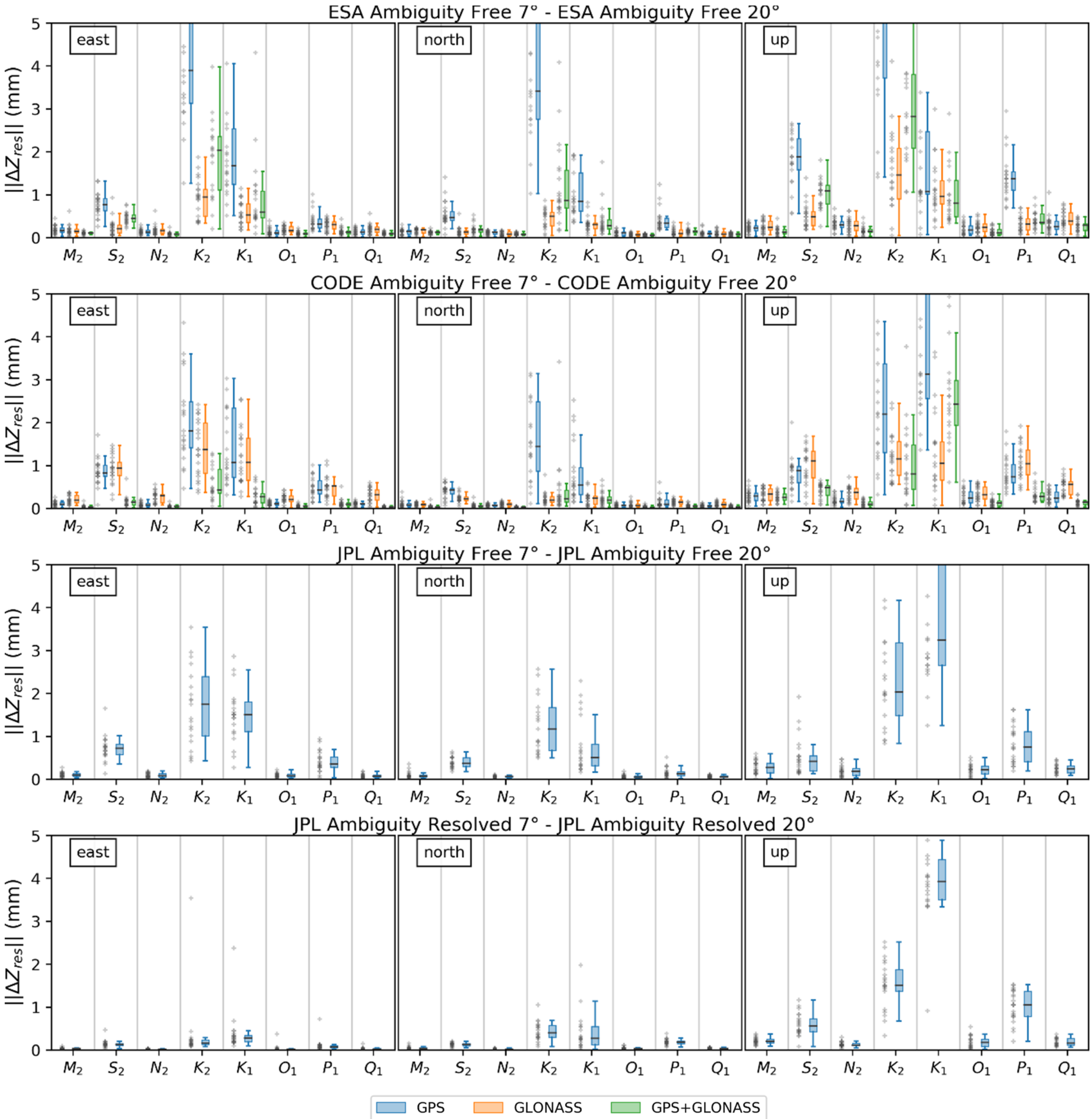

FIGURE A.3: Magnitude of vector distance between estimated Z_{res} values computed with 7 °and 20 °elevation cutoff angles, $\|\Delta Z_{\mathrm{res}}\|$, within the same set of orbits and clocks (from top to bottom: ESA, CODE, JPL, JPL AR) for east, north and up coordinate components (left, middle and right, respectively). Grey crosses are as per Figure 2.3.

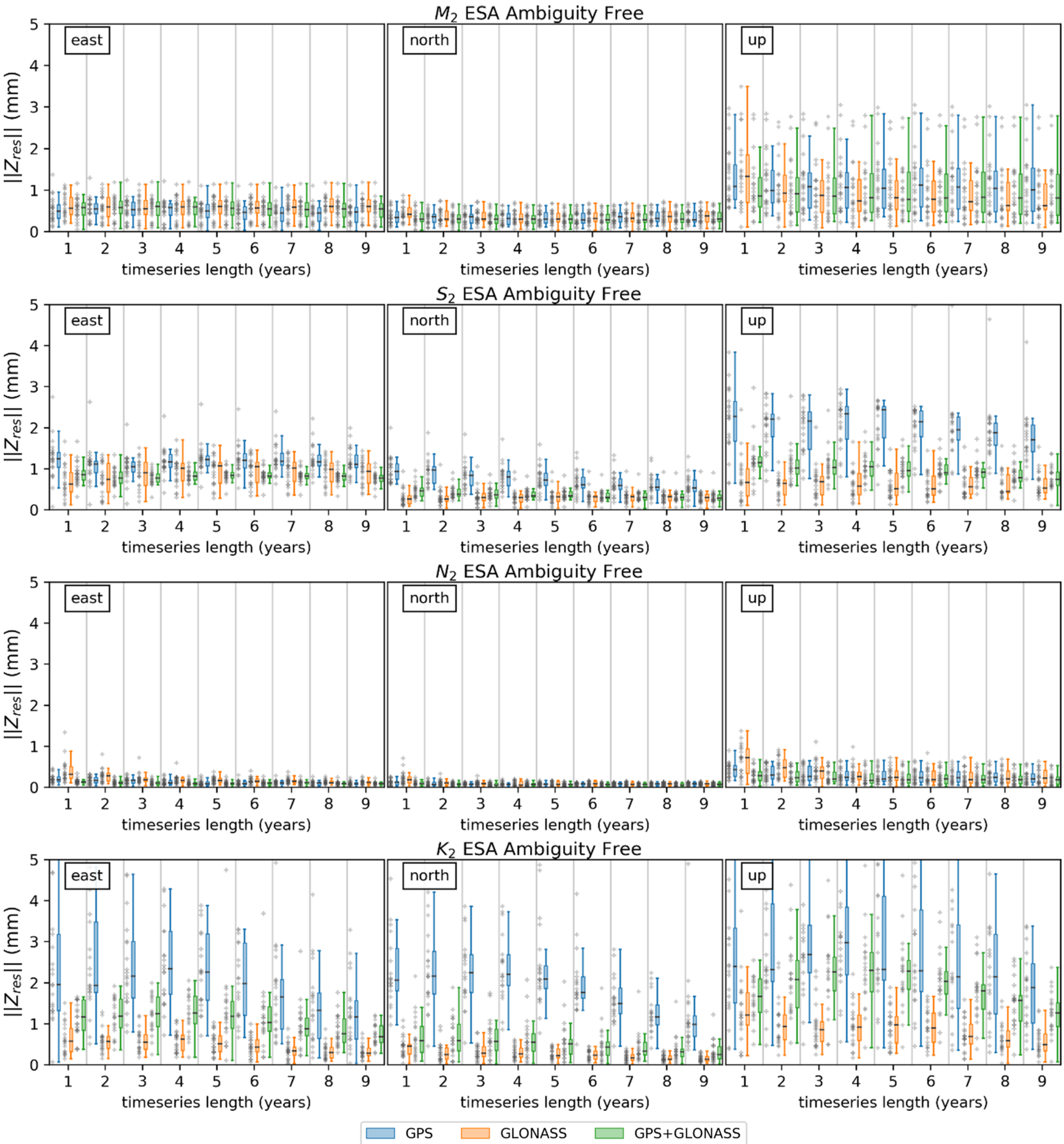

FIGURE A.4.1: Dependency of estimated $\|Z_{\text{res}}\|$ and timeseries' length in years: GPS, GLONASS and GPS+GLONASS PPP solutions in blue, orange and green, respectively using ESA products. Note that 1 to 4 years of timespan use ESA repro2 while the rest uses a combination of ESA repro2 and ESA operational products. Grey crosses are as per Figure 2.3.

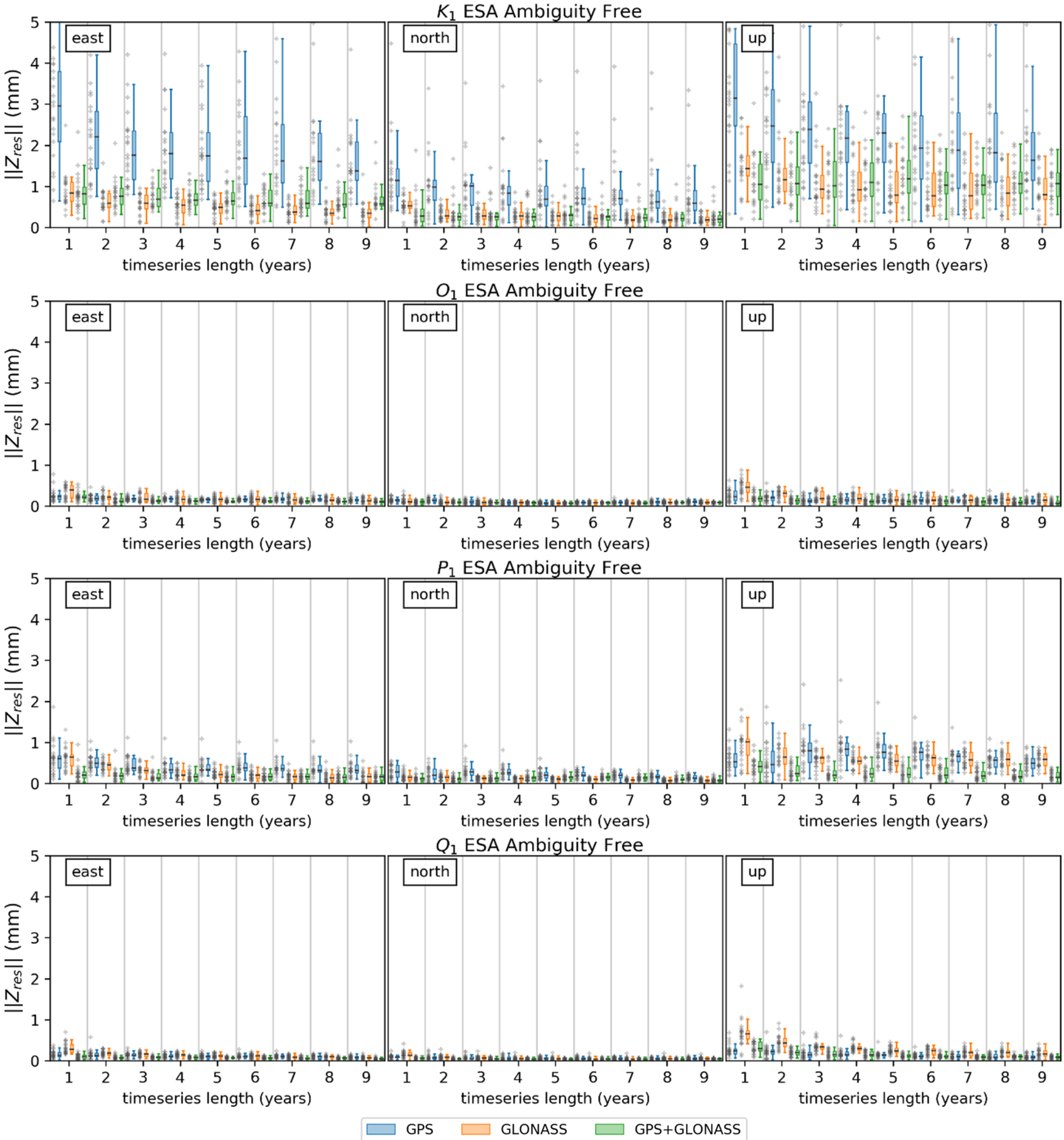

FIGURE A.4.2: Dependency of estimated $\|Z_{\mathrm{res}}\|$ and timeseries' length in years: GPS, GLONASS and GPS+GLONASS PPP solutions in blue, orange and green, respectively using ESA products. Note that 1 to 4 years of timespan use ESA repro2 while the rest uses a combination of ESA repro2 and ESA operational products. Grey crosses are as per Figure 2.3.

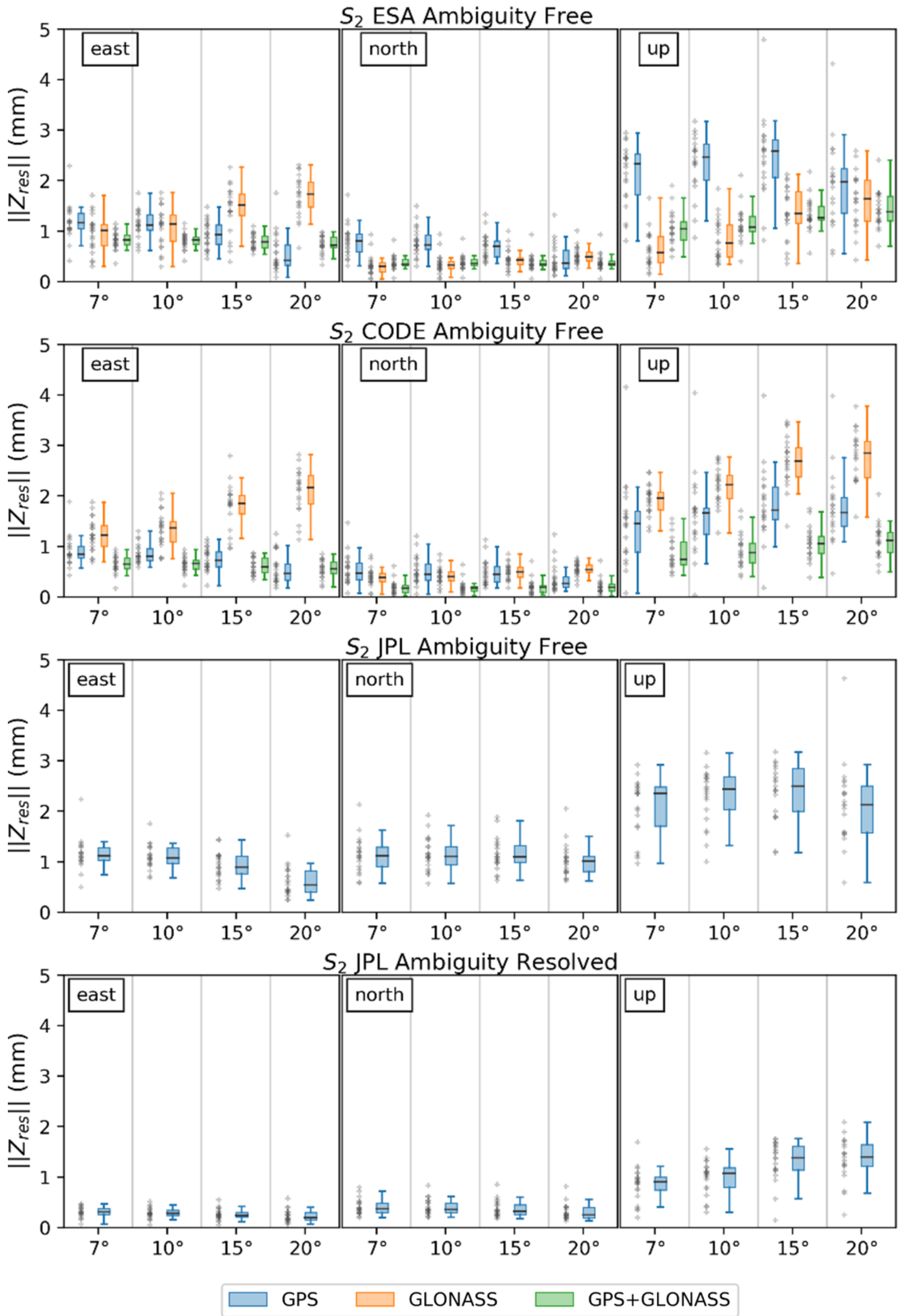

FIGURE A.5: S_2 $\|Z_{res}\|$ as a function of elevation cutoff angle, computed with (top to bottom): ESA, CODE, JPL, JPL AR products. Grey crosses are as per Figure 2.3.

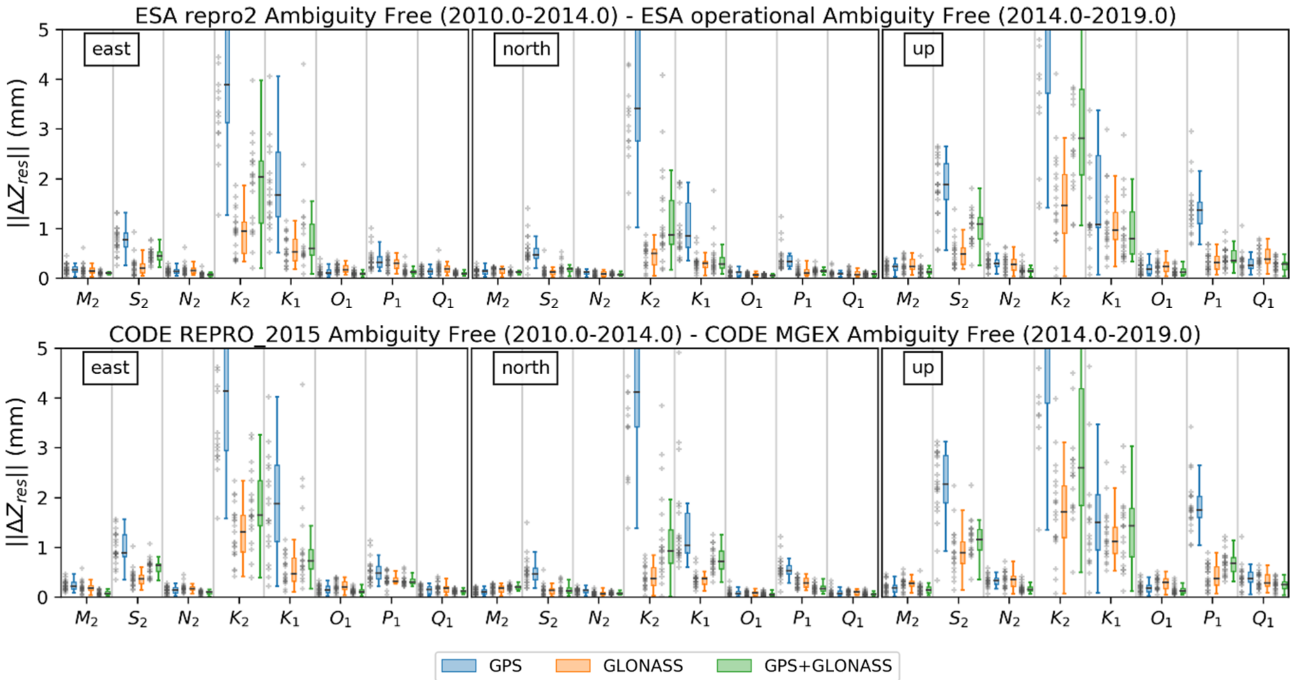

FIGURE A.6: OTLD vector differences between: ESA repro2 (2010.0-2014.0) and ESA operational (2014.0-2019.0) OTL estimates (top); CODE REPRO_2015 (2010.0-2014.0) and CODE MGEX (2014.0-2019.0) OTL estimates (bottom). GPS (blue), GLONASS (orange), GPS+GLONASS (green) constellation modes present. Grey crosses are as per Figure 2.3.

A.2 Supporting tables

TABLE A.1: List of sites used in the analysis.

#	Site name	Latitude	Longitude	Height
0	ANLX	51.6893	-5.0792	73.9241
1	APPL	51.0569	-4.1996	68.3622
2	BRAE	57.0067	-3.3956	401.6938
3	BRST	48.3805	-4.4966	65.9518
4	CAMO	50.2183	-5.3273	143.0296
5	CARI	51.5311	-3.1068	93.2636
6	CHIO	51.1490	-1.4383	130.8018
7	EXMO	50.6134	-3.4100	65.3600
8	HERT	50.8675	0.3344	83.7702
9	LERI	60.1383	-1.1837	131.8205
10	LOFT	54.5629	-0.8634	209.4150
11	PADT	50.5411	-4.9368	66.2363
12	PBIL	50.5218	-2.4575	107.5874
13	PMTH	50.4165	-4.1262	175.5181
14	POOL	50.7759	-1.9106	68.5589
15	PRAE	50.2029	-3.7203	113.1618
16	SANO	50.6503	-1.2130	91.6935
17	SWAS	51.5655	-3.9818	92.3176
18	TAUT	51.0234	-3.0787	81.0980
19	WEAR	54.7491	-2.2304	409.1663
20	ZIM2	46.8771	7.4650	956.8810

A.3 Copyright and License details

Appendix B

Supporting Information for Chapter 3

B.1 Supporting figures

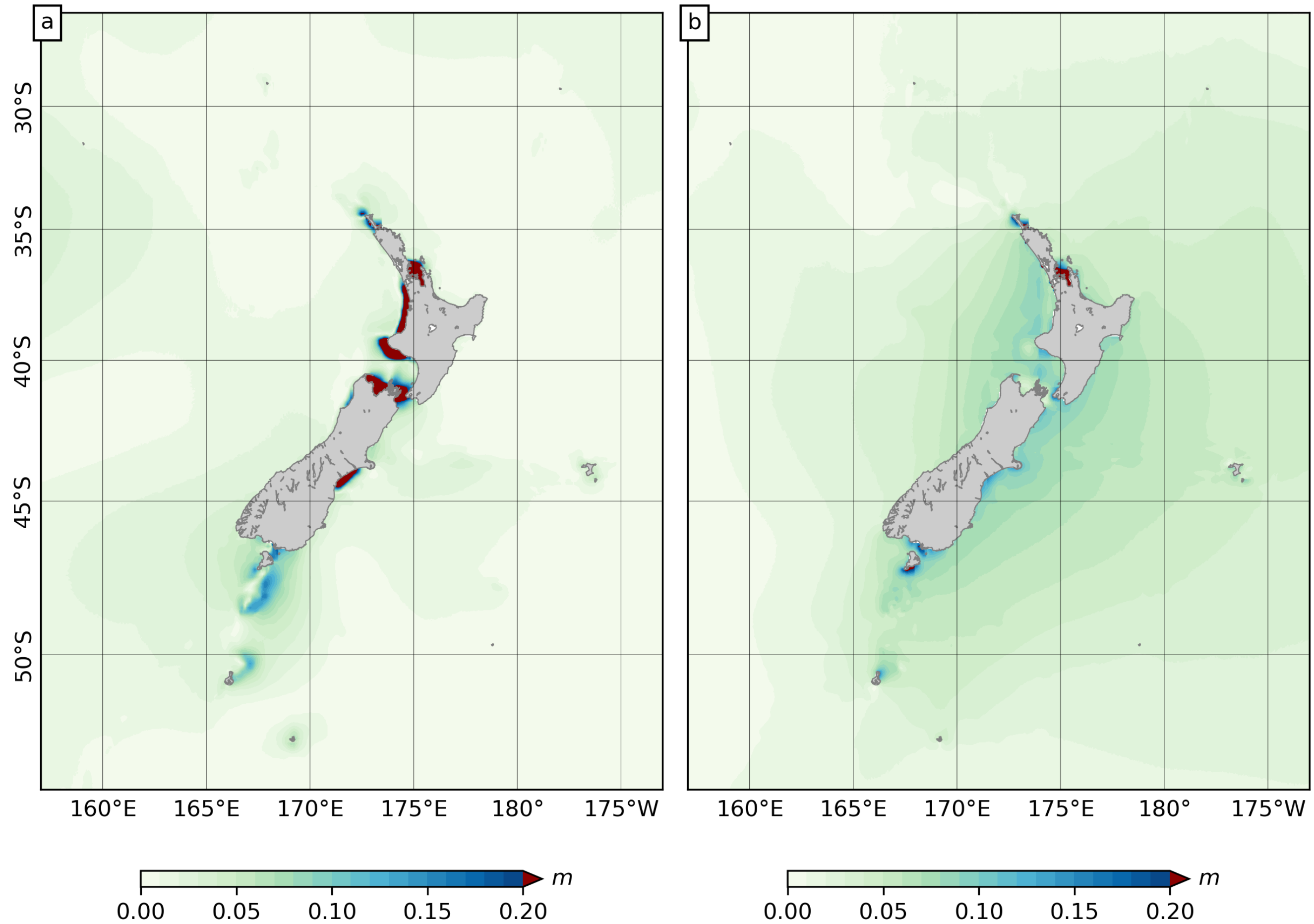

FIGURE B.1: Vector differences between the mean model and FES2004 global tide model (a) and regional EEZ ocean tide model (b). Differences are concentrated in the shallow waters in the case of FES2004 while EEZ differences show the presence of uniform bias (∼0.1 m), which reduces away from the coast. Note the scale saturation above 0.2 m. The peak values are 1 m and 0.7 m for (a) and (b), located at the Hauraki Gulf in both cases.

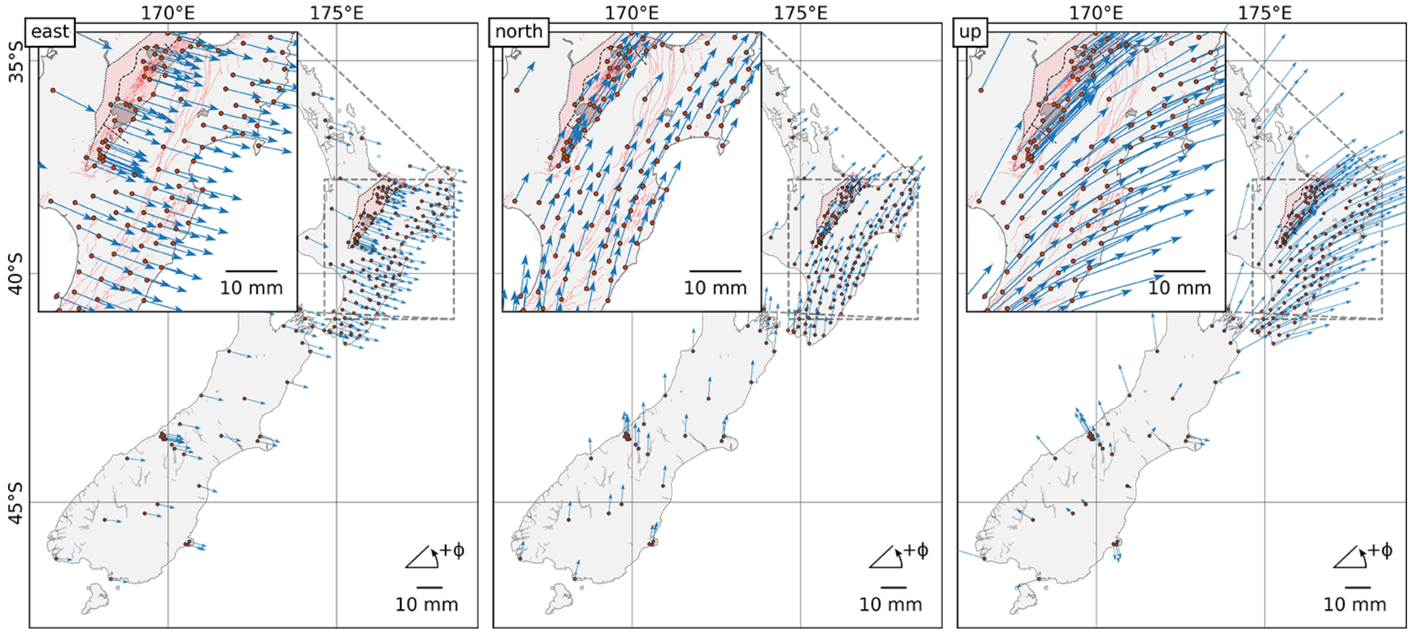

FIGURE B.2: FES2004 restored GPS-derived ocean tide loading in the east, north and up components.

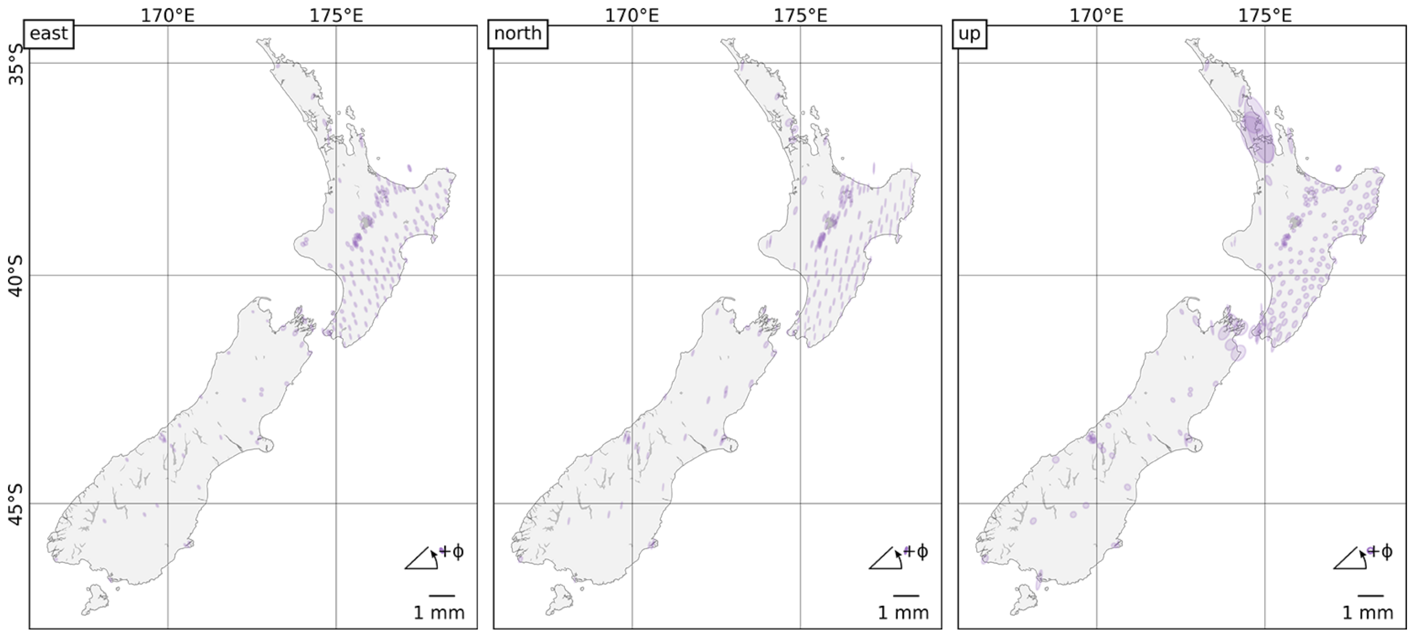

FIGURE B.3: Influence of errors in the ocean-tide models on the modeled OTLD values shown as 95% confidence ellipsoids of vector differences between OTL values based on FES2014b, TPXO9.v1 and GOT4.10c ocean tide models. The Green's function was kept fixed to STW105d. The errors were computed separately for in-phase and out-phase components. The scale is consistent with the rest of OTLD residuals maps.

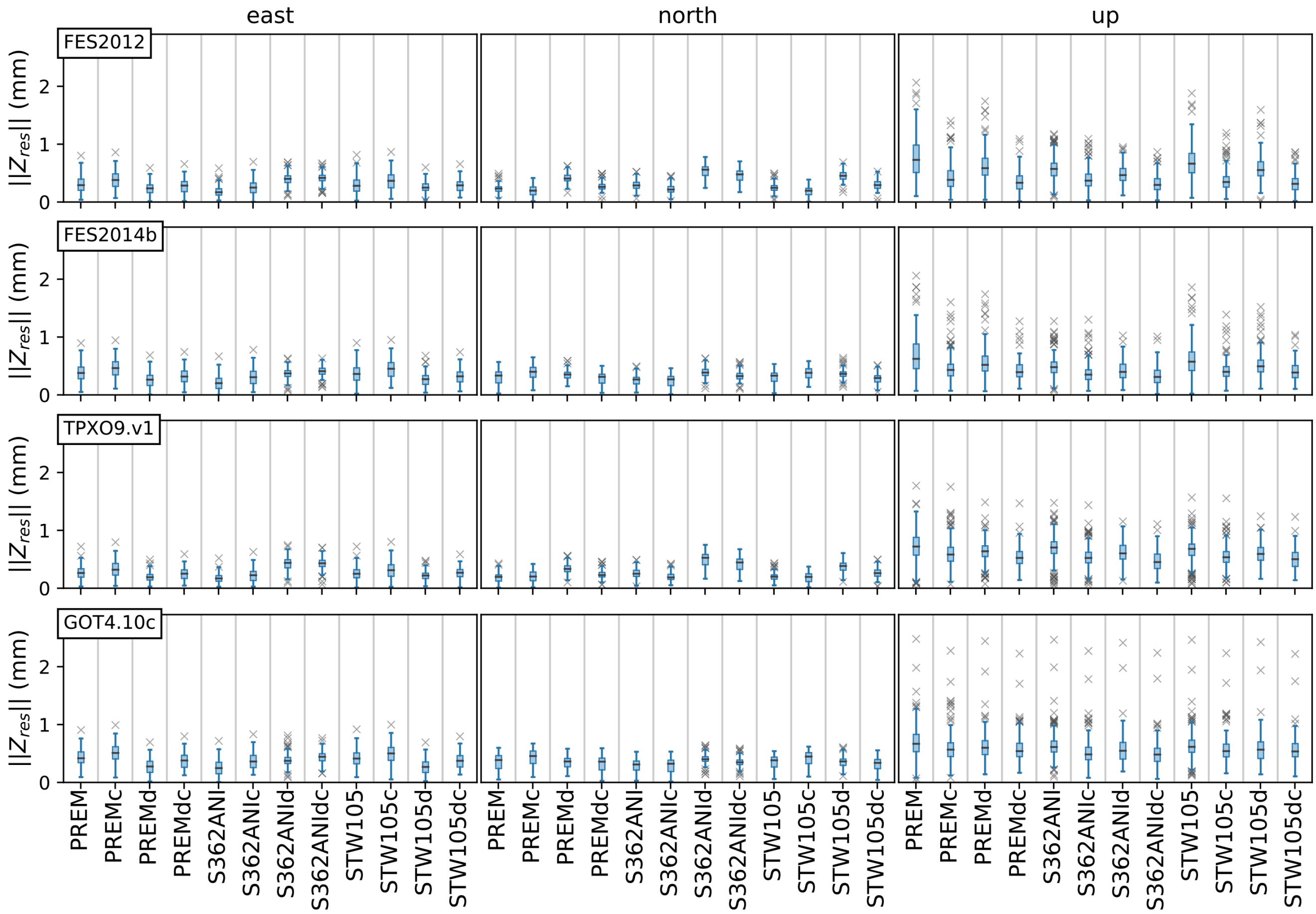

FIGURE B.4: Residual OTLD, $\|Z_{\text{res}}\|$, relative to (top to bottom) FES2012, FES2014b, TPXO9.v1, GOT4.10c ocean tide models and a set of Green's functions for the east, north and up components (left to right).

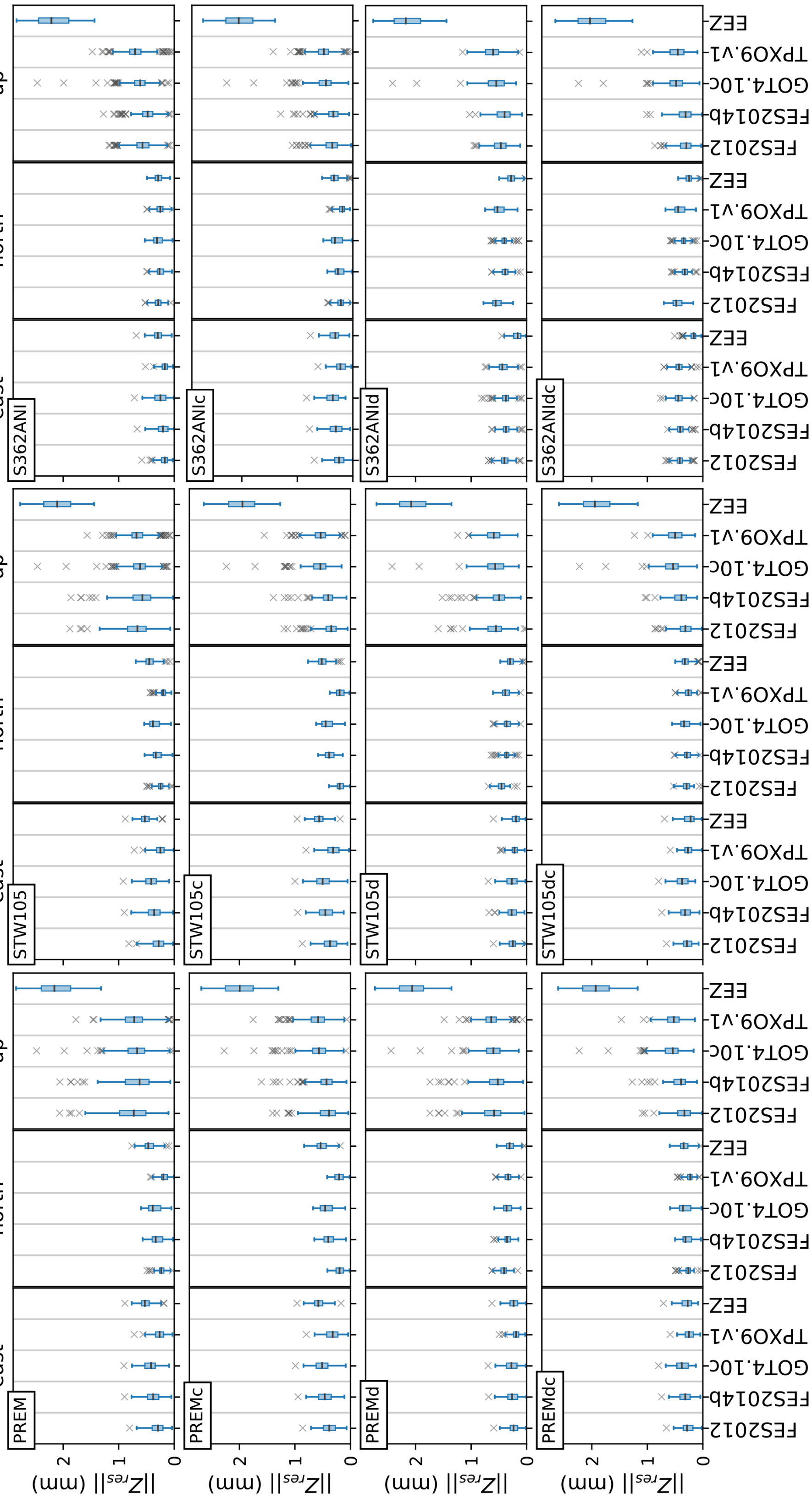

FIGURE B.5: Comparison of FES2012, FES2014b, TPXO9.v1 and GOT4.10c ocean tide models over a range of Green's functions and corrections of compressibility and dissipation.

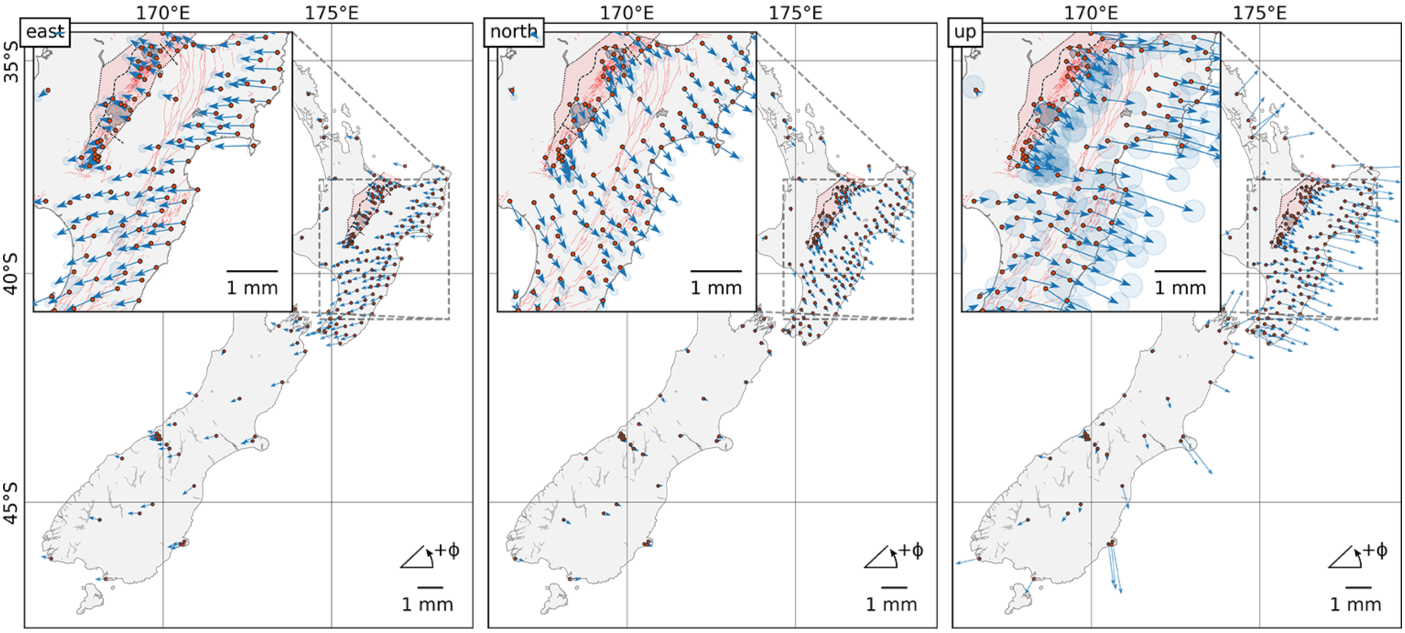

FIGURE B.6.1: Residual OTL, $\|Z_{\mathrm{res}}\|$, relative to FES2014b ocean tide model and PREM Green's function in the east, north and up components.

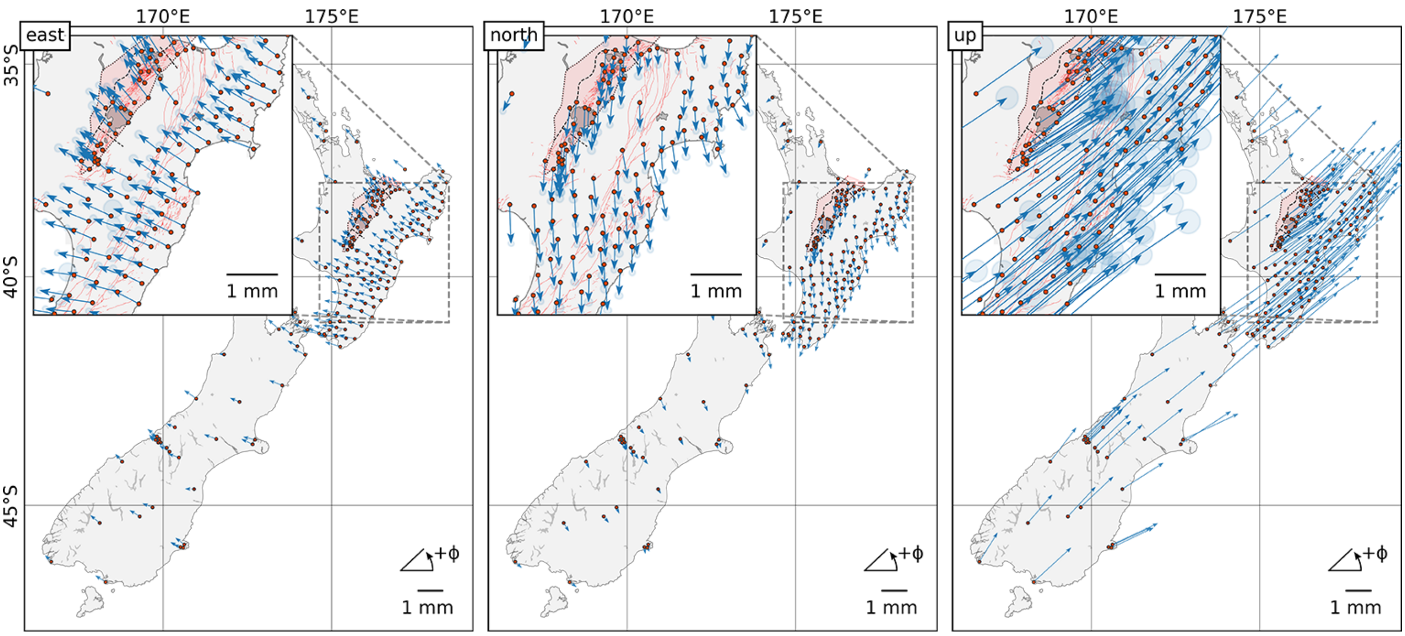

FIGURE B.6.2: Residual OTL, $\|Z_{\mathrm{res}}\|$, relative to EEZ regional ocean tide model (FES2014b outside EEZ's coverage) and PREM Green's function in the east, north and up components.

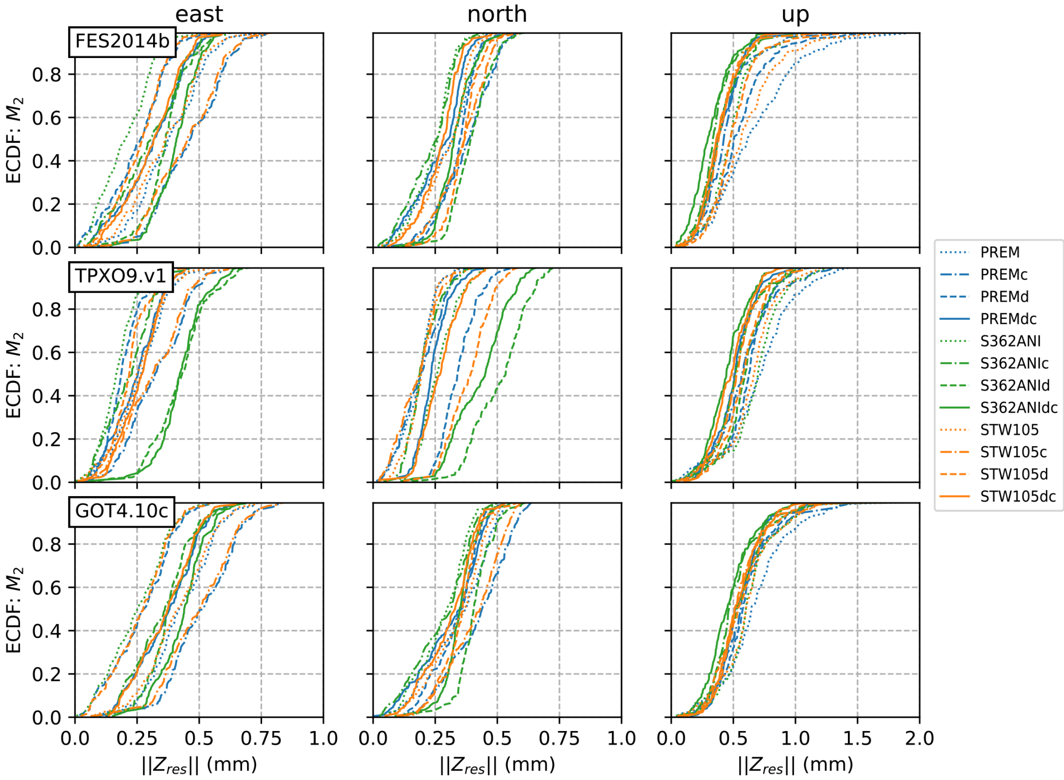

FIGURE B.7.1: ECDF plots for three recent global ocean tide models ocean tide models and a set of Green's functions for the east, north and up components.

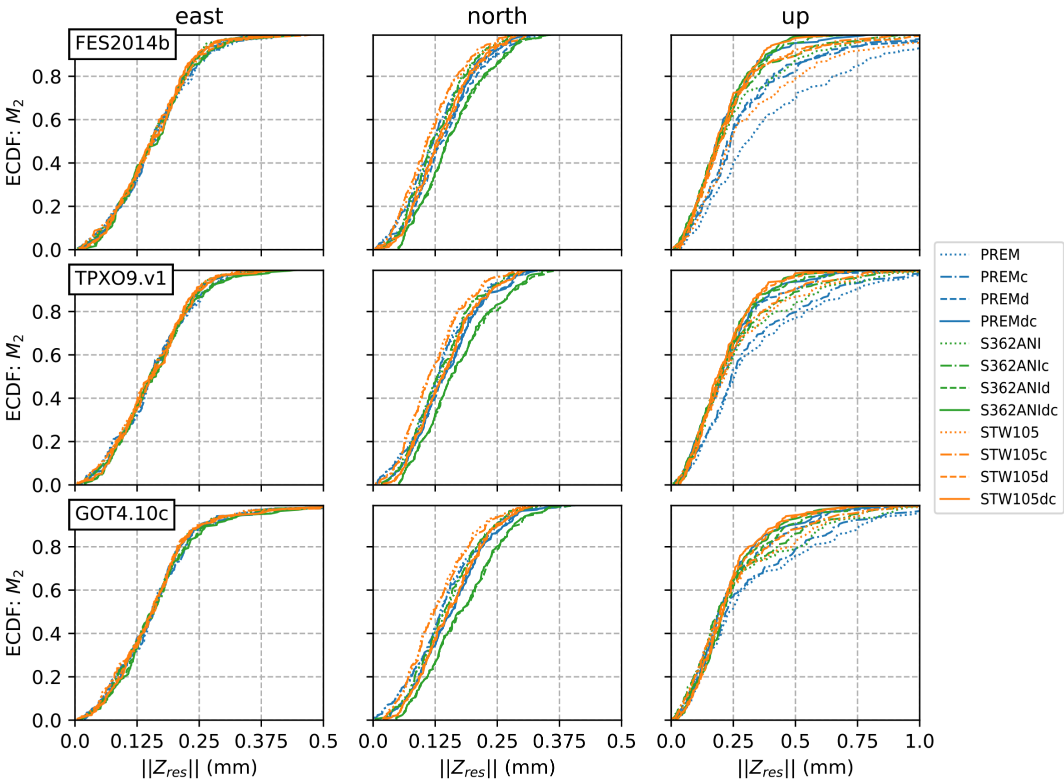

FIGURE B.7.2: Same as Figure B.7.1 but with mean residual OTL vector removed for each set of modeled values for the east, north and up components.

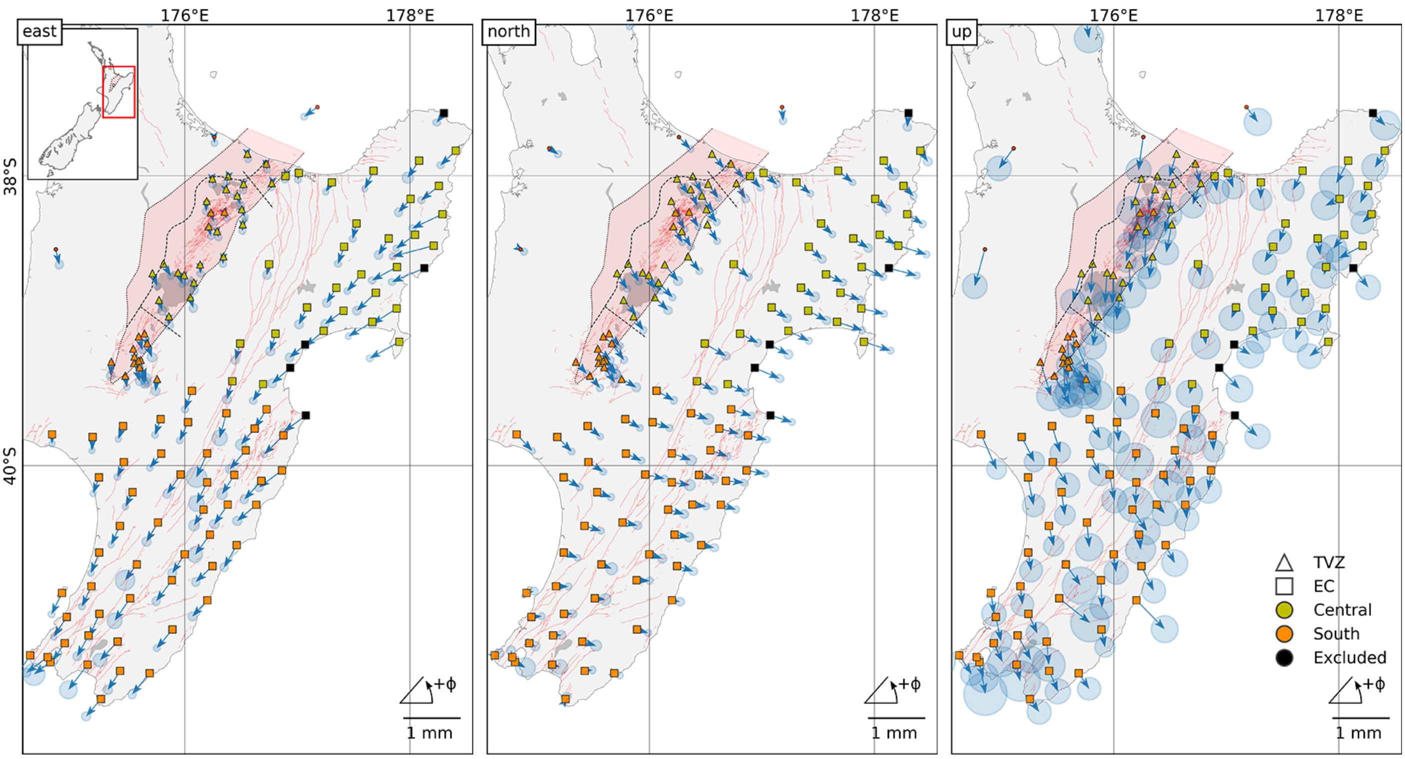

FIGURE B.8: GPS-derived M_2 OTLD residuals for a section of the North Island using FES2014b_STW105dc for east, north and up components. Sites are categorized into Taupo Volcanic Zone (TVZ) and East Coast (EC) regions (symbol shape) with subdivision of each into central and south along the TVZ central/south boundary (symbol color).

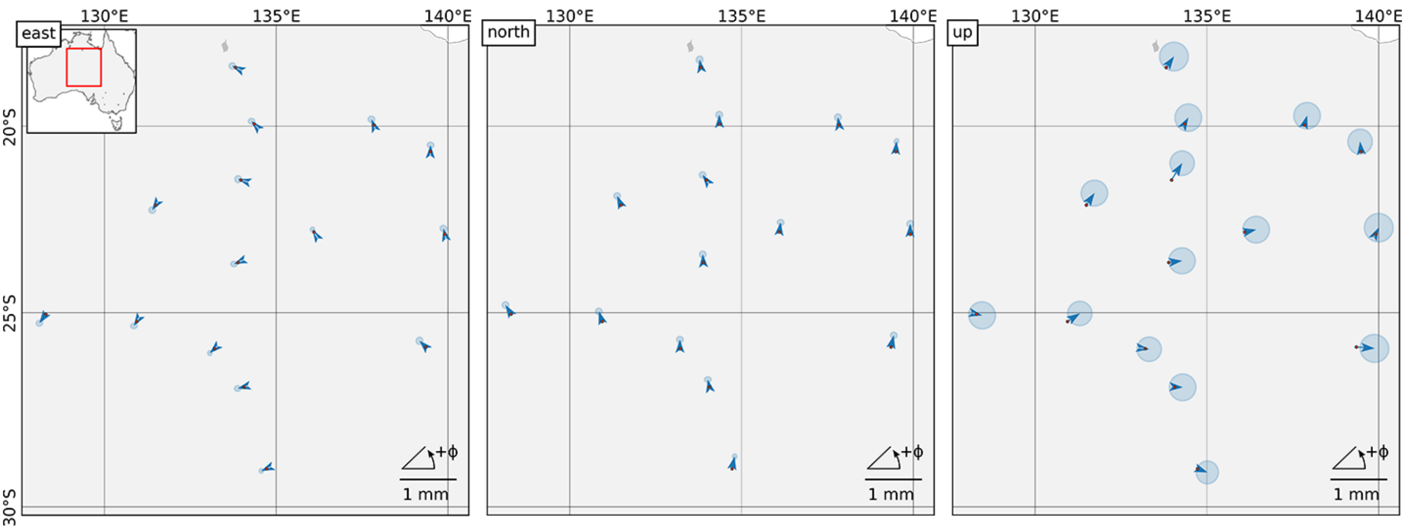

FIGURE B.9: Residual OTL, $\|Z_{res}\|$, relative to FES2014b ocean tide model and STW105d Green's function (maximum bias in New Zealand dataset) for the east, north and up components derived at 14 inland Australian sites.

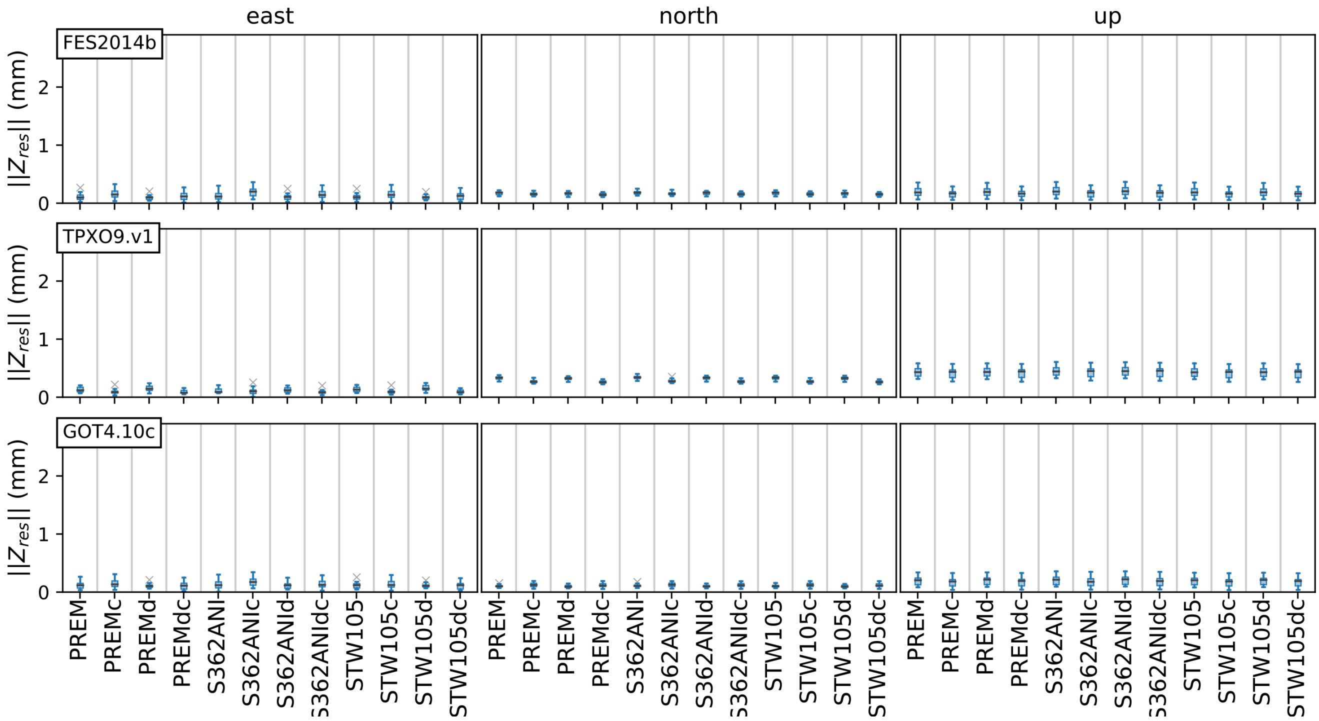

FIGURE B.10: Residual OTLD magnitudes, $\|Z_{\mathrm{res}}\|$, derived in the inland Australia relative to FES2014b, TPXO9.v1, GOT4.10c ocean tide models and a set of Green's functions for the east, north and up components.

B.2 Supporting tables

TABLE B.1: List of New Zealand sites used in the analysis.

#	Site name	Latitude	Longitude	Height
0	2406	-38.6919	175.9948	443.2143
1	AHTI	-38.4114	178.0460	563.5929
2	AKTO	-40.5398	176.4612	433.3045
3	ANAU	-38.2682	178.2912	229.7377
4	ARTA	-38.6176	176.1364	370.1697
5	AUCK	-36.6028	174.8344	133.0921
6	AUKT	-36.8438	174.7704	40.5281
7	AVLN	-41.1964	174.9329	39.9678
8	BHST	-39.4892	176.0632	882.8938
9	BIRF	-40.6798	176.2461	309.4375
10	BLUF	-46.5851	168.2921	125.0956
11	BNET	-43.8625	170.1901	758.2052
12	BTHL	-41.3405	175.1365	79.3252
13	CAST	-40.9098	176.2016	174.0706
14	CHTI	-43.7355	-176.6171	76.1009
15	CKID	-39.6579	177.0764	235.3472
16	CLIM	-41.1447	175.1455	831.1588
17	CMBL	-41.7490	174.2138	257.4383
18	CNCL	-43.6662	169.8559	1222.7494
19	CNST	-38.4880	178.2111	243.0549
20	CORM	-36.8654	175.7496	170.6036
21	DNVK	-40.2989	176.1667	458.0291
22	DUND	-45.8837	170.5972	389.2877
23	DUNT	-45.8143	170.6294	13.9516
24	DURV	-40.8018	173.9216	468.8835
25	FRTN	-38.9393	177.4099	169.8661
26	GISB	-38.6353	177.8860	87.6150
27	GLDB	-40.8266	172.5296	303.0115
28	GNBK	-40.0803	175.2381	90.7462
29	GRNG	-39.9763	175.4593	366.2102
30	HAAS	-44.0732	168.7856	1053.9824
31	HAMT	-37.8068	175.1092	69.7612
32	HANA	-38.6868	177.5694	574.5224
33	HAST	-39.6170	176.7266	152.7544
34	HIKB	-37.5610	178.3034	107.6757
35	HOKI	-42.7129	170.9843	54.0544
36	HOLD	-40.8972	175.5152	470.1340
37	HORN	-43.7773	170.1055	960.7896
38	KAHU	-39.7938	176.8763	654.7804
39	KAIK	-42.4255	173.5337	315.9254
40	KAPT	-40.8609	174.9098	367.9924
41	KARA	-43.6084	169.7752	1403.7321
42	KAWK	-39.4240	176.4228	831.4322
43	KERE	-39.6432	176.3701	521.3591
44	KOKO	-39.0161	177.6678	302.2332
45	KORO	-40.4093	175.4241	52.0339
46	KTIA	-35.0689	173.2731	127.9049
47	KUTA	-39.1723	177.0698	181.3711

Continued on next page

Table B.1 – continued from previous page

#	Site name	Latitude	Longitude	Height
48	LDRZ	-45.0383	169.6841	379.7074
49	LEVN	-40.5888	175.2406	96.5620
50	LEXA	-45.2310	169.3082	332.2221
51	LEYL	-39.3323	176.9367	114.5248
52	LKTA	-42.7834	172.2663	713.3794
53	LYTT	-43.6058	172.7222	18.9161
54	MAHA	-41.2914	173.7938	442.3598
55	MAHI	-39.1526	177.9070	322.8243
56	MAHO	-38.5130	174.8541	302.8712
57	MAKO	-38.6438	178.1291	231.4098
58	MANG	-40.6687	175.5749	418.4764
59	MATW	-38.3338	177.5262	646.6916
60	MAVL	-45.3665	168.1182	592.9197
61	MCNL	-39.4442	176.6965	366.6392
62	METH	-43.5914	171.5753	453.0757
63	MING	-38.6169	176.7497	458.4456
64	MKNO	-39.7034	176.0288	832.6386
65	MNHR	-40.4686	176.2234	296.0365
66	MQZG	-43.7027	172.6547	155.1245
67	MTBL	-40.1814	175.5362	157.1678
68	MTJO	-43.9857	170.4649	1044.1042
69	MTPR	-43.3364	170.3505	1549.2777
70	MTQN	-41.0016	175.2414	1207.7499
71	NLSN	-41.1835	173.4337	302.5573
72	NMAI	-39.0970	176.8066	858.0312
73	NPLY	-39.1826	174.1182	417.3352
74	NRRD	-40.3854	175.7613	501.0955
75	NRSW	-40.1133	176.2000	364.4925
76	OHIN	-39.9183	175.7907	531.0566
77	OKOH	-41.0193	174.0603	334.4024
78	OPTK	-38.0465	177.3076	127.9182
79	OROA	-40.1044	176.6807	279.4363
80	OTAK	-40.8165	175.1704	245.5603
81	OUSD	-45.8695	170.5109	26.6069
82	PAEK	-41.0218	174.9521	443.6320
83	PAKI	-37.8940	178.0826	828.3839
84	PALI	-41.5692	175.2548	624.5964
85	PARI	-38.9226	177.8833	507.8682
86	PARW	-41.3816	175.4269	557.3052
87	PAWA	-40.0331	176.8639	159.4421
88	PILK	-43.6606	169.9215	1753.7525
89	PKNO	-39.8048	175.1819	328.7868
90	PNUI	-39.9168	176.2005	788.3064
91	PORA	-40.2664	176.6352	306.7580
92	PRTU	-38.8142	177.6979	635.0739
93	PTOI	-40.6011	175.9993	512.0830
94	PUKE	-38.0714	178.2574	468.5114
95	PYGR	-46.1662	166.6807	253.6502
96	QUAR	-43.5317	169.8158	58.4505
97	RAHI	-38.9162	177.0861	467.5145

Continued on next page

Table B.1 – continued from previous page

#	Site name	Latitude	Longitude	Height
98	RAKW	-39.7472	176.6212	335.2444
99	RAUL	-29.2447	-177.9290	92.6587
100	RAUM	-37.9650	177.6775	1141.3906
101	RAWI	-38.4956	177.4154	932.4055
102	RDLV	-41.1869	175.4043	111.0562
103	RGAR	-38.5620	176.3430	410.6770
104	RGAW	-38.0032	176.8962	105.2168
105	RGHD	-38.0937	176.3659	515.9071
106	RGHL	-38.2519	176.3523	691.5146
107	RGHR	-38.3858	176.2880	644.4466
108	RGKA	-38.0201	176.2441	497.7319
109	RGKW	-38.0525	176.7728	101.4883
110	RGLI	-38.0033	176.3857	387.3242
111	RGMK	-38.1383	176.4671	956.0021
112	RGMT	-37.9155	176.7247	399.9716
113	RGON	-38.2566	176.2323	595.6886
114	RGOP	-37.8459	176.5563	259.5259
115	RGRE	-38.0573	176.5212	552.3764
116	RGRR	-38.3389	176.5146	553.1720
117	RGTA	-38.2338	176.5061	1063.7757
118	RGUT	-38.1766	176.1942	560.5317
119	RGWI	-37.5181	177.1778	292.7221
120	RGWV	-38.3526	176.2109	490.4269
121	RIPA	-39.1655	176.4925	734.4927
122	SNST	-38.7796	177.3475	597.4412
123	TAKP	-40.0616	175.9629	699.2744
124	TAUP	-38.7427	176.0810	427.4446
125	TAUW	-38.1624	178.0059	713.9226
126	TEMA	-41.1066	175.8905	515.6053
127	TGHO	-38.8129	175.9963	386.4079
128	TGHR	-38.6781	175.7119	570.7322
129	TGOH	-38.8458	176.0475	661.5332
130	TGRA	-38.8634	175.7701	570.4692
131	TGRI	-38.9771	175.8585	521.0513
132	TGTK	-38.6110	175.8108	637.5611
133	TGWH	-38.6734	175.9390	660.4029
134	THAP	-39.6825	175.7856	573.2304
135	TINT	-40.7760	175.8857	538.9673
136	TKAR	-38.4375	177.8114	287.4320
137	TORY	-41.1916	174.2801	499.5230
138	TRAV	-41.3980	175.6879	366.0596
139	TRNG	-37.7288	176.2609	151.5663
140	TRWH	-41.2781	174.6276	470.7360
141	TURI	-40.2650	176.3826	538.6234
142	VEXA	-43.6377	169.8932	1495.1516
143	VGFW	-39.2550	175.5525	2049.8721
144	VGKR	-39.0944	175.6413	1210.9147
145	VGMO	-39.4074	175.7543	899.9889
146	VGMT	-39.3846	175.4705	836.9912
147	VGOB	-39.1998	175.5422	1161.6367

Continued on next page

Table B.1 – continued from previous page

#	Site name	Latitude	Longitude	Height
148	VGOT	-39.1631	175.6651	1508.5909
149	VGPK	-39.2893	175.3464	788.4961
150	VGTR	-39.2984	175.5483	2085.4882
151	VGTS	-39.2773	175.6089	1766.9992
152	VGWH	-39.2824	175.5890	2088.5827
153	VGWN	-39.3269	175.5979	1565.1511
154	VGWT	-39.1151	175.5897	1190.1204
155	WAHU	-39.0772	177.2344	219.3547
156	WAIM	-44.6557	170.9203	1045.2995
157	WAKA	-43.5840	169.8853	1416.5591
158	WANG	-39.7869	174.8214	290.1262
159	WARK	-36.4344	174.6628	111.7098
160	WEST	-41.7447	171.8062	665.7768
161	WGTN	-41.3235	174.8059	26.4862
162	WGTT	-41.2904	174.7816	43.4511
163	WHKT	-37.9817	177.0139	232.2347
164	WHNG	-35.8038	174.3146	173.2044
165	WHVR	-39.7301	175.4517	690.4988
166	WITH	-41.5606	173.9843	408.3585
167	WMAT	-37.8250	178.4087	356.4571
168	WPAW	-39.8959	176.5430	293.8815
169	WPUK	-40.0642	176.4406	344.8498

TABLE B.2: Australian inland sites used as a baseline for the analysis of the New Zealand network.

#	Site name	Latitude	Longitude	Height
0	ALIC	-23.6701	133.8855	603.7671
1	BDVL	-25.9004	139.3479	69.5547
2	BULA	-22.9135	139.9031	200.9784
3	COOB	-29.0347	134.7226	229.6383
4	JERV	-22.8605	136.1007	382.3573
5	LAMB	-26.9386	134.0629	311.6505
6	MTCV	-25.9457	133.2067	545.6636
7	MTDN	-22.1328	131.4927	672.9093
8	MTIS	-20.6904	139.4864	398.4523
9	NTJN	-21.4572	133.9700	619.7262
10	RKLD	-19.9676	137.8348	276.6468
11	RNSP	-18.3879	133.8165	348.8764
12	WARA	-25.0372	128.2962	587.6008
13	WMGA	-19.9334	134.3545	417.9501
14	YULA	-25.2311	130.9416	512.6471

TABLE B.3: M_2 amplitude differences computed over 15 tide gauges relative to a set of ocean tide models. The bottom row shows an average amplitude difference per ocean tide model. The low value of FES2004 is associated with a low tide anomaly in the Hauraki Gulf in the north-west of North Island (the area of high SD in Fig. 2b). All values in meters.

TG	FES2004	FES2012	FES2014b	GOT4.10c	TPXO9	EEZ
AUCT	0.3371	1.0155	1.0042	0.8271	1.1103	1.2265
CHST	1.1169	1.0863	1.1056	1.1116	1.0897	1.1643
CPIT	0.6303	0.6275	0.6262	0.6199	0.6247	0.6642
GBIT	0.7730	0.7797	0.7895	0.8643	0.7698	0.8007
GIST	0.6313	0.6313	0.6316	0.6405	0.6305	0.6496
KAIT	0.6583	0.6423	0.6515	0.6405	0.6375	0.7078
LOTT	0.6947	0.7008	0.6946	0.7015	0.6933	0.7097
MNKT	1.1792	1.0872	1.0914	1.1545	1.0806	1.2510
NAPT	0.6694	0.6659	0.6595	0.6815	0.6476	0.7001
NCPT	0.7950	0.8070	0.7990	0.8021	0.7972	0.8150
OTAT	0.6939	0.7194	0.7179	0.7375	0.7590	0.7931
PUYT	0.7747	0.7782	0.7901	0.7604	0.7639	0.8394
SUMT	0.7838	0.8530	0.8481	0.8143	0.8235	0.9054
TAUT	0.7291	0.7177	0.7224	0.7225	0.7183	0.7566
WLGT	0.6251	0.3819	0.3809	0.3030	0.4199	0.5130
Avg. difference (m)	-0.0080	0.0295	0.0305	0.0113	0.0232	0.0841

TABLE B.4: Q-values profiles* for PREM and STW105.

PREM

Depth (km)	Q
600.0	143.0
400.0	143.0
220.0	80.0
80.0	600.0
24.4	600.0
15.0	600.0

STW105

Depth (km)	Q
600.0	165.0
410.0	165.0
220.0	70.0
120.0	200.0
30.0	200.0
24.4	300.0
15.0	300.0

* from depth 220-80km PREM uses a Q of 80 and from a depth of 220-120km, STW105 uses a Q of 70. The last layer goes from a depth of 15km to the surface. No information is provided by the authors of either model on the uncertainty of Q values.

TABLE B.5: Average residual amplitude (A) and phase (ϕ) values per each block. "c" and "s" indices stand for central and south blocks.

	TVZ_c		TVZ_s		EC_c		EC_s	
	A, mm	$\phi, ^\circ$	A, mm	$\phi, ^\circ$	A, mm	$\phi, ^\circ$	A, mm	$\phi, ^\circ$
east	0.15	-83.31	0.29	-78.61	0.37	-127.69	0.39	-122.87
north	0.32	-53.03	0.30	-43.96	0.33	-30.85	0.25	-8.62
up	0.51	-102.07	0.51	-70.29	0.26	-109.60	0.36	-71.66

B.3 Copyright and License details

Appendix C

Supporting Information for Chapter 4

C.1 Supporting figures

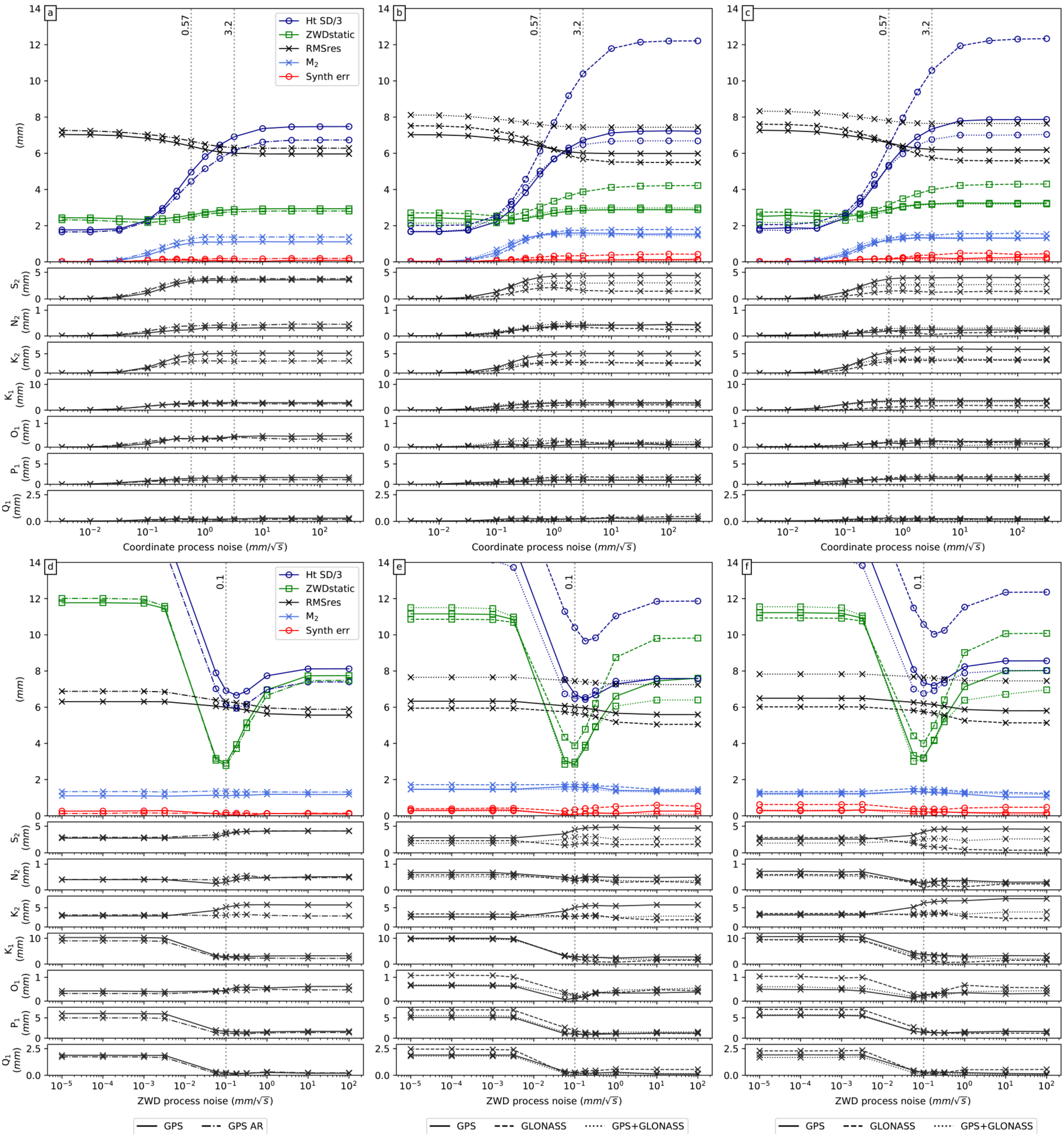

FIGURE C.1.1: The effect of varying coordinate process noise (a-c) and zenith wet delay (d-f) at test site BRO1 (2015.001–2020.152) computed with JPL (a, d), ESA (b, e) and CODE (c, f) products according to Penna et al. (2015) and extended as per Matviichuk et al. (2020). GPS solutions were computed with both floating and integer ambiguity resolution (AR) using JPL products while ESA and CODE products were used to compute GPS, GLONASS and GPS+GLONASS solutions with floating AR. GPS, GPS AR, GLONASS and GPS+GLONASS solutions are marked with solid, dash-dotted, dashed and dotted lines respectively.

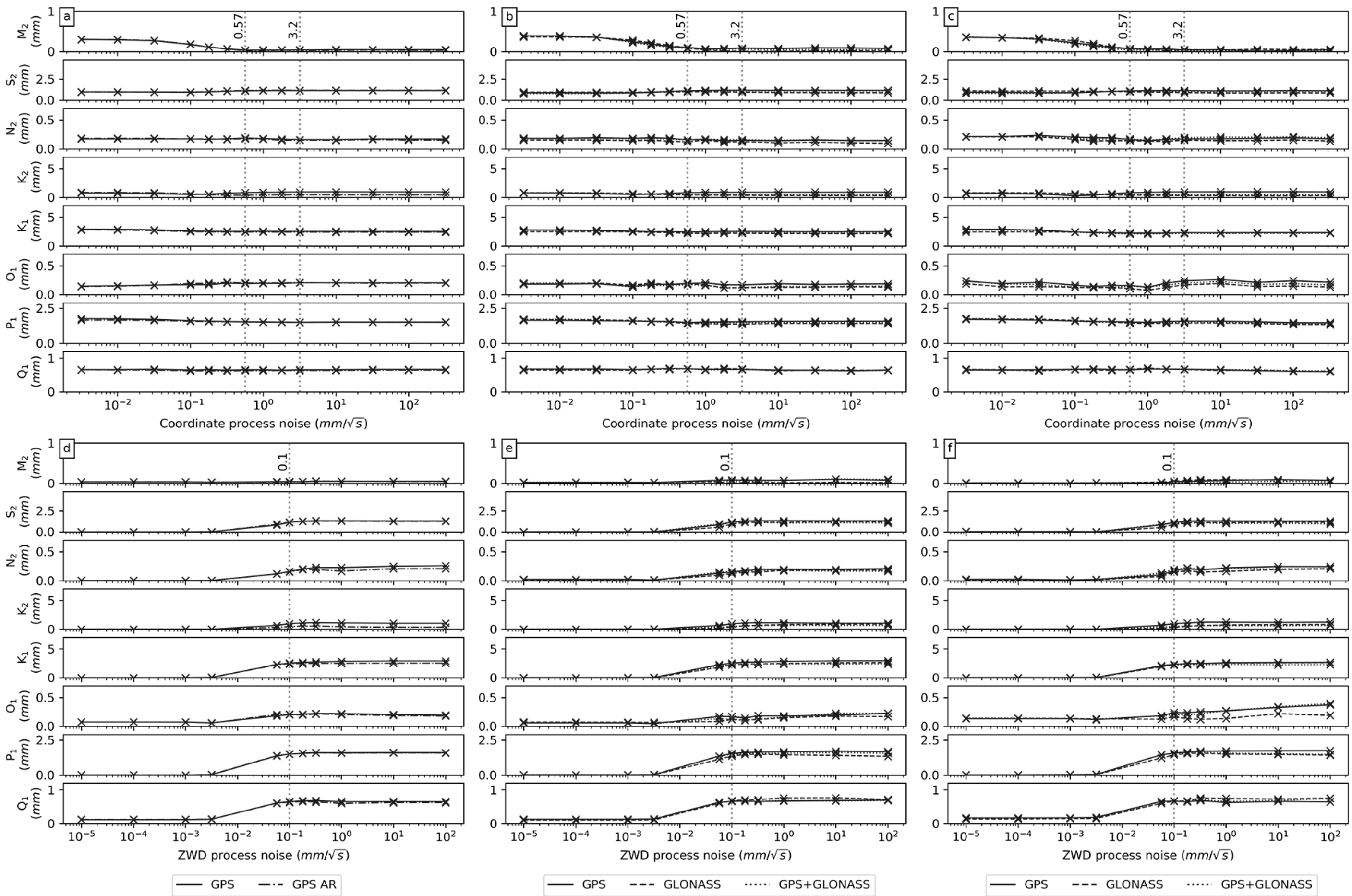

FIGURE C.1.2: The effect of varying coordinate process noise (a-c) and zenith wet delay (ZWD) (d-f) on the tidal constituents magnitude change in resulting ZWD computed as vector difference between OTLD derived from a priori ZWD (VMF1) and resulting ZWD timeseries. Subplots configuration and line styles same as in Fig. C.1.2

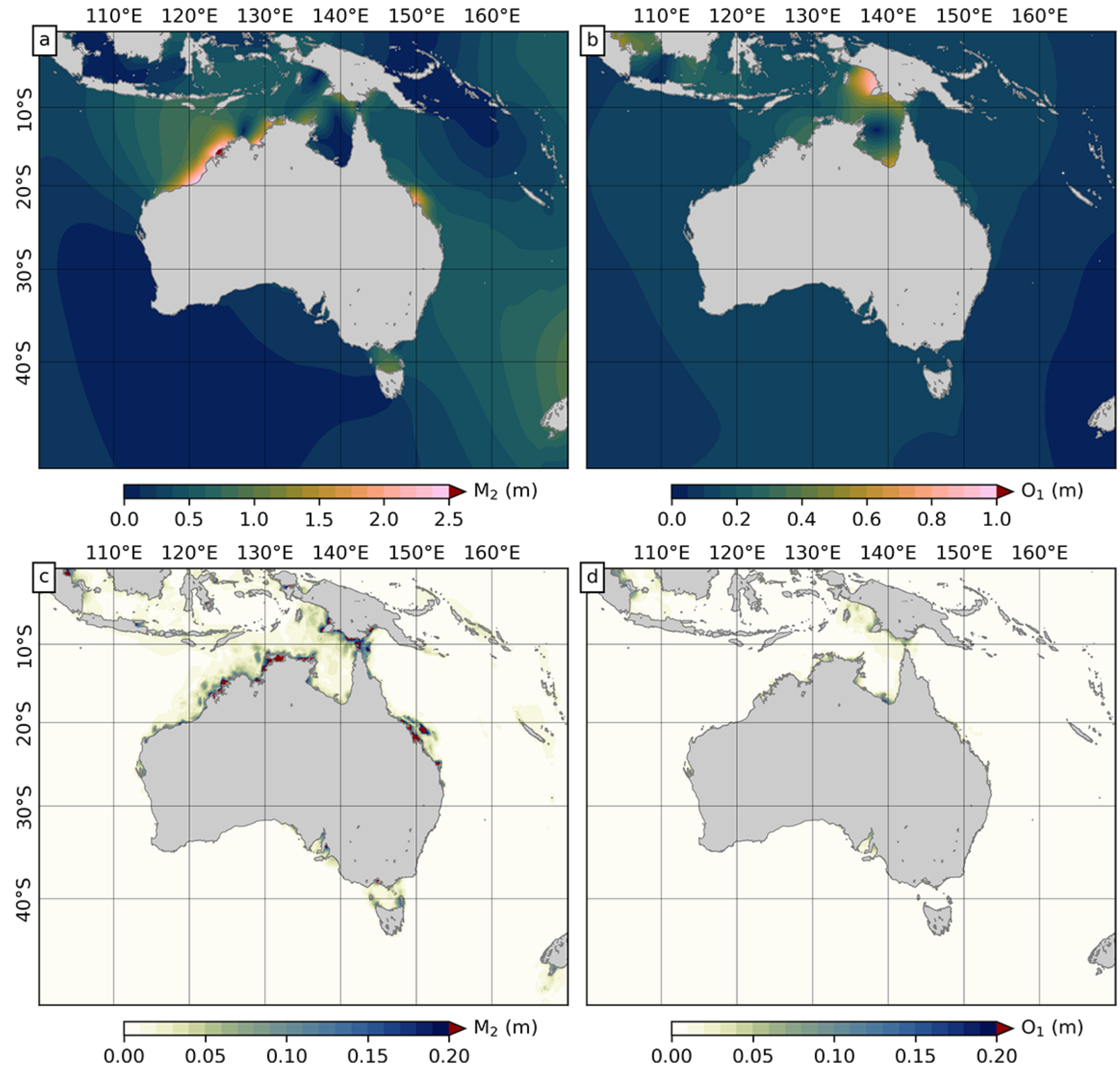

FIGURE C.2: Assessment of a set of recent global ocean tide models around Australia: mean tidal amplitude over FES2012, FES2014b, GOT4.8, GOT4.10c, TPXO8, TPXO9.v1 and TPXO9.v2a at M_2 (a) and O_1 (b); standard deviation of the vector differences between the same set of ocean tide models for M_2 (c) and O_1 (d). Note the color bar range difference between M_2 and O_1 mean models (a, b) and scale extend above the maximum range.

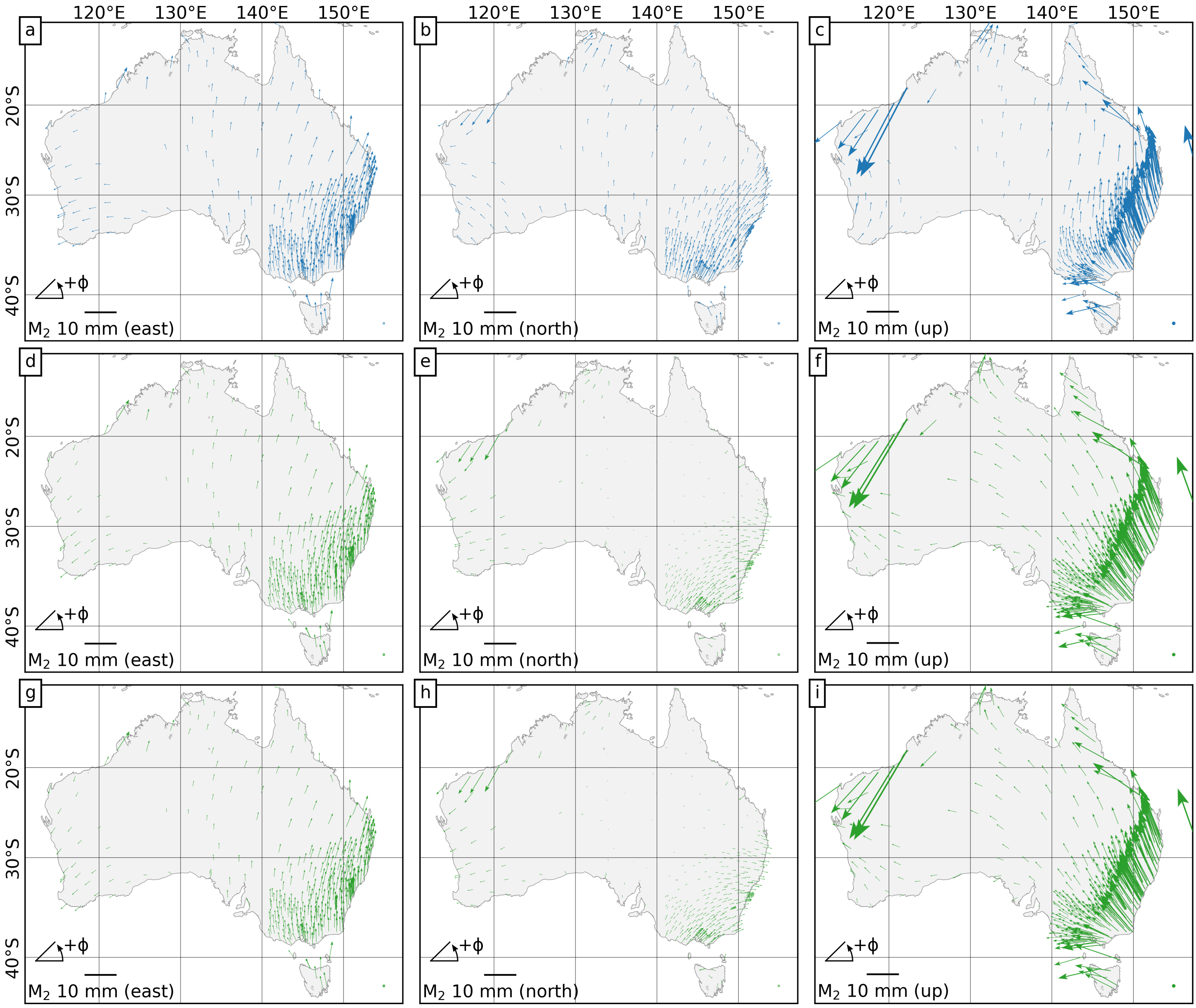

FIGURE C.3.1: Observed M_2 OTLD for the east, north and up components derived from solutions based on JPL (a, b, c), ESA (d, e, f) and CODE (g, h, i) satellite orbit and clock products. Solutions based on JPL products used GPS only with AR, while those based on ESA and CODE products used GPS+GLONASS. Circle in the bottom right of each plot represents a median 95 % confidence error ellipse over all sites (almost invisible at this scale)

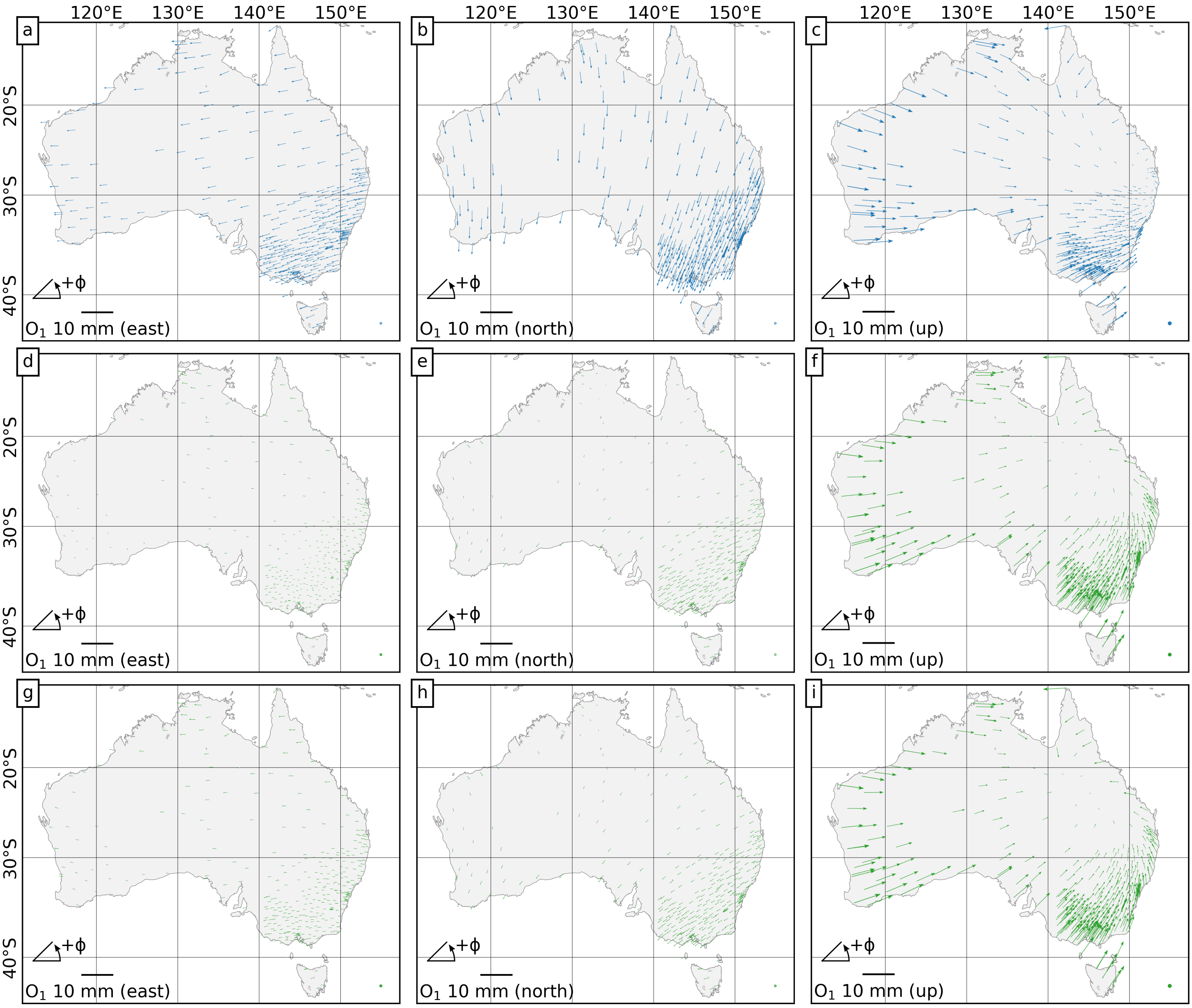

FIGURE C.3.2: Same as Fig. C.3.1 but for O_1

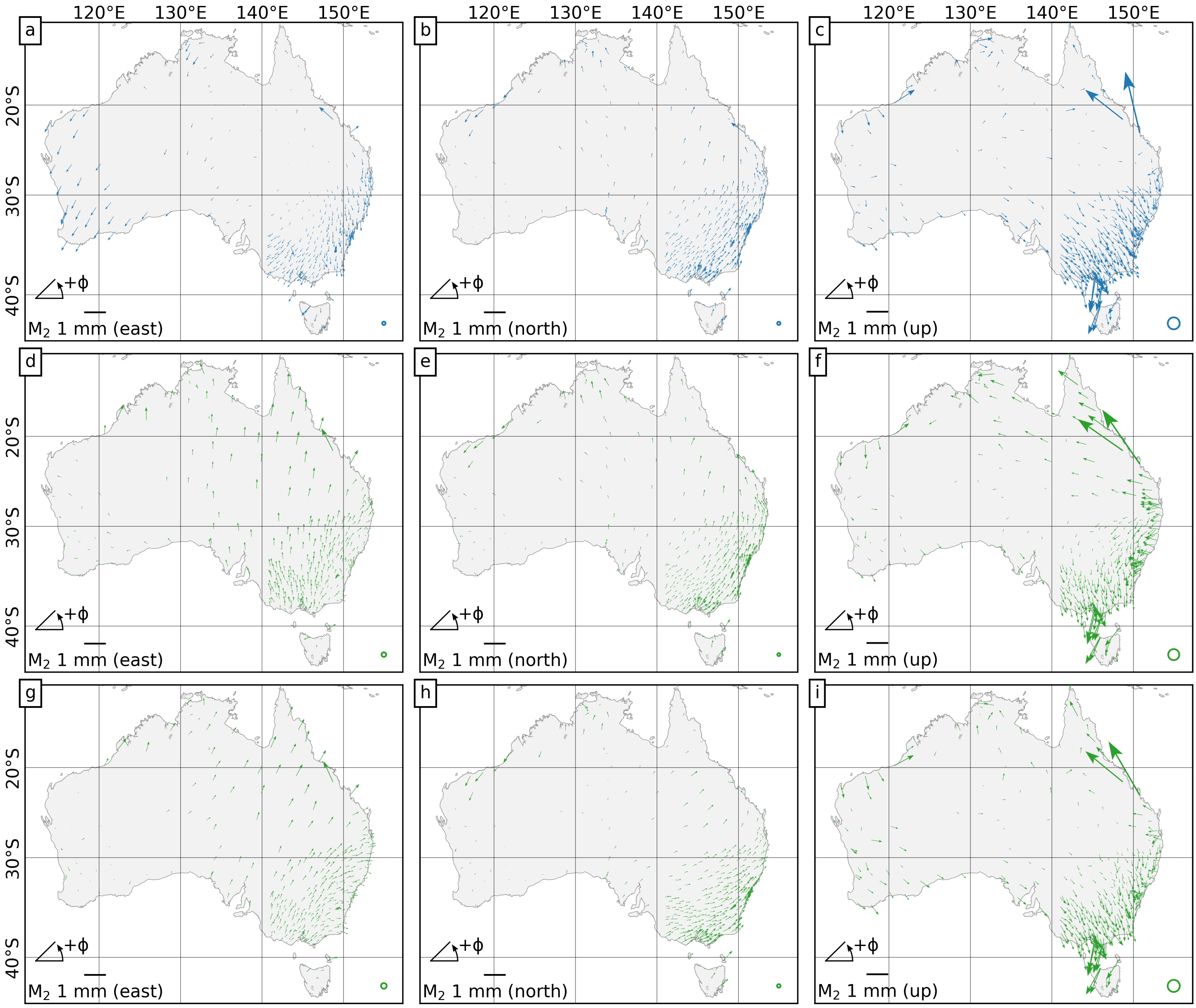

FIGURE C.4.1: M_2 residual OTLD, Z_{res}, relative to FES2014b ocean tide model and STW105dc Green's function for the east, north and up components derived using JPL (a, b, c), ESA (d, e, f) and CODE (g, h, i) products solutions. Solutions based on JPL products used GPS only with AR, while those based on ESA and CODE products used GPS+GLONASS. Circle in the bottom right of each plot represents a median 95 % confidence error ellipse over all sites

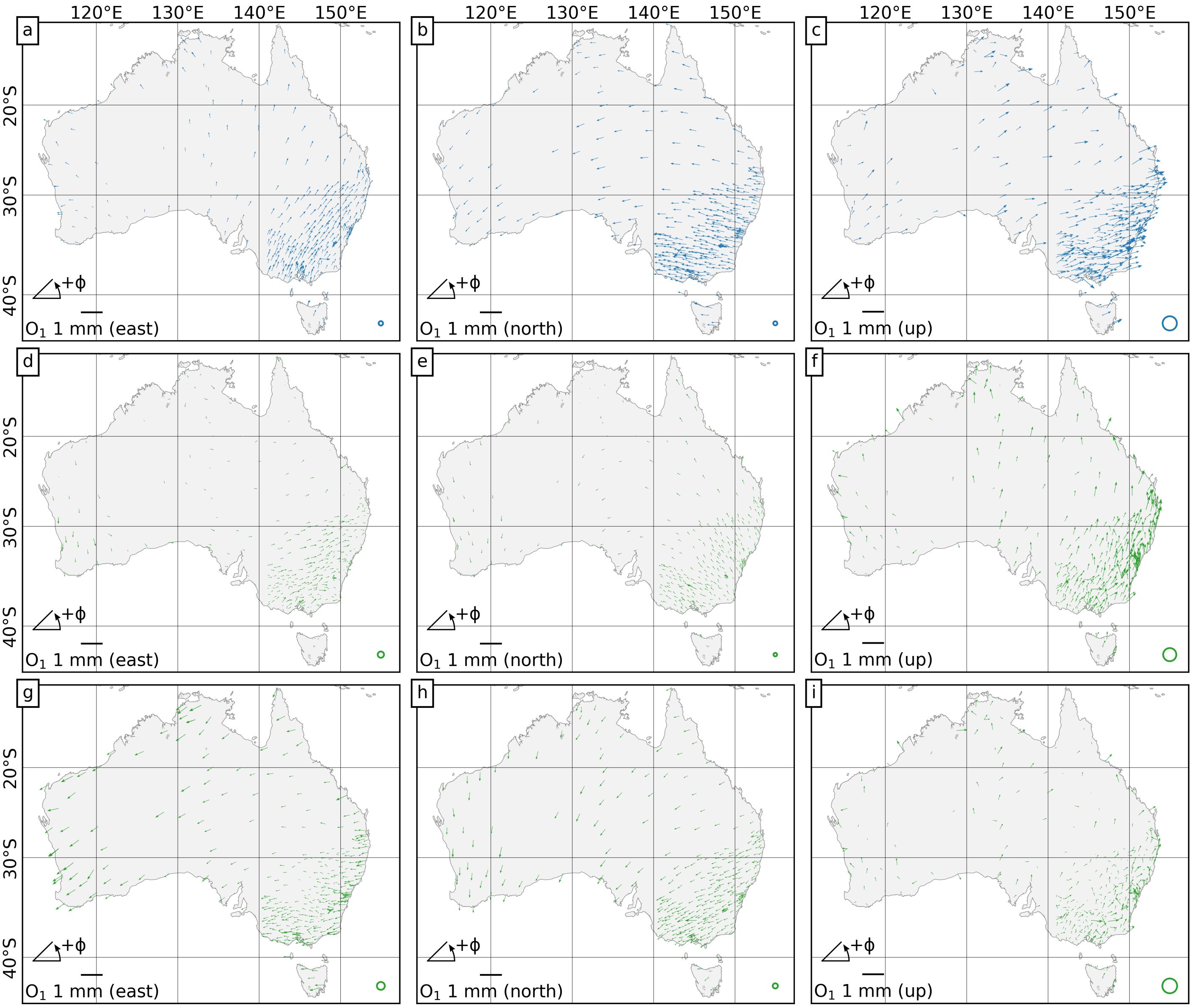

FIGURE C.4.2: Same as Fig. C.4.1 but for O_1.

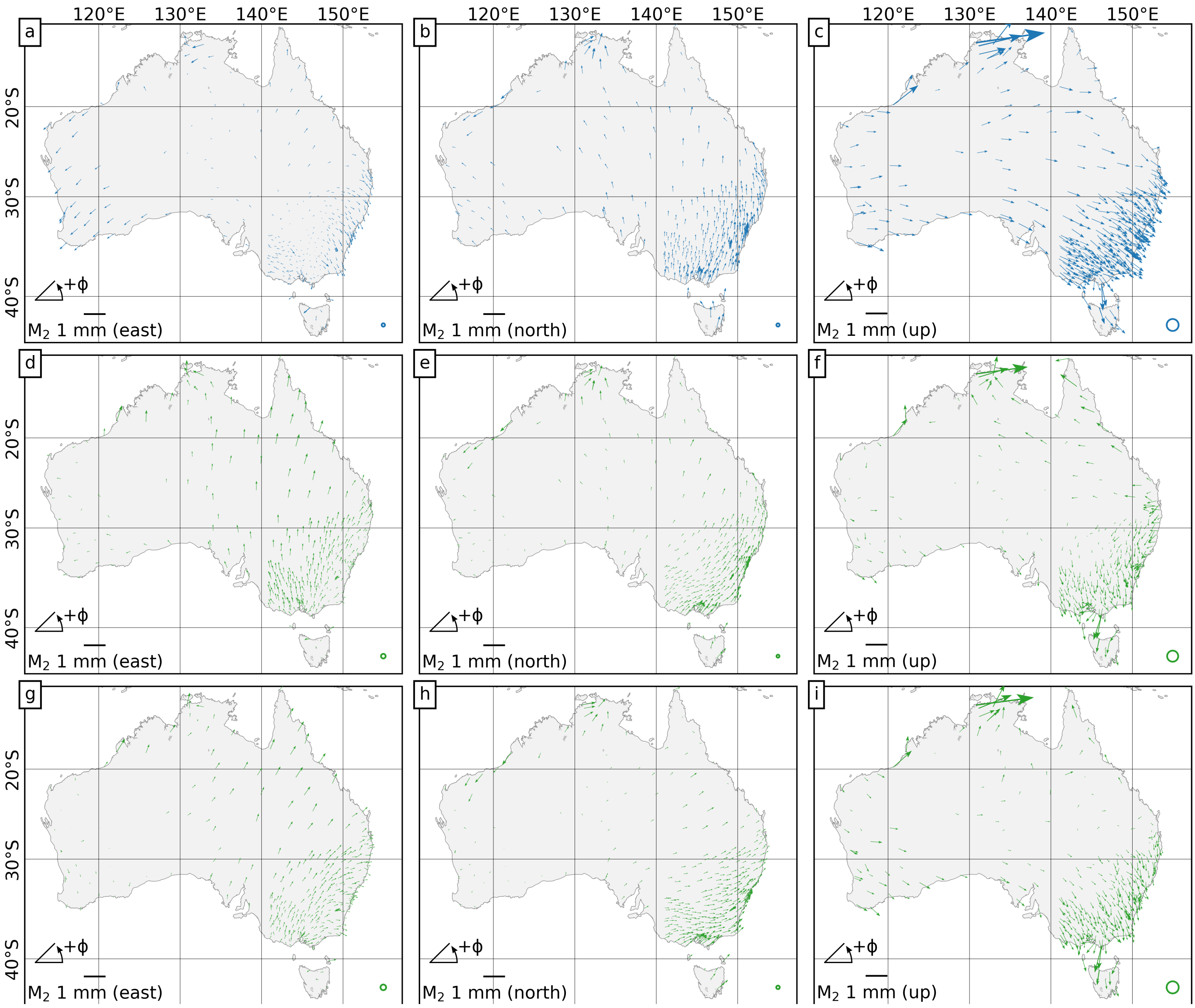

FIGURE C.5.1: M_2 Z_{res} as in Fig. C.4.1 but relative to TPXO9 ocean tide model.

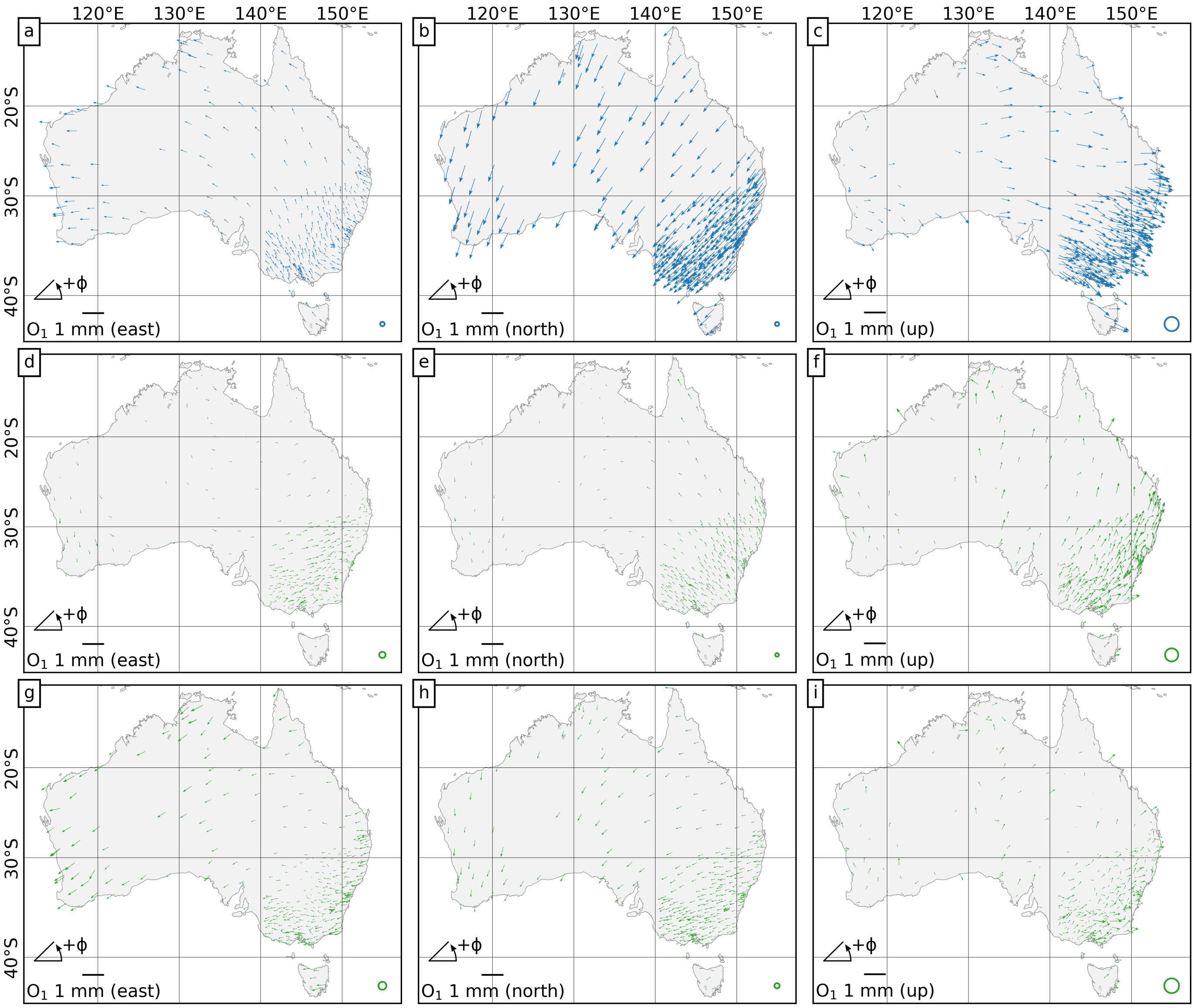

FIGURE C.5.2: Same as Fig. C.5.1 but for O_1.

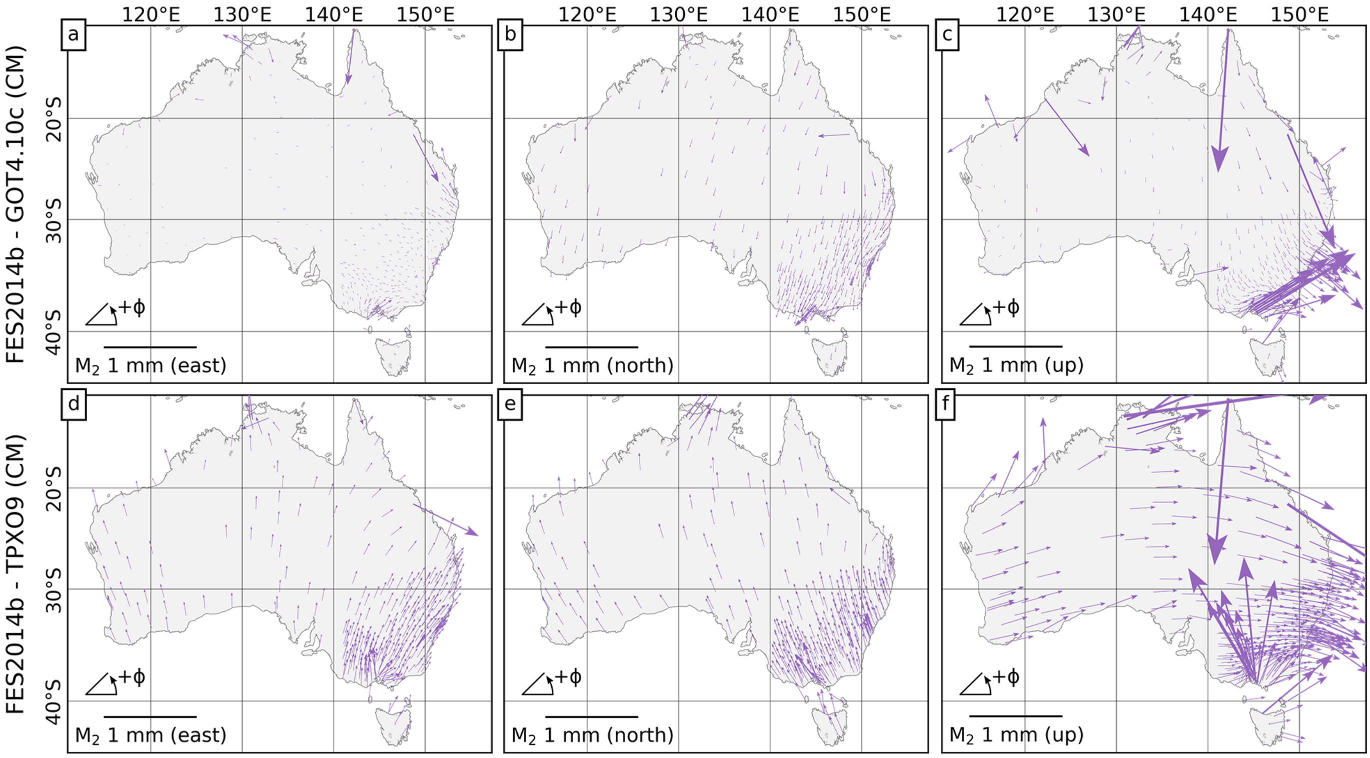

FIGURE C.6.1: Vector difference between pairs of modeled OTLD values in **CE** frame: FES2014b and GOT4.10c (a-c); FES2014b and TPXO9 (d-f). The Green's function is kept fixed.

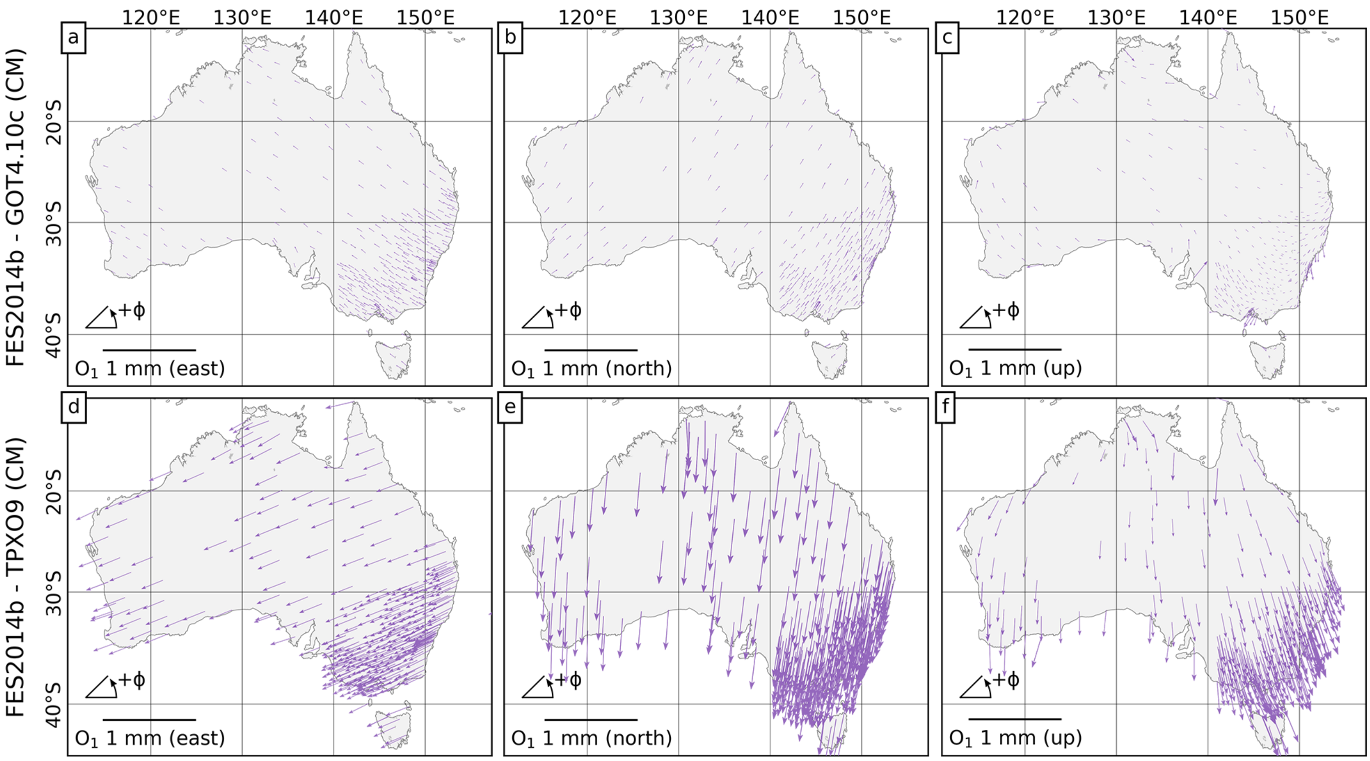

FIGURE C.6.2: Same as Fig. C.6.1 but for O_1

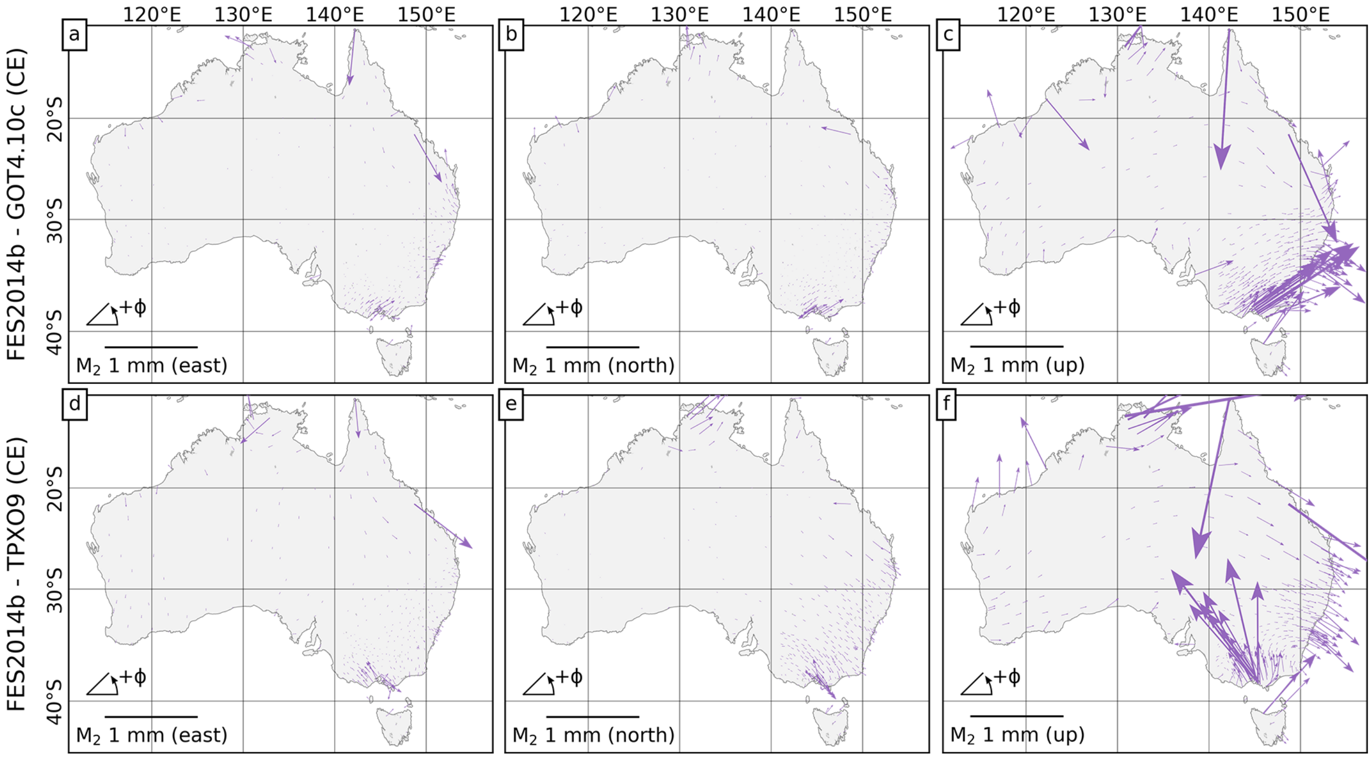

FIGURE C.7.1: Vector difference between pairs of modeled OTLD values in **CM** frame: FES2014b and GOT4.10c (a-c); FES2014b and TPXO9 (d-f). The Green's function is kept fixed.

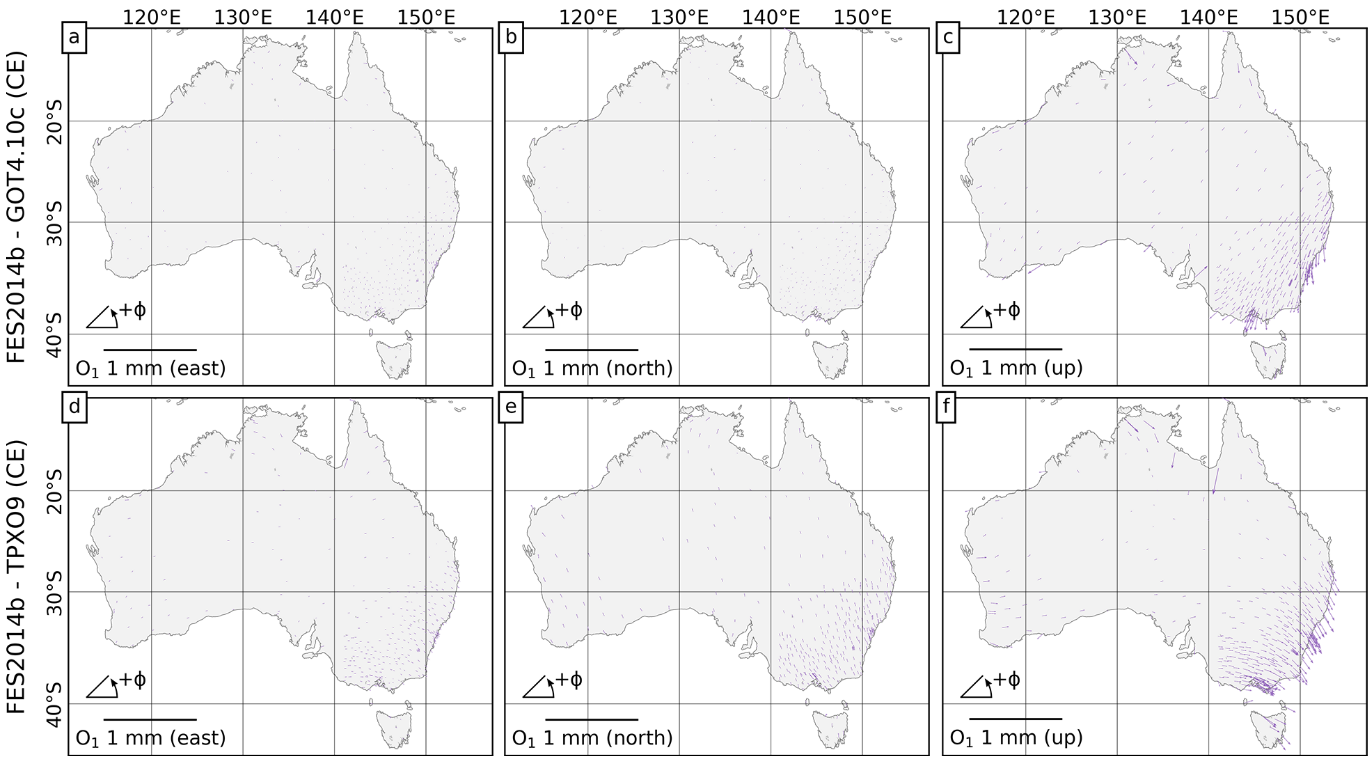

FIGURE C.7.2: Same as Fig. C.7.1 but for O_1

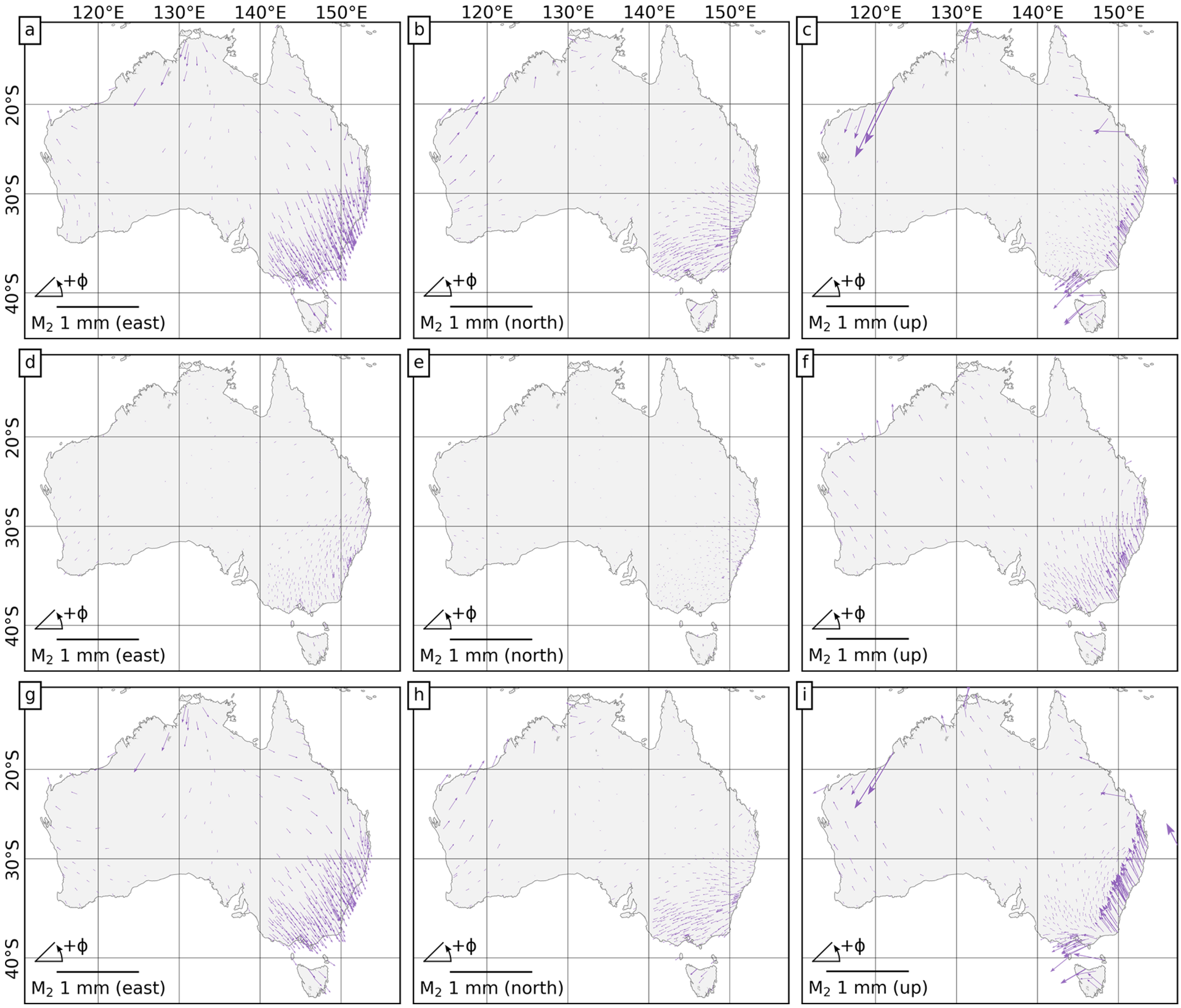

FIGURE C.8.1: Effect of including asthenosphere dissipation at M_2 correction (a-c), spatial water density and compressibility correction (d-f), and both corrections combined (g-i) on the modeled OTLD. Modeled OTLD used FES2014b and STW105 in this test.

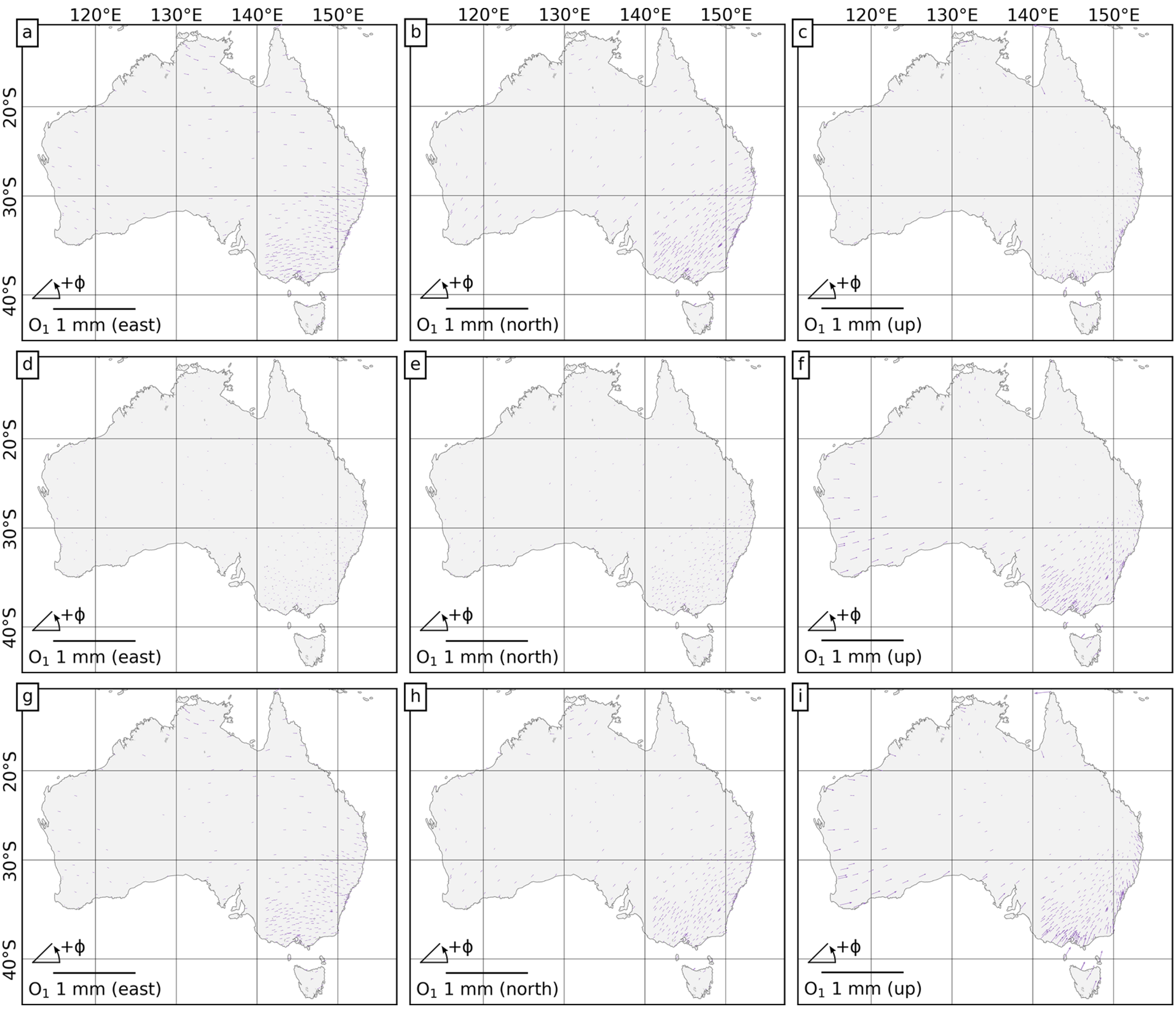

FIGURE C.8.2: Same as Fig. C.8.1 but for O_1. Note that Green's function was corrected for the dissipation at M_2 and not at O_1 in this test

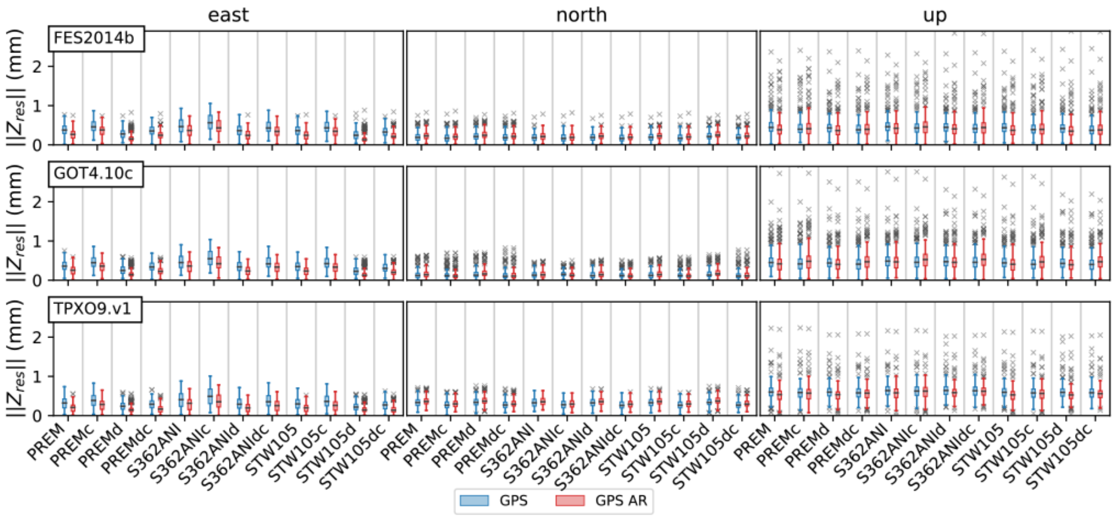

FIGURE C.9.1: M_2 residual OTLD magnitudes, $\|Z_{\text{res}}\|$, using JPL products.

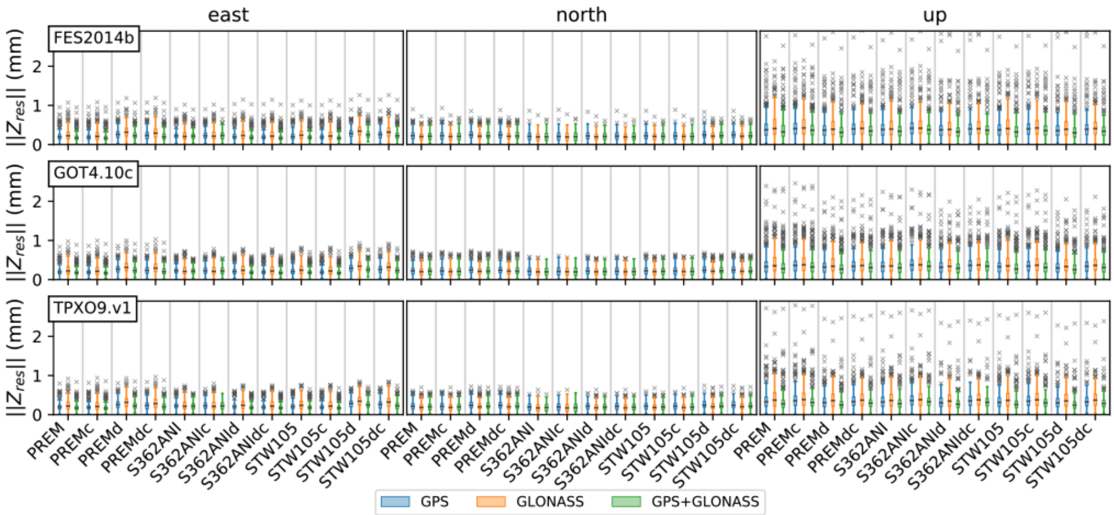

FIGURE C.9.2: Same as Fig. C.9.1 but using solutions derived from ESA products.

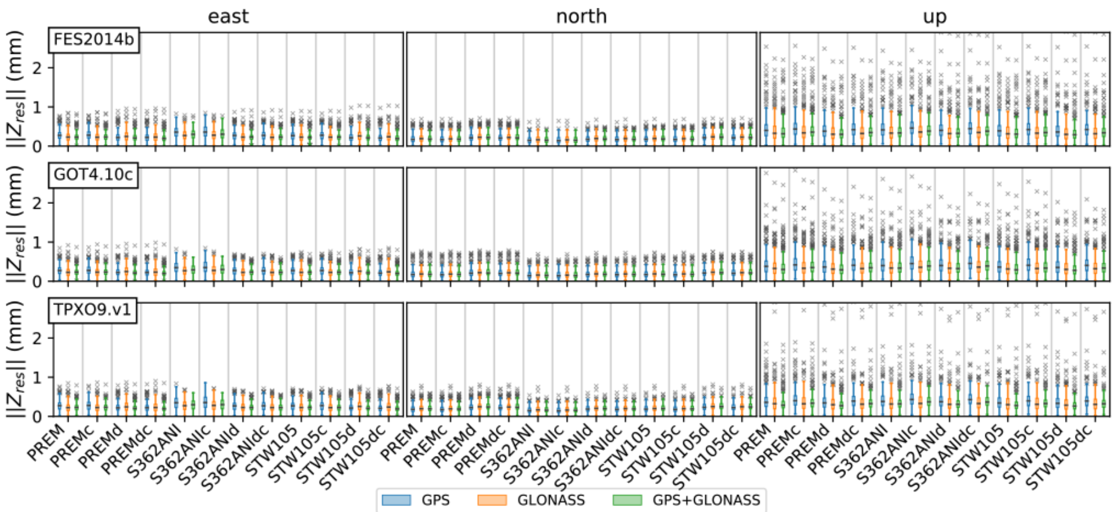

FIGURE C.9.3: Same as Fig. C.9.1 but using solutions derived from CODE products.

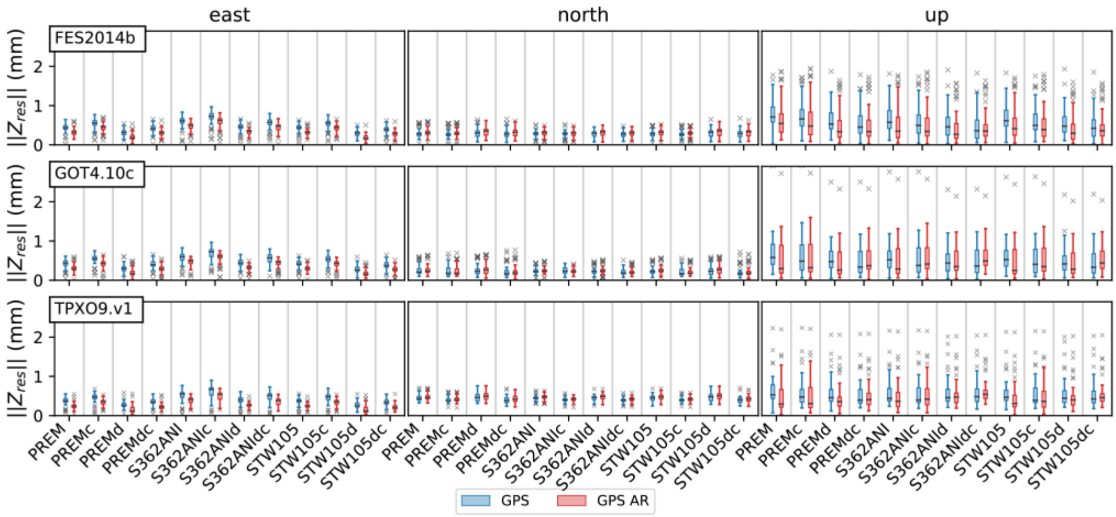

FIGURE C.9.4: M_2 residual OTLD magnitudes, $\|Z_{\text{res}}\|$, of 50 coastal stations using JPL products.

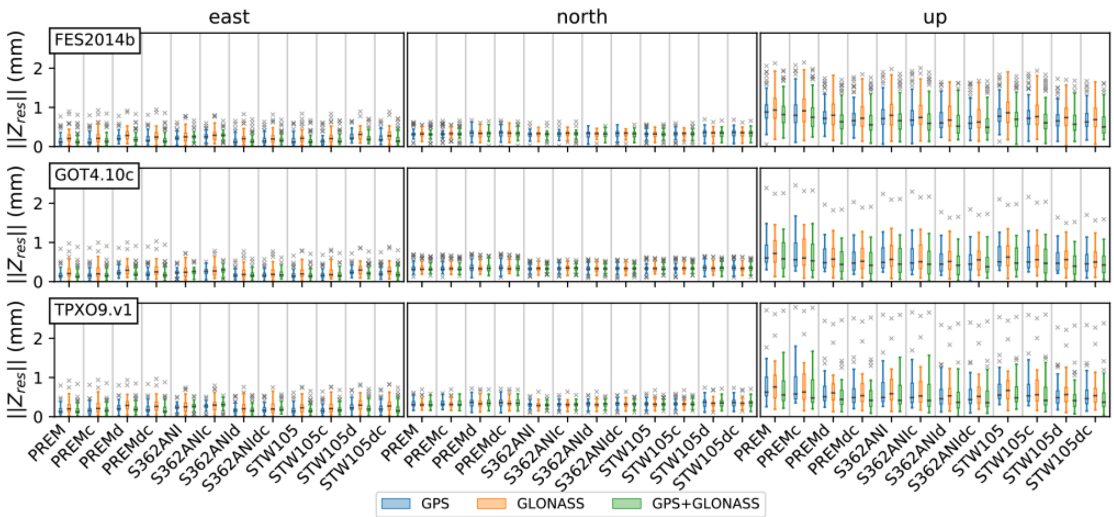

FIGURE C.9.5: Same as Fig. C.9.4 but using solutions derived from ESA products

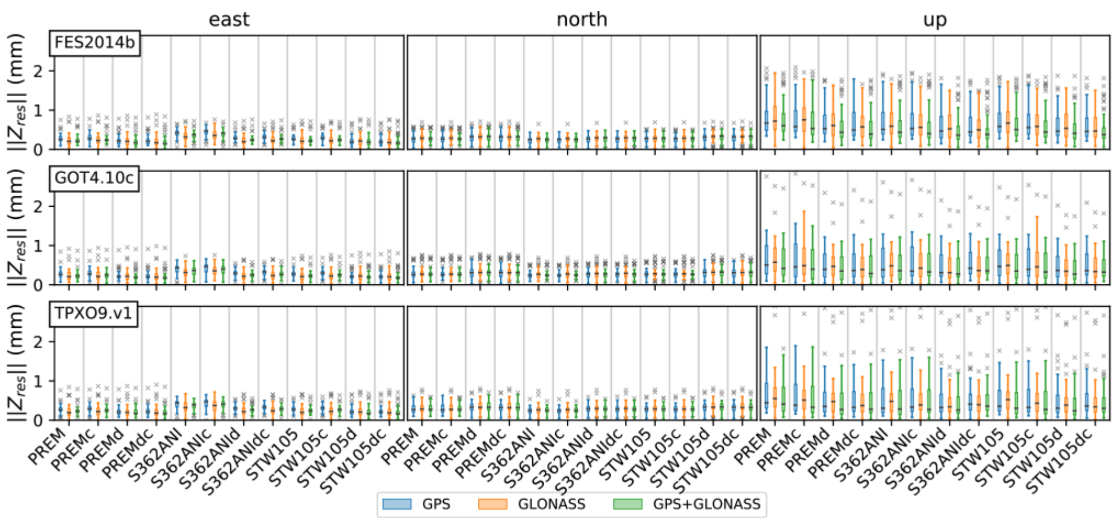

FIGURE C.9.6: Same as Fig. C.9.4 but using solutions derived from CODE products

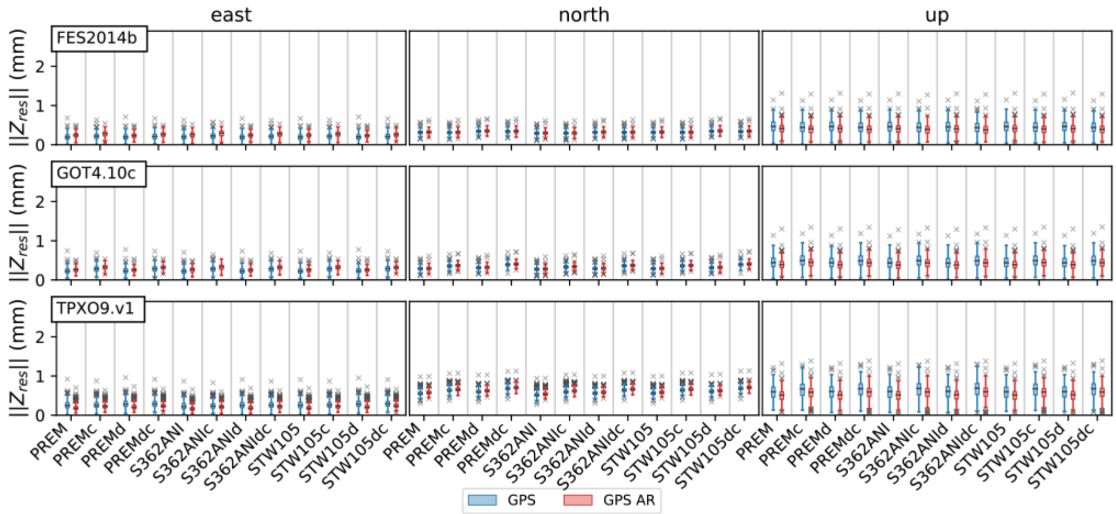

FIGURE C.10.1: O_1 residual OTLD magnitudes, $\|Z_{\mathrm{res}}\|$, using JPL products.

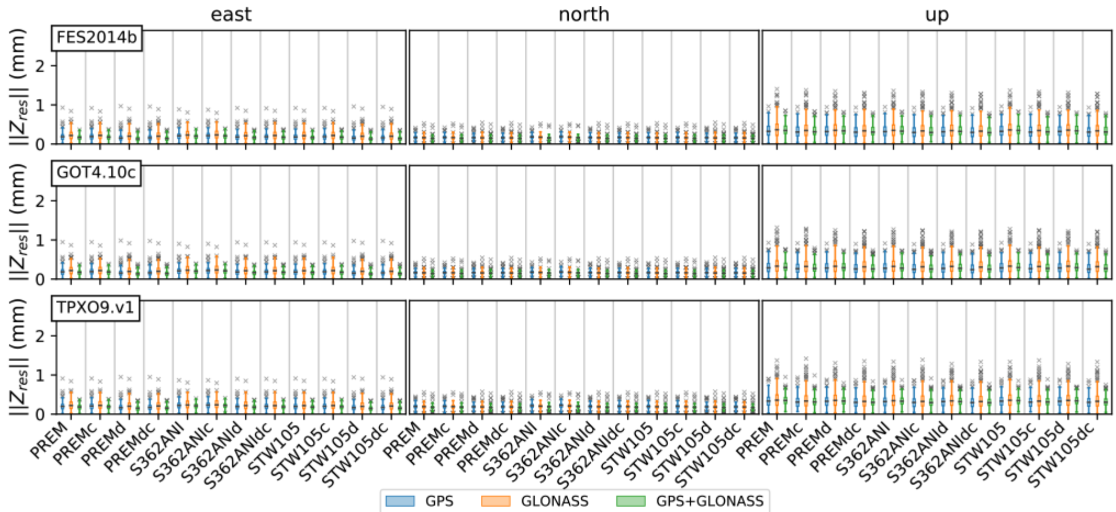

FIGURE C.10.2: Same as Fig. C.10.1 but derived from solutions based on ESA products

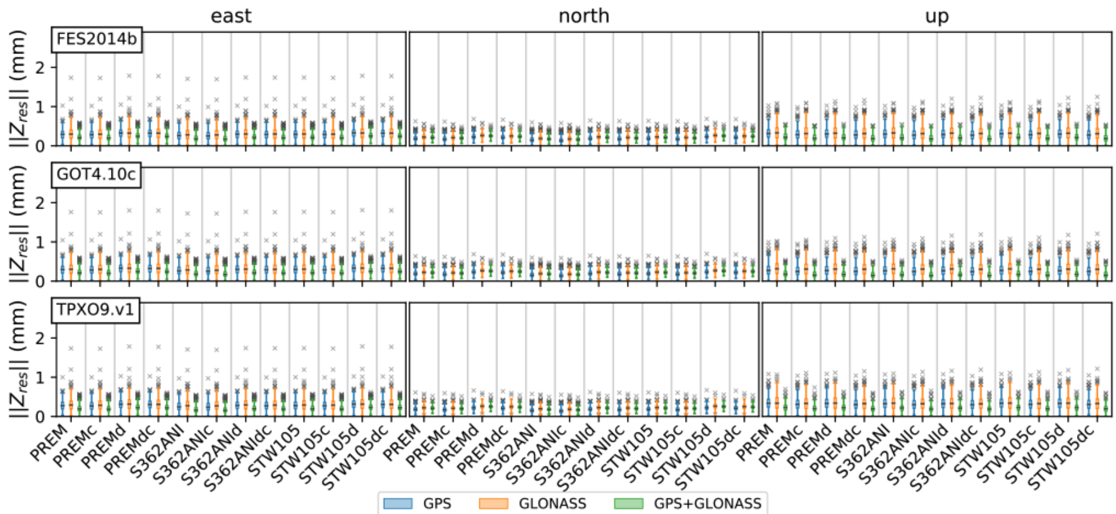

FIGURE C.10.3: Same as Fig. C.10.1 but derived from solutions based on CODE products

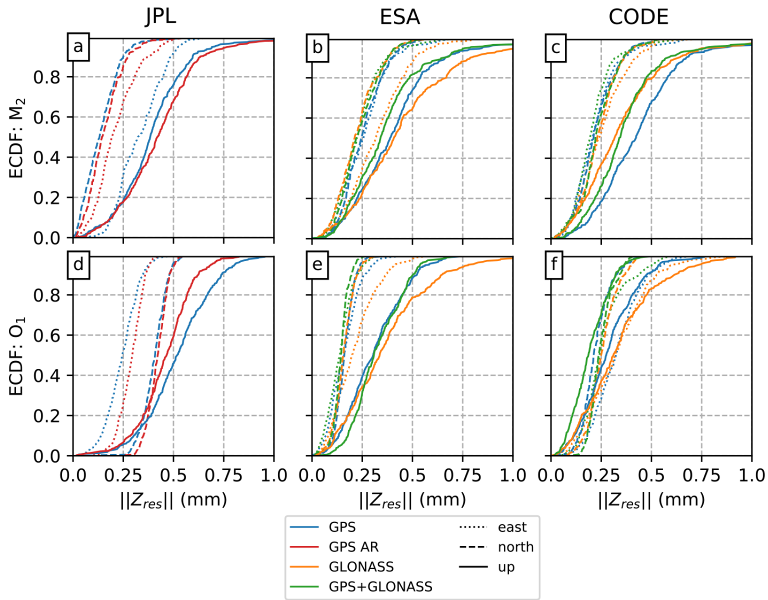

FIGURE C.11: Empirical cumulative distribution functions (ECDFs) of OTLD residuals (east, north, up) relative to the FES2014b ocean tide model and STW105dc Green's function for JPL, ESA and CODE solutions for M_2 (a-c) and O_1 (d-f) constituents. The mean OTLD residual vector was not subtracted. "GPS AR" stands for integer ambiguity resolution only available with JPL products.

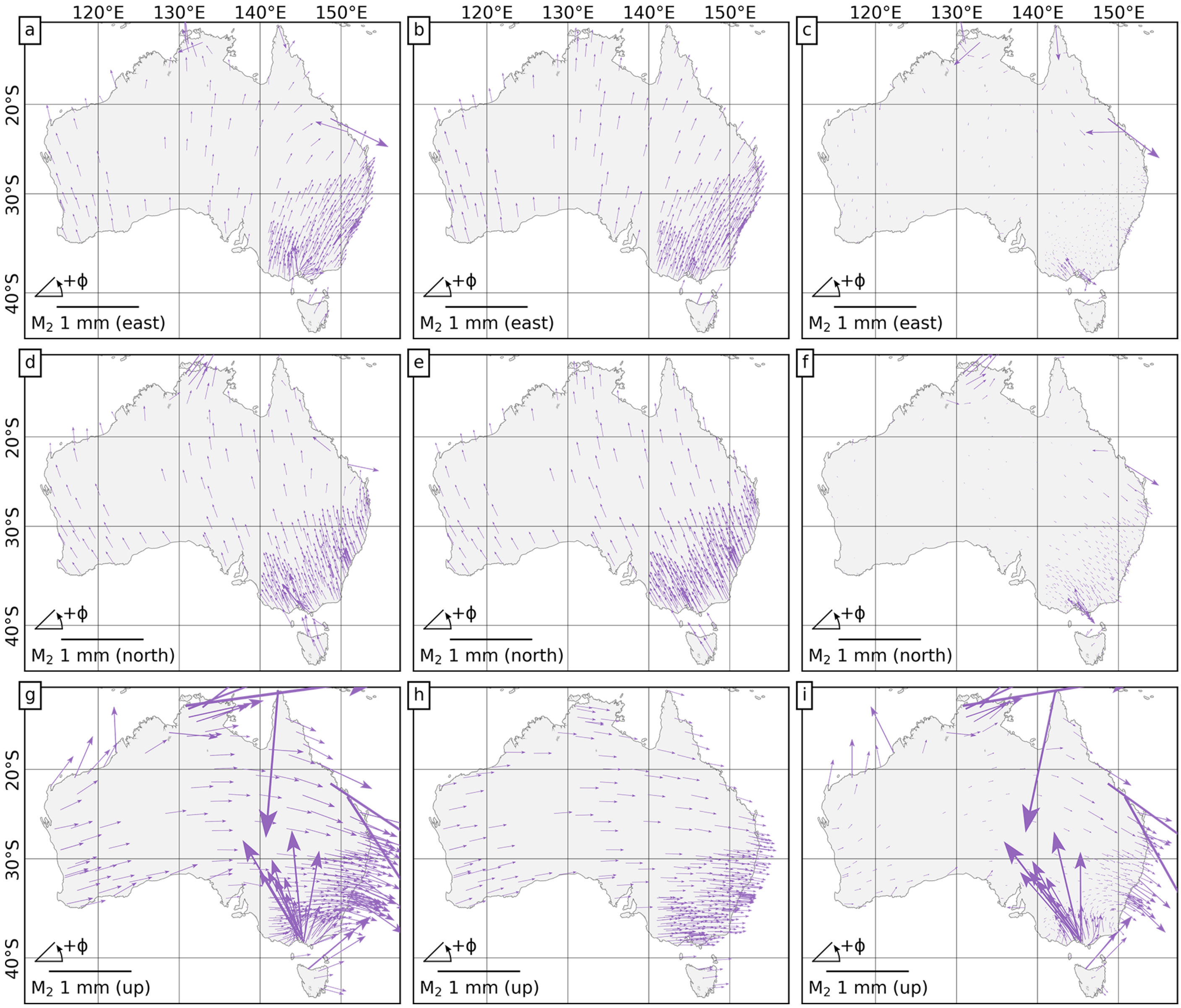

FIGURE C.12.1: Site vector differences for the east, north and up components between CM OTLD values based on the full FES2014b and TPXO9.v1 loading field (a, d, g), the vector difference between the respective CoM values only (b, e, h) and the vector difference between the two (c, f, i).

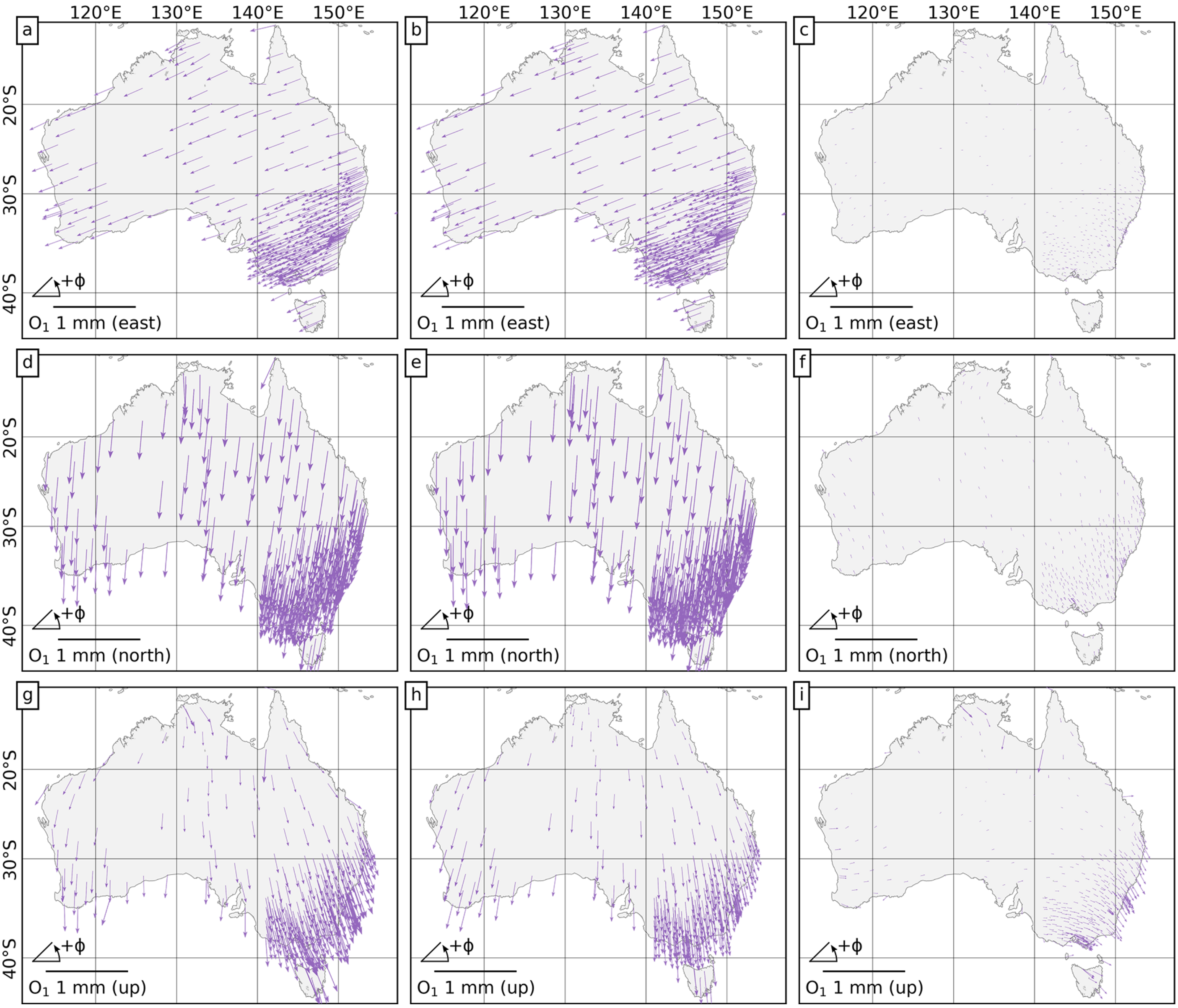

FIGURE C.12.2: Same as C.12.1 but for O_1

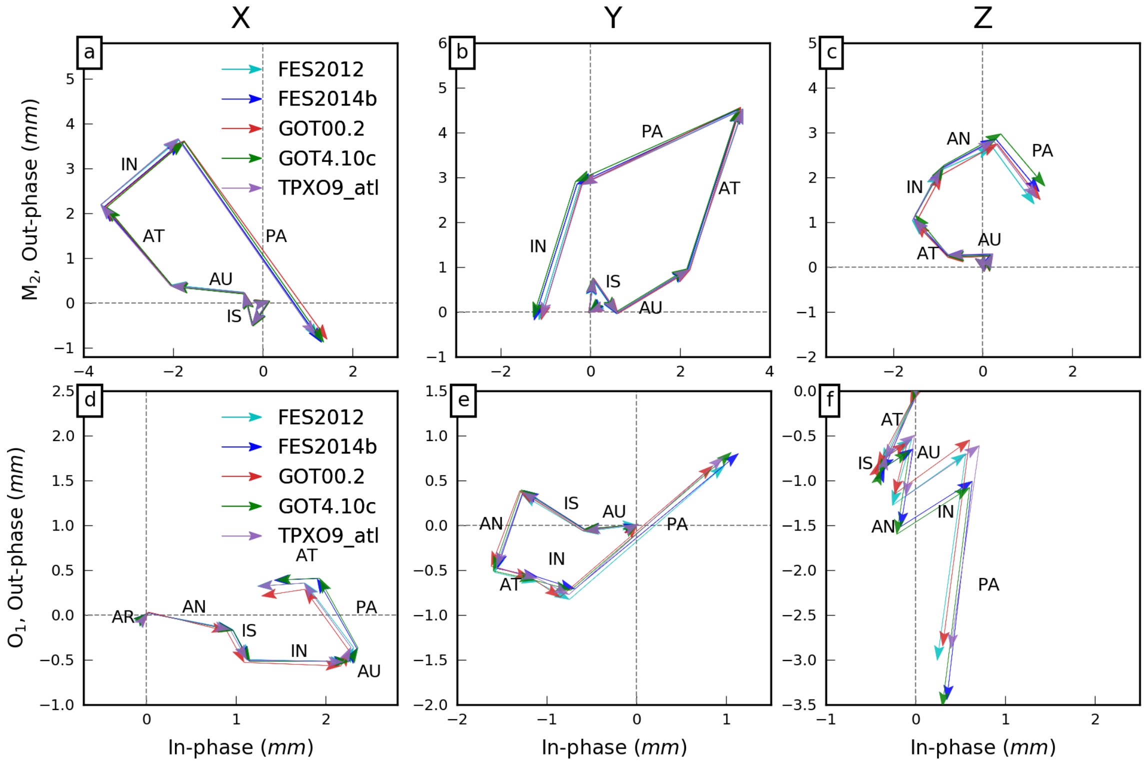

FIGURE C.13: Reconstructed phasors of CoM for M_2 (a-c) and O_1 (d-f) constituents for X, Y and Z components. The seven two-letter indices represent regions of global ocean: AN – Antarctic, AR – Arctic, AT - Atlantic, AU – Australia (local), PA – Pacific, IN - Indian, IS – Indonesian; see Fig S11 for regions configuration.

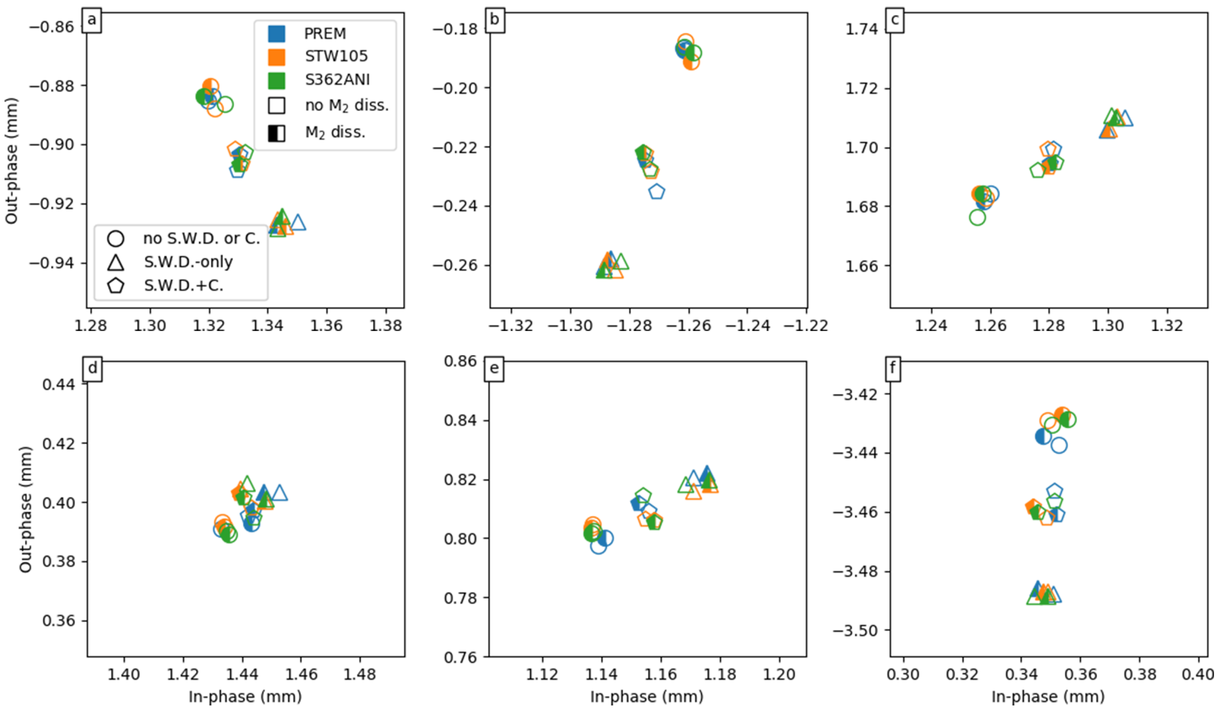

FIGURE C.14.1: Impact of modeling spatial water density and compressibility on the CoM values per each of X, Y and Z components for a set of Green's functions. The ocean tide model was fixed to FES2014b.

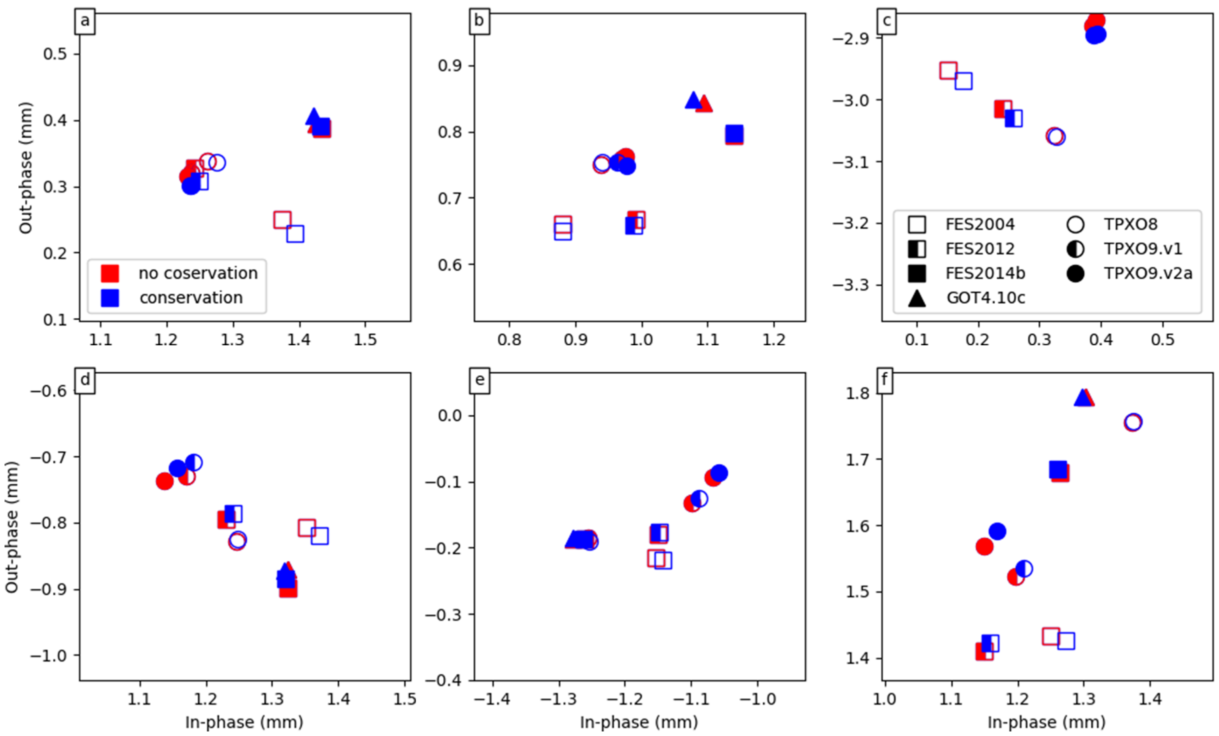

FIGURE C.14.2: Impact on the CoM values of water conservation enabled (blue) and disabled (red) per each of X, Y and Z components for a set of ocean tide models. The Green's function was fixed to STW105d.

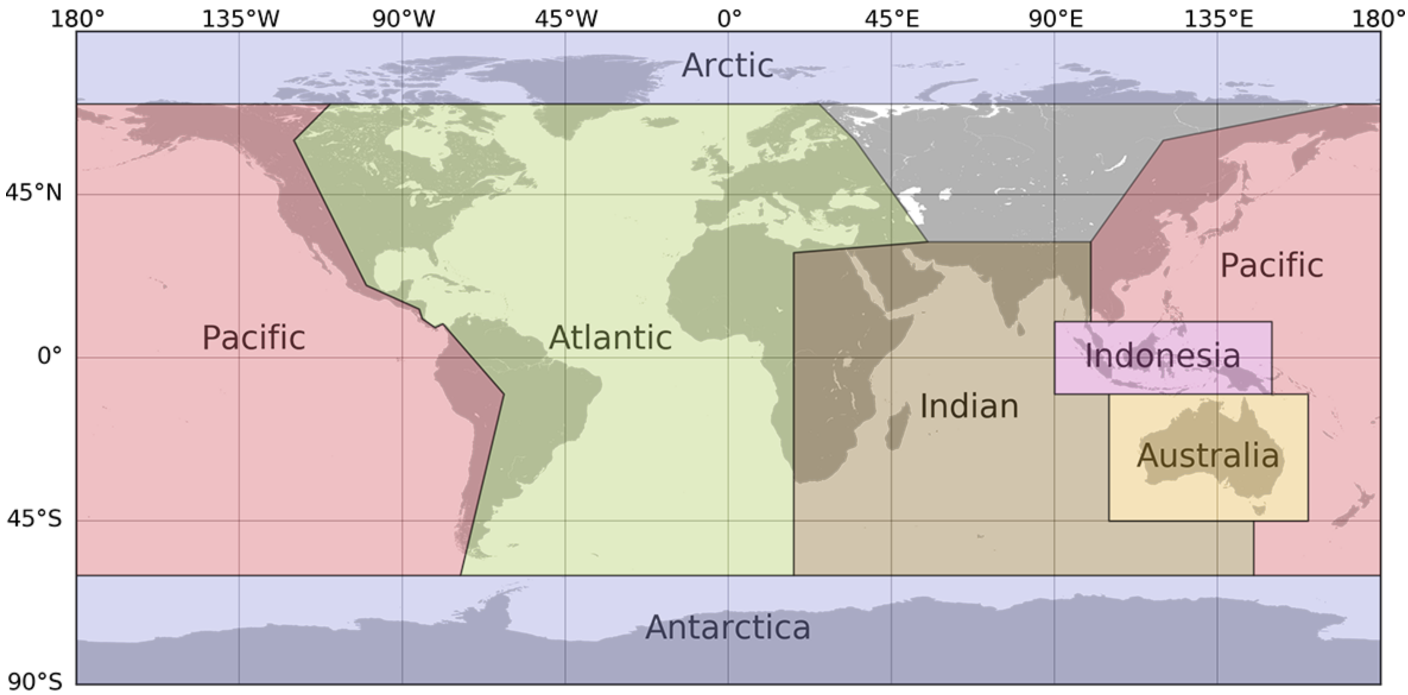

FIGURE C.15: Polygons map used for CoM phasors reconstruction

C.2 Supporting tables

TABLE C.1: List of sites used in the analysis. The coastal sites used to illustrate impact of dissipation correction are marked with *

#	Site name	Latitude	Longitude	Height
0	ALBU	-36.0775	146.9156	198.0593
1	ALBY	-34.9502	117.8102	37.1399
2	ALIC	-23.6701	133.8855	603.7671
3	ANDA	-30.4533	137.1601	103.2324
4	ANGS	-38.3963	144.1932	20.0637
5	ANNA*	-32.7848	152.0863	42.1132
6	ANTW	-36.2954	142.0268	104.0590
7	APSL	-36.9676	141.0832	112.6196
8	ARDL	-34.3509	146.9035	237.9522
9	ARMC	-22.9568	145.2454	274.7445
10	ARMD	-30.5146	151.6658	1035.1986
11	ARRT	-37.2828	142.9313	336.4420
12	ARUB	-31.8091	125.9243	104.6929
13	ASHF	-29.3244	151.0931	465.3226
14	BALA	-32.4608	123.8681	131.2095
15	BALL	-37.5589	143.8549	463.6972
16	BALM	-37.2488	141.8422	191.8413
17	BALN*	-28.8727	153.5641	44.9043
18	BANK*	-33.9151	151.0363	101.8711
19	BARR*	-34.5642	150.8583	45.6061
20	BATH	-33.4297	149.5672	757.0404
21	BBOO	-32.8104	136.0587	289.1428
22	BCUS	-37.6768	144.4421	112.9121
23	BDST	-27.9871	152.9951	101.5101
24	BDVL	-25.9004	139.3479	69.5547
25	BEE2*	-27.7203	153.2025	55.2401
26	BEEC	-36.3464	146.6577	443.4626
27	BEGA	-36.6759	149.8420	53.1322
28	BEUA	-35.9400	142.4147	97.6886
29	BIGG	-36.2808	148.0262	330.5869
30	BING	-32.4118	151.6523	487.2872
31	BJCT	-30.1017	148.9642	198.5775
32	BKNL	-31.9963	141.4701	307.9307
33	BLCK	-31.6543	150.2447	420.3218
34	BLRN	-34.6459	143.5674	78.0421
35	BMAN	-31.1063	138.7070	617.0459
36	BNDC	-37.1475	148.8849	848.6309
37	BNDY*	-24.9082	152.3210	80.5405
38	BNLA	-36.5439	146.0060	187.8719
39	BOLC	-37.7116	142.8409	220.5127
40	BOMB	-36.9121	149.2371	723.5627
41	BOOR	-34.4383	148.7017	520.0020
42	BORA	-31.5122	150.6408	391.3717
43	BORT	-36.1359	143.7226	114.3198
44	BRBA	-30.3804	150.6073	537.6350
45	BRDW	-35.4465	149.7852	679.9762
46	BRLA	-16.0545	136.3023	96.5029

Continued on next page

Table C.1 – continued from previous page

#	Site name	Latitude	Longitude	Height
47	BRO1*	-18.0040	122.2091	43.6670
48	BROC	-36.0314	144.2040	132.8912
49	BRWN	-29.9684	146.8608	149.9774
50	BUCH	-37.4980	148.1678	184.8985
51	BULA	-22.9135	139.9031	200.9784
52	BUR2*	-41.0501	145.9148	4.3257
53	BURA	-30.5255	117.1746	328.3890
54	BURK	-30.0953	145.9343	136.8223
55	CANR	-37.5649	149.1575	137.6006
56	CARG	-33.2884	146.3659	205.8454
57	CBAR	-31.5137	145.8362	261.0496
58	CBLA	-26.6713	150.3404	370.7599
59	CBLE	-30.9535	148.3782	209.7350
60	CBLT*	-27.0844	152.9515	84.3626
61	CBRA	-35.9120	145.6442	131.2432
62	CEDU	-31.8667	133.8098	145.2310
63	CKWL	-34.4561	149.4725	916.5945
64	CLAC	-38.3424	143.5851	145.0902
65	CLAH	-31.8305	149.7149	517.3649
66	CLBI	-29.5426	148.5855	180.2720
67	CLBN	-36.5919	144.7982	130.2512
68	CLEV	-27.5262	153.2665	67.4223
69	CLYT	-37.9140	145.1290	106.9052
70	CNBN	-31.3333	149.2696	675.2291
71	CNDA	-30.4653	147.6881	161.6720
72	CNDO	-33.0852	147.1510	230.1554
73	COBG	-37.7395	144.9735	64.2210
74	COEN	-13.9588	143.1767	255.0836
75	COFF*	-30.3001	153.1383	47.0070
76	COLE	-34.8070	145.8802	141.4229
77	COMA	-36.2354	149.1272	823.8805
78	COOB	-29.0347	134.7226	229.6383
79	COOL	-26.7421	145.6803	334.1103
80	COPS	-29.5809	152.7735	105.4251
81	CRAN	-38.1080	145.2869	64.3444
82	CRDX*	-34.3248	150.7676	402.6016
83	CRSY	-38.0282	143.6397	158.3028
84	CSNO	-28.8656	153.0476	69.4953
85	CTMD	-34.6393	148.0256	356.6110
86	CUT0	-32.0039	115.8948	24.4031
87	CWN2*	-33.5937	151.1716	218.4959
88	CWRA	-33.8312	148.7023	333.7906
89	DARW*	-12.8437	131.1327	125.5993
90	DBBO	-32.2494	148.6021	298.0857
91	DKSN	-35.2508	149.1357	614.2614
92	DLQN	-35.5316	144.9646	110.4609
93	DODA*	-13.8346	131.1868	90.9348
94	DORA	-37.6809	145.0644	141.6509
95	DORR	-30.3504	152.7130	834.4682
96	DRGO	-37.4591	147.2515	221.8083

Continued on next page

Table C.1 – continued from previous page

#	Site name	Latitude	Longitude	Height
97	DUNE	-32.0119	149.3882	413.1726
98	DWHY*	-33.7513	151.2870	67.0065
99	EBNK	-38.2435	145.9360	182.3715
100	ECHU	-36.1403	144.7536	112.5948
101	ECOR	-34.3756	150.9108	43.1883
102	EDEN	-37.0718	149.9093	21.2611
103	EDSV	-25.3758	151.1198	288.7986
104	EPSM	-36.7181	144.3146	207.3879
105	ERMG	-26.7122	143.2623	200.6264
106	ESPA	-33.8743	121.8943	32.9396
107	EXMT	-21.9607	114.1134	16.8816
108	FLND*	-40.2144	148.2416	7.9360
109	FORB	-33.3853	148.0070	270.2160
110	FORS*	-32.2011	152.5224	38.5272
111	FROY	-18.1260	125.8004	156.5934
112	FTDN*	-33.8551	151.2252	28.3451
113	GABO	-37.5681	149.9152	24.5242
114	GASC	-24.6326	115.3386	182.7909
115	GATT	-27.5439	152.3311	140.9960
116	GFEL	-33.8930	148.1607	412.9922
117	GFTH	-34.2863	146.0368	162.0801
118	GGTN	-18.3060	143.5406	367.6365
119	GILG	-31.7110	148.6625	319.8745
120	GLB2	-34.7464	149.7111	693.6624
121	GLBN	-34.7557	149.7177	679.1440
122	GLDN*	-38.2089	147.4027	25.6983
123	GLEN	-36.9090	142.6619	181.1026
124	GLIN	-29.7436	151.7517	1206.1008
125	GNGN	-35.1850	149.1305	645.6183
126	GNOA	-37.4769	149.5895	32.4637
127	GONG	-34.4272	150.8988	76.0334
128	GOOL	-33.9845	145.7069	138.9255
129	GORO	-36.7182	141.4728	171.1858
130	GUNN	-30.9782	150.2563	304.2452
131	GURL	-29.7348	149.7955	256.4101
132	HATT	-34.7557	142.3395	62.0730
133	HAY1	-34.5055	144.8525	108.2363
134	HERN	-30.3266	152.4869	1242.1402
135	HILL	-33.4849	145.5313	141.1522
136	HLBK	-35.7244	147.3174	285.0307
137	HNSB*	-33.7003	151.0976	228.5538
138	HOB2	-42.8047	147.4387	41.5529
139	HOTH	-36.9821	147.1418	1774.4288
140	HRSM	-36.7228	142.1749	144.7237
141	HUGH	-20.9474	144.2045	524.3941
142	HYDN	-32.4494	118.8919	300.5595
143	IHOE	-32.8641	143.4921	151.4403
144	INVL	-29.7764	151.1144	627.6273
145	IPSR	-27.6147	152.7554	75.9133
146	IRYM	-34.2197	142.1912	72.6862

Continued on next page

Table C.1 – continued from previous page

#	Site name	Latitude	Longitude	Height
147	JAB2*	-12.6602	132.8945	83.0328
148	JERI	-35.3553	145.7255	130.1352
149	JERV	-22.8605	136.1007	382.3573
150	JLCK	-20.6693	141.7390	169.8150
151	KALG	-30.7844	121.4593	338.5061
152	KARR	-20.9814	117.0972	109.6540
153	KAT1	-14.3760	132.1533	184.7882
154	KAT2	-14.3751	132.1525	184.6940
155	KELN	-31.6223	117.7026	253.4759
156	KEPK	-37.7211	144.8479	89.9740
157	KGIS*	-39.9418	143.8471	6.5874
158	KILK	-26.0842	152.2521	251.4038
159	KILM	-37.2922	144.9514	358.3226
160	KIRR*	-34.0434	151.0731	119.0212
161	KMAN	-16.1177	130.9555	128.6286
162	KRNG	-35.7354	143.9223	90.9640
163	KTMB	-33.6958	150.3182	1017.9590
164	KTON	-37.2475	144.4532	529.2269
165	KULW	-32.3262	145.0098	269.5049
166	KUNU*	-15.6770	128.7626	92.3868
167	LALB	-35.6735	143.3753	98.0950
168	LAMB	-26.9386	134.0629	311.6505
169	LARR	-15.5732	133.2128	229.7485
170	LGOW	-33.4810	150.1598	969.8293
171	LIAW	-41.9023	146.6731	1054.7718
172	LILY	-41.2516	147.2148	170.5791
173	LIPO	-34.1054	141.0112	64.5516
174	LIRI	-29.4297	147.9829	186.4404
175	LKHT	-35.2273	146.7058	169.9407
176	LKYA*	-12.4555	130.8247	69.8053
177	LONA	-28.8784	121.3191	354.6374
178	LORD*	-31.5199	159.0612	71.9133
179	LOTH	-30.5335	145.1168	123.1483
180	LURA	-15.5775	144.4570	151.0395
181	MACK*	-30.7104	152.9184	43.8510
182	MAFF	-37.9722	146.9853	43.1671
183	MAIN	-14.0462	134.0929	162.5822
184	MANY	-35.0486	141.0619	85.4926
185	MARY	-37.0054	143.7598	220.0099
186	MCHL	-26.3589	148.1450	535.0041
187	MEDO	-26.7574	114.6096	110.2305
188	MENA	-34.1261	150.7438	111.8561
189	MENO	-34.2724	141.8066	62.7805
190	MGRV	-33.6265	150.8310	45.6563
191	MIMI	-36.5322	147.3732	291.1076
192	MITT	-35.1560	142.6577	73.0716
193	MLAK	-38.0816	142.8084	140.6772
194	MNDE	-32.3928	142.4179	80.2961
195	MNGO	-38.7798	143.6517	62.5660
196	MNSF	-37.0655	146.0865	357.2503

Continued on next page

Table C.1 – continued from previous page

#	Site name	Latitude	Longitude	Height
197	MOBS	-37.8294	144.9753	40.9997
198	MOOR	-37.4022	142.1314	279.9374
199	MOUL	-35.0911	144.0360	84.4687
200	MRBA	-17.0180	145.3238	645.9328
201	MREE	-29.4577	149.8255	246.3842
202	MRNO	-37.7197	141.5487	88.4764
203	MRNT	-38.2293	145.0663	60.6739
204	MRO1	-26.6966	116.6375	354.4802
205	MRWA	-32.1398	150.3553	288.6682
206	MSVL	-34.5505	150.3734	703.6099
207	MTBU	-37.1451	146.4488	1601.1022
208	MTCV	-25.9457	133.2067	545.6636
209	MTDN	-22.1328	131.4927	672.9093
210	MTEM	-37.5874	143.4489	499.4204
211	MTHR	-32.6154	151.0991	96.5481
212	MTIS	-20.6904	139.4864	398.4523
213	MTMA	-28.1153	117.8431	389.8779
214	MUDG	-32.5900	149.5847	482.8276
215	MULG	-30.2820	134.0586	215.8352
216	MURR	-35.2626	141.1811	78.0319
217	MWAL	-35.9931	145.9885	144.6757
218	MYRT	-36.5580	146.7222	227.6936
219	NBRI	-30.3301	149.7864	254.1446
220	NBRK	-29.6772	145.8140	181.8873
221	NCLF	-34.7084	116.1233	71.5958
222	NDRA	-34.7519	146.5375	169.5692
223	NEBO	-21.6403	148.6985	341.9637
224	NELN	-38.0479	141.0062	9.9052
225	NEWE*	-32.9240	151.7887	30.5965
226	NEWH*	-38.5140	145.3521	21.3542
227	NGAN	-31.5639	147.1946	204.4563
228	NHIL	-36.3084	141.6460	139.7457
229	NMBN	-28.5978	153.2316	112.5334
230	NMTN	-17.6717	141.0692	61.0708
231	NNOR	-31.0487	116.1927	235.2477
232	NORS	-32.2600	121.7872	461.6734
233	NRMN	-32.2345	148.2387	270.2450
234	NSTA	-29.0456	150.4441	458.7121
235	NTJN	-21.4572	133.9700	619.7262
236	NWCS*	-32.9296	151.7652	53.3696
237	NWRA*	-34.8738	150.6048	46.9929
238	NYMA	-32.0662	146.3156	332.8054
239	OBRN	-33.7040	149.8576	1137.8191
240	OMEO	-37.1020	147.6006	712.8592
241	ORNG	-33.2852	149.0980	907.3583
242	OVAL	-32.7539	148.6460	409.8922
243	PACH	-35.3829	142.1909	82.5288
244	PARK	-32.9988	148.2646	397.7739
245	PBOT*	-33.9740	151.2121	34.9552
246	PERI	-36.4113	148.4100	1754.2294

Continued on next page

Table C.1 – continued from previous page

#	Site name	Latitude	Longitude	Height
247	PERT	-31.8020	115.8852	13.1881
248	PIAN	-35.0543	143.3277	79.2113
249	PKVL	-37.7998	144.9609	67.9204
250	PMAC*	-31.4619	152.8977	44.3139
251	POCA	-38.6174	142.9970	13.0527
252	POON	-33.3825	142.5669	57.1020
253	PRCE	-35.3636	149.0890	640.1821
254	PRKS	-33.1347	148.1765	367.9672
255	PRTF	-38.3850	142.2383	13.1430
256	PTHL	-20.5397	118.6789	41.3956
257	PTKL	-34.4756	150.9137	34.9729
258	PTSV	-35.0947	138.4857	60.5654
259	PUTY	-32.9530	150.6595	296.8751
260	QCLF	-38.2703	144.6381	12.6559
261	QUAM	-30.9330	147.8700	185.8990
262	RAND	-35.5938	146.5785	179.7254
263	RANK	-33.8420	146.2616	240.9443
264	RAVN	-33.5967	120.0709	206.1431
265	RBVL	-34.5903	142.7699	84.5272
266	RGLN	-33.4157	149.6550	781.3629
267	RHPT*	-41.0651	145.9618	26.3865
268	RKLD	-19.9676	137.8348	276.6468
269	RNBO	-35.9098	141.9929	116.7599
270	RNSP	-18.3879	133.8165	348.8764
271	ROBI*	-28.0770	153.3813	65.7134
272	RUTH	-36.0985	146.5089	211.6357
273	RUUS	-34.0425	141.2690	39.5468
274	RYLS	-32.7925	149.9767	611.4507
275	SA45	-32.4703	137.9343	202.3939
276	SCON	-32.0514	150.8696	247.9977
277	SEAL	-35.5045	142.8487	71.3850
278	SEMR	-37.0242	145.1392	157.0105
279	SKIP	-37.6849	143.3595	302.6395
280	SNGO	-32.5582	151.1757	75.6858
281	SPBY*	-42.5464	147.9308	1.5848
282	SPWD	-33.6985	150.5639	399.9221
283	SRVC	-36.3779	140.9892	127.7634
284	STHG	-24.3502	143.2853	196.1051
285	STNY*	-38.3752	145.2140	29.8339
286	STR1	-35.3155	149.0100	800.4510
287	STR2	-35.3162	149.0102	802.9989
288	STR3	-35.3157	149.0099	799.4354
289	STRH	-37.7288	141.1365	70.8256
290	SWNH	-35.3435	143.5602	90.4827
291	SYDN*	-33.7809	151.1504	86.1010
292	SYM1	-35.3425	149.1611	592.6509
293	TAMW	-31.0929	150.9309	440.0610
294	TARE*	-31.9122	152.4638	45.2993
295	TATU	-36.4397	145.2704	130.1012
296	TBOB	-29.4502	142.0574	191.5637

Continued on next page

Table C.1 – continued from previous page

#	Site name	Latitude	Longitude	Height
297	TELO	-36.1260	141.1109	144.8450
298	THEV	-32.1286	133.6968	7.9507
299	THOM	-37.8435	146.3982	480.2044
300	TID1	-35.3992	148.9800	665.8588
301	TITG*	-10.5865	142.2220	76.3772
302	TLPA	-30.8670	144.4138	184.3981
303	TMBA	-35.7777	148.0115	667.4199
304	TMBO	-24.7717	146.2841	589.9590
305	TMRA	-34.4465	147.5344	319.9854
306	TMUT	-35.3011	148.2202	306.5320
307	TNTR	-29.0548	152.0199	901.5924
308	TOMP	-22.8465	117.4003	435.0228
309	TOOG	-27.0833	152.3664	194.0151
310	TOTT	-32.2534	147.3697	263.1794
311	TOW2*	-19.2693	147.0557	88.6409
312	TULL	-32.6322	147.5697	271.8028
313	TURO*	-36.0352	150.1222	53.7523
314	UCLA	-31.6796	128.8832	67.0276
315	ULLA	-35.3620	150.4653	63.5282
316	UNDE	-35.1712	141.8126	69.0185
317	VLWD*	-33.8806	150.9772	43.0942
318	WAGN	-33.3331	117.4101	289.4217
319	WAKL	-35.4553	144.3810	92.1450
320	WALW	-35.9660	147.7342	242.7072
321	WARA	-25.0372	128.2962	587.6008
322	WARI	-29.5406	150.5742	372.5231
323	WARW	-28.2135	152.0304	507.8475
324	WBEE	-37.9061	144.6686	33.7431
325	WDBG	-28.3934	152.6071	435.5603
326	WEDD	-36.4255	143.6140	199.5609
327	WEEM	-29.0133	149.2545	204.0893
328	WEND	-37.5378	143.8302	472.4569
329	WFAL*	-34.1342	150.9950	252.0812
330	WGGA	-35.1072	147.3693	216.4085
331	WILU	-26.6257	120.2184	494.0226
332	WLAL*	-19.7786	120.6435	21.5516
333	WLCA	-31.5553	143.3751	97.2486
334	WLGT	-30.0234	148.1169	170.7406
335	WLWN	-30.9306	152.6255	90.1148
336	WMGA	-19.9334	134.3545	417.9501
337	WORI	-37.7771	145.5300	118.3757
338	WOTG*	-38.6081	145.5909	52.3057
339	WRRN	-31.7008	147.8364	229.5361
340	WTCF	-30.8533	143.0930	169.1672
341	WWLG	-33.7034	147.3217	360.1698
342	WYCH	-36.0775	143.2259	120.9002
343	WYNG	-33.2826	151.4240	58.3418
344	YALL	-38.1821	146.3490	65.1665
345	YANK*	-38.8123	146.2069	30.3260
346	YAR2	-29.0466	115.3470	241.7038

Continued on next page

Table C.1 – continued from previous page

#	Site name	Latitude	Longitude	Height
347	YAR3	-29.0465	115.3471	243.0873
348	YARO	-31.2363	151.9222	997.0579
349	YARR	-29.0466	115.3470	241.7951
350	YARS	-34.5280	141.4546	97.4983
351	YASS	-34.8449	148.9132	523.1342
352	YEEL	-34.1442	135.7844	170.2284
353	YELO	-31.2907	119.6458	347.5629
354	YIEL	-35.9279	145.2358	117.5557
355	YMBA*	-29.4474	153.3579	44.0501
356	YNKI*	-38.8122	146.2183	30.4220
357	YRRM	-38.5652	146.6752	36.1961
358	YULA	-25.2311	130.9416	512.6471
359	YUNG	-34.3038	148.2827	445.3800

Appendix D

List of publications and research output

D.1 Peer-reviewed journal papers

Year	Citation
2020	Matviichuk, B., King, M. A., & Watson, C. S. (2020). Estimating ocean tide loading displacements with GPS and GLONASS. *Solid Earth*, *11*(5), 1849–1863. https://doi.org/10.5194/se-11-1849-2020
2021	Matviichuk, B., King, M. A., Watson, C. S., & Bos, M. S. (2021b). Limitations in One-Dimensional (an)Elastic Earth Models for Explaining GPS-Observed M2 Ocean Tide Loading Displacements in New Zealand. *Journal of Geophysical Research: Solid Earth*, *126*(6). https://doi.org/10.1029/2021JB021992
2021	Matviichuk, B., King, M. A., Watson, C. S., & Bos, M. S. (2021a). Comparison of state of the art observed and predicted OTL displacements across the Australian continent. *Journal of Geodesy*, (in review)

D.2 Poster presentations

Year	Event
2017	Matviichuk, B., King, M. A., Watson, C. S., *How elastic is the subdaily motion of the earth's plates?*, Graduate Research Conference, 7-8 September, Hobart, Australia.
2019	Matviichuk, B., King, M. A., Watson, C. S. and Bos M. S., *Advantages of GPS+GLONASS combined processing for estimating tidal deformations of the solid Earth*, The International Union of Geodesy and Geophysics 8-18 July, Montreal, Canada.
2019	Matviichuk, B., King, M. A., Watson, C. S. and Bos M. S., *Estimating tidal deformations with GPS+GLONASS: results from the UK and New Zealand*, American Geophysical Union Fall Meeting, 8-13 December, San Francisco, United States of America.
2020	Matviichuk, B., King, M. A., Watson, C. S. and Bos M. S., *M_2 Ocean Tide Loading displacements in New Zealand with GPS*, American Geophysical Union Fall Meeting, 13-17 December, San Francisco, United States of America.

D.3 Software

Year	Citation
2020	Matviichuk, B. (2020). *GipsyX_Wrapper* (Version v0.1.0). Zenodo. https://doi.org/10.5281/zenodo.4001166